

Investigations on Rupture Disc under Pressure Impulse

THESIS

Submitted in partial fulfilment
of the requirements for the degree of

DOCTOR OF PHILOSOPHY

by

KANAKADANDI GOPINATH

ID. No. 2017PHXF0701H

Under the Supervision of
Prof. VENKATA DASESWARA RAO YENDLURI
BITS-PILANI, HYDERABAD

and

Under the Co-supervision of
Dr. VIJAYABASKAR NARAYANAMURTHY
DEFENCE R & D ORGANISATION, INDIA



BITS Pilani
Pilani | Dubai | Goa | Hyderabad

BIRLA INSTITUTE OF TECHNOLOGY AND SCIENCE - PILANI
2023

BIRLA INSTITUTE OF TECHNOLOGY AND SCIENCE, PILANI

CERTIFICATE

This is to certify that the thesis entitled “**Investigations on Rupture Disc under Pressure Impulse**” submitted by **KANAKADANDI GOPINATH**, ID No. **2017PHXF0701H** for award of Ph.D. of the Institute embodies original work done by him under our supervision.

Signature of the Supervisor :

Name in capital letters : **Prof. VENKATA DASESWARA RAO YENDLURI**

Designation : Professor

Date : 03-05-2023

Signature of the Supervisor :

Name in capital letters : **Dr. VIJAYABASKAR NARAYANAMURTHY**

Designation : Technology Advisor (Defence Technology)

Defence R&D Organisation, Embassy of India,
Washington D.C., USA

Date : 03-05-2023

DECLARATION

I, Kanakadandi Gopinath, declare that

- a. The work contained in this thesis is original and has been done by myself under the general supervision of my supervisors.
- b. The work has not been submitted to any other Institute for any degree or diploma.
- c. I have followed the guidelines provided by the institute in writing the thesis.
- d. I have conformed to the norms and guidelines given in the Ethical Code of Conduct of the Institute.
- e. Whenever I have used materials (data, theoretical analysis, and text) from other sources, I have given due credit to them by citing them in the text of the thesis and giving their details in the references.
- f. Whenever I have quoted written materials from other sources, I have put them under quotation marks and given due credit to the sources by citing them and giving the required details in the references.

Signature of the Student :

Name in capital letters : KANAKADANDI GOPINATH

2017PHXF0701H

Date :

ACKNOWLEDGEMENT

I would like to express my sincere gratitude to the various individuals who have contributed to my research work in one way or another. Firstly, I extend my heartfelt thanks to my **research supervisors, Prof. Venkata Daseswara Rao Yendluri and Dr. Vijayabaskar Narayanamurthy**, for their exceptional guidance, unwavering encouragement, immense patience, and valuable advice throughout my research journey. Their support and constructive criticism have been instrumental in the successful completion of my research work and dissertation. I deeply appreciate their moral support and for standing by me during all situations, which has been crucial in keeping me motivated and focused. Without their constant assistance, this work would not have been possible.

I thank **Prof. Sabareesh Geeta Rajasekaran** and **Prof. Nithin Kotkunde**, the Doctoral Advisory Committee members in the Department of Mechanical Engineering, BITS-Pilani, Hyderabad Campus, for their valuable time in reviewing my thesis and providing insightful suggestions. I also thank Dr. Supradeepan and all the faculties in the Department of Mechanical Engineering, BITS-Pilani, Hyderabad Campus, for their encouragement and support during my research work. Furthermore, I would like to convey my special thanks to **Prof. N Suresh Kumar Reddy**, Head and **Prof. Amit Kumar Gupta**, former Head, Department of Mechanical Engineering, BITS-Pilani, Hyderabad Campus, for their kind encouragement and support. Additionally, I thank Dr. T. Janardhana Reddy (Tech-Mahindra), my senior at BITS-Pilani, for his valuable moral support during my challenging times.

I am grateful to the Seniors, Director, and Technology Director at **Research Centre Imarat, Defence R&D Organization, Hyderabad**, for allowing me to conduct my research work.

Additionally, I extend my thanks to DRDL and Prof. Syed Nizamudhin Khaderi from IIT Hyderabad for their support in material testing and experiments. I would also like to express my appreciation to Shri Vidyasagar from M/s Venkateswara Associates for his invaluable and unconditional support in experimentation.

I place my deep sense of gratitude and thanks to my wife, Archana, children-Alekhya and Karthik and mother Lakshmi and grandparents Shri Viswapathi Sastry and Smt Annapoorna, my sisters Smt Archana and Smt Srividya and brother Shri Rajesh and brother-in-law Shri K Jaganmohan for their unconditional support and loving encouragement throughout my life.

Very importantly, I am always grateful to the *Almighty* for everything in my life.

Kanakadandi Gopinath

Dedicated to my Father Late Shri. Kanakadandi Satyanarayana Sastry

Abstract

Motor containers are closed vessels used for storing motors. They are sealed from external environment by maintaining an internal pressure marginally higher than the atmospheric pressure. They are provided with covers (lids) which need to be removed without manual intervention just before or during the initiation of motor. Rupture disc or explosive panel stands as an excellent choice in such application. Rupture disc is a thin metallic disc, designed to fail at a predetermined pressure and pattern. Its design must meet loading under inside storage pressure and fail instantaneously upon initiation of the motor, experiencing very high loading rates.

In general engineering, rupture disc is used as a sacrificial element in high pressure systems as safety valves, explosive vent for protecting explosive chambers, and as a separating member in shock tubes to generate a required shock wave. In these applications, size of the rupture disc is small, and fail suddenly under very low loading rate upon increase in the pre-set pressure. Established design codes and guidelines exist to select the rupture disc for a given operating and failure pressures. On the other hand, only a very limited knowledge exist to design rupture disc for a motor container. The present thesis is initiated to address this research gap.

In the *initial phase*, a non-linear explicit FEA methodology is established to simulate the failure of a flat scored metallic disc (FSMD) made of S235JR structural steel and validated with available experimental results. Here, an elasto-plastic material model and continuum damage mechanics based failure model proposed by Johnson-Cook are used where the initial material and damage parameters are taken from the literature but finalised after several attempts to match the response observed in experiments. In the *second phase*, this FEA methodology extended to study the flat scored metallic disc (FSMD) and domed scored metallic disc (DSMD) to understand its behaviour under the influence of various geometric and operating parameters. *Operating ratio*, a ratio of maximum static operating pressure to the burst pressure and *impulse transmitted*, the energy absorbed up to burst of the disc are proved to be decisive factors in finalising the design of rupture disc for the motor container. Accordingly, an initial design of DSMD made of E250 structural steel is proposed for the present application considering the material availability, suitability, manufacturing feasibility and further experimentations.

The *third phase* of the research is devoted to experimentation. As J-C's material and damage model parameters for E250 structural steel are not available in literature, they are determined by conducting several experiments at different strain rates, temperatures and stress tri-axialities and verified through three different experimental validations. As the manufacturing of DSMD posed challenges through conventional manufacturing approach, hydroforming technique is explored to form the dome shape. An experimental setup is designed and realised with appropriate instrumentation considering the experimentation feasibilities within the laboratory to achieve maximum possible pressure loading rate. Burst experiments are conducted on ten discs under hydrostatic and pneumatic loads. The results

are compared with numerical simulations. Close agreement is observed between the experiments and numerical simulations on the burst pressure, damage pattern and strain evolution at different critical locations. Difference of 1.5% and 3.1% respectively, are found for FSMD and DSMD on the burst pressure.

Even with a high operating ratio close to 17%, the DSMDs exhibit high burst pressure (~ 6 bar) and high impulse. Therefore, in the *fourth i.e. final phase* of research, non-monolithic rupture disc configurations are explored. Several variants of design are developed and numerically analysed for container application. The responses of all variants are compared with respect to operating parameters such as *burst pressure*, *factor of safety* under static pressure, *operating ratio* and *impulse transmitted* and proposed an *RD selection criterion* to finalise and recommend an optimum configuration for given application. Finally, based on the proposed *RD selection criterion*, a variant of non-monolithic configuration of rupture disc having double slits joined by scores is recommended and this design resulted in a burst pressure of 2.3 bar, 65% lesser than the DSMD and an operating ratio of 11%.

Thus, the thesis provides a clear understanding on the behaviour of monolithic and non-monolithic configurations of rupture discs, simulation and experimentation approaches and their adaptability for the container.

Table of Contents

Certificate	i
Declaration	ii
Acknowledgement	iii
Abstract	vi
Table of Contents	viii
List of Tables	xiv
List of Figures	xvi
List of Abbreviations	xxx
List of Symbols	xxxi
Chapter 1 Introduction	1 - 22
1.1 Background	1
1.2 Introduction to rupture discs	1
1.2.1 Classification of RDs	2
1.2.2 Applications of rupture discs or rupture panels	7
1.2.3 Materials for construction of RD	10
1.2.4 General design guidelines and important terminologies	11
1.2.5 Design considerations for rupture discs for the present application	12
1.3 Large deformation and rupture of thin flat metallic discs under impulsive loading and failure modes	14
1.4 Existing knowledge on rupture disc	15
1.5 Research gap	16
1.6 Research objectives	17
1.7 Research methodology	17
1.8 Organisation of the thesis	20
1.9 Summary	22
Chapter 2 Material Characterization for Constitutive and Damage Model Parameters	23-50
2.1 Introduction	23

2.2	Evaluation of J-C material model constants	26
2.2.1	Johnson-Cook strength model	26
2.2.2	Johnson-Cook damage model	26
2.2.3	Implementation of damage evolution	27
2.3	Experiments	28
2.3.1	Specimen geometry	28
2.3.2	Tensile experiments at various strain rates	30
2.3.3	SHPB experiments at higher strain rates	32
2.3.4	Tensile experiments of notched specimens	35
2.3.5	Tensile experiments at elevated temperatures	36
2.4	Determination of parameters	38
2.4.1	J-C strength model parameters	38
2.4.2	J-C damage model parameters	40
2.4.3	Damage evolution	44
2.4.4	J-C material and damage parameters	45
2.5	Validation of J-C material and damage model parameters	45
2.5.1	Validation-1: Plain tensile specimen	45
2.5.2	Validation-2: Notched tensile specimen	46
2.5.3	Validation-3: Hydrostatic burst experiment of FSMD	47
2.6	Modification of J-C material model	47
2.6.1	Modification of strain rate effect in J-C material model	48
2.6.2	Comparison of predicted and experimental stress-strain response	50
2.7	Summary	50

Chapter 3 Flat Scored Metallic Disc-Numerical Simulation and Experimental Validation 51-75

3.1	Introduction	51
3.2	Simulation methodology and validation with experiment	51
3.2.1	Geometry	51
3.2.2	Experimental setup	52
3.2.3	Material and damage models	52
3.2.4	FEA simulation	53

3.2.5	Results of numerical simulation	55
3.2.6	Experimental validation of simulation results	56
3.3	Studies on FSMD	57
3.3.1	Geometry for FEA	57
3.3.2	FSMD under constant internal pressure	58
3.3.3	FSMD under impulsive loading	59
3.4	Summary	75
Chapter 4	Behaviour of Domed Scored Metallic Disc	76-117
4.1	Introduction	76
4.2	Operating parameters	77
4.2.1	Operating ratio	77
4.2.2	Impulse	77
4.3	Domed SMD under storage pressure	77
4.3.1	Actual geometry and model for FEA	77
4.3.2	Domed SMD under constant internal pressure	79
4.3.3	FEA and results	79
4.4	Simulation of domed SMD under impulsive loading	80
4.4.1	Effect of loading rate	82
4.4.2	Influence of geometrical features on the behavior of domed SMD	85
4.4.3	Results and discussions	106
4.5	Comparison on behaviour of FSMD and DSMD	110
4.5.1	Effect of loading rate (\dot{P})	110
4.5.2	Effect of D/t ratio	111
4.5.3	Effect of t_1/t ratio	112
4.5.4	Effect of b/t ratio	113
4.5.5	Effect of l/R ratio	114
4.5.6	Effect of number of scores (N)	115
4.5.7	Effect of score's geometry	116
4.6	Preliminary DSMD configuration	117
4.7	Summary	117

Chapter 5	Manufacturing of Domed Metallic Disc	118-133
5.1	Introduction	118
5.2	Hydro-forming of GS (galvanised steel) disc	119
5.2.1	Evaluation of GS material properties	120
5.2.2	Numerical simulation of hydro-forming process	121
5.2.3	Simulation results	121
5.2.4	Hydro-forming experimental setup	124
5.2.5	Results and discussions on GS disc	126
5.3	Hydro-forming of E250 structural steel disc	127
5.3.1	Disc geometry	127
5.3.2	FE model setup and analysis of E250 structural steel disc	128
5.3.3	FE simulation results	128
5.3.4	Hydro-forming experimental setup	130
5.3.5	FE analysis of hydro-forming experimental setup	130
5.3.6	Experimental setup and hydro-forming experiment	132
5.3.7	Results and discussions on hydro-forming of E250 disc	132
5.4	Summary	133
Chapter 6	Experiments on Scored Metallic Discs	134-155
6.1	Introduction	134
6.2	Geometry of discs	134
6.2.1	Flat scored metallic disc	134
6.2.2	Domed scored metallic disc	135
6.3	Design and analysis of experimental setup	136
6.3.1	Configuration of the experimental setup	136
6.3.2	Measurement plan	138
6.3.3	FE analysis of the experimental setup	138
6.4	Experimental procedure	141
6.5	Observations and results	141
6.5.1	Hydraulic experiment of FSMD – F2	141
6.5.2	Pneumatic experiment of FSMD – F3	143
6.5.3	Pneumatic experiment on FSMD – F4	143

6.5.4	Hydraulic experiment on DSMD – D1	144
6.5.5	Pneumatic experiment of DSMD – D2	145
6.5.6	Pneumatic experiment of DSMD – D3	146
6.5.7	Summary of experimental results	146
6.6	Numerical simulation	147
6.6.1	Numerical simulation of FSMD	147
6.6.2	Numerical simulation of DSMD	149
6.7	Comparison of experimental results with predictions	151
6.7.1	Comparison of results for FSMD	151
6.7.2	Comparison of results for DSMD	153
6.8	Summary	154
Chapter 7	Non-Monolithic Design of Rupture Disc	156-170
7.1	Introduction	156
7.2	RD selection criteria	157
7.2.1	Burst pressure and Factor of Safety	157
7.2.2	Operating ratio	157
7.2.3	Impulse	157
7.3	Geometrical configurations	157
7.4	Numerical simulation of slit disc (Variant-1)	162
7.4.1	FE model, loads and boundary conditions	162
7.4.2	Simulation under static loading	162
7.4.3	Simulation under impulsive loading	163
7.5	Results and discussions	164
7.5.1	FE analysis results	164
7.5.2	Summary of results	168
7.5.3	Discussion of results and recommendation	169
7.6	Summary	170
Chapter 8	Conclusions and Future Work	171-176
8.1	Conclusions	171
8.1.1	Studies on scored metallic discs	171
8.1.2	Effect of influencing parameters on the behaviour of DSMD	172

8.1.3	RD selection for motor container	173
8.1.4	Johnson-Cook material and damage models	174
8.1.5	Hydro-forming for domed RDs	174
8.1.6	Overall conclusion	174
8.2	Specific research contributions	174
8.3	Limitation in present research	175
8.4	Scope for future work	175
References		177-183
List of Publications		184
Biography of the Candidate		185
Biography of Supervisors		186-187

List of Tables

Table No.	Description	Page No.
1.1	Classification of rupture discs	8
1.2	Operating ratios for different RD configurations	8
1.3	Materials used for rupture discs	11
1.4	Important terminology used in RD	11
2.1	Applicable material and damage models available in commercial FEA software	24
2.2	Chemical composition of E250 structural steel (% mass)	28
2.3	Details of experiments and specimens for determining parameters of Johnson-Cook material and damage models	30
2.4	Determined parameters of Johnson-Cook strength and damage models	45
3.1	Elastic and material constants in JC material and damage models	53
3.2	Influence of D/t on response of FSMD	64
3.3	Influence of t_1/t on response of FSMD	66
3.4	Influence of b/t on response of FSMD	68
3.5	Influence of l/R on response of FSMD	70
3.6	Predicted failure pattern without and with the number of scores in the FSMD	71
3.7	Influence of number of scores on response of FSMD	73
3.8	Influence of score's geometry on response of FSMD	75
4.1	Initial values of geometric features for DSMD	78
4.2	Influence of D/t on response of DSMD	87
4.3	Influence of H/D on response of DSMD	90
4.4	Influence of t_1/t on response of DSMD	93
4.5	Influence of b/t on response of DSMD	96
4.6	Influence of l/R on response of DSMD	99
4.7	Predicted failure pattern without and with number of scores in DSMD	100
4.8	Influence of number of scores on response of DSMD	103
4.9	Influence of score geometrical features on response of DSMD	105

5.1	Results for static structural analysis of hydro-forming setup components	131
6.1	Results for static structural analysis of experimental setup components	139-140
6.2	Comparison of experimental and numerical simulation results	155
7.1	Variants of RD considered for the present study	158-161
7.2	Results of numerical simulation for RD variants	164-167
7.3	RD selection	170

List of Figures

Figure No.	Description	Page No.
1.1	Typical rupture disc	2
1.2	Flat plate type rupture disc: tension/ shear loaded	3
1.3	Forward domed rupture disc: tension loaded	4
1.4	Reverse domed rupture disc: compression loaded	5
1.5	Solid material rupture disc	6
1.6	Scored rupture disc	6
1.7	Composite (non-monolithic) rupture disc	7
1.8	Rupture disc as a pressure relief valve	9
1.9	Rupture disc as diaphragm in the shock tube	9
1.10	Explosion panel attached to explosion chamber: a) Explosion panel b) Explosion chamber	10
1.11	Temperature / burst pressure relationship	13
1.12	Research methodology adopted in present work	19
1.13	Overall organisation of thesis chapters	21
2.1	Implementation of Damage evolution	27
2.2	Experimental setup for stress-strain behaviour: a) UTM for uniaxial tensile tests at room temperature b) UTM for uniaxial tensile tests at higher temperatures c) SHPB setup for experiments at high strain rates	29
2.3	Plain specimens for uniaxial tensile experiments at various strain rates at room temperature a) Specimen geometry (thickness = 2.0 mm) b) Tested specimens 1 to 6 (Batch E1)	31
2.4	Averaged true stress-true strain curves of plain tensile specimens at various strain rates, obtained from tensile experiments at room temperature	31
2.5	Specimens for SHPB experiments at higher strain rates: a) Specimen geometry	33

	b) Tested specimens 7 and 8 (Batch E1)	
2.6	Typical strain signals from SHPB setup and true stress-true strain curves obtained from SHPB experiments:	34
	a) Typical strain signals obtained from SHPB setup. The inset shows the force balance of the sample. Stress acting on the sample-incident bar and sample-transmission bar interfaces are represented by P_1 and P_2 , respectively	
	b) Averaged true stress-true strain curves of specimens at higher strain rates	
2.7	Averaged true stress-true strain curves of specimens at different strain rates	35
2.8	Notched specimens at different stress triaxiality (σ^*) (at strain rate value = 0.0003/s):	36
	a) Specimen geometry (thickness = 2.0 mm)	
	b) Specimens after the experiments 9 to 12 (Batch E1)	
2.9	Averaged true stress-true strain curves of specimens at various σ^* (at strain rate value = 0.0003/s)	36
2.10	Specimens for tensile experiments at elevated temperatures (at strain rate value = 0.0003/s):	37
	a) Specimen geometry (thickness = 2.0 mm)	
	b) Specimens after the experiments 13 to 16 (Batch E1)	
2.11	Averaged true stress-true strain curves of specimens at elevated temperatures (at strain rate value = 0.0003/s)	37
2.12	Determination of B and n	38
2.13	Determination of C	39
2.14	Determination of m	40
2.15	Computation of accumulated critical plastic strain	41
2.16	Obtaining stress triaxiality of notched specimens (9 to 12 shown in Figure 2.8)	42
2.17	Determination of D_1 , D_2 and D_3	42
2.18	Determination of D_4	43
2.19	Determination of D_5	44
2.20	Comparison of experimental and J-C model predictions for plain	46

	tensile specimen:	
	a) Specimen Geometry	
	b) FEA model	
	c) Tested specimen	
	d) Experimental vs predicted results	
2.21	Comparison of experimental and J-C model predictions for a notched tensile specimen:	47
	a) Specimen Geometry	
	b) FEA model	
	c) Tested Specimen	
	d) Experimental vs predicted results	
2.22	Determination of C_1 and C_2 from the proposed method	48
2.23	Comparison of experimental and J-C prediction at various strain rates	49
3.1	Flat metallic disc with scores:	51
	a) Flat scored metallic disc (FSMD)	
	b) FSMD in conditional burst application	
3.2	Experimental disc geometry:	52
	a) Geometry of flat SMD	
	b) Score geometry	
	c) Strain gauge locations	
3.3	Experimental setup for a flat SMD	53
3.4	The simulation model of flat disc:	54
	a) FE model	
	b) Loads and boundary conditions	
3.5	Failure initiation and propagation:	55
	a) At $t = 43$ ms	
	b) At $t = 216$ ms	
	c) At $t = 416$ ms	
	d) At $t = 478$ ms	
3.6	Comparison of deformed pattern, burst pressure and burst time between present simulation and experiment:	56
	a) Present simulation	

	b) Experiment	
3.7	Comparison of strains between present simulation and experiments at locations mentioned in Figure 3.2(c):	57
	a) Location-1 at SG-1 (45° from horizontal-left score)	
	b) Location-2 at SG-2 (135° from horizontal-left score)	
3.8	Geometry of flat metallic disc with scores:	58
	a) Disc geometry	
	b) Score geometry	
3.9	Loads and boundary conditions for FSMD	59
3.10	Deformation and stresses in flat metallic disc under uniform pressure loading:	59
	a) Deformed pattern	
	b) Equivalent stress ($r = 0$ is at disc center)	
3.11	Effect of the loading rate on flat scored disc:	61
	a) Equivalent stress with respect to the applied pressure	
	b) Equivalent strain with respect to the applied pressure	
	c) Strain rate with respect to applied pressure	
	d) Reaction force with respect to central deflection	
	e) Responses with respect to the loading rate	
3.12	Failure initiation location with respect to loading rate	62
3.13	Effect of diameter-to-plate thickness (D/t) ratio:	63
	a) Equivalent stress with respect to applied pressure	
	b) Equivalent strain with respect to applied pressure	
	c) Strain rate with respect to applied pressure	
	d) Reaction force with respect to central deflection	
	e) Responses with respect to (D/t) ratio	
3.14	Effect of score's depth-to-plate thickness ratio (t_1/t):	65
	a) Equivalent stress with respect to the applied pressure	
	b) Equivalent strain with respect to applied pressure	
	c) Strain rate with respect to the applied pressure	
	d) Reaction force with respect to central deflection	
	e) Responses with respect to (t_1/t) ratio	
3.15	Effect of score's width-to-plate thickness (b/t) ratio:	67

	a) Equivalent stress with respect to applied pressure	
	b) Equivalent strain with respect to applied pressure	
	c) Strain rate with respect to applied pressure	
	d) Reaction force with respect to central deflection	
	e) Responses with respect to (b/t) ratio	
3.16	Effect of score's length-to-disc radius (l/R) ratio:	69
	a) Equivalent stress with respect to applied pressure	
	b) Equivalent strain with respect to applied pressure	
	c) Strain rate with respect to applied pressure	
	d) Reaction force with respect to central deflection	
	e) Responses respect to (l/R) ratio	
3.17	Effect of number of scores:	72
	a) Equivalent stress with respect to applied pressure	
	b) Equivalent strain with respect to applied pressure	
	c) Strain rate with respect to applied pressure	
	d) Reaction force with respect to central deflection	
	e) Responses with respect to the number of scores	
3.18	Effect of the score's geometry:	74
	a) Equivalent stress with respect to applied pressure	
	b) Equivalent strain with respect to applied pressure	
	c) Strain rate with respect to applied pressure	
	d) Reaction force with respect to central deflection	
	e) Responses with respect to the score's geometry	
4.1	Forward domed metallic rupture disc with scores:	76
	a) Domed scored metallic disc (DSMD)	
	b) DSMD in conditional burst application	
4.2	Geometry of domed metallic disc with scores:	78
	a) Disc geometry	
	b) Score geometry	
4.3	Loads and boundary conditions for DSMD	79
4.4	Deformation and stresses in domed metallic disc under uniform pressure loading:	79
	a) Deformed pattern	

	b) Equivalent stress ($r = 0$ is at disc centre)	
4.5	Results from mesh convergence studies of domed SMD:	80
	a) Equivalent stress and strain with respect to the applied pressure	
	b) Strain rate with respect to the applied pressure	
	c) Reaction force with respect to the central deflection	
	d) Responses with respect to the element size	
4.6	Failure initiation and propagation in domed scored disc under $\dot{P} = 500$ MPa/s:	81
	a) At time = 1 ms	
	b) At time = 2 ms	
	c) At time = 3.8 ms	
	d) At time = 4.6 ms	
4.7	Effect of loading rate on domed scored disc:	83
	a) Equivalent stress and strain with respect to the applied pressure	
	b) Strain rate with respect to the applied pressure	
	c) Equivalent stress along the radius of the disc in the score	
	d) Equivalent strain along the radius of the disc in the score	
	e) Reaction force with respect to the central deflection	
	f) Responses with respect to loading rate	
4.8	Failure initiation location with respect to the loading rate	84
4.9	Operating parameters with respect to the loading rate:	84
	a) Operating ratio with respect to the loading rate	
	b) Impulse with respect to the loading rate	
4.10	Effect of the diameter-to-plate thickness (D/t) ratio:	86
	a) Equivalent stress and strain with respect to the applied pressure	
	b) Strain rate with respect to the applied pressure	
	c) Equivalent stress along the radius of the disc in the score	
	d) Equivalent strain along the radius of the disc in the score	
	e) Reaction force with respect to the central deflection	
	f) Responses with respect to (D/t) ratio	
4.11	Operating parameters with respect to the (D/t) ratio:	88
	a) Operating ratio with respect to the (D/t) ratio	
	b) Impulse with respect to the (D/t) ratio	

4.12	Effect of the dome height-to-plate diameter (H/D) ratio:	89
	a) Equivalent stress and strain with respect to the applied pressure	
	b) Strain rate with respect to the applied pressure	
	c) Equivalent stress along the radius of the disc in the score	
	d) Equivalent strain along the radius of the disc in the score	
	e) Reaction force with respect to the central deflection	
	f) Responses with respect to the (H/D) ratio	
4.13	Operating parameters with respect to the (H/D) ratio:	91
	a) Operating ratio with respect to the (H/D) ratio	
	b) Impulse with respect to the (H/D) ratio	
4.14	Effect of the score's depth-to-plate thickness ratio (t_1/t); $t=2$ mm:	92
	a) Equivalent stress and strain with respect to the applied pressure	
	b) Strain rate with respect to the applied pressure	
	c) Equivalent stress along the radius of the disc in the score	
	d) Equivalent strain along the radius of the disc in the score	
	e) Reaction force with respect to the central deflection	
	f) Equivalent strain around the score just before the failure	
4.15	Responses with respect to the score's depth-to-plate thickness (t_1/t) ratio:	93
	a) $t=2$	
	b) $t=1$	
4.16	Operating parameters with respect to the (t_1/t) ratio:	94
	a) Operating ratio with respect to the (t_1/t) ratio	
	b) Impulse with respect to the (t_1/t) ratio	
4.17	Effect of the score's width-to-plate thickness (b/t) ratio:	95
	a) Equivalent stress and strain with respect to the applied pressure	
	b) Strain rate with respect to applied pressure	
	c) Equivalent stress along the radius of the disc	
	d) Equivalent strain along the radius of the disc	
	e) Reaction force with respect to the central deflection	
	f) Summary of responses with respect to the (b/t) ratio	
4.18	Operating parameters with respect to the (b/t) ratio:	97
	a) Operating ratio with respect to the (b/t) ratio	

	b) Impulse with respect to the (b/t) ratio	
4.19	Effect of the score's length-to-disc radius (l/R) ratio:	98
	a) Equivalent stress and strain with respect to the applied pressure	
	b) Strain rate with respect to the applied pressure	
	c) Equivalent stress along the radius of the disc in the score	
	d) Equivalent strain along the radius of disc in the score	
	e) Reaction force with respect to the central deflection	
	f) Responses with respect to the score's (l/R) ratio	
4.20	Operating parameters with respect to the (l/R) ratio:	99
	a) Operating ratio with respect to the (l/R) ratio	
	b) Impulse with respect to the (l/R) ratio	
4.21	Effect of the number of scores:	101
	a) Equivalent stress and strain with respect to the applied pressure	
	b) Strain rate with respect to the applied pressure	
	c) Equivalent stress along the radius of the disc in the score	
	d) Equivalent strain along the radius of the disc in the score	
	e) Reaction force with respect to the central deflection	
	f) Responses with respect to the number of scores	
4.22	Operating parameters with respect to the number of scores:	103
	a) Operating ratio with respect to number of scores	
	b) Impulse with respect to the number of scores	
4.23	Effect of the score geometry:	104
	a) Equivalent stress and strain with respect to applied pressure	
	b) Strain rate with respect to the applied pressure	
	c) Equivalent stress at the score along the radius of the disc	
	d) Equivalent strain at the score along the radius of the disc	
	e) Reaction force with respect to the central deflection	
	f) Responses with respect to the geometry of scores	
4.24	Operating parameters with respect to the score's geometry:	106
	a) Operating ratio with respect to score's geometry	
	b) Impulse with respect to the score's geometry	
4.25	Comparison of FSMD and DSMD with respect to the loading rate:	110
	a) Burst pressure with respect to the loading rate	

	b) Burst time with respect to the loading rate	
	c) Central deflection with respect to the loading rate	
4.26	Comparison of FSMD and DSMD with respect to the (D/t) ratio:	111
	a) Burst pressure with respect to the (D/t) ratio	
	b) Burst time with respect to the (D/t) ratio	
	c) Central deflection with respect to the (D/t) ratio	
4.27	Comparison of FSMD and DSMD with respect to the (t_1/t) ratio:	112
	a) Burst pressure with respect to the (t_1/t) ratio	
	b) Burst time with respect to the (t_1/t) ratio	
	c) Central deflection with respect to the (t_1/t) ratio	
4.28	Comparison of FSMD and DSMD with respect to the (b/t) ratio:	113
	a) Burst pressure with respect to the (b/t) ratio	
	b) Burst time with respect to the (b/t) ratio	
	c) Central deflection with respect to the (b/t) ratio	
4.29	Comparison of FSMD and DSMD with respect to the (l/R) ratio:	114
	a) Burst pressure with respect to the (l/R) ratio	
	b) Burst time with respect to the (l/R) ratio	
	c) Central deflection with respect to the (l/R) ratio	
4.30	Comparison of FSMD and DSMD with respect to the number of scores:	115
	a) Burst pressure with respect to the number of scores	
	b) Burst time with respect to the number of scores	
	c) Central deflection with respect to the number of scores	
4.31	Comparison of FSMD and DSMD with respect to the score's geometry:	116
	a) Burst pressure with respect to the score's geometry	
	b) Burst time with respect to the score's geometry	
	c) Central deflection with respect to the score's geometry	
4.32	Proposed preliminary disc configuration:	117
	a) Disc geometry	
	b) Score geometry	
5.1	Thin flat metallic GS disc before and after hydro-forming:	119
	a) Initial geometry	

	b) Expected domed geometry	
5.2	Material properties evaluation of GS:	120
	a) Specimen geometry	
	b) Tensile test specimens	
	c) Stress-strain diagram	
5.3	Loads and boundary conditions of GS disc FE analysis	121
5.4	Equivalent plastic strain and stress after hydro-forming of GS disc:	122
	a) Equivalent plastic strain distribution	
	b) Equivalent plastic stress distribution	
5.5	Response of GS disc under pressure loading:	123
	a) Central deflection versus applied pressure	
	b) Percentage of thickness variation along the radius	
	c) Variation in equivalent plastic strain along radius	
	d) Variation in equivalent plastic stress along radius	
5.6	Hydro-forming die setup:	124
	a) Before forming	
	b) Just after forming	
5.7	Hydro-forming setup: (a) assembly, (b) exploded view of components, and (c) individual fabricated components	125
5.8	Experimental setup:	126
	a) Die assembly connected to the hydraulic supply	
	b) Hydraulic pump	
5.9	Hydro-formed domed GS disc (finished component)	126
5.10	Percentage reduction in thickness of domed GS disc along radius - experiment vs simulation	127
5.11	E250 structural steel disc before and after hydro-forming:	127
	a) Initial geometry	
	b) Expected domed disc	
5.12	Equivalent plastic strain and stress after hydro-forming of E250 disc:	128
	a) Equivalent plastic strain distribution	
	b) Equivalent plastic stress distribution	
5.13	Response of E250 disc subjected to the hydro-forming:	129

	a) Central deflection versus applied pressure	
	b) Percentage of thickness variation along the radius	
	c) Variation in equivalent plastic strain along radius	
	d) Variation in equivalent plastic stress along radius	
5.14	Hydro-forming setup for E250 steel Disc for E250 steel disc	130
	a) Assembly	
	b) Hardware	
	c) Exploded view	
5.15	FE model, loads and boundary conditions for E250 steel disc:	131
	a) Discretized model	
	b) Loads and Boundary conditions	
5.16	Hydro-forming of E250 domed disc:	132
	a) Hydro-forming setup	
	b) Hydro-formed E250 disc	
5.17	Thickness of E250 domed disc along radius from simulation	133
6.1	Experimental disc geometry of FSMD:	134
	a) Geometry of FSMD	
	b) Score geometry	
6.2	Realized FSMDs:	135
	a) Flat Disc-F2	
	b) Flat Disc-F3	
	c) Flat Disc-F4	
6.3	Experimental disc geometry of DSMD:	135
	a) Geometry of DSMD	
	b) Score geometry	
6.4	Realized DSMDs	136
	a) Domed Disc-D1	
	b) Domed Disc-D2	
	c) Domed Disc-D3	
6.5	Schematic view of the experimental setup	136
6.6	Experimental setup:	137
	a) Three-dimensional configuration of the setup	
	b) Realized hardware	

6.7	Model for proof pressure experiment and FE analysis:	138
	a) Assembly	
	b) Sectional view	
6.8	FE model, loads and boundary conditions:	139
	a) Discretized model	
	b) Loads and boundary conditions	
6.9	Proof pressure experimental setup:	140
	a) Preparation for the experiment	
	b) Experimental setup with pressure gauge reading (inset)	
6.10	Experiment on FSMD F2:	142
	a) Before experiment	
	b) After experiment	
	c) Crack formed during the experiment	
6.11	Experiment on FSMD F2 during crack initiation:	143
	a) Pressure with respect to time	
	b) Crack initiation	
6.12	Experiment on FSMD F3:	143
	a) Before experiment	
	b) After experiment	
	c) Pressure with respect to time	
6.13	Experiment on FSMD F4:	144
	a) Before experiment	
	b) After experiment	
	c) Pressure with respect to time	
6.14	Experiment on DSMD D1:	144-145
	a) Pressure with respect to time	
	b) Before experiment	
	c) Crack initiation during experiment	
6.15	Experiment on DSMD D2:	145
	a) Before experiment	
	b) After experiment	
	c) Pressure with respect to time	
6.16	Experiment on DSMD D3:	146

	a) Before experiment	
	b) After experiment	
	c) Pressure with respect to time	
6.17	FE model, loads and boundary conditions of FSMD:	147
	a) FE model	
	b) Loads and boundary conditions	
6.18	Failure initiation and propagation in FSMD:	148
	a) $P = 0.2$ MPa	
	b) $P = 0.326$ MPa	
	c) $P = 0.327$ MPa	
	d) $P = 0.335$ MPa	
6.19	Hydro-forming operation on DSMD	149
6.20	FE model, loads and boundary conditions of DSMD:	149
	a) FE model	
	b) Loads and boundary conditions	
6.21	Failure initiation and propagation in DSMD:	150
	a) $P = 0.25$ MPa	
	b) $P = 0.618$ MPa	
	c) $P = 0.62$ MPa	
	d) $P = 0.625$ MPa	
6.22	Comparison of experimental and numerical results for FSMD:	151-152
	a) Strain gauge location at S1	
	b) Strain gauge location at S8	
	c) Strain gauge location at S2	
	d) Strain gauge location at S7	
	e) Strain gauge location at S3	
	f) Strain gauge location at S5	
	g) Strain gauge location at S4	
	h) Strain gauge location at S6	
6.23	Comparison of experimental and Numerical Results for DSMD:	153-154
	a) Strain gauge location at S1	
	b) Strain gauge location at S8	
	c) Strain gauge location at S2	

	d) Strain gauge location at S7	
	e) Strain gauge location at S3	
	f) Strain gauge location at S7	
	g) Strain gauge location at S4	
	h) Strain gauge location at S6	
7.1	Slotted type non-monolithic rupture disc:	156
	a) Typical slit type RD	
	b) Configuration of Slit type RD	
7.2	Geometric configuration of slit RD	158
7.3	FE model, loads and boundary conditions in RD variants:	162
	a) FE model of Variant-1	
	b) Loads and boundary conditions	
7.4	Failure initiation and propagation in Slit disc (Variant-1):	163
	a) $P = 0.2$ MPa	
	b) $P = 0.435$ MPa	
	c) $P = 0.44$ MPa	
	d) $P = 0.6$ MPa	
7.5	Burst pressure for RD variants	168
7.6	Factor of safety in different RD variants	168
7.7	Operating ratio of different RD variants	169
7.8	Transmitted impulse from different RD variants	169
7.9	RD selection meeting minimum criteria	170

Note: Dimensions in all the figures are specified in mm.

List of Abbreviations

RD	Rupture Disc
FEA	Finite Element Analysis
J-C	Johnson-Cook
SMD	Scored Metallic Disc
FSMD	Flat Scored Metallic Disc
DSMD	Domed Scored Metallic Disc
MSOP	Maximum Static Operating Pressure
SHPB	Split Hopkinson Pressure Bar
UTM	Universal Testing Machine
GS	Galvanised Steel
DOF	Degree of Freedom
OR	Operating Ratio
FS	Factor of Safety

List of Symbols

Symbol	Description
A	J-C variable representing yield stress (MPa)
A_0	Initial cross-sectional area of tensile specimen (mm ²)
A_e	Nozzle exit area (m ²)
A_f	Cross-sectional area of tensile specimen after experiment (mm ²)
A_s	Cross-sectional area of SHPB specimen (mm ²)
A_t	Cross-sectional area of the incident and transmitter bars (mm ²)
B	Strain hardening coefficient (MPa)
b	Score/groove width (mm)
C	Strain rate coefficient
c_0	Fundamental longitudinal velocity of elastic stress wave (m/s)
C_1, C_2	Strain rate parameters
D	Diameter of rupture disc (mm)
D_1, D_2, D_3	Stress triaxiality dependent fracture strain parameters
D_4	Strain rate dependent fracture strain parameter
D_5	Temperature dependent fracture strain parameter
D_i	Damage initiation variable
E	Young's modulus (GPa)
F	Support reaction force (N)
F_t	Thrust force (N)
FS	Factor of safety
G_f	Fracture energy (N/mm)
h	Finite element size (mm)
H	Dome or crown height of the disc (mm)
k	Material constant for rupture disc material
l	Length of the score (mm)
L_s	Thickness of the specimen in SHPB test (mm)
m	Thermal softening exponent
\dot{m}	Mass flow rate (kg/s)
N	Number of scores/grooves

n	Strain hardening exponent
OR	Operating ratio
P	Pressure (MPa)
\dot{P}	Pressure loading rate (MPa/s)
p_0	Ambient pressure (N/m ²)
P_1, P_2	Forces on left and right end of the specimen in SHPB test (N)
P_b	Burst Pressure (MPa)
p_e	Nozzle exit pressure (N/m ²)
P_e	Equivalent force in incident and transmitted bar (N)
r	Radius of disc (mm)
R or r_{max}	Maximum radius of the disc (mm)
T	Temperature in material (°C)
T^*	Homologous temperature (°C)
T_0	Reference temperature (°C)
T_m	Melting temperature of the material (°C)
t	Rupture disc plate/sheet thickness (mm)
Δt	Reduction in sheet thickness (mm)
t_0	Initial sheet thickness (mm)
t_0	Initial sheet thickness (mm)
t_1	Score/groove depth (mm)
t_b	Burst time <i>i.e.</i> time taken for burst (s)
t_d	Natural time period (s)
t_d	Loading duration (s)
t_s	Time interval for the stress wave propagation (s)
u_1, u_2	Displacements at left and right end of the specimen in SHPB test (mm)
u_x, u_y, u_z	Displacements in $x, y,$ and z directions, respectively (mm)
V_e	Nozzle exit velocity (m/s)
w_l	Crack tip opening displacement (mm)
w_{max}	Central deflection <i>i.e.</i> maximum deflection at centre of disc (mm)
x, y	Graphs nomenclature in horizontal and vertical axes respectively
ε	Strain
$\Delta\varepsilon$	Incremental plastic strain

$\dot{\epsilon}$	Strain rate (/s)
$\dot{\epsilon}^*$	Dimensionless normalised plastic strain rate
$\dot{\epsilon}_0$	Reference strain rate (/s)
$\dot{\epsilon}_{max}$	Maximum strain rate (/s)
$\dot{\epsilon}_s$	Strain rate in SHPB specimen (/s)
ϵ_0	Equivalent plastic strain at onset of damage
ϵ_{eq}	Equivalent plastic strain
ϵ_f	Fracture strain
ϵ_i	Incident strain pulse
ϵ_{max}	Maximum equivalent plastic strain
ϵ_r	Reflected strain pulse
ϵ_s	Strain in SHPB specimen
ϵ_t	Transmitted strain pulse
ϵ_{xx}	Strain in x -direction
ϵ_{yy}	Strain in y -direction
μ	Poisson's ratio
ρ	Density of the material (Ton/mm ³)
σ	True stress / von-Mises tensile flow stress (MPa)
$\bar{\sigma}$	Von-Mises equivalent stress / scalar damage equation (MPa)
σ^*	Dimensionless pressure, <i>i.e.</i> stress ratio or stress triaxiality
σ_0	Stress at the onset of damage (MPa)
σ_{eq}	Equivalent stress <i>i.e.</i> von-Mises stress (MPa)
σ_m	Average of the three normal stresses <i>i.e.</i> mean stress (MPa)
σ_{max}	Maximum equivalent stress (MPa)
σ_D	Stress at damaged state (MPa)
σ_t	Tensile strength of material (MPa)
σ_u	Ultimate strength of material (MPa)
σ_y	Yield stress (MPa)
ω_n	Fundamental natural frequency (Hz)

Chapter 1

Introduction

1.1 Background

Containers are used to store the motor at a higher gauge pressure than the atmospheric pressure to protect the motor from external corrosive and volatile environment [1]. Typically, they are designed for a storage duration of more than 10 years. The containers are provided with front and back covers (lids) which are designed to withstand storage pressure and open up automatically during launch. They are designed to open remotely without manual intervention.

In one of such designs, the container can be fitted with a bottom cover which can break-open due to the transient pressure impulse generated by the motor plume gases. This initiates the opening of the bottom cover without any manual intervention. Such an openable bottom cover under a transient pressure impulse is called as a rupture disc or a burst disc and can be opened automatically due to the initiation of the motor. During storage, the disc acts as a protective cover and it withstands an internal storage pressure but fails only at a designed motor plume pressure during the launch of the motor.

This bottom cover can be a rupture disc system which is made of thin sheet (s) that ruptures when plume pressure reaches certain critical value. When the rupture disc bursts or ruptures, ideally a clean and an obstruction free rupture is desired *i.e.* the parts of the ruptured disc shall not obstruct the path for the plume of motor. Because, if any obstructions are on the plume path due to ruptured disc, it induces undue generation of back pressure locally at the obstructions created by ruptured disc which in turn affects the generated motor thrust. Motor thrust equation is given by

$$F_t = \dot{m}V_e + (p_e - p_0)A_e \quad (1.1)$$

where, \dot{m} is mass flow rate at nozzle exit, V_e is flow velocity at exit, p_e is pressure at nozzle exit, A_0 is the area at nozzle exit, p_0 is ambient pressure. If due to any obstruction at exit, back pressure develops and as a result ambient pressure p_0 exceeds exit pressure p_e , the second term in the Eq. (1.1) becomes negative reducing the motor thrust.

1.2 Introduction to rupture discs

A *rupture* or *burst disc* is a thin metallic plate or sheet designed to fail at a given transverse pressure. The loading rate on the disc can be quasi-static or dynamic, depending on the application. It is used as a sacrificial element in high-pressure pneumatic or hydraulic equipment in conjunction with safety relief valve to protect the equipment from sudden high or low surge pressures [2]. A typical rupture disc is shown in Figure 1.1. The rupture disc is also being used as a quick-release element in the shock tube apparatus where it is sandwiched between the high and low-pressure chambers. Upon its failure, it allows a sudden flow of high-

pressure fluid into a low-pressure chamber, thus generating a required shock wave [3]. Shock wave can be used for aerodynamic studies. In both the above cases, the rate of change of loading is low. In applications of blast and explosion, it is called as an *explosion vent* or a *rupture panel* and is used to protect large equipment or buildings during an internal explosion or blast. In all applications, the rupture discs provide compactness, quick response, and leak-proof.

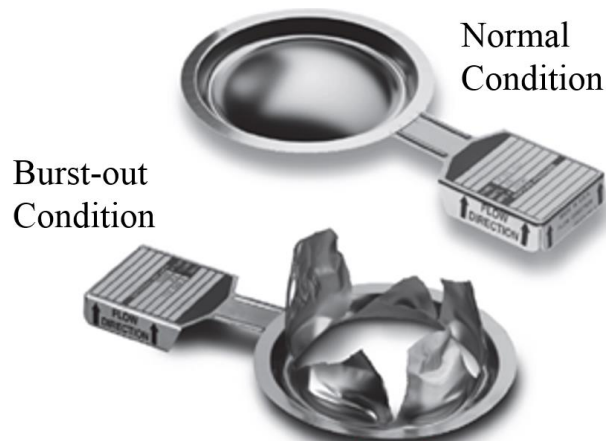


Figure 1.1: Typical rupture disc [4]

A rupture disc is a sacrificial element that bursts when the pressure inside the system exceeds a certain desired limit or the designed burst pressure. The main advantages of rupture discs are:

- Fast-acting and large volumes of fluid can be expelled quickly;
- Simple and reliable with no moving parts;
- Light weight; and
- No or very limited maintenance.

Their disadvantages include:

- One-time operation;
- Care must be taken during handling, installation, and operation where even a scratch on the disc may alter the burst characteristics or failure behaviour of the disc; and
- Burst pressure can be influenced by clamping force on the disc.

Rupture discs are selected in general engineering applications based on two important characteristics, *burst pressure* which is the maximum pressure at which a rupture disc has to fail and *operating ratio* which is the ratio of the working pressure to the burst pressure.

1.2.1 Classification of RDs

Usually the rupture discs are circular and provided with mounting features to facilitate its clamping between two flanges. They are pre-domed to i) increase the burst pressure, ii) improve the predictability of burst pressure, and iii) reduce the total energy absorption for a

given size before failure. In general engineering, the rupture discs are classified based on geometry as *flat*, *forward dome* and *reverse dome* types; and based on construction and design as *solid*, *scored* and *composite* with slit and tabs.

1.2.1.1 Types of rupture discs depending on geometry and material

The rupture discs in general engineering applications can be classified based on geometry [2, 5] and material as discussed below.

- a) Flat plate type -
 - Tension loaded with ductile material
 - Shear loaded with brittle material
- b) Forward domed type - Tension loaded with ductile material
- c) Reverse domed type - Compression loaded with ductile material

A brief explanation of these rupture discs is described in the following sections.

a) Flat plate type rupture disc

A flat plate rupture disc is clamped between two flanges and exposed to pressure on one side as shown in Figure 1.2.

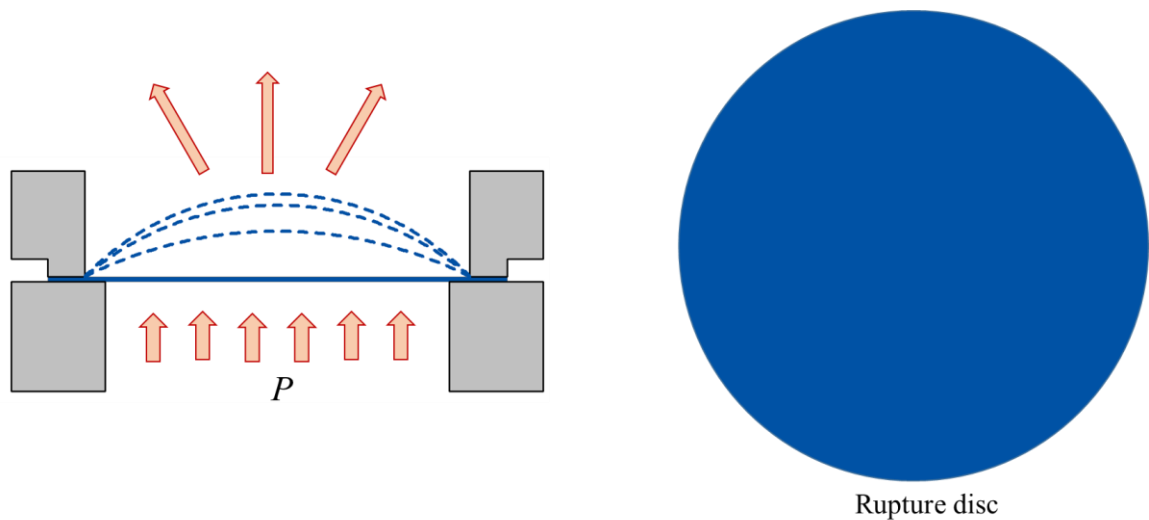


Figure 1.2: Flat plate type rupture disc: tension/ shear loaded

Flat plate rupture disc with ductile material

Pressure can be applied in any direction. In the event of any excess pressure, the plate stretches in the form of a hemispherical dome and bursts subsequently. But, the predictability of burst pressure in flat plate burst discs is generally poor. This failure is even accompanied by some

fragmentation of the disc. Flat thin metallic discs are extensively used in low-pressure applications.

Flat plate rupture disc with brittle material

A flat plate rupture disc with brittle material is generally made of graphite. These rupture discs are typically machined from a bar of fine graphite that has been impregnated with a sealing compound to seal the porosity of the graphite matrix. Material is very brittle and ruptures almost without any deformation. Its structure is homogeneous and strength is very low as compared to metals. It can be used for low pressure applications and can be made thicker compared to metallic rupture discs. Because of low strength, the operating pressure is almost 80% of burst pressure.

(b) Forward domed rupture disc with ductile material

Forward-domed rupture discs with ductile material are pre-domed discs with pressure acting on the concave side of the disc as shown in Figure 1.3. As the pressure increases beyond the allowable operating pressure, the rupture disc starts to grow. This growth will continue with localized thinning in the region of the dome centre until the tensile strength of the material is reached and subsequently followed by the occurrence of rupture. This failure is even accompanied by some fragmentation of the disc. Operating pressure is almost 70% of burst pressure. Since the tensile strength of ductile material is fairly high, it must be made of thin foils for a higher operating ratio of operating pressure to burst pressure. They are advantageous in terms of cost-effectiveness and are suitable for liquids and gases. Their limitations are that the operating pressure ratio is limited to 70%, not suitable for back pressure and the disc may fragment upon failure.

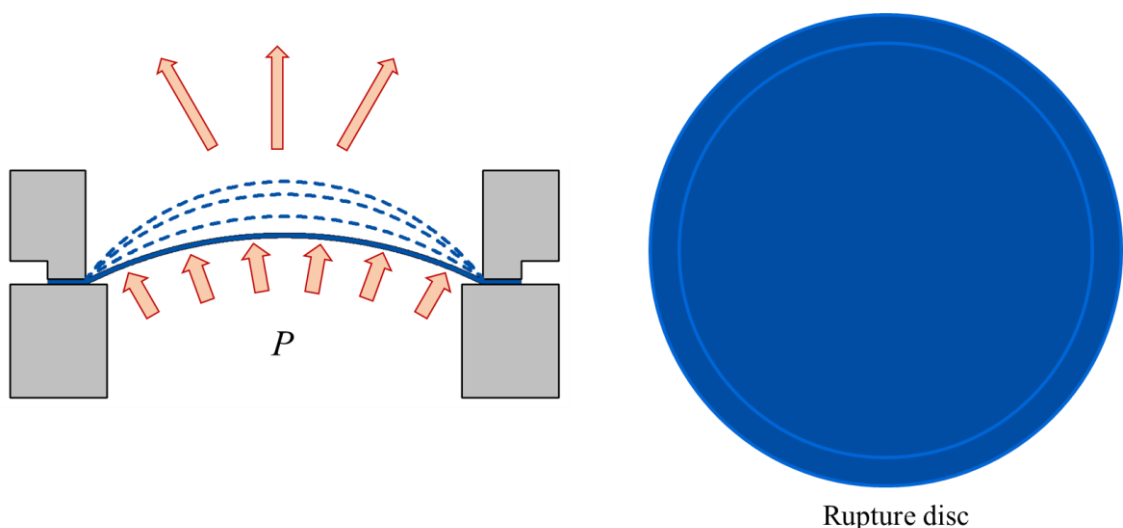


Figure 1.3: Forward domed rupture disc: tension loaded

(c) Reverse-domed rupture disc with ductile material

Reverse-domed rupture discs with ductile material as shown in Figure 1.4 are pre-domed rupture discs with pressure acting on the convex side of the disc. The disc is under compression loading and as the pressure reaches buckling pressure, buckling of the disc occurs. The disc does not burst open on itself. This is achieved by either a cutting device against which the disc must be slammed or by the scoring of the disc.

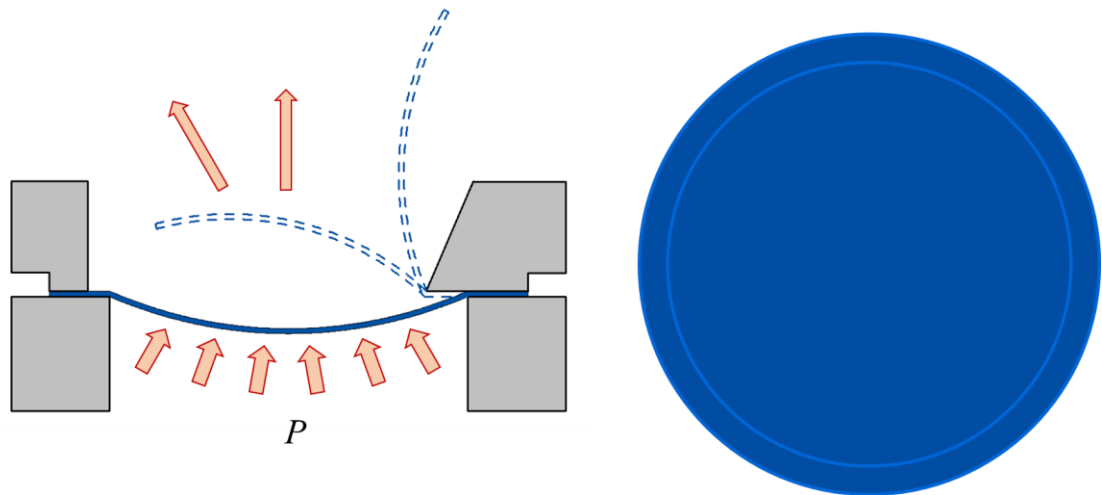


Figure 1.4: Reverse domed rupture disc: compression loaded

The buckling pressure depends on the elastic modulus of the material which is much more constant for a given material and reproducible. Therefore, the buckling pressure can be well predicted and is less dependent on temperature variation. Further, the buckling stress is substantially lesser than the tensile stress for a given material. So, they are made of considerably thicker material than forward-domed discs. Operating pressure is almost more than 90% of burst pressure. Their advantages include low burst pressure capabilities, higher operating ratio, and higher material thickness for a given pressure. Their disadvantage is that a separate system is to be provided for burst.

1.2.1.2 Types of rupture discs depending on construction

The rupture discs are also classified based on the type of their construction [2, 5] as follows:

- a) Solid material rupture disc
- b) Scored rupture discs
- c) Composite or multi-piece construction discs with slits and tabs

The above types of constructions are briefly discussed below.

(a) *Solid material rupture disc*

Solid material rupture disc is made of a plain sheet or thin foil as shown in Figure 1.5. During the burst of the rupture disc, the opening configuration is random and fragments can generate from the rupture.

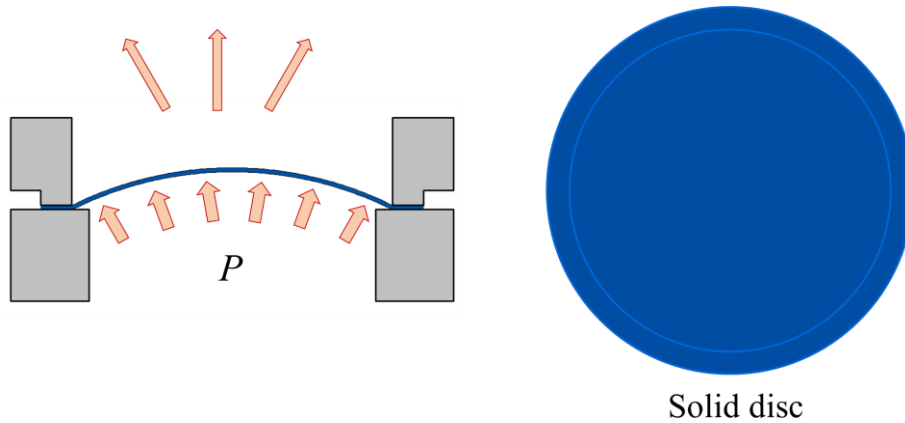


Figure 1.5: Solid material rupture disc

(b) *Scored rupture disc*

Scored rupture discs are featured with cross scores on the convex side of the dome as shown in Figure 1.6. The disk is designed to burst along the scored lines. Scoring allows the disc to be made of thicker material for a higher ratio of operating pressure to burst pressure. The higher thickness gives additional resistance to mechanical damage. These score lines provide a predictable opening pattern so that the disc upon burst does not produce fragments. Operating pressure can be raised to 85% to 90% of burst pressure.

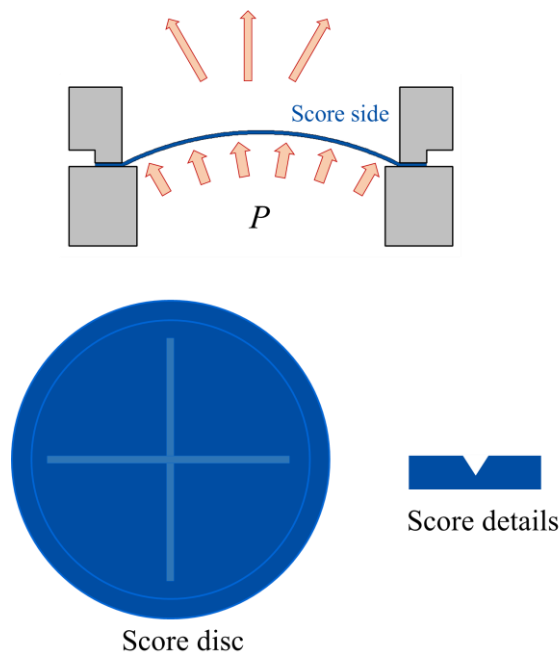


Figure 1.6: Scored rupture disc

(c) Composite or multi-piece construction or non-monolithic discs with slits and tabs

The composite type of rupture disc features a multi-layered disc in which the top member is slotted with thin holes pierced at each end, the second layer is a seal member and the third layer may be vacuum support in case of back pressure as shown in Figure 1.7.

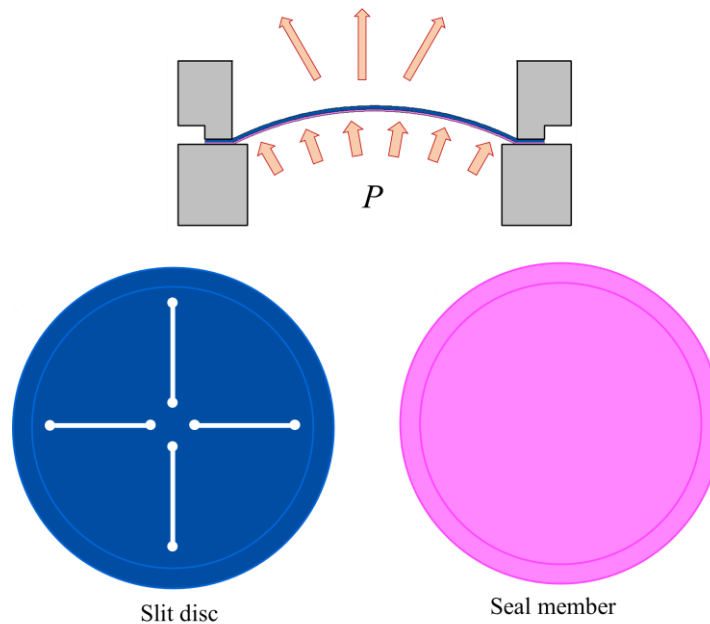


Figure 1.7: Composite (non-monolithic) rupture disc

The burst pressure is controlled by the combination of slits and tabs in the top section and a metallic or non-metallic seal member below the top section. This allows a higher thickness for the rupture discs which helps in a higher ratio of operating pressure to burst pressure. Composite rupture discs may offer a longer service life as a result of the corrosion-resistant properties of the selected seal material. The slits and tabs in the top section provide a predetermined opening pattern for the rupture disc. The composite rupture disc generally provides satisfactory service life when the operating pressure is 80 % or less of the marked burst pressure. The broad classification of RDs and their corresponding Operating ratios are given in Table 1.1 and Table 1.2 respectively.

1.2.2 Applications of rupture discs or rupture panels

Rupture discs are rupture panels that are mainly used in applications where they are designed to burst or fail at a designated pressure. Some of the applications of rupture discs include but not limited to pressure relief valves, shock generating devices, and explosion venting devices.

Table 1.1: Classification of rupture discs

Classification based on geometry and material		
Flat	Forward domed	Reverse domed
Pressure applied on flat face.	Pressure applied on concave side of disc.	Pressure applied on concave side of disc.
Tension or shear loaded depending on type of material.	Tension loaded.	Compression loaded.
Fails on its own under load	Fails on its own under load	Requires additional member to initiate failure
Classification based on construction		
Solid	Scored	Composite
Made of single material.	Made of single material	Multi-piece construction with different materials where low strength material used as seal
Plain disc	Scores are provided to aid stress concentration and initiate failure	Slits and tabs are provided to aid stress concentration and initiate failure
Poor predictability of burst pressure.	Better predictability of burst pressure	Better predictability of burst pressure
Very low burst pressure applications.	Relatively high burst pressure applications	Low burst pressure applications
Easy to manufacture	Difficult to produce scores	Relatively easy to manufacture

Table 1.2: Operating ratios for different RD configurations

Types of RD	Solid	Scored	Composite
Flat	Ductile - 50% Brittle – 80%	70%	50%
Forward acting	70%	85%	80%
Reverse acting	95%	90%	-

1.2.2.1 Pressure relieving devices

Rupture discs in general engineering applications are used as pressure relief valves [2, 5] as shown in Figure 1.8 [4]. Here, the use of a rupture disc is the basic method of protecting a system from over-pressurization or vacuum. The rupture disc is connected to high-pressure equipment as shown in Figure 1.8. When the pressure inside the equipment exceeds the designated over pressure, the rupture disc fails to let the fluid escape and thus protects the system.

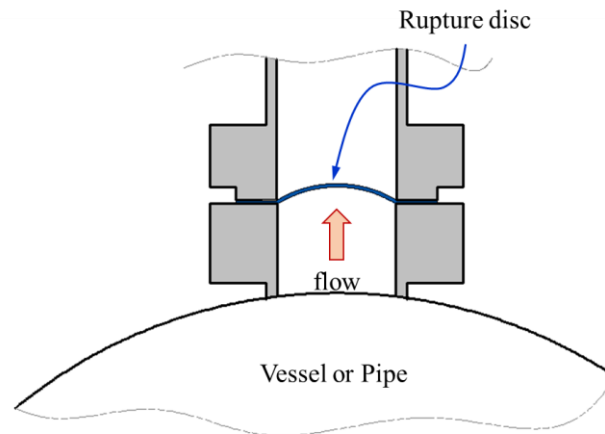


Figure 1.8: Rupture disc as a pressure relief valve [2]

1.2.2.2 Diaphragm in shock tube

Shock tubes can be used in the field of gas dynamics and experimental aerodynamics to generate an intended shock wave profile on an aerodynamic surface. The shock tube consists of a high pressure and low-pressure chambers separated by diaphragm or rupture disc as shown in Figure 1.9. When the rupture disc breaks under the action of suddenly released high-pressure air from an accumulator, a shock wave is generated on the other side of the rupture disc which is imparted to the aerodynamic surface such as a nosecone/wing/fin.

By using a relatively small ratio between the lengths of the high-pressure and low-pressure chambers, shock tube can be designed in the way such that the reflected rarefaction waves catch up with the shock wave resulting in pressure profiles similar to the blast wave from an explosive detonation.

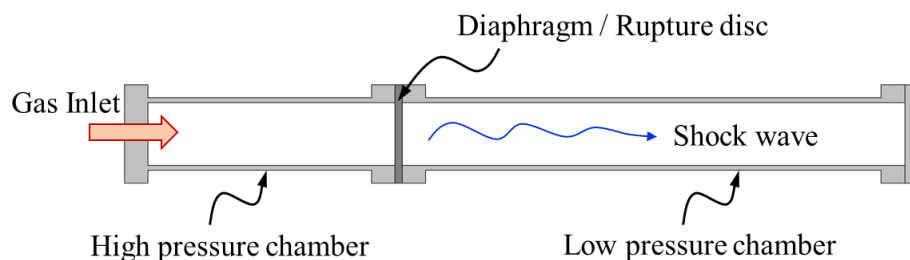


Figure 1.9: Rupture disc as diaphragm in the shock tube

1.2.2.3 Explosion relief panel or explosion vent or rupture panel

In order to minimise the effect of gas and dust explosions in confined spaces such as chemical plants, fuel-fired plants processing flammable stock, and gas fired plants, they are often provided with explosion relief through the installation of explosion relief panels [2] as shown in Figure 1.10(a-b).

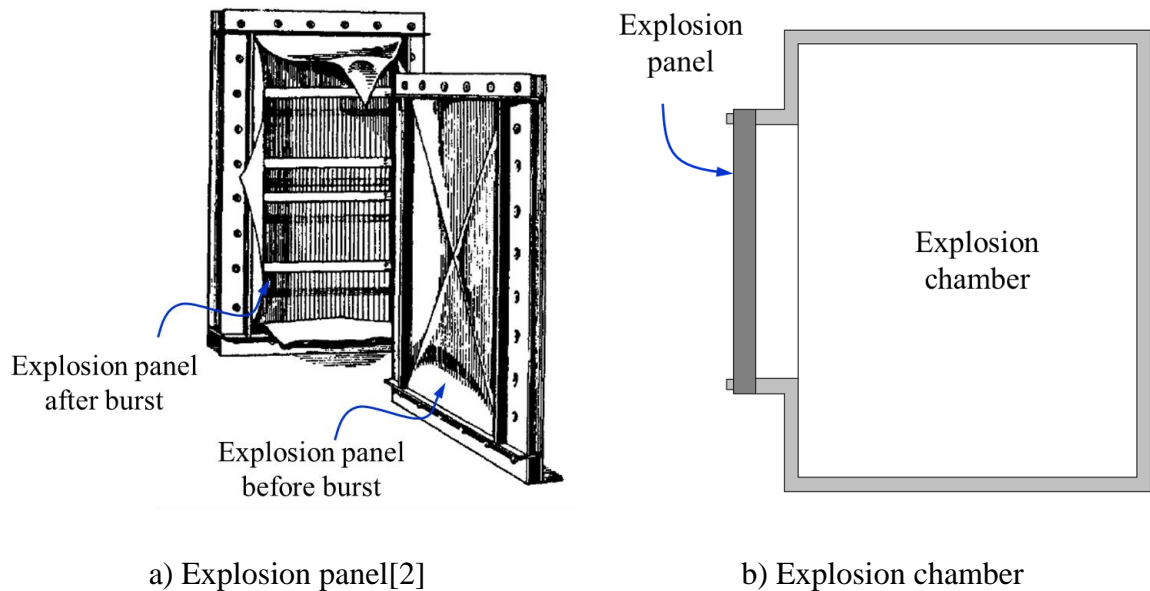


Figure 1.10: Explosion panel attached to explosion chamber

These rupture panels are designed not only to fail at peak pressure but to fail at a pressure whose generated force acting on the effective area of the panel is less than the force required to damage the structure.

In the all the above applications, RDs are subjected to pressure loading rates varying from quasi-static in safety devices to as high as 10 MPa/s in shock tubes and explosion panels.

1.2.3 Materials for construction of RD

Rupture discs are usually made of ductile materials for better predictability of burst pressure. Brittle materials are also used but limited to low-pressure applications. All material details are given in Table 1.3. These rupture discs are protected with coatings depending on the end application such as protecting from high corrosive fluid or high operating temperature.

Table 1.3: Materials used for rupture discs [2]

Commonly used materials	Less commonly used materials
Stainless steel	Tantalum
Aluminium	Platinum
Inconel	Gold
Nickel	Silver
Monel	Titanium
Hastelloy B and C	
Carbon steels	
Resin impregnated graphite (Brittle)	

1.2.4 General design guidelines and important terminologies [6-9]

1.2.4.1 General design guidelines

In selecting the rupture disc for a given application, the flow area, fluid loading rates or characteristics and required burst pressure are the main driving parameters. Standards and codes [6-9] provide general guidelines for selection of rupture discs used as safety pressure relief valves.

ASME Section VIII, Division 3[6] provides rules for the use of rupture disc devices for over-pressure protection. ISO standards that apply to selection of rupture discs are ISO 4126-1 [7], ISO 4126-2 [8] and ISO 6718 [9] and provide general guidelines for rupture discs used as safety relief valves. Following are some important terminology specified in the handbooks and codes.

1.2.4.2 Important terminologies

Important terminologies generally used in rupture discs are given in Table 1.4

Table 1.4: Important terminologies used in RD

Burst pressure	:	The differential pressure at which rupture disc bursts at a specified temperature.
Marked or rated burst pressure	:	Nominal value of burst pressure at which the rupture disc bursts.
Maximum marked burst pressure	:	Marked burst pressure at top end of range.
Minimum marked burst pressure	:	Marked burst pressure at bottom end of range.
Burst tolerance	:	Tolerance specified on the burst pressure by the manufacturer

Specified temperature of rupture disc	:	The allowable temperature at which a rupture disc operates.
Operating ratio	:	It is the ratio of maximum operating pressure of rupture disc to minimum burst pressure of rupture disc
Deflagration	:	Burning that takes place at a flame speed below the velocity of sound in the medium
Explosion	:	The bursting or rupture of an enclosure or a container due to the development of internal pressure from a deflagration

1.2.5 Design considerations for rupture discs for the present application

There are several established design codes for the rupture discs used in general engineering. Regular designs are available in Standards and Codes. Researchers have attempted to examine the behaviour of common as well as uncommon rupture discs under different loadings and boundary conditions. Different considerations for analysis of rupture discs for the current application are discussed in this section.

1.2.5.1 Analysis of rupture discs

Rupture discs are specified by their burst pressure and it is influenced by factors such as material of construction, disc diameter, disc thickness, temperature and fluid pressure. The burst pressure can be calculated as

$$P_b = \frac{\sigma_u t_0}{kd} \quad (1.2)$$

where t_0 is the initial thickness and d is the diameter of the disc, k is a constant for a given material and can be found from experiment [10]. Traditionally the design of rupture disc is based on elaborate experimentations. Based on the finite element analyses (FEA) [11] of a forward domed rupture disc made of copper alloy 122, in which analysis was done up to ultimate tensile strength of the material neglecting fracture, the deflections of the plate was obtained by modelling the disc as shell elements fixed at the outer edge. Both material and geometric non linearity were considered. Pressure was applied as constant and time dependent. The variation of burst pressure predicted was 15.02% from experimental data [11]. A similar FEA of pure nickel was carried out [12] and found a considerable difference with respect to the experimental values. In both cases, the difference was attributed to the neglect of fracture [11, 12]. *It is understood that while characterising the rupture disc through FE simulation, it is important to consider the material damage.*

1.2.5.2 Blast loading

The plume of the motor suddenly impinges on the rupture disc which can be simulated as an impulsive or a blast load with very high slope of pressure with respect to time. Analysis of rupture disc under an impulsive pressure can be very similar to the concepts available in [13-20] that deal with analyses and experiments on structures under blast loadings. Under this

impulsive loading, rupture disc undergoes large deformations followed by fracture. In a study on steel rectangular plates subjected to blast loading, experimental data was successfully compared with FEA and simplified analytical solution based on kinematic approach [13]. Under explosive loading, the failure will be in *three modes namely, large deformation (mode-1), tensile tearing (mode-2) and shear failure (mode-3)*. The strain rate effects were included using Cowper-Symonds relation [14]. Somayajulu and Narayanamurthy [1] conducted a numerical study on flat plate rupture disc used for container bottom cover. Rupture disc was made out of AISI 4340 steel and subjected to impulsive pressure and temperature assumed from blast loading. Material was assumed to be isotropic elasto-plastic behaviour. Effect of notch size and its placement on the proper breakage is also studied [1].

In the FE simulation of rupture disc subjected to high loading rates, the effects of material non-linearity, geometric non-linearity and large deformation effects must be considered during simulation.

1.2.5.3 Effect of fluid temperature on the burst pressure

The design of rupture disc depends on both pressure and temperature of the fluid medium. As the temperature influences the strength of material, the relationships are established experimentally between burst pressure and operating temperature for various materials used for rupture disc construction. A typical temperature and burst pressure relationship for solid metal forward domed rupture discs is shown in Figure 1.11[2]. Burst pressure of the rupture disc significantly reduces with the operating temperature of rupture disc.

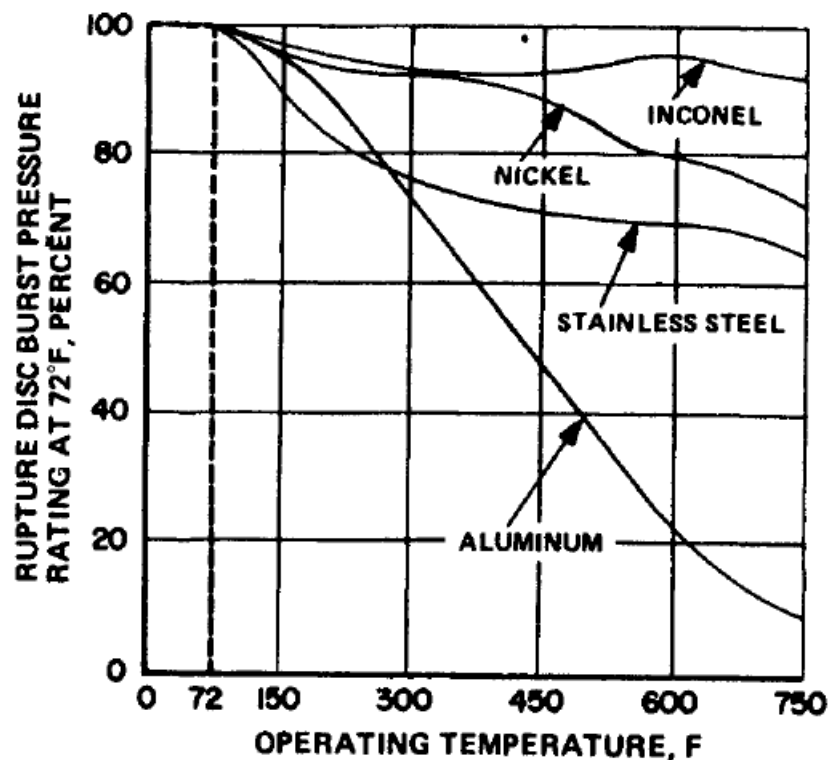


Figure 1.11: Temperature / burst pressure relationship [2]

Even though the operating temperature of rupture disc plays a significant role in the burst pressure of rupture disc, temperature will not affect the basic rupture disc characteristics at room temperature. So, this effect can be neglected to characterise the rupture disc.

1.3 Large deformation and rupture of thin flat metallic discs under impulsive loading and failure modes

Flat plates undergo large inelastic deformation and rupture under higher loading rates and have been studied extensively under air blast and explosive loadings [13,21-34]. They provide a base for the present study on the behaviour of scored-thin metallic rupture disc. A comprehensive review by Nurick and Martin [21,22] compares the theoretical and experimental results of fully clamped flat circular plates subjected to impulsive load. The central deflection from experiment is comparable to theoretical prediction up to a very small deflection *i.e.* up to one plate thickness. The research findings between 1989 and 2016 on thin plates subjected to impulsive load have been reviewed by Yuen *et al.* [23] and they summarized the advancements in theoretical and empirical formulae for predicting the central deflection. Close agreement between theory and experiment is reported even after neglecting the effects of strain hardening and strain rate sensitivity. They further discussed in detail about the failure of flat plates under uniform and localized impulsive loads. Failures in metallic discs are observed in three different modes namely, *failure mode-I* in which disc exhibits a large plastic deformation under low impulse levels, *failure mode-II* where a tensile failure is observed at the boundary or central area of the disc when the impulse increases to a threshold limit, and *failure mode-III* in which transverse shear occurs at the boundary of the disc upon further increase in the impulsive load.

From the large number of experiments conducted since 1989, it has been found that the failure mode progression of circular and quadrangular plates is similar [23,24]. The mode-I deformation profile of uniformly loaded plates was characterized by a single global dome, whereas locally loaded plates exhibited a local inner dome atop a global dome profile. Petalling is observed under localised impulsive loads. Capping and petalling failure occurred at the center of locally loaded plates, as opposed to tensile and shear failures at the boundaries of uniformly loaded plates. The locally loaded plates exhibited tearing at the boundary when the load-to-plate diameter ratio is increased above 0.4 [25]. Boundary conditions have significant influence on the tearing and shear failures of plates due to the difference in the in-plane movement achieved with each boundary condition.

The edge sharpness at the fixed boundary played a significant role in initiation of failure at the boundary [26, 27]. Rigid boundaries, such as built-in welded boundaries, will initiate necking and tearing failures at lower impulses compared to the clamped boundaries [28]. The effect of edge sharpness on the tensile boundary failure of clamped plates shown that filleting the clamp delayed the onset of tearing by preventing indentation of the plate boundary [26, 29]. This phenomenon of edge sharpness at the clamped boundary was also studied by Nurick *et al.* [24] where they related the necking localization and/or ductile fracture at the support to the overall performance of rectangular plates under impulsive loadings.

Increasing the stand-off distance resulted in less localised loading on the plates. It is reported that when the stand-off distance exceeded the largest of plate dimensions, loading was observed to be uniform. Also, it depends on the load diameter of the charge. Marchand and Marchand and Alfawakhiri [30] reported that when the charge stand-off exceeds one-half of the structure or element width or height (assuming the charge is centered on the structure or element) loads can be reasonably and accurately averaged over the structure or element. For shorter stand-offs, the loading was a non-uniform distribution. The effects of both strain hardening and strain rate sensitivity have not been specifically considered in most analyses and both effects are embedded in the empirical equations [25, 31]. Including strain rate effects in the numerical simulation reduces the central point deflection which can be attributed to increase in yield strength of the material and higher elastic modulus than the plastic modulus, Goel *et al.* [32] and Nurik *et al.* [26] studied the failure of clamped circular metallic plates subjected to uniformly loaded air blasts and investigated the failure onset and subsequent tearing at the clamped plate boundary. The diameter of plates ranged from 60 to 120 mm with different clamped edge conditions such as sharp edge and edge with radii.

Nagesh and Gupta [33] numerically analysed the large deformations and tearing of circular plates under impulsive loading to simulate mode-II and mode-III failures and compared the results with experiments conducted by Nurick *et al.* [26, 34] gave the experimental and numerical results for fully built-in stiffened square plates subjected to blast pressure loading. The strain rate-sensitive plates exhibited mode-I (large ductile deformation) and mode-II (tensile tearing) failure as the load intensity increases. Yuan and Tan [35] studied the impulsive response of rectangular plates and shown that an increase in the blast duration delays the transition between various deformation modes. Rudrapatna *et al.* [36] provided the numerical results for clamped thin square plates subjected to blast loads by considering the nonlinear effects of geometry and material including strain rate sensitivity and proposed a phenomenological interactive failure criterion comprising bending, tension and transverse shear to predict various modes of failure.

Smith and Nurick [27] examined the failure of fully clamped mild steel circular plates subjected to uniformly distributed impulse and formulated an energy balance equation relating input, deformation, tearing and disc energies. The input and disc energies are obtained from experimental measurements; and the deformation energy is predicted by making use of the final deformed height, a shape function and a rigid-plastic analysis. Sharma *et al.* [37] conducted numerical simulation of spherical shell subjected to a blast load and shown that it exhibit minimum radial displacement as compared to the flat plate.

1.4 Existing knowledge on rupture disc

Lee *et al.* [38] experimentally studied the effect of radius of curvature of the forward domed rupture disc with and without grooves, and the thickness of disc on the valve opening time and shock formation distance. This study revealed a reduction in opening time and increase in shockwave formation distance with decrease in radius of curvature. Jeong *et al.* [39] numerically simulated the effect of groove thickness on the failure of forward domed rupture

disc by calculating local primary membrane equivalent stress to find the burst pressure of the disc for the given design parameters. Aune *et al.* [40] experimentally and numerically studied the dynamic response of blast loaded steel plates with and without pre-formed holes and concluded that the predicted failure pattern is highly dependent on the initial mesh size and damage threshold.

Zhu *et al.* [41] investigated the effect of temperature on the fracture behavior of plain forward domed rupture disc. Finite element analysis methodology based on non-linear buckling and static analyses were adopted to predict the burst pressure; and shown that the burst pressure decreases with increase in temperature. Colombo *et al.* [42] studied the failure of flat plate with rectangular scores with cross configuration under uniform quasi-static pressure loading and concluded that the plates with minimum score depth-to-plate thickness ratio of 0.4 is essential for the failure to initiate in the scored region of the plate.

1.5 Research gap

General guidelines for selection of rupture discs are not applicable for rupture discs or rupture panels subjected to impulsive and higher loading rates. The design guidelines are not available in open literature and so are the studies on the failure of pre-domed rupture panels. Analytical methods for solving problems of dynamic and static behaviour of domed-scored thin metallic discs is not available due to the complexities in deriving analytical solution for the domed disc in presence of scores. The investigations on the rupture disc (panel) intended for applications in motor containers where the disc needs to meet withstanding storage pressure for long duration and instantaneous failure condition under the effect of impulsive motor plume pressure, are also unavailable. Although a number of literature exists based on current research, the gaps in the existing research are as summarised below.

- i. *Non-availability of studies on rupture disc meeting both storage and instant failure conditions*

Most of the research were focussed mostly on standard rupture discs which are used as pressure relief valves. Their loadings are steady state, static or quasi-static and incremental. There are no studies available on studies on behaviour of rupture discs subjected to impulse loading conditions.

- ii. *Lack of information on failure time and opening pattern after initiation of failure*

In the present research, there is no time constraints for the completion of rupture operation as long as it is meeting required failure condition. Studies on propagation of failure which is responsible for formation of petals to allowing obstruction free flow is not available.

- iii. *No studies on large diameter rupture disc to fail at low impulse and its design criterion*

When diameter of the rupture disc increases as in the case of motor container where size can be of the order of 300-1000 or more in diameter, the force due to fluid pressure on the rupture disc during static storage condition will be very high. Designing the disc with

higher factor of safety in static condition makes the rupture disc bulky and increase the pressure requirement for failure and upon failure generates high impulse and shock to attaching structure which must be reduced. There is no design criterion available in open literature which allows to design the rupture disc for meeting this condition.

1.6 Research objectives

The primary objectives of the thesis are to overcome the research gap and develop a basic understanding of the behaviour of the rupture disc under two different contradicting loading and failure requirements, and to suggest a practically viable design backed by exhaustive numerical studies validated with suitable experiments. The objectives of the thesis are delineated below.

- i. Establish a non-linear explicit FEA methodology for analysis of Rupture Disc (RD) under impulsive pressure loading
- ii. Investigate Flat and Domed scored RDs – study their response due to variations in
 - a. Loading rate,
 - b. Disc diameter and dome height and
 - c. Score's depth-width-geometry-length-pattern.
- iii. Propose a RD configuration for motor container meeting both storage and break-away conditions.
- iv. Characterize the J-C strength and damage model parameters of E250 steel.
- v. Design a suitable experimental setup, realise and experimentally validate RDs.
- vi. Develop a RD variant (non-monolithic) to minimize the burst pressure for motor container application

1.7 Research methodology

The research methodology followed for present research work is shown in Figure 1.12. The main aim of the present research work is to arrive at a criterion to design a rupture disc for motor container application. It is carried-out on four phases and the detailed work carried out in each phase is described below.

Phase-I: Establishing FEA methodology

In Phase-I of the research work, numerical simulation methodology established for FEA simulation of rupture disc under impulsive pressure loading. The methodology is validated by comparing FEA results with the experimental results of a scored flat metallic disc made of S235 JR structural steel subjected to quasi-static pressure loading which are available in literature. During FEA simulations, Johnson-Cook material and damage models are chosen to represent the constitutive and damage behaviour of the S235 JR structural steel. While J-C material model of S235 JR structural steel are directly taken from literature, J-C damage model parameters are iterated to arrive at the final values. Damage evolution is neglected.

Phase-II: Investigation on Flat and Domed RDs and propose a preliminary RD for current application

In the next phase, Flat and Domed RDs are investigated with the help of established FEA methodology and selected material model and damage models. The behavior of RDs are studied due to variations in quasi-static to impulsive pressure loading rates; Disc geometry *viz.* Diameter-to-plate thickness ratio and Dome height-to-Diameter ratio; Score geometry *viz.* score length-to-disc radius ratio, score depth-to-plate thickness ratio, score width-to-plate thickness ratio, score geometry and number of scores. Apart from basic RD characteristics *viz.* *factor of safety* under static pressure load and *burst pressure* under impulsive pressure load, two critical parameters *viz.* *operating ratio* and *impulse transmitted* are identified to characterize RDs. Operating ratio is redefined so that it can be found from numerical simulation.

Based on these studies, a preliminary Domed Scored RD geometry is proposed with an aim to minimize burst pressure yet feasible to manufacture; to be made of E250 structural steel which is an alternative material available in market.

Phase-III: Experimentation

In the next phase, experimentation is carried-out on proposed RD in four stages

Stage 1: To manufacture Domed RDs, hydro-forming method is explored. Three numbers of Flat RDs and three numbers of Domed RDs are realized. Scores are made using milling operation.

Stage 2: Since J-C material and damage model parameters for E250 structural steel are not available in literature, experimentation is carried out to determine the J-C material and damage parameters. A unique method to implement damage initiation and fracture energy based damage evolution are proposed which can be directly implementable in commercial FEA software. The material model is validated by comparing FEA results with results of separate tensile experiments.

Stage 3: Experimental setup is designed to conduct the failure experiment on RDs at maximum possible loading rate with the available facilities with in the laboratory. Burst experimentation is carried out on all six discs under hydraulic and pneumatic loads. Strains with respect to chamber pressure are monitored during experimentation.

Stage 4: Experimental results are compared with the results from FE simulation. The variations in disc geometry due to manufacturing (from Stage-1) and determined E250 structural steel material parameters (from Stage-2) are used for FE simulation of experimented discs.

The FE simulation methodology, E250 structural steel material parameters are experimentation procedure are validated in this phase.

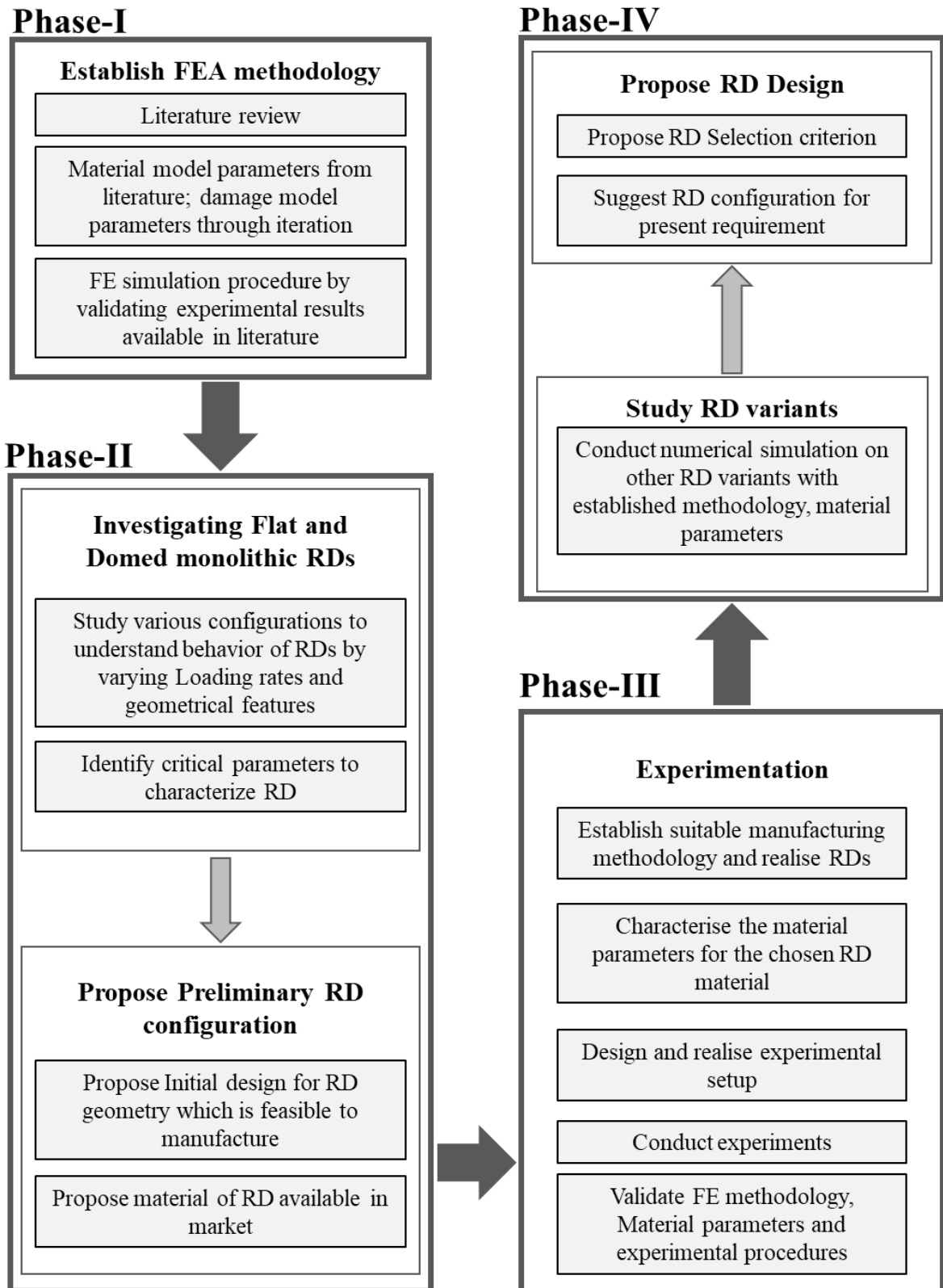


Figure 1.12: Research methodology adopted in present work

Phase-IV: Study RD variants and propose RD design for current application

Final phase is covered in two stages. **Stage 1:** In this stage, numerical simulation is carried out on another design of RD which is a non-monolithic configuration with the aim of reducing the burst pressure. The material parameters and variations in disc geometry due to manufacturing which are validated from previous phase are used for numerical simulations. Several variants are numerically simulated.

Stage 2: Finally, proposed an RD selection criterion to select the best configuration from studied variant designs (from Stage 1).

This criterion can be used for comparisons of discs with different geometric configurations and materials, and choose the best design for the given requirement which is the main objective of present research.

1.8 Organisation of the thesis

The thesis is organized into eight chapters as schematically shown in Figure 1.13.

Chapter-1 provides an introduction to the thesis research area and discusses the application of the rupture disc as a cover for the motor container. It also covers the background, type and various applications of rupture discs, selection criterion available in open literature, failure mechanisms in rupture discs and a detailed analysis of research gaps, formulated objectives for the research, and the organization of the thesis.

Chapter-2 presents the material characterization for the constitutive and damage model parameters which are necessary for the numerical simulation of the response of the rupture discs. This chapter covers the characterization of Johnson-Cook's material and damage model parameters for E250 structural steel which is used for the proposed rupture disc.

Chapter-3 focusses on a flat-scored metallic disc (FSMD). It proposes an FEA (finite element analysis) methodology to numerically simulate the failure of a flat-scored metallic disc and validate the results with the experiments available in literature. This chapter also presents parametric studies conducted to understand the behaviour of the FSMD with respect to variations in different geometric features. **Chapter-4** analyses the behaviour of the domed scored metallic disc (DSMD) for container. This chapter shows the necessity of domed geometry of rupture disc and presents the results of parametric studies to understand the various responses of DSMD with respect to detailed variations in geometric features and proposes a geometry which is suitable for the present application.

Chapter-5 discusses the hydro-forming manufacturing process required for realization of the domed metallic disc. This chapter covers the proposed methodology for manufacturing of forward domed rupture disc *i.e.* hydroforming for dome formation, numerical simulation of the dome formation process through a non-linear explicit FEA and prediction of the thickness variation in rupture disc sheet due to hydroforming.

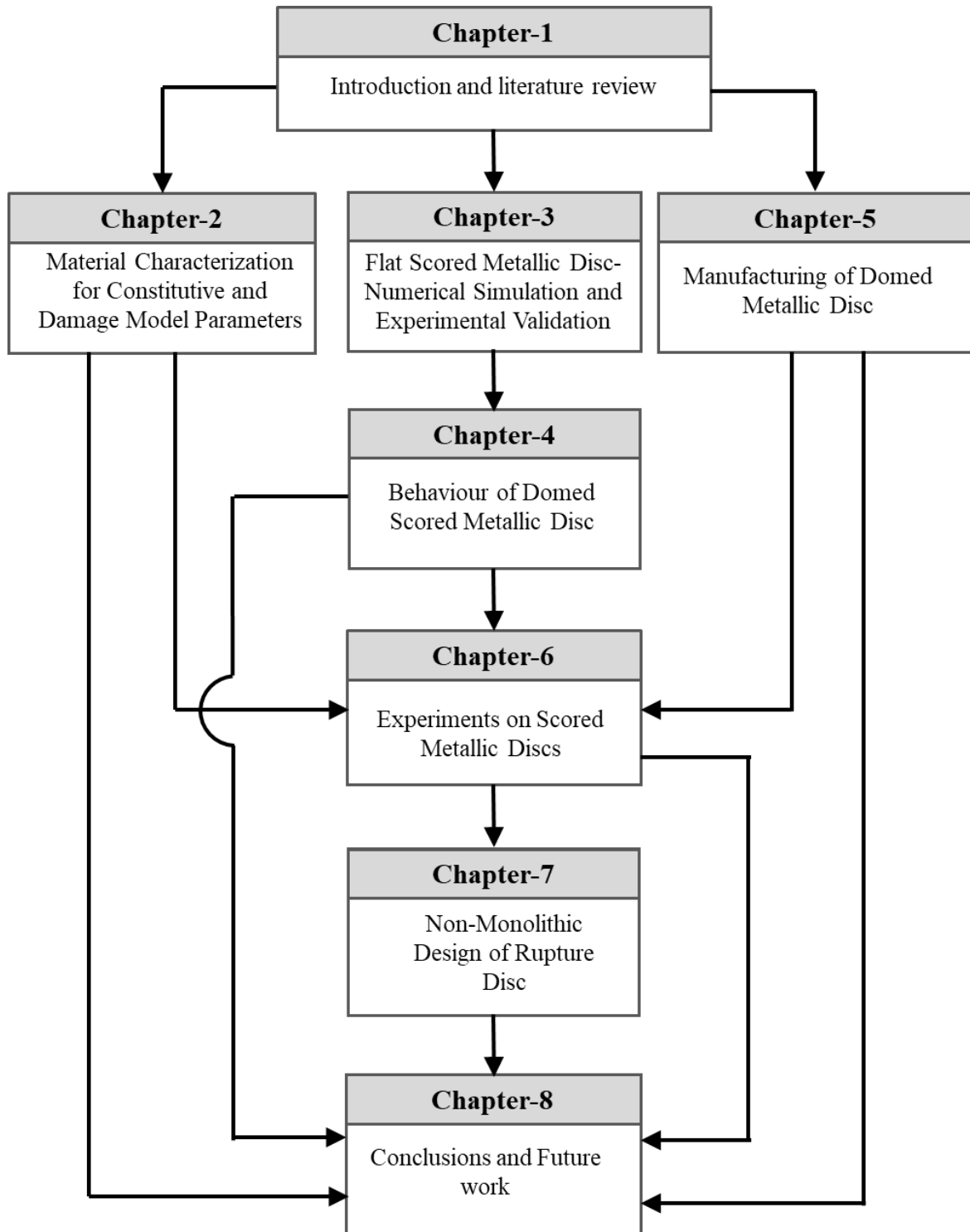


Figure 1.13: Overall organisation of thesis chapters

Chapter-6 details the experiments conducted on both FSMD and DSMD under hydrostatic and pneumatic loading conditions. This chapter covers the design of the experimental setup for experimenting with the rupture discs, numerical simulation of the burst pressure and failure patterns, experimentation procedure, and discussion of experimental results. **Chapter-7** provides an approach for developing a practically viable design of a rupture disc suitable for the container. This chapter covers numerical simulation of non-monolithic rupture disc

configuration and proposes a methodology to select the best disc configuration which is suitable for the container application. Finally, **Chapter-8** presents the conclusions, contributions, limitations of present research and suggest recommendations for carrying out further research in this area.

1.9 Summary

The containers are protective vessels for the motors. The bottom cover of this container needs to withstand the storage pressure and must break away under the instantaneous plume pressure generated during the initiation of motor. Rupture disc can be used as a bottom cover for motor container. Rupture discs are the sacrificial devices which are designed to fail at designated pressure. Literature review has been done to understand the standard practices for selection of rupture disc in safety applications, behaviour of thin plates subjected to impulsive loading conditions and crack initiation and propagation in scored and slit discs. This review helped in understanding existing methods available to simulate the failure of rupture disc. There are limitations involved in designing and characterising the larger diameter rupture discs suitable for both storage and failure conditions. Gaps in the existing research are discussed and research objectives are formulated research methodology followed in present research presented.

Chapter - 2

Material Characterization for Constitutive and Damage Model Parameters

2.1 Introduction

In the present research, structural steel of two different grades is considered. In the initial part of research, numerical simulation methodology is established with the help of the experimental results of S235JR structural steel, and the details are explained in Chapter 3. However, for the later part, the experimentation in the present research is carried out with E250 structural steel which is an equivalent steel available in the Indian market. This chapter focuses on material characterization of E250 structural steel.

Structural steel with E250 grade is a work-horse material used in several engineering applications due to its low cost and manufacturability through several methods. Typically, it is used as blast discs, explosion vents, structural construction, etc. These structures and components are subjected to loadings at different loading rates ranging from quasi-static to high strain rates caused by different sources of events such as impact, blast, explosion, etc. Material behavior under extreme dynamic events is much different from the behavior under static loading conditions. The material undergoes large deformation, strain hardening, strain rate hardening, thermal softening and, eventually, leading to damage initiation and failure.

The behavior of this material under such extreme loadings can be numerically simulated using non-linear explicit finite element analyses (FEA) based on Lagrangean, Eulerian, arbitrary Lagrangean-Eulerian, or meshless methods along with appropriate models to capture the material's constitutive (*i.e.* strength) and damage behavior. Literature review has been carried-out to find the material and damage models suitable to simulate the deformation and failure behavior of RDs subjected to impulsive pressure loads and readily available in commercial FEA software are given in Table 2.1

Of several material and damage models available in the literature, the strength and damage models of Johnson-Cook (J-C) are quite popular [43-45]. Although J-C models are one of the oldest and fairly accurate models, they are increasingly finding their applications in impact simulations due to their several advantages. The primary advantage is that the material behaviours or effects can be isolated independently, and appropriate material and damage model parameters can be determined from simple experiments. However, the number of experiments and their conditions depend on the level of accuracy and scope required. Several researchers have attempted to determine the strength and damage model parameters of J-C for different engineering materials through various experimental techniques. Few have resorted to obtaining these parameters through several numerical iterations, starting with approximate values until their intended responses match with benchmark experiments.

Table 2.1: Applicable material and damage models available in commercial FEA software [43,51]

Model	Large strain (ϵ)	High strain rate ($\dot{\epsilon}$)	High temperature (T)	Remarks
<i>Material model</i>				
Plastic-Kinematic hardening	Yes	Yes	No	
Thermo-Elastic plastic	Yes	No	Yes	
Power-law isotropic plasticity	Yes	Yes	No	
Johnson-Cook material model	Yes	Yes	Yes	
Zerilli-Armstrong material model	Yes	Yes	Yes	Dependent on lattice structure
Modified Zerilli-Armstrong material model	Yes	Yes	Yes	
Combined J-C Zerilli-Armstrong material model	Yes	Yes	Yes	
Steinberg-Guinan material model	Yes	Yes	Yes	$\dot{\epsilon} > 10^5$
<i>Damage model</i>				
Hancock and Mackenzie fracture strain model	-	No	No	
Jonson-Cook failure model	-	Yes	Yes	

Researchers have attempted to determine either few or all (A , B , n , C , and m) material parameters of the J-C strength model and ($D_1 \dots D_5$) damage parameters of the J-C damage model for different engineering materials through various experimental techniques such as uniaxial tensile experiments, Split Hopkinson Pressure Bar (SHPB) experiments, etc., conducted at different strain rates and temperatures. Vedantam *et al.* [46] attempted for Mild steel and DP590 steel; Xu *et al.* [47] for 603 Armour steel; Banerjee *et al.* [48] for Armour steel; Farahani *et al.* [49] for Inconel-718; Murugesan *et al.* [50] for AISI-1045; Majzoobi *et al.* [51] for an unspecified engineering material; and Bal *et al.* [52] for Aluminium alloy 7068 –T651. Few have obtained these parameters through several numerical iterations, starting with approximate values until their intended responses match with benchmark experiments.

Vedantam *et al.* [46] obtained the J-C strength model constants (except temperature dependent parameter, m) of mild steel and DP590 steel using uniaxial tensile experiments at a strain rate of 0.001 /s and SHPB experiments at strain rates of 267 /s, 800 /s, and 1800 /s and concluded that mild steel having lower yield strength exhibited higher strain rate sensitivity than DP590 steel having higher yield strength. Xu *et al.* [47] investigated the plastic behavior of 603 Armour steel (a low-alloy medium carbon steel heat treated to produce a tempered martensitic microstructure) through quasi-static uniaxial compression tests at strain rates ranging from

0.001/s to 0.1/s and dynamic compression tests using SHPB at strain rates 200/s, 2000/s and 4500/s at temperatures ranging from 15⁰C to 600⁰C. The evaluated J-C strength model parameters are assessed by comparing the predicted results with strain rate jump test experiments of a separate specimen and shown that the error in prediction of flow stress by the J-C model is 16.6% in quasi-static condition and 13% in dynamic condition for this steel. Banerjee *et al.* [48] attempted to determine all the J-C strength and damage model parameters of the Armour steel through uniaxial tension tests at various strain rates between 0.0001/s to 150/s and temperatures ranging from room temperature to 500⁰C. They also validated their determined J-C model parameters by comparing numerical simulations with Charpy impact test.

Farahani *et al.* [49] determined the J-C plasticity model parameters of Inconel-718 except strain rate dependent parameters using quasi-static uniaxial tension tests at a strain rate of 0.1/s and at temperatures of 400⁰C, 475⁰C, 550⁰C, and 625⁰C. Since the strain rate dependent parameter was required at strain rate more than 10⁶/s for their intended application, they determined this parameter iteratively through trial-and-error method by comparing the crater produced by indentation of steel ball in an impact experiment with the numerical simulation. Murugesan *et al.* [50] extracted the J-C strength and damage model parameters of AISI-1045 medium carbon steel by several isothermal hot uniaxial tensile tests at strain rates varying from 0.05/s to 0.1/s and at temperatures ranging from 650⁰C to 950⁰C. They also proposed a non-linear algorithm to optimize the extracted parameters and to minimize the error between predicted and experimental flow stress.

Majzoobi *et al.* [51] determined the J-C's material and damage model constants (except temperature dependent parameters) of an unspecified engineering material. They performed limited experiments and determined the strain rate-independent material model parameters from the quasi-static experiment of a regular specimen and strain rate-independent damage parameters through numerical iterations. They finalised the model parameters by matching the experimental damage profile with FEA simulations of a notched specimen using an optimisation technique. They also adopted a similar optimisation approach for determining the strain rate dependent strength and damage parameters of J-C models from the experimental results of flying wedge high rate testing device and validated the extracted model parameters through FEA simulations of fractured specimens and comparison with experiments. Bal *et al.* [52] determined the J-C material parameters of Aluminium alloy 7068 –T651 by conducting experiments using uniaxial tests at quasi-static strain rate, Gleeble tests at temperatures up to 300⁰C and strain rates up to 100/s and SHPB tests at higher strain rates. They proposed three different sets of values for J-C model parameters for different applications with maximum, average and minimum plastic strains.

Although structural steel (E250 grade) is used in several engineering applications which involve different loadings ranging from quasi-static to high strain rates, the J-C strength and damage model parameters needed for its numerical simulation are not available in literature. In this Chapter, the processes and procedures involved in determining 10 different strength and damage parameters of J-C model for E250 structural steel through several experiments

involving tensile tests at different temperatures (30 °C to 800 °C), strain rates (0.0003 /s) to 1.0 /s) and stress triaxialities (0.33 to 0.95) and SHPB experiments (at 3000 /s and 8000 /s). A different approach is proposed here to determine the critical fracture strain and J-C damage parameters which facilitates the adoption of the determined damage parameters in any commercial available non-linear explicit FEA code. The determined model parameters are validated by numerically simulating i) a tensile experiment of a plain specimen, ii) a separate tensile experiment of a notched specimen, and iii) a hydrostatic experiment of a flat scored metallic disc.

2.2 Evaluation of J-C material model constants

The material's constitutive behaviour is modeled with Johnson-Cook strength model, and its failure with Johnson-Cook damage model. These two models define the material's viscoplasticity and damage behavior during loading in numerical simulation.

2.2.1 Johnson-Cook strength model

The dynamic flow stress-plastic strain relationship for metallic materials undergoing plastic deformation is best described by Johnson-Cook constitutive relation [43, 44] which is given as

$$\sigma = [A + B\varepsilon^n][1 + C \ln \dot{\varepsilon}^*][1 - T^{*m}] \quad (2.1)$$

where σ is the von-Mises flow stress, ε is the equivalent plastic strain, $\dot{\varepsilon}^* = \dot{\varepsilon}/\dot{\varepsilon}_0$ is the dimensionless normalised plastic strain rate considering the reference strain rate $\dot{\varepsilon}_0$, $\dot{\varepsilon}$ is the strain rate, and $T^* = (T - T_0)/(T_m - T_0)$ is the homologous temperature of the material. A is the yield strength of the material, B is the strain hardening coefficient, n is the strain hardening exponent, C is the strain rate coefficient, m is the thermal softening parameter, T_0 is the reference temperature, and T_m is the melting temperature of the material. The first, second and third terms in Eq. (2.1) respectively capture the large strain, strain rate and thermal softening effects during loading.

2.2.2 Johnson-Cook damage model

The Johnson-Cook damage model is based on the fracture strain of the metallic material and depends on stress triaxiality, strain rate and temperature [43, 45]. The initiation of damage in the material element is defined by

$$D_i = \sum \frac{\Delta\varepsilon}{\varepsilon_f} \quad (2.2)$$

where $\Delta\varepsilon$ is the incremental plastic strain during the integration cycle and ε_f is the fracture strain which is given by the equation

$$\varepsilon_f = [D_1 + D_2 \exp(D_3\sigma^*)][1 + D_4 \ln \dot{\varepsilon}^*][1 + D_5 T^*] \quad (2.3)$$

where $\sigma^* = \sigma_m/\bar{\sigma}$ is the dimensionless pressure *i.e.* stress ratio, σ_m is the mean stress, $\bar{\sigma}$ is the von-Mises equivalent stress, and $D_1 \dots D_5$ are the damage constants for the material which can be determined from experiments. This model assumes that the fracture suddenly occurs when $D_i = 1$. However, material strength degrades after certain critical strain due to the development of internal cracks, which is further explained in the next section.

2.2.3 Implementation of damage evolution

A typical stress-strain response of metals under uniaxial loading conditions is shown in Figure 2.1. Curve **a-b** represents the linear elastic phase, and curve **b-c** represents the strain hardening (including yielding, if any) phase, where point **c** represents the onset of damage beyond which the load carrying capacity of the material decreases due to the development of macro cracks. Curve **c-d** represents material behaviour with damage evolution. In the absence of damage evolution, stress-strain response follows curve **c-d'**. At point **c**, σ_0 and ε_0 are the stress and equivalent plastic strain at the onset of damage where $D = 0$ and, ε_f is the equivalent plastic strain at failure where damage variable $D = 1$.

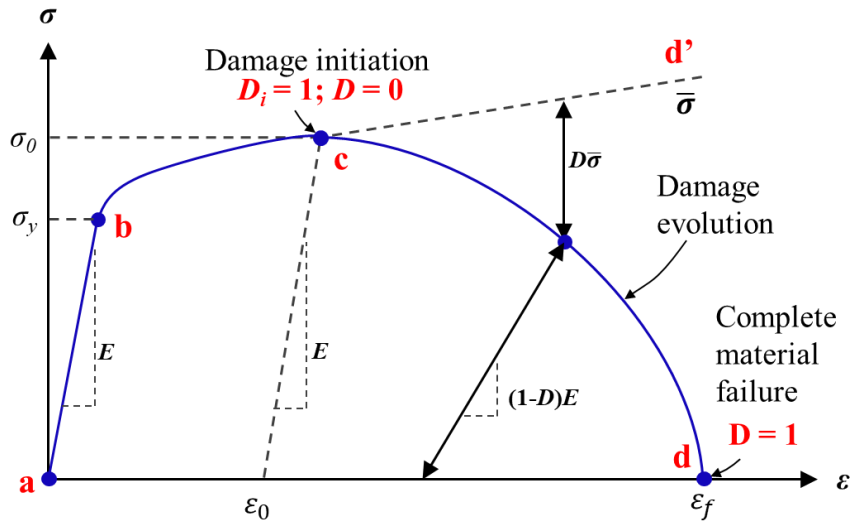


Figure 2.1: Implementation of Damage evolution

In damage evolution phase, material strength reduces due to degradation of elastic stiffness of material and σ at any point of loading is governed by scalar damage equation

$$\sigma_D = (1 - D)\bar{\sigma} \quad (2.4)$$

where σ_D is stress at the damaged state, D is the damage propagation variable, and $\bar{\sigma}$ is the undamaged stress which is the stress obtained from the Johnson-Cook constitutive relation given in Eq. (2.1)

The damage model proposed by Johnson-Cook assumes that damage accumulates in the material element during plastic straining and that the material fails immediately when damage reaches a critical value. But material strength degrades with damage and experiments indicates, the effect of damage on material strength remains zero during the buildup of

dislocations generating micro cracks [53]. Based on these observations, a unified model for damage [53] is given by,

$$\sigma = (1 - D)[A + B\varepsilon^n][1 + C \ln \varepsilon^*][1 - T^{*m}] \quad (2.5)$$

where $D = 0$ for undamaged material and $D = 1$ for fully fractured material. There exists a threshold of accumulated plastic strain at which damage starts to evolve [53, 54]. In the present work, damage initiation is assumed to be starting when the accumulated plastic strain reaches a critical value, and then the stress-strain relation follows Eq. (2.5) after the initiation of damage. In the present work, fracture mechanics based damage evolution is followed, which is explained in detail in Section 2.4.3.

2.3 Experiments

2.3.1 Specimen geometry

E250 Structural steel is a medium carbon steel with minimum yield strength of 250MPa and its chemical composition obtained from a spectroscopic analysis is given in Table 2.2.

Table 2.2: Chemical composition of E250 structural steel (% mass)

C	Mn	Si	P	S	Fe
0.2 - 0.23	1.5	0.4	0.045 (max)	0.045 (max)	Remainder

The specimens are made from 2 mm thick hot rolled sheet by laser cutting operation. Two batches of specimens are experimented and the results are averaged. First batch of specimens in experiments are represented by E1 second batch by E2. In total, 16 types of experiments are conducted on 32 specimens and their list is given in Table 2.3. All tensile experiments at room temperature are conducted on BiSS make servo hydraulic controlled universal testing machine with a maximum capacity of 25 kN which is shown in Figure 2.2(a). High temperature tensile experiments are conducted on INSTRON make electro-mechanically controlled UTM with an attached furnace having a maximum capacity of 600 KN which is shown in Figure 2.2(b). All the tensile experiments at room temperature and conducted as per ASTM-E8 [55] standard and elevated temperature are conducted as per ASTM E21 [56] SHPB testes are conducted on circular specimens to obtain stress-strain curves at higher strain rates and the setup is shown in Figure 2.2(c). For SHPB experiments, there is no standard available and test is conducted as per the guidelines prescribed by testing lab.

All the experiments are broadly classified into four categories *viz.* 1) tensile experiments at different strain rates, 2) SHPB experiments at higher strain rates, 3) tensile experiments of notched specimens, and 4) tensile experiments at different temperatures, to obtain the Johnson-Cook model parameters as shown in Table 2.3.

In SHPB set-up all the bars are made of D2 tool steel that has a hardness of more than 50 HRC and have a diameter of 12 mm. The incident bar and transmission bars have a length of 1200 mm. For low and high strain rate experiments striker length was 300 mm and 200 mm,

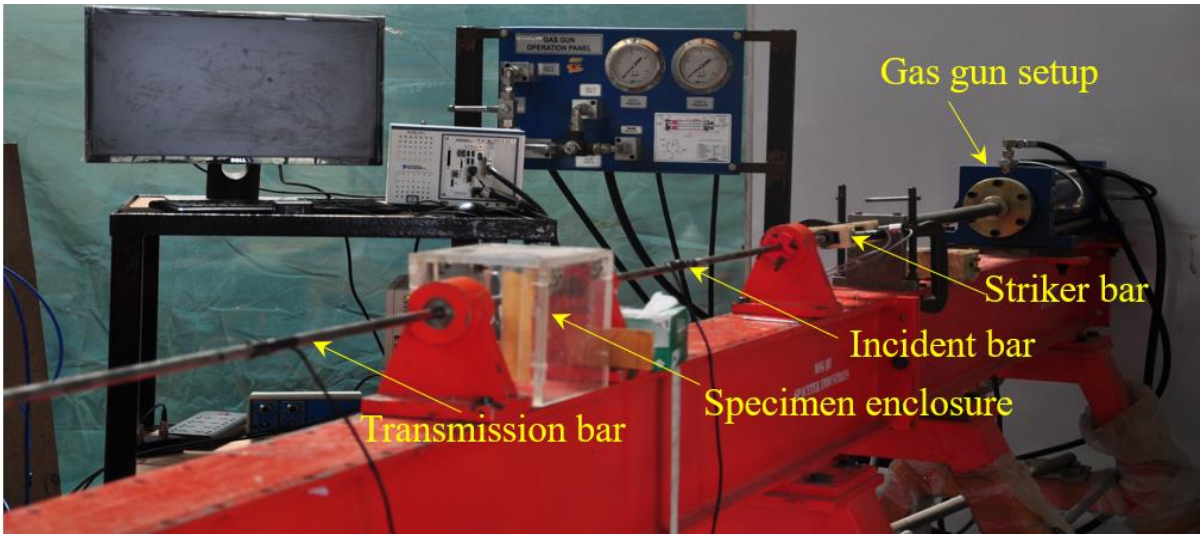
respectively. The strain pulses were recorded using foil strain gauges of gauge length 2 mm through a high-speed amplifier and National Instruments data acquisition system.



(a) UTM for uniaxial tensile tests at room temperature



(b) UTM for uniaxial tensile tests at higher temperatures



(c) SHPB setup for experiments at high strain rates

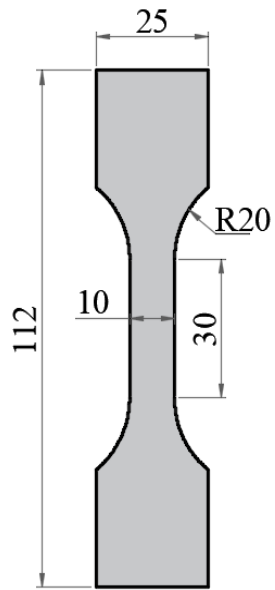
Figure 2.2: Experimental setup for stress-strain behaviour

Table 2.3: Details of experiments and specimens for determining parameters of Johnson-Cook material and damage models

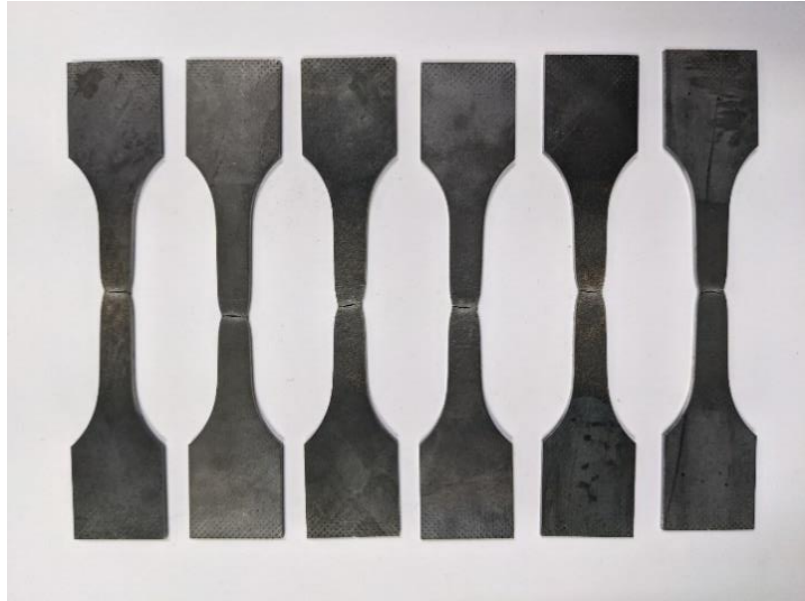
J-C parameter	Experiment	Specimen No. E1 – Experiment 1 E2 – Experiment 2	Temperature (°C)	Stress triaxiality	Strain rate (1/s)
A, B, n	Tensile test	1 (E1,E2)	30	$\sigma^* = 0.33$	3×10^{-4}
C	D_4	Tensile test	30	$\sigma^* = 0.33$	3×10^{-4}
		1 (E1,E2)		$\sigma^* = 0.33$	3×10^{-3}
		2 (E1,E2)		$\sigma^* = 0.33$	3×10^{-2}
		3 (E1,E2)		$\sigma^* = 0.33$	3×10^{-1}
		4 (E1,E2)		$\sigma^* = 0.33$	4×10^{-1}
		5 (E1,E2)		$\sigma^* = 0.33$	1×10^0
	SHPB	7 (E1,E2)	30	-	3×10^3
	8 (E1,E2)	-	8×10^3		
D_1, D_2, D_3	Tensile test (notched specimens at various σ^*)	9 (E1,E2)	30	$\sigma^* = 0.33$	3×10^{-4}
		10 (E1,E2)		$\sigma^* = 0.49$	3×10^{-4}
		11 (E1,E2)		$\sigma^* = 0.70$	3×10^{-4}
		12 (E1,E2)		$\sigma^* = 0.95$	3×10^{-4}
m, D_5	Tensile test	13 (E1,E2)	200	$\sigma^* = 0.33$	3×10^{-4}
		14 (E1,E2)	400	$\sigma^* = 0.33$	3×10^{-4}
		15 (E1,E2)	600	$\sigma^* = 0.33$	3×10^{-4}
		16 (E1,E2)	800	$\sigma^* = 0.33$	3×10^{-4}

2.3.2 Tensile experiments at various strain rates

Six types of tensile experiments were conducted on 12 Specimens at room temperature at strain rates of 0.0003/s, 0.003/s, 0.03/s, 0.3/s, 0.4/s and 1.0/s. Specimen geometry used in these experiments are shown in Figure 2.3(a) and first batch of specimens after experiments are shown in Figure 2.3(b).



(a) Specimen geometry
(thickness = 2.0 mm)



(b) Tested specimens 1 to 6 (Batch E1)

Figure 2.3: Plain specimens for uniaxial tensile experiments at various strain rates at room temperature

The average true stress-true strain curves obtained from experiments are shown in Figure 2.4. The material has exhibited strain rate sensitivity as seen in the stress strain curves where its yield and ultimate tensile strengths increased with increase in strain rate.

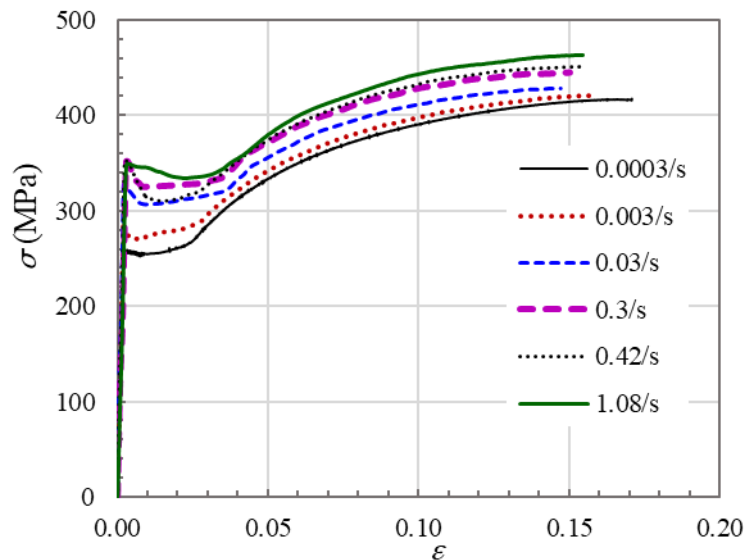


Figure 2.4: Averaged true stress-true strain curves of plain tensile specimens at various strain rates, obtained from tensile experiments at room temperature

2.3.3 SHPB experiments at higher strain rates

The basic principle governing the SHPB is that the impact stress waves travelling through the specimen (*i.e.* material to be tested) are fast enough that the time interval for propagation is much smaller than the total time of test. This permits several reflections to occur at the ends of the tested specimen which reasonably presents a uniform state of stress and strain. This uniaxial stress state is ensured through the use of a lubricant between the ends of bars and specimen. Finally, it is assumed that the stresses and velocities in the specimen ends are transmitted through the input and output bars without any dispersion. Simple expressions for stress, strain and strain rate in the specimen are obtained by assuming and adopting the same material and cross sectional area for both input and output bars.

Let c_0 be the fundamental longitudinal velocity of elastic stress wave in the bar and is given by

$$c_0 = \sqrt{\frac{E}{\rho}} \quad (2.6)$$

in which E and ρ are respectively the elastic modulus and density of the material of the bar. The displacements u_1 and u_2 at the left and right ends of the specimen can be written in terms of the incident ε_i , reflected ε_r and transmitted ε_t strain pulses as

$$u_1 = c_0 \int_0^{t_s} (\varepsilon_i - \varepsilon_r) dt \quad (2.7a)$$

and

$$u_2 = c_0 \int_0^{t_s} \varepsilon_t dt \quad (2.7b)$$

where, t_s is the time interval for the stress wave propagation through the specimen. Here the compressive stresses and strains have positive sign. Due to the assumption of uniform state of stress and strain through the length *i.e.* thickness of the specimen L_s , the strain in the specimen ε_s is given by

$$\varepsilon_s = \frac{u_1 - u_2}{L_s} \quad (2.8)$$

Substituting Eqs. (2.7 a-b) into Eq. (2.8) provides

$$\varepsilon_s = \frac{c_0}{L_s} \int_0^{t_s} (\varepsilon_i - \varepsilon_r - \varepsilon_t) dt. \quad (2.9)$$

The forces P_1 and P_2 acting respectively at the left and right ends of the specimen are given by

$$P_1 = EA_t (\varepsilon_i + \varepsilon_r) \quad (2.10a)$$

and

$$P_2 = EA_t \varepsilon_t \quad (2.10b)$$

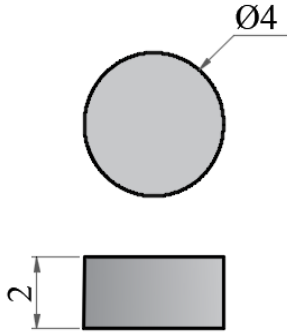
where A_t is the cross sectional area of the incident and transmitter bars. The specimen is in equilibrium under the action of the above forces, *i.e.* $P_1 = P_2 = P_e$. So, Eqs (2.10a-b) yields $\varepsilon_t = \varepsilon_i + \varepsilon_r$. Therefore, the stress, strain and the strain rate acting on the specimen can be obtained respectively from the following equations.

$$\sigma_s = \frac{P_e}{A_s} = E \varepsilon_t \frac{A_t}{A_s} \quad (2.11a)$$

$$\varepsilon_s = \frac{-2c_0}{L_s} \int_0^{t_s} \varepsilon_r dt \quad (2.11b)$$

$$\dot{\varepsilon}_s = \frac{-2c_0}{L_s} \varepsilon_r \quad (2.11c)$$

where A_s is the cross sectional area of the specimen.



(a) Specimen geometry

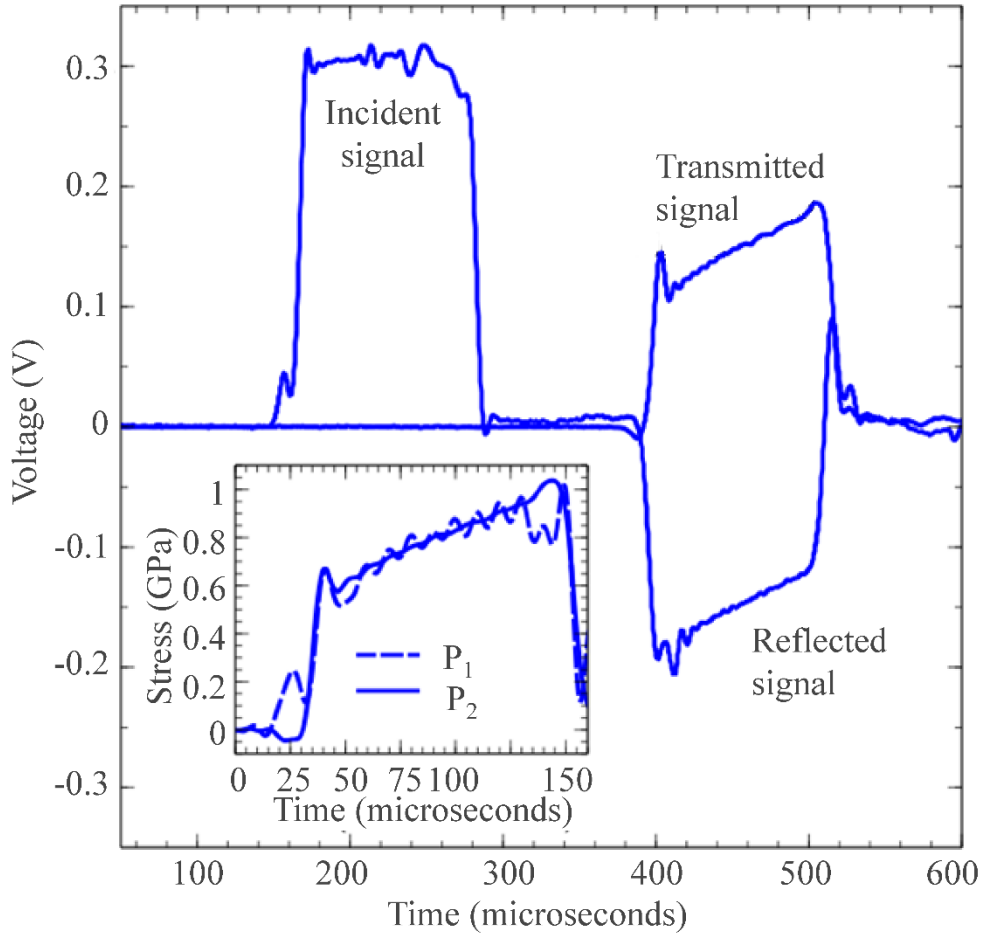


(b) Tested specimens 7 and 8 (Batch E1)

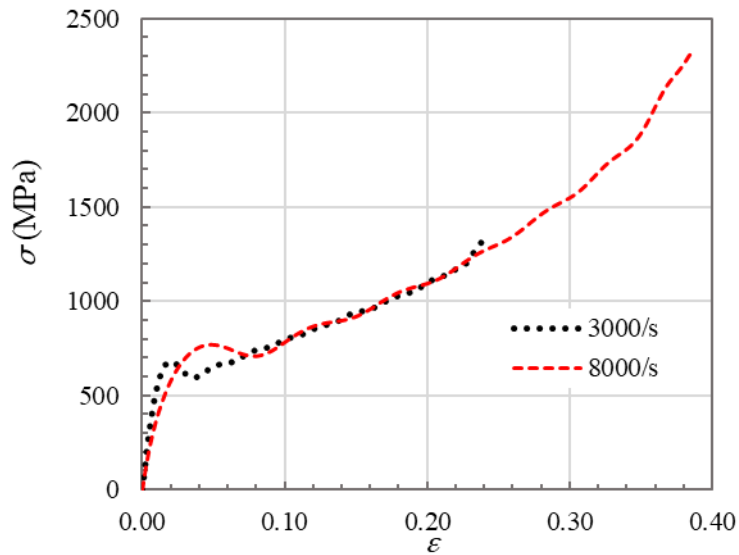
Figure 2.5: Specimens for SHPB experiments at higher strain rates

Thus we can characterize the response of the specimen material under dynamic loads if we can accurately measure the reflected and transmitted impact waves and by knowing the elastic modulus, density and cross-section area of the bar; and the cross sectional area and length of the specimen.

SHPB experiments were conducted on four circular specimens at room temperature and at strain rates of 3000 /s and 8000 /s. Specimen geometry used in these experiments are shown in Figure 2.5(a) and specimens after experiments are shown in Figure 2.5(b). The impact waves are measured with strain gauges, as shown in Figure 2.6(a), by acquiring the strain signals from the strain gauge mounted on the bars. The inset of Figure 2.6(a) shows the force balance of the sample *i.e.* the specimen. Stress acting on the sample-incident bar and sample-transmission bar interfaces are represented by P_1 and P_2 , respectively. The sample is in equilibrium.



(a) Typical strain signals obtained from SHPB setup. The inset shows the force balance of the sample. Stress acting on the sample-incident bar and sample-transmission bar interfaces are represented by P_1 and P_2 , respectively.



(b) Averaged true stress-true strain curves of specimens at higher strain rates

Figure 2.6: Typical strain signals from SHPB setup and true stress-true strain curves obtained from SHPB experiments

The averaged true stress-true strain curves obtained from SHPB experiments using Eq. (11a-c) are shown in Figure 2.6(b). These stress-strain data demonstrated a phenomenal increase in strength of the material at higher strain rates. True stress-true strain curves at all strain rates are shown in Figure 2.7.

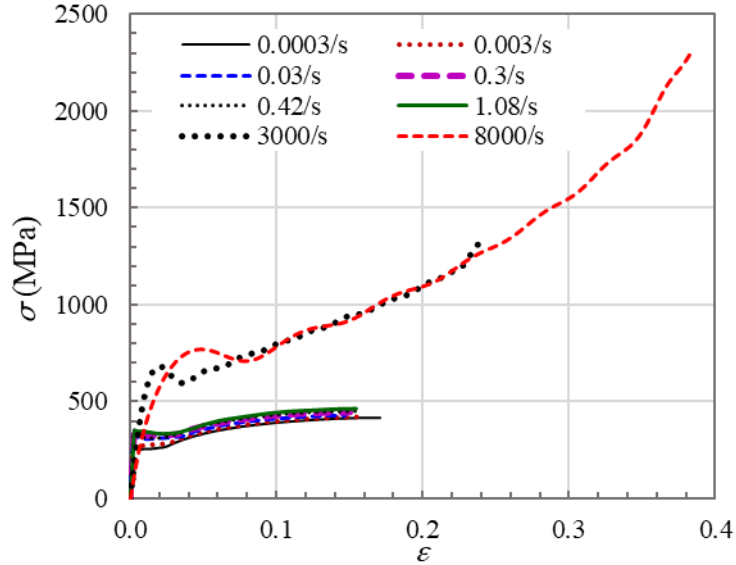
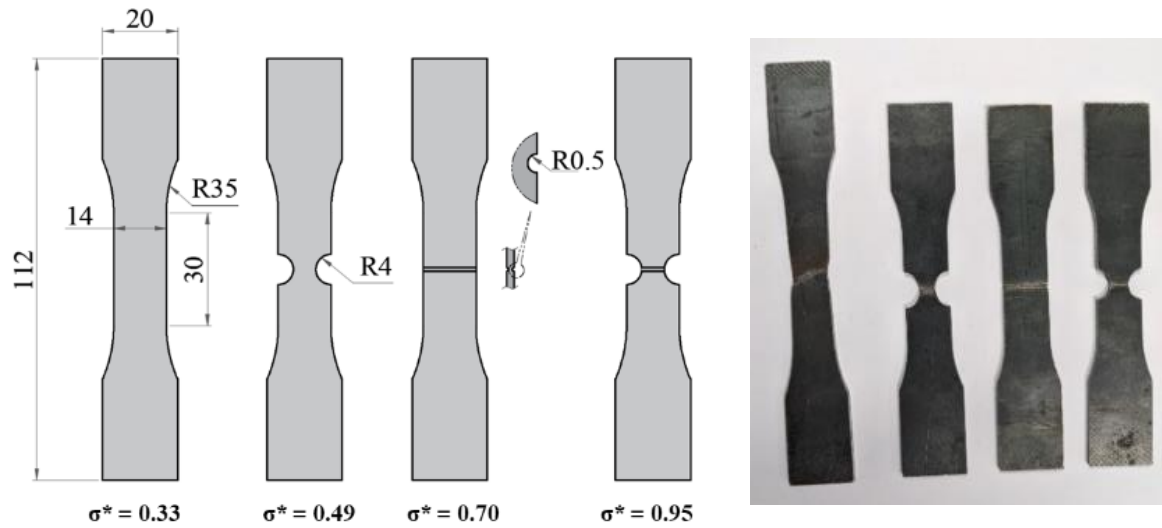


Figure 2.7: Averaged true stress-true strain curves of specimens at different strain rates

2.3.4 Tensile experiments of notched specimens

Tensile experiments were conducted on two sets of four notched specimens having various values of stress triaxiality (σ^*). The values of stress triaxialities are found to be 0.33, 0.49, 0.7, and 0.95. These values are obtained through the FEA simulation of each notched specimen, and the procedure followed to obtain these values is explained in Section 2.4.2.2. Specimen geometry of these notched specimens is shown in Figure 2.8(a) and first batch of experimented specimens in Figure 2.8(b).

Averaged true stress-true strain curves of notched specimens obtained from these experiments are shown in Figure 2.9. The experimental results exhibited a substantial decrease in failure strain and a marginal change in ultimate strength when the stress triaxiality is increased from 0.33 to 0.49; and from 0.49 to 0.7, a decrease in failure strain and an increase in ultimate strength are observed, but after 0.7, the changes in responses are minimal.



(a) Specimen geometry
(thickness = 2.0 mm)

(b) Specimens after the experiments 9 to 12 (Batch E1)

Figure 2.8: Notched specimens at different stress triaxiality (σ^*) (at strain rate value = 0.0003 /s)

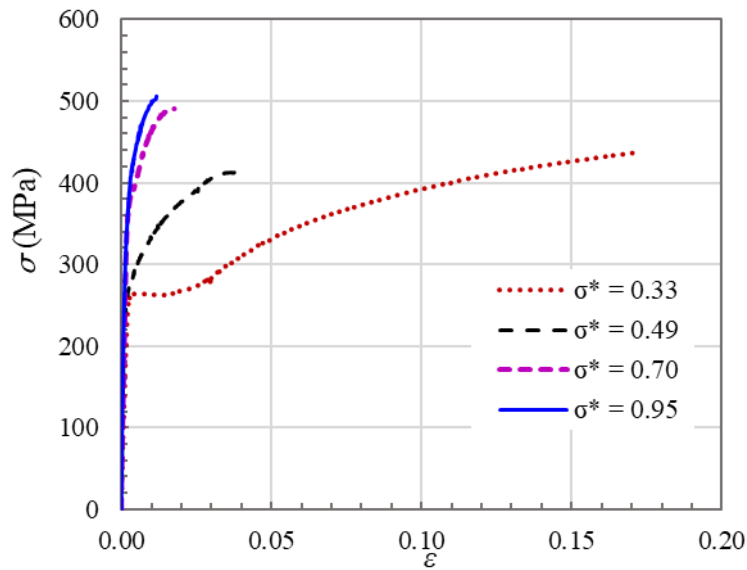
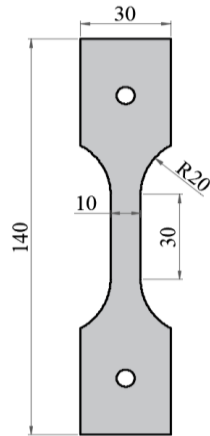


Figure 2.9: Averaged true stress-true strain curves of specimens at various σ^* (at strain rate value = 0.0003 /s)

2.3.5 Tensile experiments at elevated temperatures

Tensile experiments were conducted on two sets of four specimens at elevated temperatures of 200 °C, 400 °C, 600 °C, and 800 °C, respectively. The geometry of these specimens is shown in Figure 2.10(a) and the first batch of damaged specimens after the experiments are shown in Figure 2.10(b).



(a) Specimen geometry (thickness = 2.0 mm) (b) Specimens after the experiments 13 to 16 (Batch E1)

Figure 2.10: Specimens for tensile experiments at elevated temperatures (at strain rate value = 0.0003/s)

The averaged true stress-strain curves obtained from these experiments are shown in Figure 2.11. The results demonstrated an increase in failure strain and reduction in ultimate strength of the material with increase in temperature.

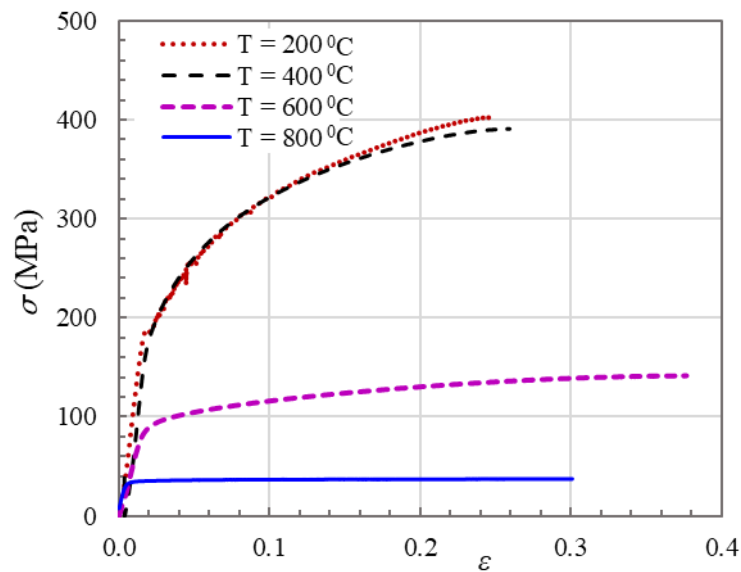


Figure 2.11: Averaged true stress-true strain curves of specimens at elevated temperatures (at strain rate value = 0.0003 /s)

The change in these responses is quite significant when temperature is increased from 400 °C to 600 °C. At 800 °C, the material behaved plastically with a constant ultimate strength of less than 40 MPa and failed with less plastic displacement compared to specimens at 600 °C.

2.4 Determination of parameters

Average material properties obtained from tension test conducted at quasi-static strain rate are, Young's modulus = 198 GPa; Poisson's ratio = 0.29; yield strength = 252.3 MPa; ultimate tensile strength = 418 MPa; and elongation at break = 22%. The Johnson-Cook's five strength model parameters (A , B , n , C and m) and five damage model parameters (D_1 to D_5) are extracted from sixteen different types of experiments conducted and discussed in this section.

2.4.1 J-C strength model parameters

2.4.1.1 Determination of A , B , n

The parameters A , B and n in Eq. (2.1) are determined from the tensile experiments conducted at a strain rate, $\dot{\epsilon} = 0.0003$ /s and room temperature $T = 30$ °C. Parameter A is the initial yield strength and is found as 252.3MPa from the experiment. For determining the strain hardening co-efficient B and strain hardening exponent n , stress-strain data in the strain hardening region up to the maximum strength is used. The data from the experiment is considered as a reference strain rate *i.e.* $\dot{\epsilon}_0 = 0.0003$ /s and reference temperature is taken as $T_0 = 30$ °C. The temperature for the experiment was also $T = 30$ °C. This in turn will lead to $\dot{\epsilon}^* = \dot{\epsilon}/\dot{\epsilon}_0 = 1$ and $T^* = 0$. Substituting these values in Eq. (2.1) yields the second and third terms as 1 and results in following expression.

$$(\sigma - A) = B(\epsilon)^n \quad (2.12)$$

The strain hardening region from the stress-strain data is plotted as $(\sigma - A)$ against ϵ as shown in Figure 2.12. A trend line with power fit to this data gives the values matching the form in Eq. (2.12) where $B = 466.72$ MPa and $n = 0.5447$.

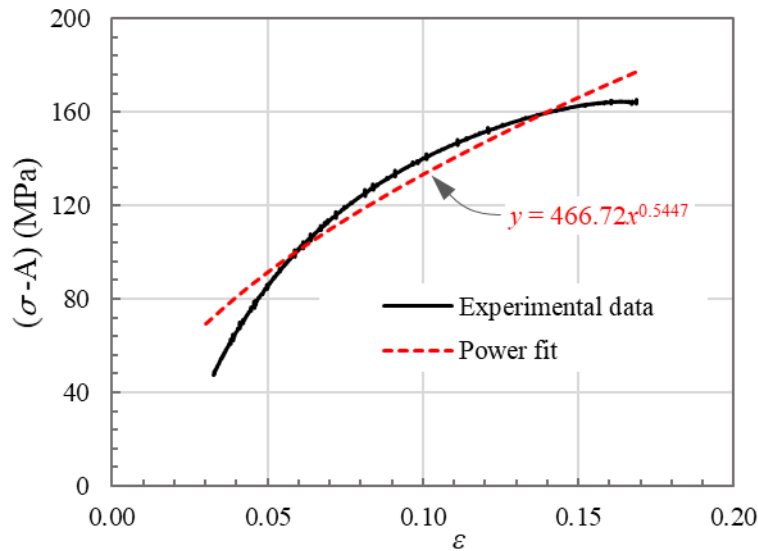


Figure 2.12: Determination of B and n

2.4.1.2 Determination of C

Data from experiments conducted at eight different strain rates and at temperature $T = 30\text{ }^{\circ}\text{C}$ which is also considered as a reference temperature T_0 as given in Table 2.3. This will lead to $T^* = 0$. Substituting this value in Eq. (2.1) yields the third term as 1 and the equation can be written as

$$\frac{\sigma}{(A+B\varepsilon^n)} - 1 = C \ln(\dot{\varepsilon}^*) \quad (2.13)$$

Using Eq. (2.13), eight data points can be obtained for the left hand side (LHS) term at any given plastic strain (say 5% or 10%) from stress-strain curves. Considering the reference strain rate as $\dot{\varepsilon}_0 = 0.0003\text{ /s}$, eight different strain rates $\dot{\varepsilon}$ give eight corresponding data points for the right-hand side (RHS) term of Eq. (2.13). Plot of eight LHS data points against corresponding RHS data for 5% and 10% plastic strain is shown in Figure 2.13.

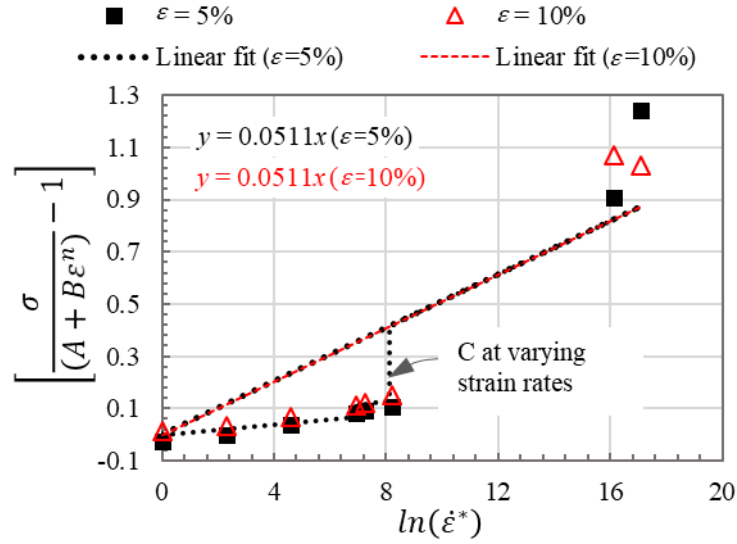


Figure 2.13: Determination of C

Linear fit of these eight data points at 5% and 10% plastic strain gives a value of C as 0.0511. However, a large error is observed between the actual data points with respect to the linear fit. In order to minimize this error, C is calculated between given range of strain rates. For strain rates less than 0.3/s, C is calculated as 0.010, for strain rates $0.3/s \geq \dot{\varepsilon} \leq 1/s$, C is calculated as 0.016 and for strain rates more than 1/s, C is taken as 0.0511.

2.4.1.3 Determination of m

In present work, isothermal heating is considered and load induced adiabatic heating is neglected to retain the simplistic nature of original J-C work. Thermal softening exponent m in Eq. (2.1) can be determined from results of tensile experiments conducted at four different elevated temperatures as mentioned in Table 2.3 and their stress-strain behaviors are shown in Figure 2.11. Reference temperature is taken as $T_0 = 30\text{ }^{\circ}\text{C}$ and melting temperature as $T_m = 1415\text{ }^{\circ}\text{C}$. These experiments were conducted at a strain rate, $\dot{\varepsilon} = 0.0003\text{ /s}$ and as earlier,

considering the reference strain rate as $\dot{\epsilon}_0 = 0.0003$ /s, the second term in Eq. (2.1) leads to unity. The Eq. (2.1) can now be written as

$$\ln\left(1 - \frac{\sigma}{(A+B\epsilon^n)}\right) = m \ln(T^*) \quad (2.14)$$

Using Eq. (2.14), four data points for LHS and RHS terms can be obtained at four different temperatures at plastic strains of 5%, 10%, 15% and 20%. The LHS term is plotted against RHS term at four different temperatures for the considered plastic strains, as shown in Figure 2.14.

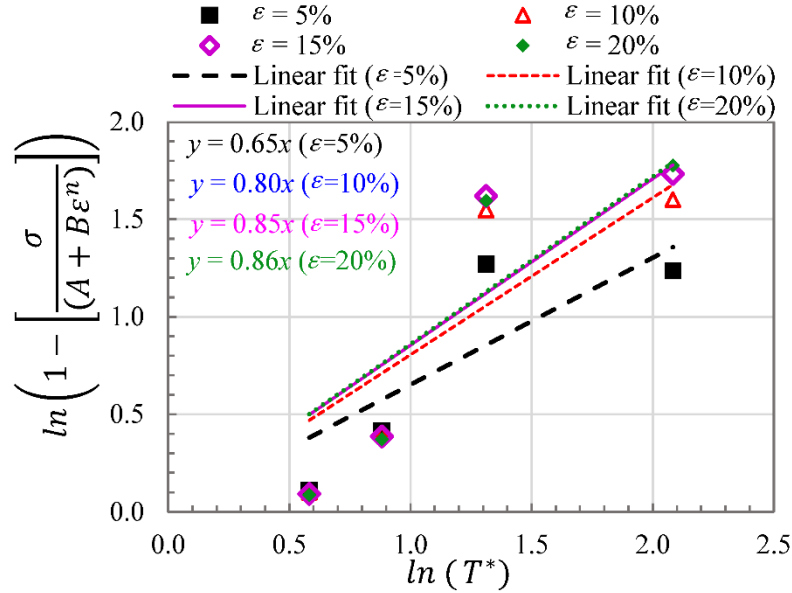


Figure 2.14: Determination of m

The linear trend line fit between these data points at each value of plastic strain gives the value of m as the slope of these lines. The slopes at four values of plastic strains *i.e.* 5%, 10%, 15% and 20%, respectively, resulted in values of m as 0.6515, 0.805, 0.8537 and 0.8597. The average value of m is found to be 0.79.

2.4.2 J-C damage model parameters

Five different J-C's damage model parameters D_1 to D_5 are determined from results of different tensile experiments. The procedures are detailed in this section.

2.4.2.1 Failure strain from experiments

Failure strain is given by an expression [45, 57]

$$\epsilon_f = \ln\left(\frac{A_0}{A_f}\right) \quad (2.15)$$

where A_0 is the initial cross-sectional area of specimen at gauge length location before experiment and A_f is the cross-sectional area after experiment. The failure strain in each

experiment is obtained by measuring the cross-sectional area of the specimens before and after the experiments using digital imaging technique and from Eq. (2.15).

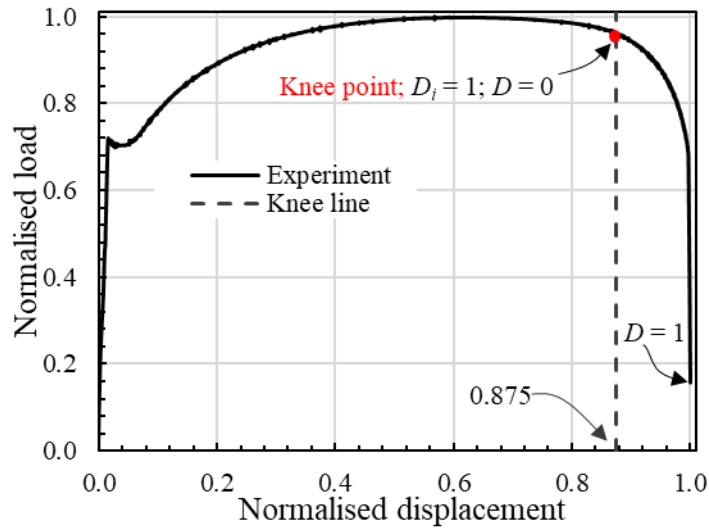


Figure 2.15: Computation of accumulated critical plastic strain

From the normalised average load deflection curve of the plain specimens at reference strain rate and temperatures shown in Figure 2.15, it can be observed that, at a certain point of deflection, load gradually reduces when deflection reaches a critical value. After reaching critical value, a sudden reduction in load can be observed. In present work, this location is assumed to be the point of change in curvature for the load-displacement curve between maximum load and failure. This location of the change in curvature (knee point) is found using the Kneedle algorithm proposed in [58]. This value is 87.5% of the total deflection. The critical value of accumulated plastic strain is also assumed to be equal to 87.5% of the fracture strain. In the present work, all the J-C failure parameters are computed by considering the critical value of plastic strains instead of fracture strains.

2.4.2.2 Determination of stress-triaxiality of notched specimens

FEA simulations are conducted on the notched specimens shown in Figure 2.8(a) using the J-C constitutive parameters obtained in Section 2.4.1. Curves obtained by plotting mean stress to von-Mises stress in the centre element at the middle cross-section of the specimens are shown in Figure 2.16. The slope of these curves remains almost constant within the elastic stage and continuously increases in the plastic stage. In the present work, the stress triaxiality of each specimen is obtained by plotting the linear curve fit to this data within the elastic limit where the distortion of the element is negligible. The values of stress triaxialities are found to be 0.33, 0.49, 0.7, and 0.95 for the specimens S9, S10, S11 and S12, respectively.

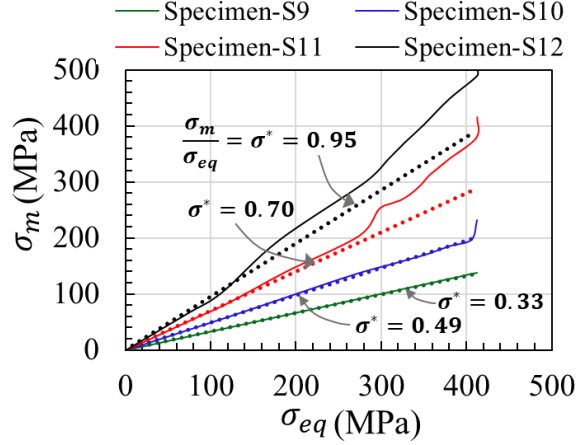


Figure 2.16: Obtaining stress triaxiality of notched specimens (9 to 12 shown in Figure 2.8)

2.4.2.3 Determination of D_1 , D_2 , and D_3

The values of damage model parameters D_1 , D_2 , and D_3 are determined from tensile experiments of notched Specimens conducted at a strain rate, $\dot{\epsilon} = 0.0003$ /s and at temperature $T = 30$ °C. Considering the reference strain rate as $\dot{\epsilon}_0 = 0.0003$ /s and reference temperature as $T_0 = 30$ °C, will lead to $\dot{\epsilon}^* = \dot{\epsilon}/\dot{\epsilon}_0 = 1$ and $T^* = 0$. Substituting these values in Eq. (2.3) yields the second and third terms as 1 and results in following expression.

$$\epsilon_f = D_1 + D_2 e^{(D_3 \sigma^*)} \quad (2.16)$$

The data of experimental failure strain ϵ_f of is plotted against the respective stress triaxiality σ^* in Figure 2.17.

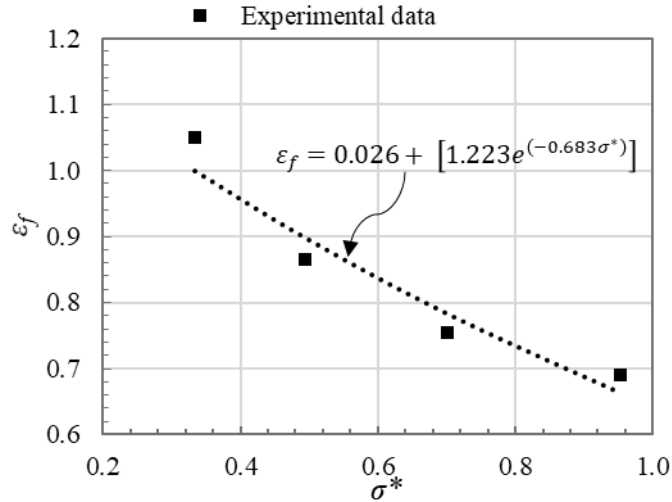


Figure 2.17: Determination of D_1 , D_2 and D_3

Fitting the curve based on the Eq. (2.16) to these data points by adopting minimization of errors based on least squares gives values for D_1 , D_2 and D_3 .

D_1 , D_2 and D_3 are taken as 0.026, 1.223 and -0.683 respectively.

2.4.2.4 Determination of D_4

The value of D_4 can be determined from tensile experimental results which were experimented at six different strain rates at temperature $T = 30\text{ }^{\circ}\text{C}$ as given in Table 2.3. Considering the reference temperature as $T_0 = 30\text{ }^{\circ}\text{C}$, leads to $T^* = 0$ which in turn results the third term in Eq. (2.3) to attain a value of 1 and the equation reduces to

$$\frac{\varepsilon_f}{[D_1 + D_2 e^{(D_3 \sigma^*)}]} - 1 = D_4 \ln \dot{\varepsilon}^* \quad (2.17)$$

Reference strain rate is considered as $\dot{\varepsilon}_0 = 0.0003/\text{s}$. Using Eq. (2.17), six data points are obtained for the LHS term from stress-strain curves. Plot of these six LHS data against corresponding RHS data is shown in Figure 2.18. D_4 is taken as the slope of the linear trend line fit to the data points. D_4 is taken as -0.0537 .

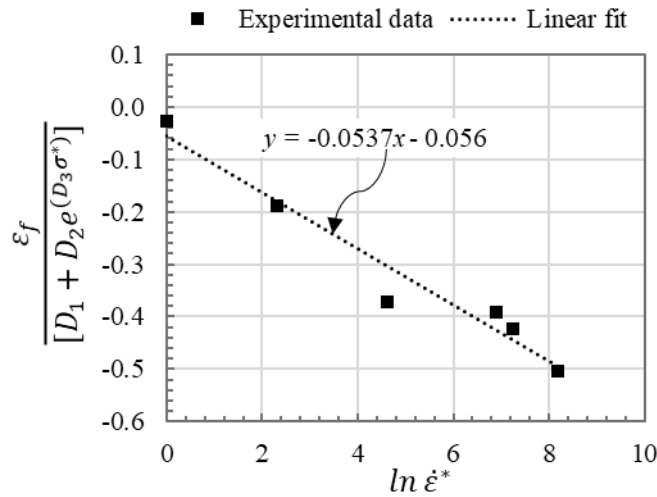


Figure 2.18: Determination of D_4

2.4.2.5 Determination of D_5

The value of D_5 is determined from results of tensile experiments at four different elevated temperatures. Since all these experiments were conducted at the reference strain rate of $0.0003/\text{s}$ itself, the second term in Eq. (2.3) leads to unity and the equation can be written as

$$\frac{\varepsilon_f}{[D_1 + D_2 e^{(D_3 \sigma^*)}]} - 1 = D_5 T^* \quad (2.18)$$

Using Eq. (2.18), four data points for LHS and RHS terms can be obtained at four different temperatures and are plotted as shown in Figure 2.19. D_5 is the value of slope of linear trend line fit between these data points. D_5 and it is taken as 1.517 .

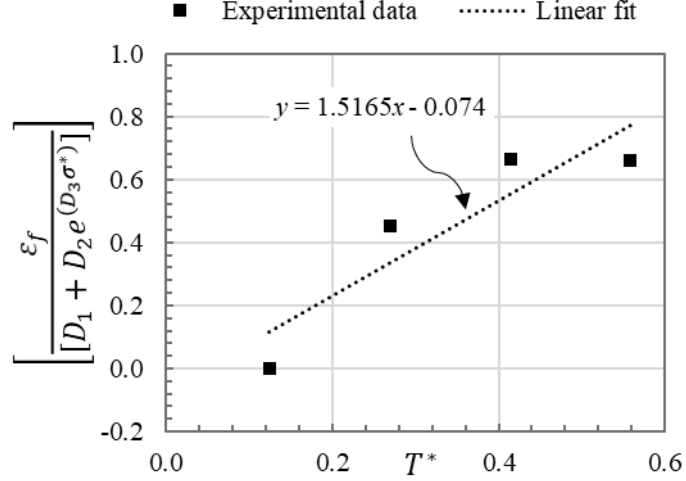


Figure 2.19: Determination of D_5

2.4.3 Damage evolution

In the present work, a different approach is followed to implement damage initiation and evolution to use the default input parameters available in Abaqus [59-61]. As explained in Section 2.2, the damage initiates when the accumulated plastic strain in the material reaches the critical value of plastic strain given by Eq. (2.3) and is shown in Figure 2.1. All the J-C damage parameters thus computed will define this critical plastic strain at which damage initiates. Then, the damage evolution is implemented in Abaqus Explicit [61] using the fracture mechanics-based stress-displacement response proposed by Hillerborg *et al.* [62] instead of the stress-strain response in order to reduce mesh dependency due to strain localisation. Stress in the material element in a damaged state, σ_D in this phase is defined by Eq. (2.4) and the value of D is obtained by assuming a linear relationship between u^{pl} , the effective plastic displacement and damage variable which is given by

$$D = \frac{u^{pl}}{u_f^{pl}} \quad (2.19)$$

where u_f^{pl} is the plastic displacement at failure. Hillerborg *et al.* [62] proposed that the crack is assumed to propagate when stress at the crack tip reaches the tensile strength of the material, σ_y and the amount of fracture energy G_f , absorbed per widening the unit crack area is given by

$$G_f = \int_0^{w_l} \sigma_y dw \quad (2.20)$$

where w_l is the crack tip opening displacement equivalent to u_f^{pl} .

It is implemented in Abaqus [59, 61] as,

$$G_f = \frac{\sigma_y u_f^{pl}}{2} \quad (2.21)$$

G_f is a material parameter and can be represented by the area under the stress-displacement curve of the pre-notched specimen. In the present work, the area under the load-displacement curve of the notched specimen (*i.e.* Specimen-12(E1 and E2) shown in Figure 2.8(a)) per unit

cross-sectional area is taken as the fracture energy required for opening unit area of the crack, which is found to be 224.6 N/mm.

The element will be deleted when $D = 1$, *i.e.* when plastic displacement in the material reaches plastic displacement at failure obtained from Eq. (2.21), which is implemented as a default algorithm in Abaqus explicit FEA code [61].

2.4.4 J-C material and damage parameters

Consolidate list of J-C material and damage parameters are given in Table 2.4.

Table 2.4: Determined parameters of Johnson-Cook strength and damage models

	A (MPa)	B (MPa)	n	C	m
J-C strength model	252.3	466.7	0.545	0.010 ($\dot{\epsilon} < 0.3/s$)	0.79
				0.016 ($0.3/s > \dot{\epsilon} < 1/s$)	
				0.051 ($\dot{\epsilon} > 1/s$)	
J-C damage model	D_1	D_2	D_3	D_4	D_5
	0.026	1.223	-0.683	-0.054	1.517

2.5 Validation of J-C material and damage model parameters

In order to validate the determined J-C model parameters, three experimental data are compared with respect to FE simulation results. First one is the average load-deflection curve of tensile experiments conducted at 1.08 /s strain rate, second one is the load-deflection curve of a separate notched specimen tensile tested at 0.3 /s strain rate, and the third one is a comparison of stress-strain curves from the burst test of a flat scored metallic disc. The experiments are numerically simulated using ABAQUS Explicit [61].

2.5.1 Validation-1: Plain tensile specimen

The tensile experiment of plain specimen at 1.08/s strain rate is considered to validate the determined J-C model parameters. Specimen geometry and the fractured specimens are shown in Figure 2.20(a) and 2.20(c). The half model is discretized using 29610 C3D8R eight node solid brick elements with reduced integration and symmetric boundary condition applied. A maximum element size of 0.5 mm is adopted after a mesh convergence study. The FEA model is fixed at one end and a displacement loading of 65 mm/s is applied at the other end and the simulation is allowed to run until the failure of the specimen. The failed specimen is shown in Figure 2.20(b).

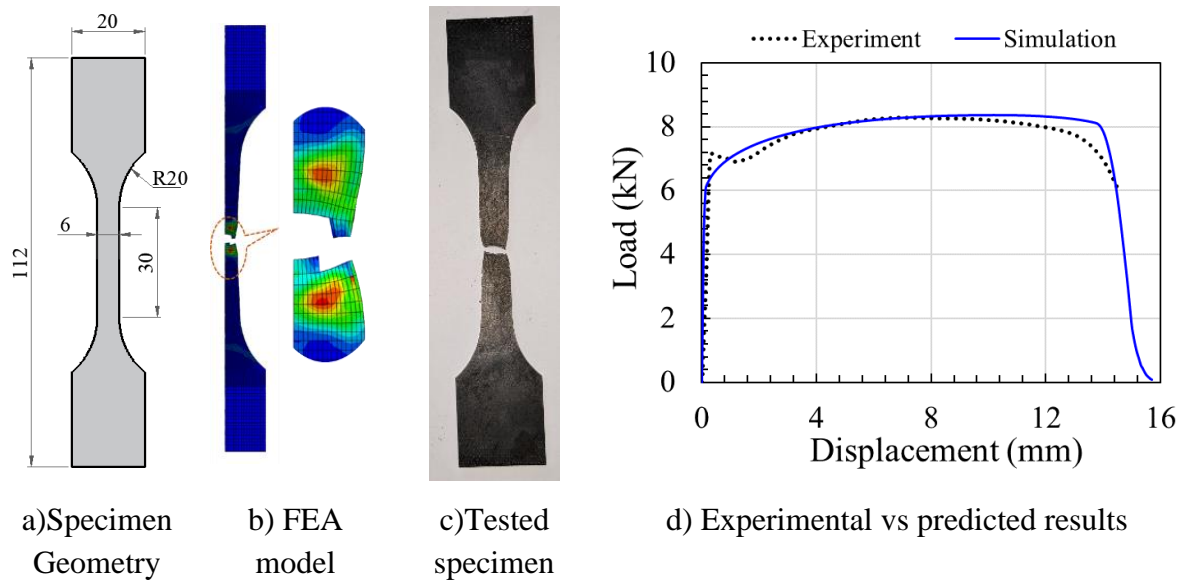


Figure 2.20: Comparison of experimental and J-C model predictions for plain tensile specimen

The specimen failed at the minimum cross-sectional region at the middle. A good agreement is obtained on the failed pattern between the experiment and simulation. Further, the load-displacement curves obtained from experiment and simulation are shown in Figure 2.20(d). The results are in close agreement with each other. The predicted load-displacement response and failure pattern matching with experimental observations.

2.5.2 Validation-2: Notched tensile specimen

In the next validation, a notched specimen is prepared with a stress triaxiality of 0.49 and is subjected to a tensile experiment at a strain rate of 0.3 /s. Specimen geometry and the fractured specimens are shown in Figure 2.21(a) and 2.21(c). The half model is discretized using 29490 C3D8R eight node solid brick elements with reduced integration and symmetric boundary condition applied. A maximum element size of 0.5 mm is adopted after a mesh convergence study. The FEA model is fixed at one end and a displacement loading of 10 mm/s is applied at the other end and the simulation is allowed to run until the failure of the specimen. The failed specimen is shown in Figure 2.21(b).

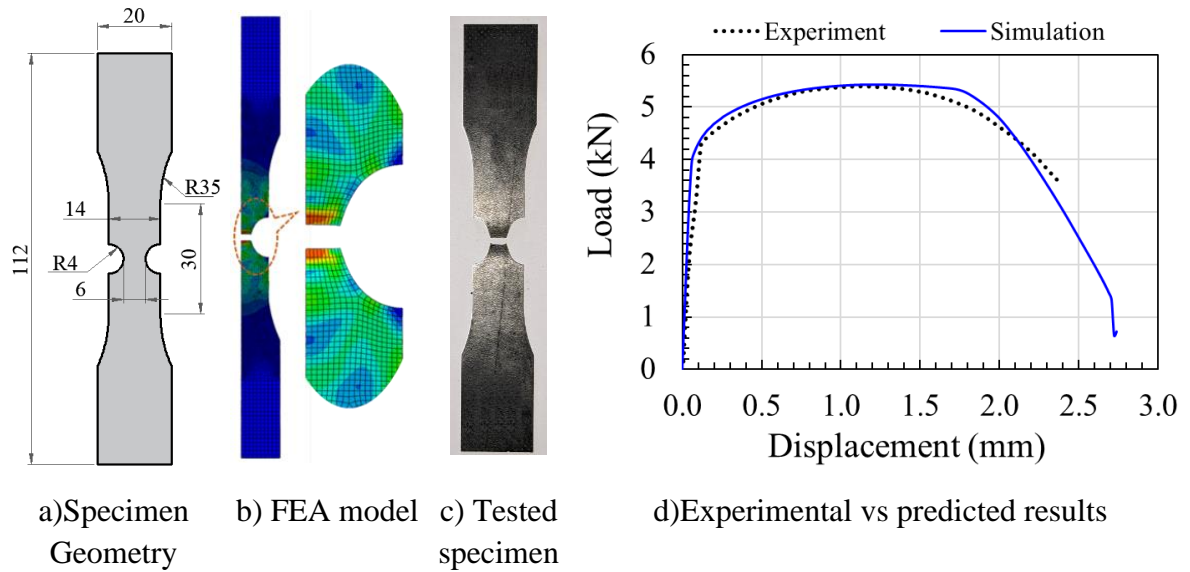


Figure 2.21: Comparison of experimental and J-C model predictions for a notched tensile specimen

The specimen failed at the minimum cross sectional region in the notched portion. A good agreement is obtained on the failed pattern between the experiment and simulation. Further, the load-displacement curves obtained from experiment and simulation are shown in Figure 2.21(d). The results are in close agreement with each other. The load-displacement response and failure pattern are matching closely with experimental observations.

2.5.3 Validation-3: Hydrostatic burst experiment of FSMD

J-C model parameters are also validated with another experiment of subjecting the flat scored burst disc (FSMD – F2) to hydraulic pressure until the failure and compared the strains developed within the disc to FE simulation results at eight locations. The experimentation and results are discussed in Chapter 6.

2.6 Modification of J-C material model

J-C material model is a constitutive model which is primarily intended for computations. There are better models available for predicting the behavior of material which are complicated to characterize or models specific to the given material [44]. Because of its simplistic nature, this model is applicable for wide range of materials with considerable errors due to the reasons like not considering the damage accumulation in material model, assumption of linear fit for C and m values etc. Few researchers have even attempted to modify the J-C material model based on its comparison with experimental results. Yu *et al.* [63] for DP600 steel; Wei *et al.* [64] for DP1000 steel; Wang *et al.* [65] for Inconel 718; Zhang *et al.* [66] for 7075-T6 aluminium; and Zhong *et al.* [67] for Weldox600E. But all these modifications on J-C material model resulted in the coupling of different material responses.

In the present J-C material model, in order to closely fit the value of C with the data points, three values of C is proposed between strain rate intervals as shown in Figure 2.13. Such

method requires to select the value of C based on the expected strain rate of the given experiment. But, it can be directly used with existing FE software.

But to avoid such range selection before simulation, a simple modification is proposed in accounting the strain rate effect in the conventional J-C model, and it also offers easiness in calibrating the material model. The modified model retains the original flexibility brought out by J-C in determining the material parameters by isolating different material effects and can be implemented with the help of user sub-routine.

2.6.1 Modification of strain rate effect in J-C material model

A different approach is followed so that the value of C varies during the simulation which is suitable for user defined material model as shown in Figure 2.22. While finding the fit between data points to obtain the value of C , it is observed that the value of C is not constant as expected in the conventional J-C model. It varies exponentially with strain rate. So, in the presently proposed (or modified) J-C model, the conventional J-C model in Eq. (2.1) is modified to include the exponential variation of strain rate given as

$$\sigma = [A + B\varepsilon_p^n][1 + C_1 e^{C_2 \ln \dot{\varepsilon}^*}][1 - T^{*m}] \quad (2.22)$$

where C_1 and C_2 are strain rate parameters that are determined by the exponential fit between the data points in Figure 2.13. The value of $C_1 = 0.0175$ and $C_2 = 0.249$. This change in the strain rate term still retains the advantage of isolating the strain rate effect in the modified J-C model for easy determination of strain rate-dependent material parameters.

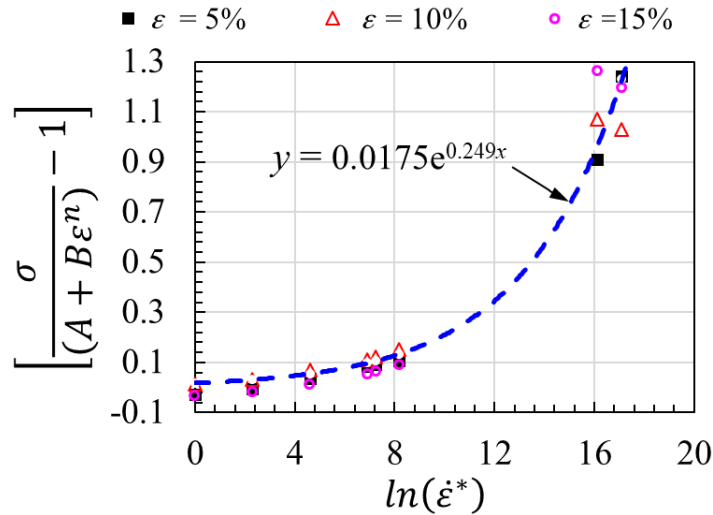


Figure 2.22: Determination of C_1 and C_2 from the proposed method

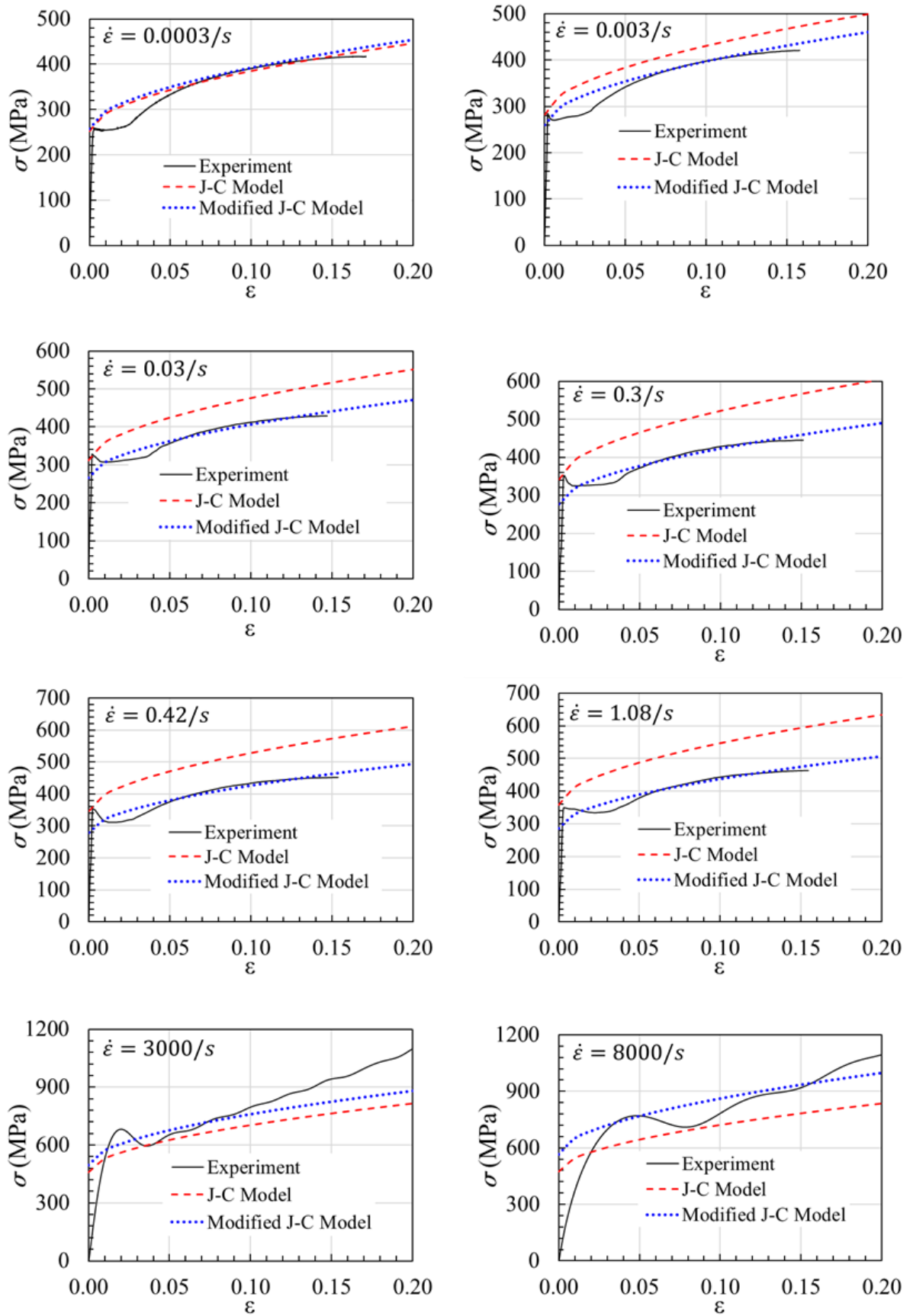


Figure 2.23: Comparison of experimental and J-C prediction at various strain rates

2.6.2 Comparison of predicted and experimental stress-strain response

The data from experimental stress-strain curves at eight different strain rates are compared with the conventional J-C model in Eq. (2.1) and the proposed J-C model in Eq. (2.22) as shown in Figure 2.23.

The comparison is made only up to the ultimate strength *i.e.* up to the strain hardening phase. It can be observed that, at a lower strain rate of 0.0003 /s, both the conventional and proposed J-C strength models are closely predicting the stress-strain behavior. However, as the strain rate increases, a considerable error is observed between the experimental data and the conventional J-C model whereas the proposed J-C model is able to closely predict the constitutive behavior at all strain rates. A similar modifications can be attempted to further improve other parameters in both J-C material and damage models.

2.7 Summary

Johnson-Cook strength and damage models are very popular in numerically simulating the large deformation, strain and strain rate hardening, thermal softening, and initiation of damage in ductile materials undergoing loadings at low to high strain rates. This Chapter has presented the procedural determination of 10 different Johnson-Cook's strength and damage model parameters for E250 structural steel. The parameters have been determined from the results of 16 types of experiments conducted at various strain rates (0.0003/s to 8000/s), stress triaxialities (0.33 to 0.95) and temperatures (30⁰C to 800⁰C). Three values of the strain hardening coefficient are proposed for various ranges of strain rates. Determined J-C's strength and damage model parameters have been employed in numerically simulating a separate notched tensile specimen and failure of FSMD under hydrostatic loading. The stress-strain response and failure pattern obtained from both simulation and experiments agreed very well, thereby validating the determined J-C model parameters. The methodology has been explained step-by-step, which can be followed for determining the J-C model parameters of any ductile material. A modification in the strain rate effect in the conventional J-C model is proposed by introducing an exponential variation in the strain rate term with only two parameters C_1 and C_2 . The proposed J-C model still retains the basic advantage of the conventional J-C model in isolating material effects for ease of calibration and offers potential flexibility to be adopted for other materials as well.

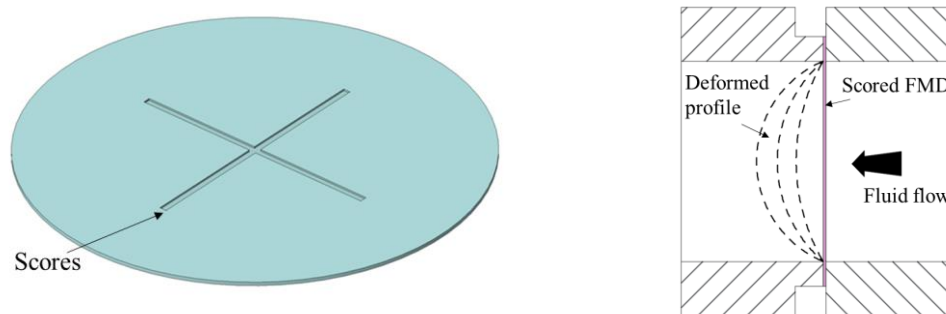
Chapter - 3

Flat Scored Metallic Disc -Numerical Simulation and Experimental Validation

3.1 Introduction

Flat thin metallic discs are commonly used in low-pressure applications like pressure relief valves. Their burst pressures are not always constant or repeatable due to the absence of predefined scores or notches. Therefore, thin flat scored metallic discs (FSMDs) are always preferred to (a) to reduce the burst pressure, (b) induce stress-triaxiality and initiate the failure in a preferred pattern along the scores, (c) provide a nearly constant burst pressure and (d) in making the disc from a thicker sheet to facilitate manufacturing [2]. Flat plates without scores undergo large inelastic deformation and rupture under higher loading rates and have been studied extensively under air blast and explosive loadings [21-35]. The behaviour of flat disc changes with the inclusion of scores and their effect is studied in this Chapter.

A flat scored metallic disc (FSMD) where scores featured on one side is shown in Figure 3.1(a), and FSMD in the application is shown in Figure 3.1(b).



(a) Flat scored metallic disc (FSMD) (b) FSMD in conditional burst application

Figure 3.1: Flat metallic disc with scores

The design guidelines and extensive studies on the failure of FSMD are unavailable in the literature. The response of this thin FSMD is influenced by its several geometric parameters and loading rate.

3.2 Simulation methodology and validation with experiment

3.2.1 Geometry

To establish the FEA methodology, the experimental work by Colombo *et al.* [42] on an FSMD is taken as the benchmark. This rupture disc is of 696 mm outer diameter with 2 mm thickness, as shown in Figure 3.2(a), and is made of structural steel. The fluid exposed area, *i.e.*, the pressure loading, is within a diameter of 481 mm. Two scores, *i.e.* grooves, are milled

on one side of the disc in a cross configuration. The scores are 5 mm in width and 0.80 mm in depth and are located at 90° to each other, as seen in Figure 3.2(b).

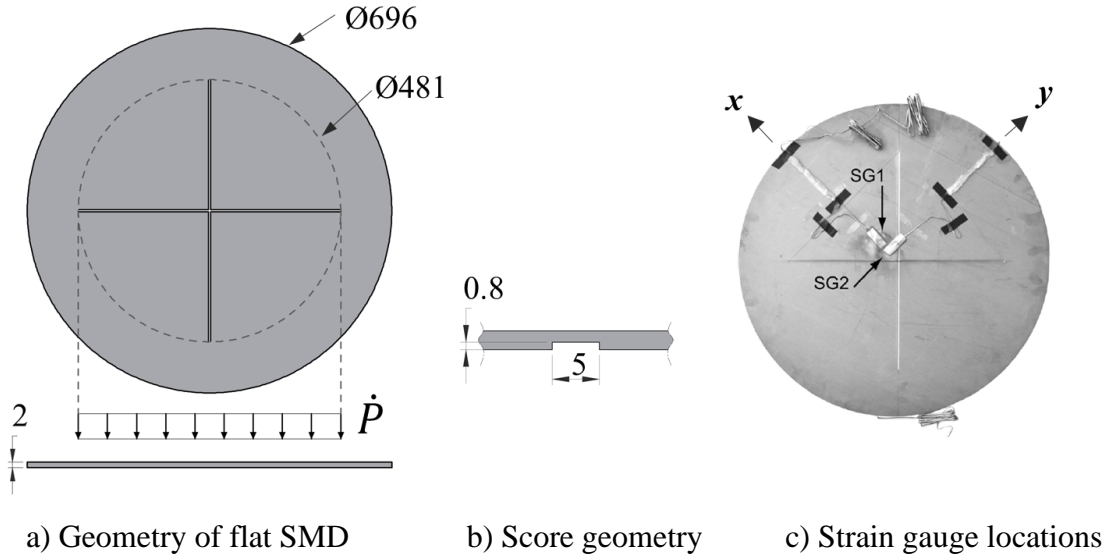


Figure 3.2: Experimental disc [42] geometry

3.2.2 Experimental setup

The experimental setup from Colombo *et al.* [42] is shown in Figure 3.3, where the disc is placed in a chamber and subjected to a quasi-static pressure loading on the plain side (*i.e.* opposite to the scored side) of the disc within 481 mm diameter which is equal to the inlet pipe diameter. The pressure inside the chamber and strain gauge readings were monitored during pressurization. Two strain gauges, SG1 and SG2, were bonded on the scored side of the disc and away from the location of the score, as seen in Figure 3.2(c), where SG1 is aligned with the x-axis and SG2 along the y-axis. Results from two strain gauges are taken to compare and validate the present FEA simulation.

3.2.3 Material and damage models

The experimented metallic disc is made of S235 JR structural steel and its mechanical properties are provided in Table 3.1. The material's constitutive behaviour is modelled with Johnson-Cook's (JC) strength model [44] and its damage and failure with the Johnson-Cook damage model [45]. In the numerical simulation, these two models define the material's viscoplasticity and damage behaviour during loading. These two models can capture the plasticity and damage in FSMD at low to high loading rates. The hydrostatic stress component of loading and the associated pressure-volume relationship is captured through a linear equation of state. The material parameters of the Johnson-Cook constitutive model are taken from Zhong *et al.* [68] for S235 JR structural steel. The damage parameters for the S235 JR structural steel are unavailable in the literature. The damage parameters adopted in numerical simulations are finalised based on several numerical iterations with the initial values taken from Banerjee *et al.* [48]. All material and damage parameters are defined at a reference strain rate of $\dot{\epsilon}_0 = 1e^{-4}$ /s. Damage evolution is defined by displacement at failure, which is taken as

0.0005, *i.e.* instantaneous failure occurs once failure strain reaches the damage initiation criterion from the J-C damage criterion.

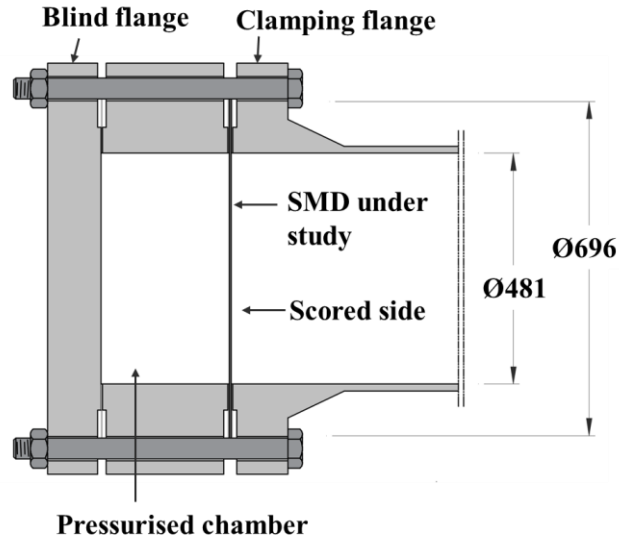


Figure 3.3: Experimental setup for a flat SMD [42]

Table 3.1: Elastic and material constants in JC material and damage models

Elastic parameters	E (MPa)	μ	ρ (kg/m ³)		
	210000	0.3	7850		
J-C material model (Initial values are taken from Zhong <i>et al.</i> [68])	A (MPa)	B (MPa)	n	C	m
	252	520	0.638	0.046	1.0
J-C damage model (Initial values are taken from Banerjee <i>et al.</i> [48])	D_1	D_2	D_3	D_4	D_5
	0.05	0.8	0.44	-0.042	0

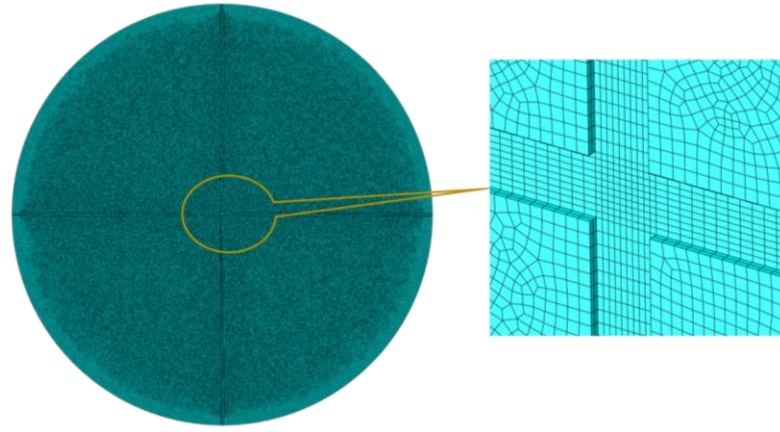
3.2.4 FEA simulation

The ABAQUS/Explicit [61] was adopted for creating the numerical model of the FSMD, as shown in Figure 3.4 and its FEA simulation. Automatic time increment was adopted. The model was discretised with 583708 elements using the C3D8R element, an eight-node brick element with reduced integration and hourglass control. All three degrees of freedom of nodes in the annular area of the disc between diameters 696 mm and 481 mm were fully constrained, as shown in Figure 3.4(b). A uniformly distributed pressure load was applied on the plain unscored side of the disc. Since the experiment was carried out at a quasi-static loading rate

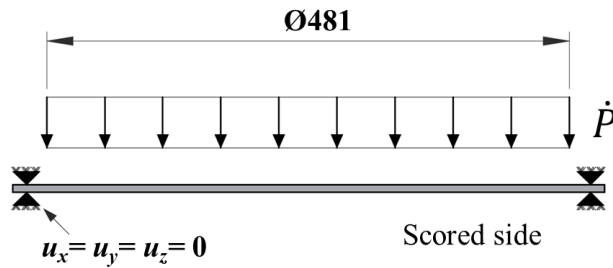
of 0.0132 MPa/s to reach a burst pressure of the disc, *i.e.*, $P_b = 1.15$ MPa, it took about 87.1 seconds to burst and rupture during experimentation. This experimental loading rate was too small for an explicit solver and needed to be accelerated in simulation to obtain an economic computation. Therefore, the approach provided by Baker *et al.* [69] for the shock response of a blast-loaded elastic oscillator was used to calculate the value of the loading rate for the simulation, wherein for a quasi-static loading regime, the ratio of loading duration t_d with respect to the natural time period ($1/\omega_n$) is given as

$$\omega_n t_d \geq 40 \quad (3.1)$$

The modal analysis of the thin FSMD shown in Figure 3.2 (a) resulted in the fundamental natural frequency ω_n as 82.29 Hz. Therefore, Eq. (3.1) results in $t_d = 0.486$ s. Considering the experimentally achieved maximum P_b of 1.15 MPa and the calculated t_d , the rate of loading rate was determined as 2.37 MPa/s and was adopted in the present numerical simulation.



(a) FE model



(b) Loads and boundary conditions

Figure 3.4: The simulation model of flat disc

Mesh convergence studies were carried out to find the optimum number of elements through the thickness of the rupture disc. The number of elements through the thickness was increased in each iteration by keeping the same aspect ratio of elements in each model, *i.e.*, the models were simulated with three, four, and six elements through the plate thickness. Burst pressure, burst time, central deflection, and maximum strain developed at the centre of the disc before the burst were studied during the mesh convergence analyses. The model with four elements through the plate thickness, *i.e.*, 0.5 mm of element size, gave an economical and converged

solution, which was considered for comparison and validation of FEA simulation with experimental results.

3.2.5 Results of numerical simulation

The deformation pattern, applied pressure P , equivalent stress σ_{eq} , and equivalent strain ε_{eq} at different time instances, as viewed from scored side of the disc during loading, are shown in Figure 3.5. At this small loading rate of 2.37 MPa/s, it is observed that the strain is concentrated along the score at the central region of the disc, as seen in Figure 3.5(b).

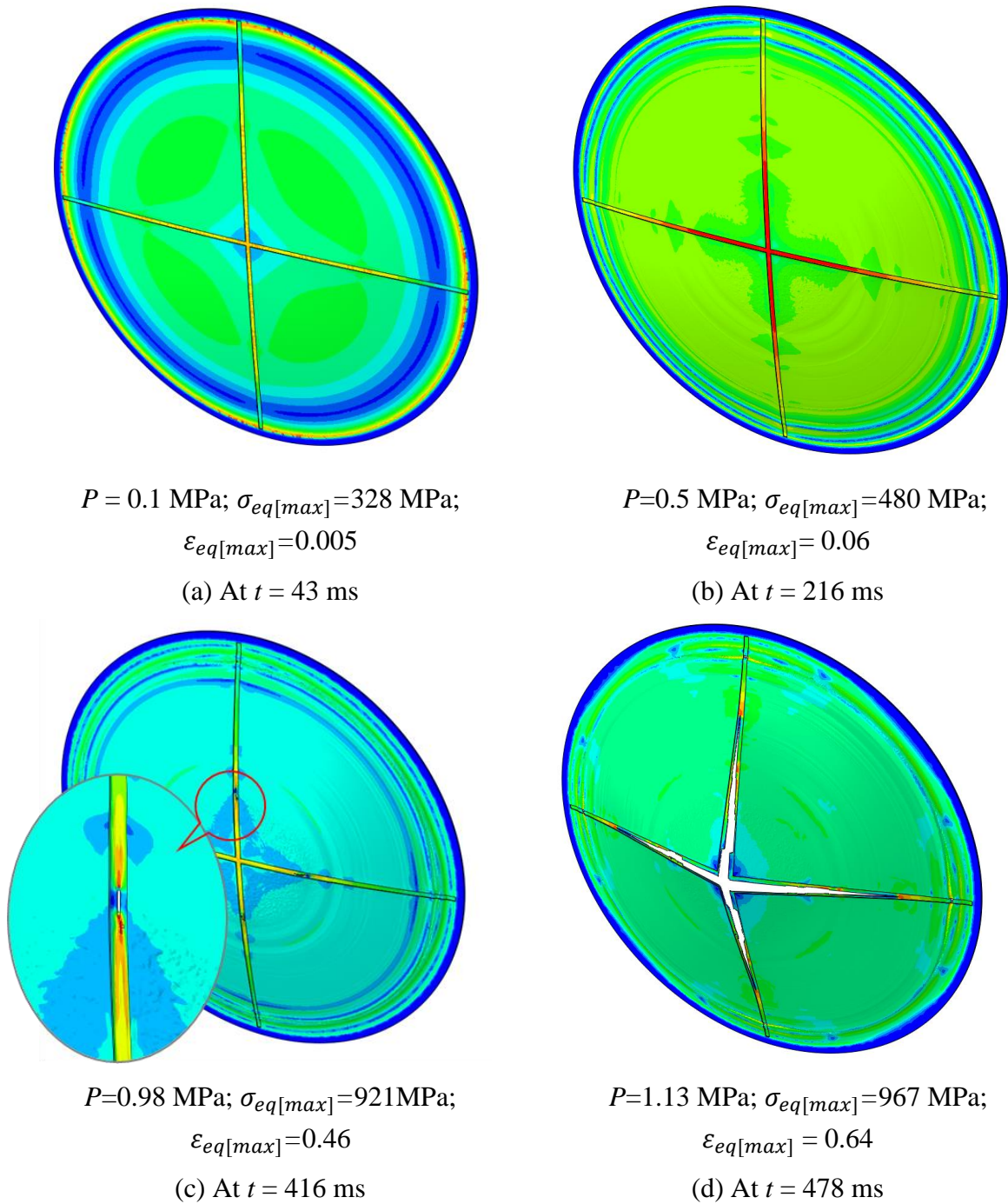


Figure 3.5: Failure initiation and propagation

Since Lagrangean approach is followed for numerical simulations, pressure continues to act on the remaining petals even after initiation of failure. So, burst pressure during FEA simulations is taken as the pressure at first element deletion. The first element deleted *i.e.* failure is initiated at the score location away from the centre of the disc at $P = 0.98$ MPa, as seen in Figure 3.5(c) and this pressure at which the first element deleted is considered as the burst pressure. This failure is initiated when the accumulated plastic strain ε_{eq} reaches the fracture strain ε_f as per the adopted JC's damage model, Eq. (2.3). The failure is subsequently propagated towards the centre of the disc upon further loading, as observed in Figure 3.5(d).

3.2.6 Experimental Validation of simulation results

A comparison of P_b and the failure pattern between the present simulation and experiments [42] is shown in Figure 3.6, where the predicted P_b is 0.98 MPa as against the experimentally reported average burst pressure of 1.01 MPa. The predicted P_b and the failure pattern after the burst, as seen from the disc's scored and unscored sides, matched reasonably well with the experimental results.

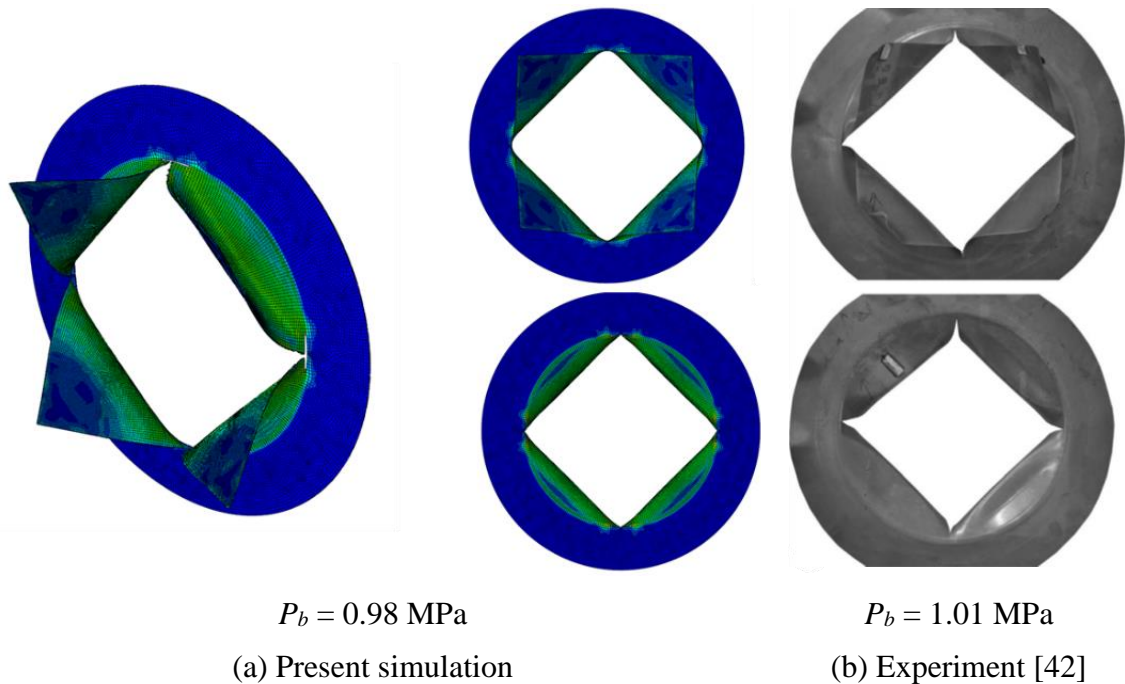


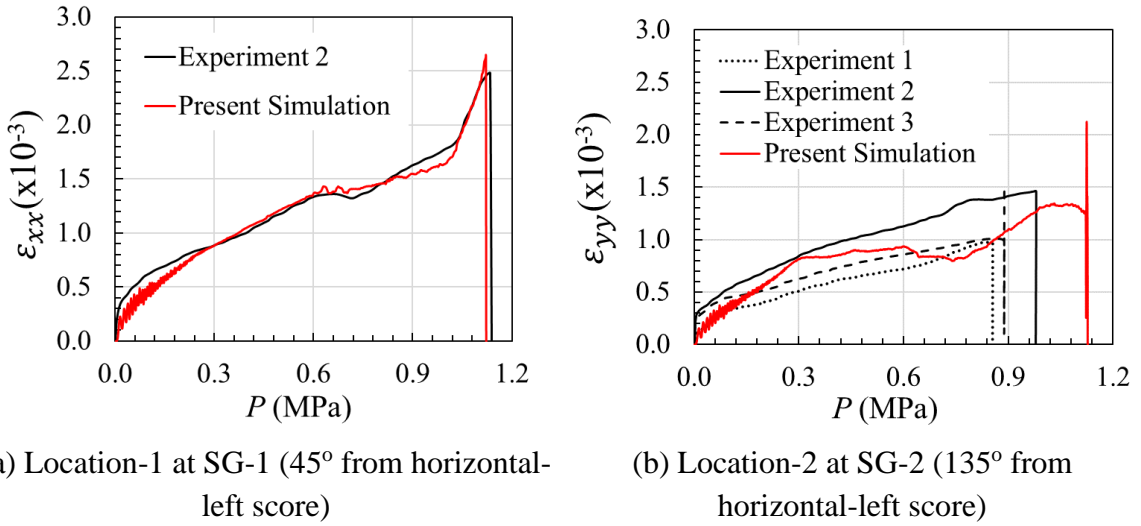
Figure 3.6: Comparison of deformed pattern, burst pressure and burst time between present simulation and experiment

Normal strains are monitored at the two strain gauge locations, SG1 and SG2, as shown in Figure 3.2(c), where experimental results are reported. The predicted strains are compared with the experimental strain values, and they are shown in Figure 3.7(a-b). Although three discs were experimented with [42], the results of strains at the SG1 location in experiment-2 are only available. The predicted strain profile matches very closely with that of the experiment, as seen in Figure 3.7(a). The strain results at SG2, the location from three experiments, gave three different profiles with respect to the applied pressure, as the bonded strain gauge SG2 would have experienced strain even after the initial burst during subsequent

deformation of the separated petals. The predicted strain at SG2 lies between the three experimental results, as seen in Figure 3.7(b).

Even though closeness in trends is observed in the developed strains in the experiment and simulation at both strain gauge locations, the strain at SG1 location continued to increase even after the initiation of failure and the strain at SG2 location stopped to increase after failure. This could be due to the stretching phenomenon happening only in the radial direction after petal separation. While comparing the experimental results with the simulation, a difference in peak strain of less than 8% is observed between experiment and simulation at both strain gauge locations at the instant of failure and a difference of 3% in burst pressure is observed. Since the data from the strain gauges might be influenced by burst phenomenon, stresses and strains at the instant of burst are not considered for comparison.

Thus, the agreement of failure pattern, burst pressure, and strain profiles between the present simulation and experiment validate the adopted FEA simulation.



(a) Location-1 at SG-1 (45° from horizontal-left score)

(b) Location-2 at SG-2 (135° from horizontal-left score)

Figure 3.7: Comparison of strains between present simulation and experiments [42] at locations mentioned in Figure 3.2(c)

3.3 Studies on FSMD

Based on the validated numerical approach, the deformation and failure behaviour of the thin FSMD is investigated elaborately subjected to the following two loading conditions.

- Constant internal pressure 0.02 MPa or maximum static operating pressure (MSOP)
- Sudden impulsive pressure during the motor's initiation, approximated as 500 MPa/s.

3.3.1 Geometry for FEA

The geometry considered for the FEA of the flat disc is shown in Figure 3.8(a), and the score geometry is shown in Figure 3.8(b). It has an outer diameter of 800 mm and an opening diameter, D , of 720 mm on which pressure is acting. It has a sheet thickness, t of 2 mm. It is

provided with scores in ‘+’ configuration as shown in Figure 3.8(a) on one side of the disc, with each score having a width, b , of 5 mm and depth, t_l , of 0.8 mm. A score length of 350 mm is maintained.

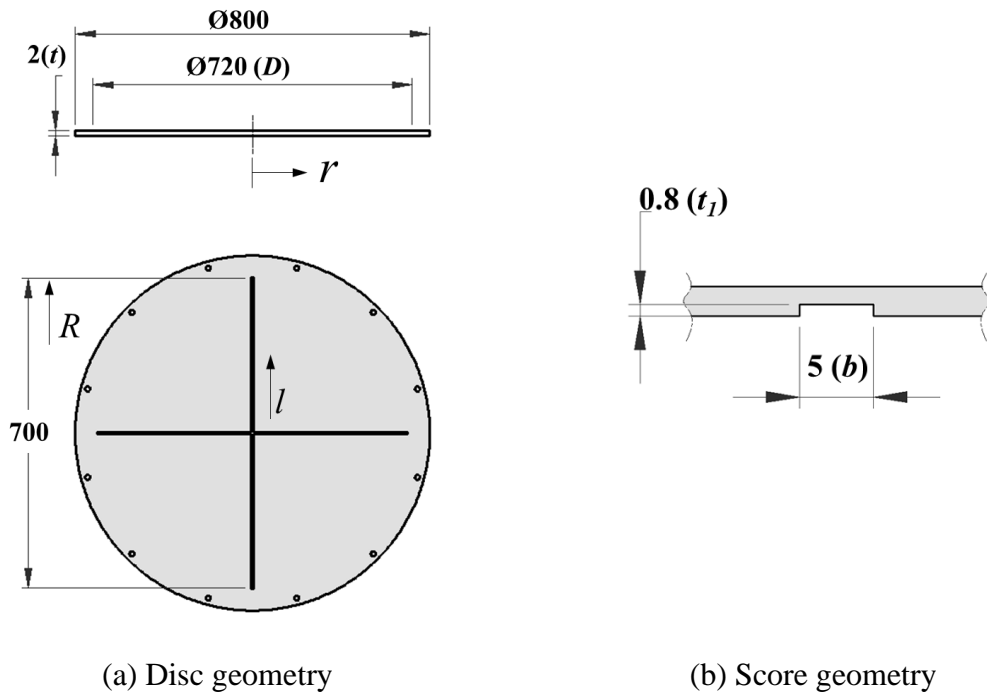


Figure 3.8: Geometry of flat metallic disc with scores

The FEA methodology adopted for the simulation of flat SMD discussed in previous sections is adopted here in modelling the geometry and material for FEA simulation. The geometry is discretised with 8-node C3D8R brick elements. Four elements are maintained through the thickness of the flat disc. A total of 1036618 elements are generated using the swept meshing technique. Scores are provided on one side of the disc and fluid pressure is applied on another side of the disc.

3.3.2 FSMD under constant internal pressure

The loading and boundary conditions are shown in Figure 3.9. All displacement degrees of freedom are constrained at all nodes in the flat portion of the disc between the diameters 720 and 800 mm. These two diameters respectively correspond to the typical outer and inner diameters of the motor container. A pressure load of 0.02 MPa is applied on the non-scored surface of the disc.

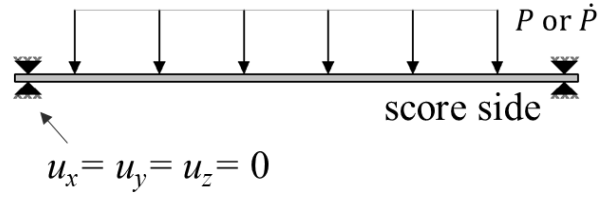


Figure 3.9: Loads and boundary conditions for FSMD

3.3.2.1 FEA and results

Static structural analysis is conducted using ABAQUS/CAE [59, 60] on FSMD and results are shown in Figure 3.10 where the deformed pattern is shown in Figure 3.10(a) and the von-Mises stresses along the score and at 45° to the score are shown in Figure 3.10(b).

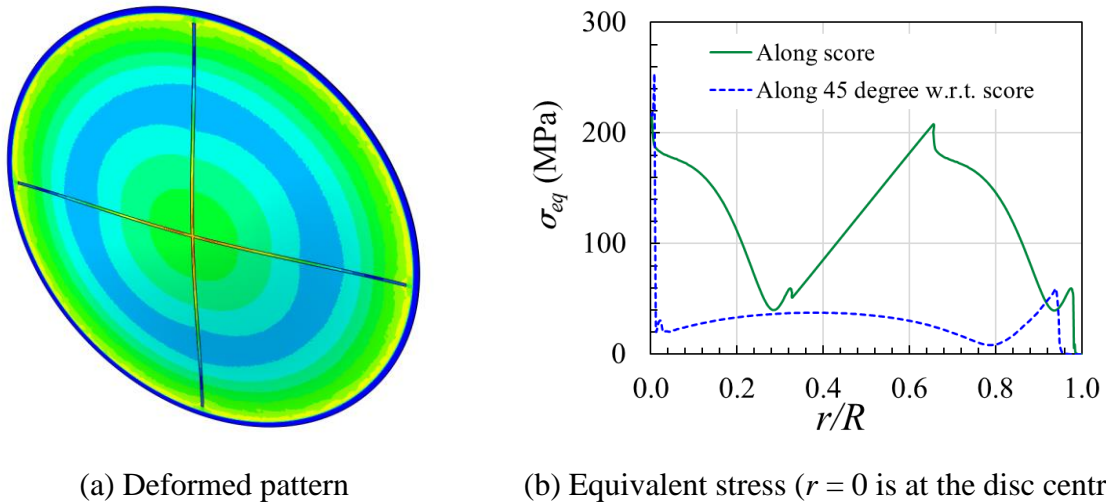


Figure 3.10: Deformation and stresses in flat metallic disc under uniform pressure loading

The maximum static operating pressure (*MSOP*) of the flat disc is 0.0095 MPa, at which the maximum stress developed is equal to the yield strength of S235JR steel. The maximum stress developed along the radius at 45° from the score is about 250 MPa near the centre of the disc.

3.3.3 FSMD under impulsive loading

The pressure loading rate on the scored metallic disc can reach as maximum as 500 MPa/s due to the instantaneous release of propulsion energy during the initiation of the motor. Therefore, the non-linear explicit dynamic analysis using ABAQUS/Explicit code [61]. The material and damage model, as adopted in the previous section, is adopted here.

3.3.3.1 Effect of loading rate

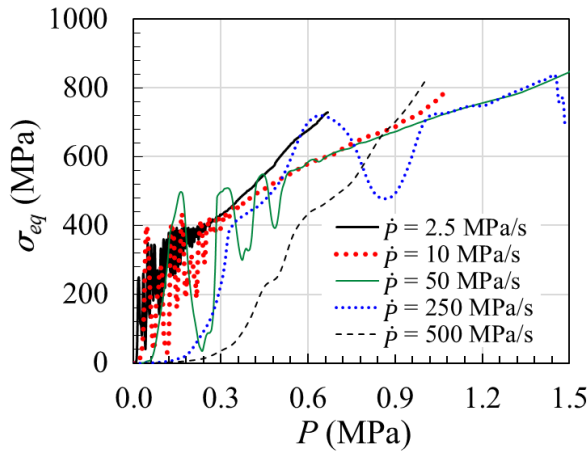
Flat scored metallic disc was subjected to five different loading rates, such as 2.5, 10, 50, 250 and 500 MPa/s, in order to understand the effect of the increase in the loading rate on the

failure behaviour of the disc. Different responses in the scored disc, such as σ_{eq} , ε_{eq} , and equivalent strain rate $\dot{\varepsilon}$ at the centre of the disc in the score location with the increase in applied P , are shown in Figure 3.11(a-c). The reaction force, F at the fixed boundary with respect to the central deflection is shown in Figure 3.11(d), and the summary of all responses is shown with respect to the applied pressure loading rate in Figure 3.11(e). It is observed that σ_{eq} increases with applied P , and its variation is almost the same irrespective of the loading rates except for the maximum higher loading rate of 500 MPa/s. On the other hand, the ε_{eq} increase is similar to that of the σ_{eq} with the applied pressure. Still, its variation is almost the same for the loading rates of 50, 100 and 250 MPa/s except for the two extreme loading rates, *i.e.* 2.5 and 500 MPa/s which differ from the intermediate loading rates as seen in Figure 3.11(b).

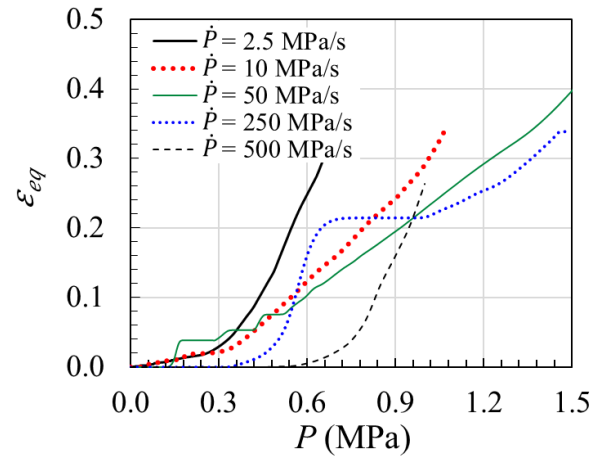
The equivalent strain rate increases with the applied loading rate \dot{P} , which is higher for higher loading rates. More fluctuations are observed in $\dot{\varepsilon}$ through the course of loading due to the large instantaneous deformation experienced at the central element of the disc at the score location, as seen in Figure 3.11(c). The reaction force, F experienced at the fixed boundary increases with the increase in w_{max} for all loading rates, but the maximum force is almost the same for all loading rates except the lowest loading rate, as seen in Figure 3.11(d).

All responses are shown in Figure 3.11(e). The P_b and w_{max} exhibit an increase and t_b decrease when the loading rate increases from 2.5 to 100 MPa/s. Beyond 100 MPa/s, these responses exhibit significantly less sensitivity to loading rates and remain almost constant. On the other hand, ε_{max} increases steeply with the increase in loading rate up to 50 MPa/s. Afterwards, it almost remained insensitive to the loading rates from 50 to 100 MPa/s, beyond which it decreases gradually with the increase in loading rate. Unlike other responses, $\dot{\varepsilon}_{max}$ increases almost linearly with the increase in loading rate because of the increase in displacement rate of the damaged element.

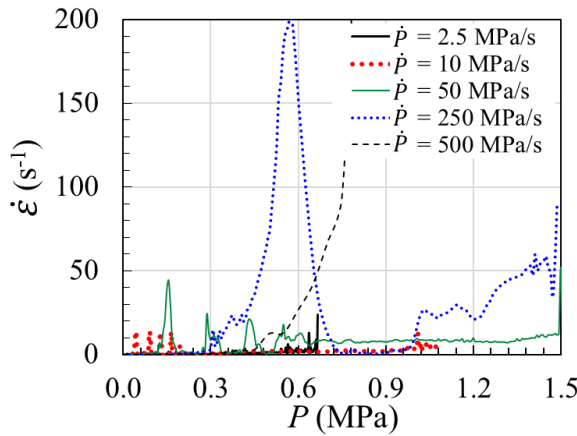
One peculiar observation is appreciable regarding the location of failure initiation with respect to the loading rates, as shown in Figure 3.12. When the loading rate varies from 2.5 to 25 MPa/s, the failure is initiated in the score location between 48 and 67 mm (*i.e.* at $r = 0.2R$ - $0.28R$) away from the centre. For loading rates > 50.0 MPa/s, the failure initiation occurs at the centre of the disc ($r = 0$) at the score location and is insensitive to the higher loading rates. This is because of the formation of plastic hinges along scores at locations away from the plate centre under low loading rates and the corresponding increase in strain localisation. At high loading rates, more than 50 MPa/s, this phenomenon could not happen anywhere along the score except at the centre of the plate.



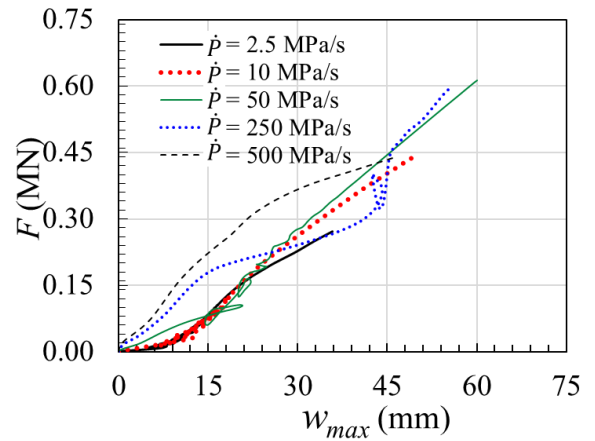
(a) Equivalent stress with respect to the applied pressure



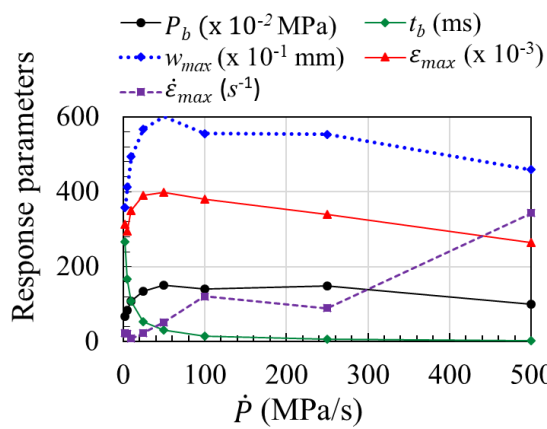
(b) Equivalent strain with respect to the applied pressure



(c) Strain rate with respect to applied pressure



(d) Reaction force with respect to central deflection



(e) Responses with respect to the loading rate

Figure 3.11: Effect of the loading rate on flat scored disc

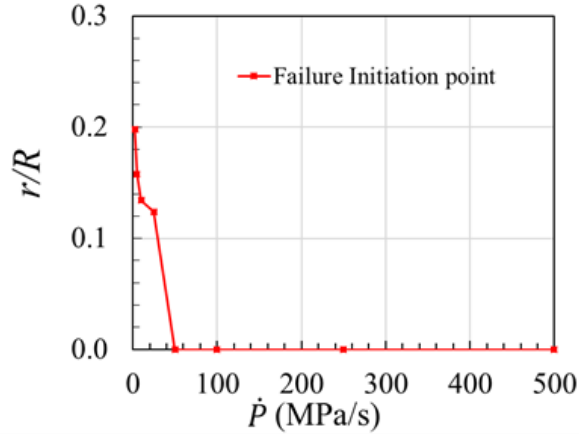


Figure 3.12: Failure initiation location with respect to loading rate

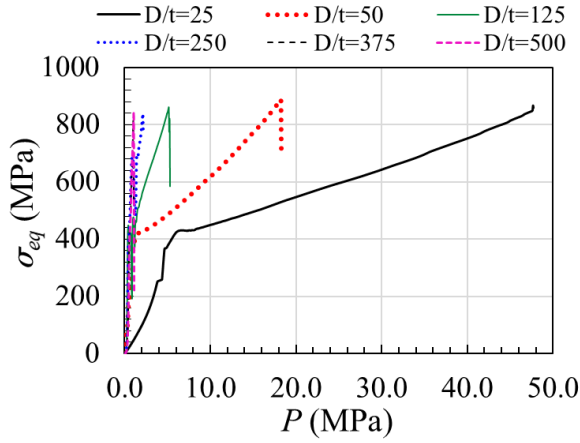
3.3.3.2 Influence of geometrical features on the behavior of flat SMD

The geometrical features in the FSMD significantly influence the deformation, failure and rupture behaviour when exposed to a given loading rate caused by fluid pressure. The influencing geometrical features can be i) diameter-to-plate (*i.e.* disc) thickness (D/t) ratio, ii) score depth-to-plate thickness (t_1/t) ratio, iii) score width-to-plate thickness (b/t) ratio, iv) score length-to-disc radius (l/R) ratio, v) score pattern, *i.e.* the number of scores (N), and vi) score geometry. Numerical studies are conducted to investigate the effect of these geometrical features on the characteristics of FSMD under a pressure loading rate of 500 MPa/s. Only one geometrical feature to be investigated varies in these sensitivity studies while maintaining the other features constant. Consolidated list of various responses *viz.* P_b , t_b , w_{max} , ε_{max} and $\dot{\varepsilon}_{max}$ at the centre (*i.e.* at the intersection of scores) taken at the time of burst are presented in Table 3.2 to Table 3.7.

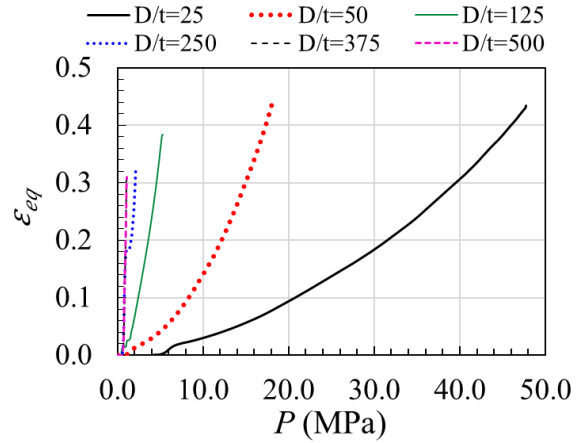
Diameter-to-plate thickness (D/t) ratio

The effect of the disc's diameter-to-plate thickness, *i.e.* D/t ratio, is investigated by varying the diameter of the disc from 50 mm to 1000 mm by keeping the plate thickness at $t = 2$ mm. This variation of the disc's diameter provides $D/t = 25$ to 500. The complete behaviour of the flat SMD extracted from simulations is shown in Figure 3.13(a-e).

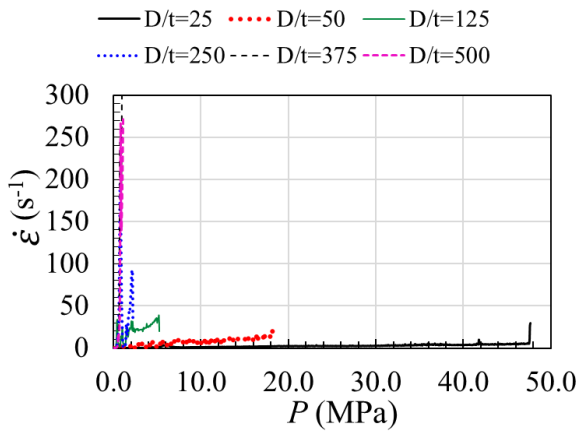
The equivalent stress, *i.e.* von-Mises stress σ_{eq} , equivalent plastic strain ε_{eq} , and plastic strain rate $\dot{\varepsilon}$ at the disc centre in score location with an increase in applied pressure, are shown in Figure 3.13(a-c). It is observed that both σ_{eq} and ε_{eq} increase with the increase in the disc's D/t ratio. Their maximum values remained almost the same for $D/t \geq 200$, but their rate of increase with applied pressure gradually increased and is significant beyond $D/t > 300$. On the other hand, their rate of rise is very shallow for $D/t < 100$, as seen in Figure 3.13(b). The plastic strain rate increases with the increase in the D/t ratio from 100 to 500, as observed in Figure 3.13(c). Its increase with an increase in applied pressure varies from very shallow to significantly steep with an increase in the D/t ratio.



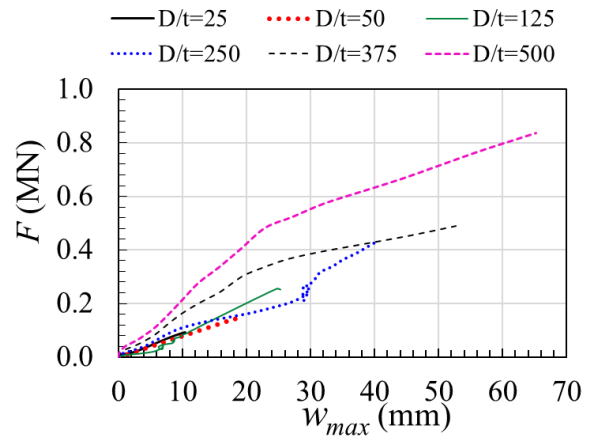
(a) Equivalent stress with respect to applied pressure



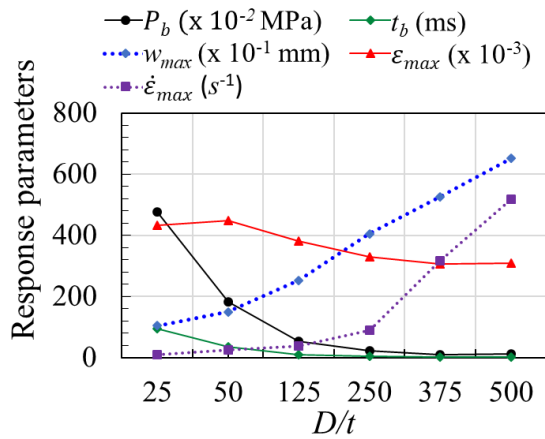
(b) Equivalent strain with respect to applied pressure



(c) Strain rate with respect to applied pressure



(d) Reaction force with respect to central deflection



(e) Responses with respect to the (D/t) ratio

Figure 3.13: Effect of diameter-to-plate thickness (D/t) ratio

The summary of all responses such as P_b , t_b , w_{max} , ϵ_{max} and $\dot{\epsilon}_{max}$ with an increase in the D/t ratio is shown in Figure 3.13(e) and is also given in Table 3.2. It can be observed that both P_b and t_b decrease exponentially with an increase in D/t up to 250, and afterwards, their variations are very marginal. Variation of $\dot{\epsilon}_{max}$ is bilinear with a shallow increase for D/t up to 250, followed by a steep increase thereafter. This is because of a considerable reduction in the plate stiffness beyond 500 mm diameter, accompanied by a large displacement of the damaged element. The ϵ_{max} exhibits less sensitivity to variation in D/t and remains almost insensitive for $D/t \leq 50$ and decreases from 0.44 to 0.30 for $25 \leq D/t \leq 500$. With the increase in D/t from 25-50, maximum mid-deflection increases almost linearly from 10 mm to 65 mm due to a consistent decrease in plate stiffness.

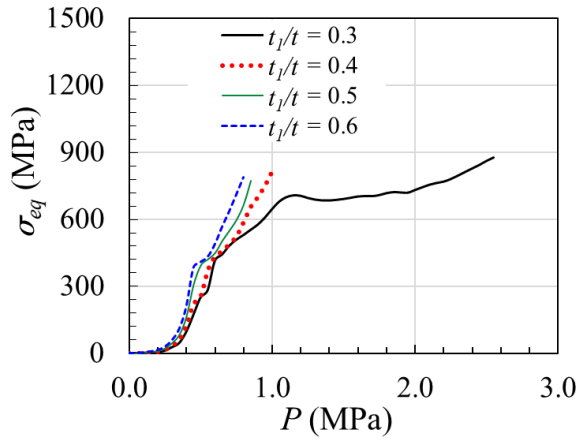
Table 3.2: Influence of D/t on the response of FSMD

	D/t					
	25	50	125	250	375	500
P_b (MPa)	47.7	18.3	5.3	2.2	1.05	1.15
t_b (ms)	95.4	36.6	10.6	4.4	2.1	2.3
w_{max} (mm)	10.5	14.9	25.3	40.1	52.7	65.2
ϵ_{max}	0.43	0.45	0.38	0.33	0.31	0.31
$\dot{\epsilon}_{max}$ (/s)	9	25	39	91	318	519

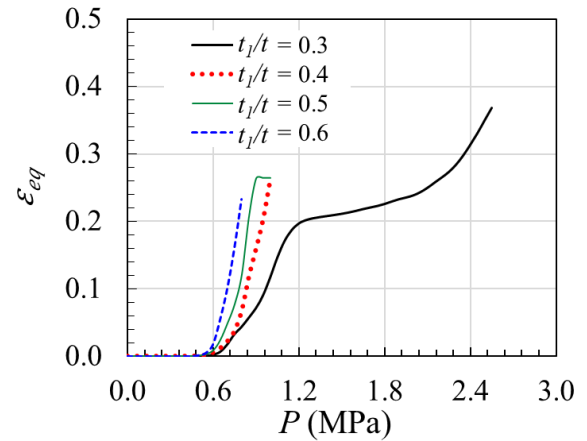
Score's depth-to-plate thickness (t_1/t) ratio

The effect of score depth t_1 is analysed by varying the score's depth from 0.6 mm to 1.2 mm in steps of 0.2 mm by keeping constant values for the plate thickness $t = 2$ mm and the score's width $b = 5$ mm. This variation of the score's depth provides a depth-to-plate thickness ratio of $t_1/t = 0.1$ to 0.7 in steps of 0.1. The complete behaviour of the flat SMD extracted from simulations is shown in Figure 3.14(a-e).

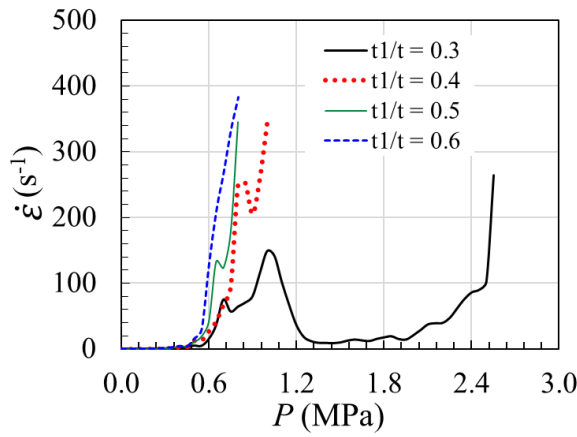
It is observed that both σ_{eq} and ϵ_{eq} decrease with an increase in the scores' t_1/t ratio, as shown in Figure 3.14(a-b). The $\dot{\epsilon}$ increases with the increase in the t_1/t ratio, as observed in Figure 3.14(c). It exhibits more oscillations at higher score depths due to more localised and instantaneous deformations occurring in the region.



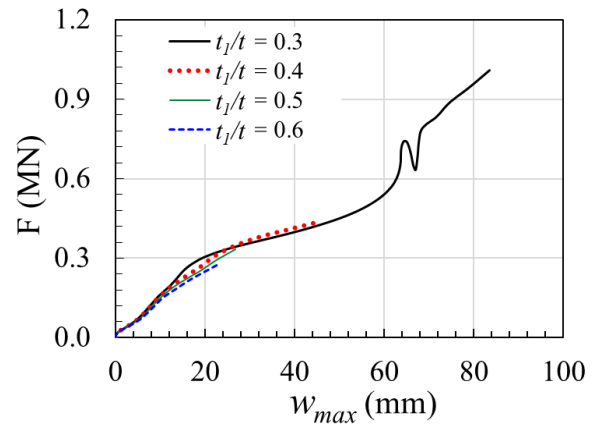
(a) Equivalent stress with respect to the applied pressure



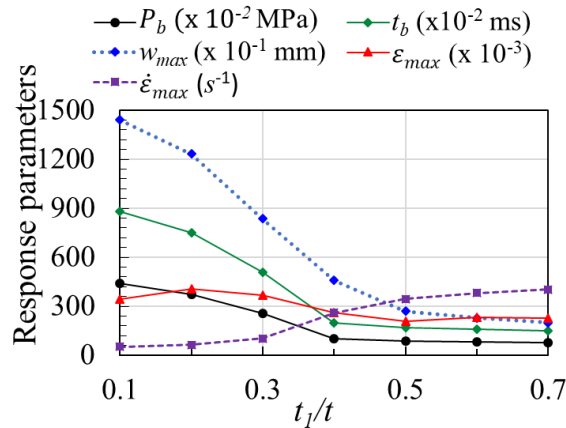
(b) Equivalent strain with respect to applied pressure



(c) Strain rate with respect to the applied pressure



(d) Reaction force with respect to central deflection



(e) Responses with respect to (t_1/t) ratio

Figure 3.14: Effect of score's depth-to-plate thickness ratio (t_1/t)

Table 3.3: Influence of t_1/t on the response of FSMD

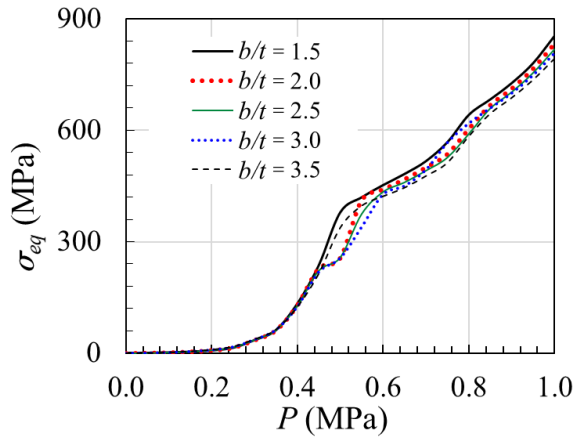
	t_1/t				
	0	0.3	0.4	0.5	0.6
P_b (MPa)	5.45	2.55	1.0	0.85	0.8
t_b (ms)	10.9	5.11	2.0	1.7	1.6
w_{max} (mm)	189	83.5	45.9	26.9	22.8
ε_{max}	0.42	0.37	0.26	0.21	0.23
$\dot{\varepsilon}_{max}$ (/s)	52	102	259	345	382

The reaction force at the fixed boundary with respect to the central deflection is shown in Figure 3.14(d), and it is noticed that both the maximum F and the w_{max} decrease considerably with an increase in the t_1/t ratio from 0.3 to 0.6. This is caused by the weakening of the score's region due to increasing the score's depth. Further, the stiffness exhibited by the flat SMD for different t_1/t ratios is almost the same until before the burst. The distribution of equivalent strain around the score just before failure is shown in Figure 3.14(e) and the summary of maximum values of all responses such as P_b , t_b , w_{max} , ε_{max} and $\dot{\varepsilon}_{max}$ with the increase in t_1/t ratio are given in Table 3.3 for t_1/t ratios ranging from 0.1 to 0.7. It can be noticed that the ratio of local strain in score to ligament strain increases with an increase in t_1/t up to 0.4 and afterwards, it decreases and remains unchanged for $t_1/t \geq 0.5$. The ε_{max} at score decreases with increased t_1/t ratios but stabilises and remains constant after $t_1/t = 0.5$. This reveals that the score weakens the flat SMD and it is significantly influenced for $0.1 \leq t_1/t \leq 0.5$ and afterwards, this influence is unnoticeable.

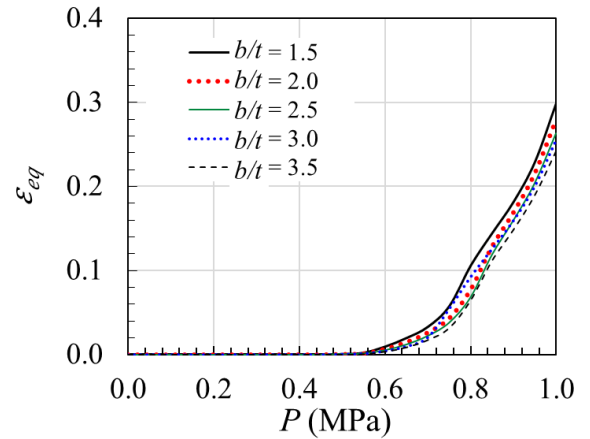
Score's width-to-plate thickness (b/t) ratio

The influence of score's width b is analysed by varying b from 3.0 mm to 7.0 mm in steps of 1.0 mm by keeping constant values for the plate thickness at $t = 2.0$ mm and score's depth at $t_1 = 0.8$ mm. This variation of the score's width provides a width-to-plate thickness ratio of $b/t = 1.5, 2.0, 2.5, 3.0$ and 3.5 . The behaviour of the flat SMD is captured from simulations and shown in Figure 3.15(a-e).

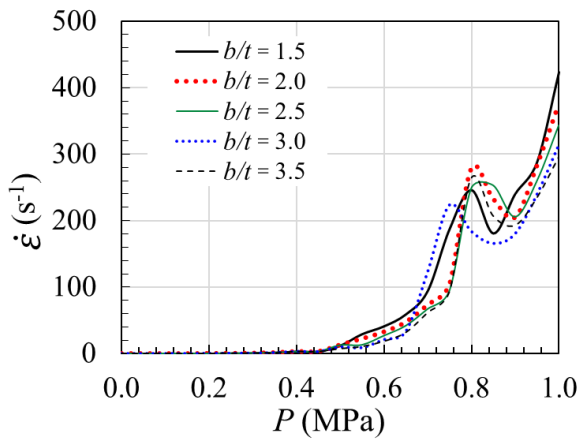
The variation of σ_{eq} , ε_{eq} and $\dot{\varepsilon}$ at the centre of the disc in score location with the increase in applied pressure is shown in Figure 3.15(a-c). These responses are almost the same irrespective of any variation in the score's b/t ratio, except for a slight decrease in the maximum strain rate with the increase in the b/t ratio before the actual burst, as seen in Figure 3.15(c). A maximum strain rate of around 296 to 423 /s is observed, with a decrease in the b/t ratio from 3.5 to 1.5.



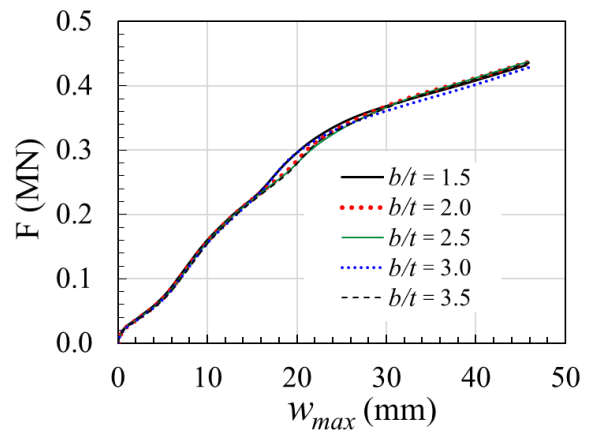
(a) Equivalent stress with respect to applied pressure



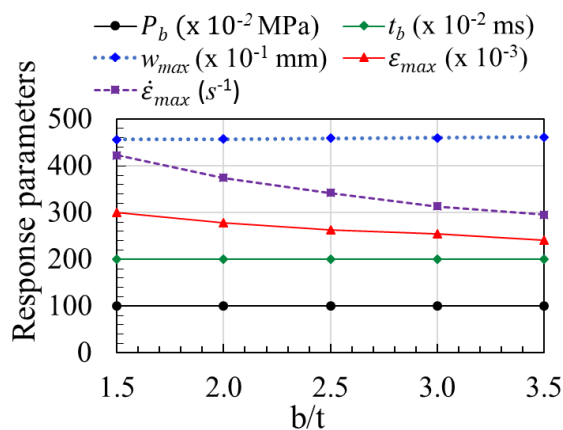
(b) Equivalent strain with respect to applied pressure



(c) Strain rate with respect to applied pressure



(d) Reaction force with respect to central deflection



(e) Responses with respect to the (b/t) ratio

Figure 3.15: Effect of score's width-to-plate thickness (b/t) ratio

The reaction force, F at the fixed boundary with respect to the central deflection w_{max} is shown in Figure 3.15(d) for different b/t ratios of the score. No significant variation is observed within the values considered for the change in the b/t ratio. Further, the stiffness exhibited by the flat SMD for different b/t ratios is almost the same until the burst. It can be observed that all response parameters remain almost constant except for slight variation for any increase in the b/t ratio from 1.5 to 3.5. Only a small variation of $\dot{\epsilon}_{max}$ is observed with the considered variation in b/t ratio. This study demonstrates that the score's b/t ratio does not significantly influence the important response parameters in the FSMD.

Table 3.4: Influence of b/t on the response of FSMD

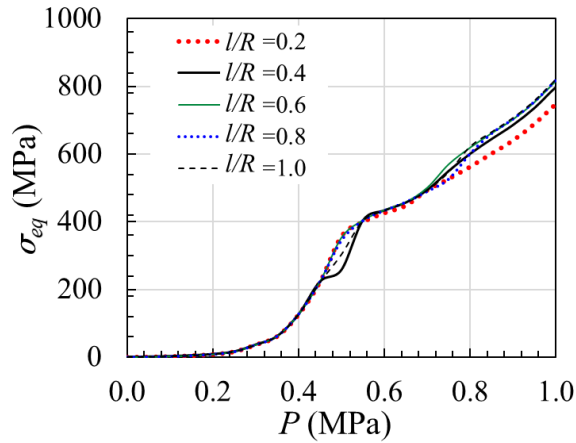
	b/t				
	1.5	2.0	2.5	3.0	3.5
P_b (MPa)	1.0	1.0	1.0	1.0	1.0
t_b (ms)	2.0	2.0	2.0	2.0	2.0
w_{max} (mm)	45.7	45.8	45.9	46.0	46.1
ϵ_{max}	0.30	0.28	0.26	0.25	0.24
$\dot{\epsilon}_{max}$ (/s)	423	375	343	314	296

Score length-to-disc radius (l/R) ratio

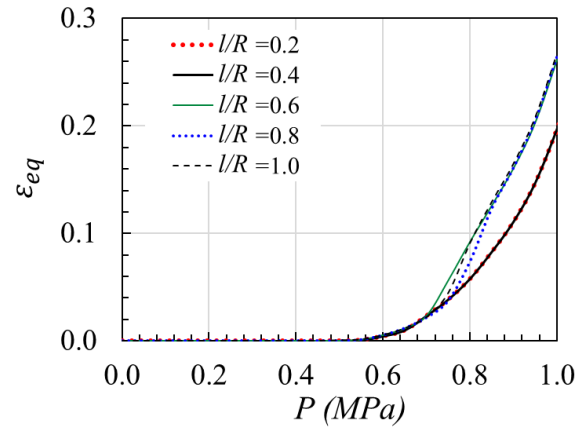
The effect of the score's length-to-disc radius (*i.e.* l/R) ratio is investigated by varying the score's length from 36 mm to 360 mm for a constant disc radius of 360 mm to achieve l/R ratios of 0.1, 0.2, 0.4, 0.5, 0.6, 0.8 and 1.0. Other geometric parameters of the disc and score are kept constant. The behaviour of the flat SMD for the analysed l/R variations is shown in Figure 3.16(a-e).

The equivalent stress, equivalent plastic strain, and plastic strain rate at the centre of the disc in the score location with the increase in applied pressure are shown in Figure 3.16(a-c). It can be noticed that σ_{eq} , ϵ_{eq} and $\dot{\epsilon}$ with respect to the applied pressure increase with the increase in l/R ratios up to 0.4, beyond which the responses are almost the same.

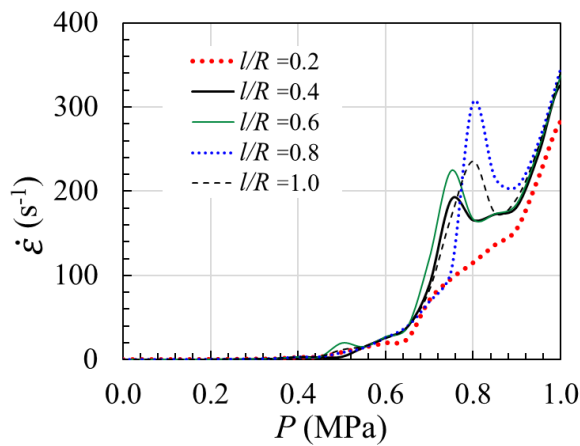
The variation of F at the fixed boundary with respect to w_{max} at every increment of loading is shown in Figure 3.16(d) for all values of l/R ratios considered. The initial and subsequent stiffness of the flat disc is almost the same for all l/R ratios. This implies that the energy absorbed before the burst is the same in all cases of $l/R \geq 0.4$.



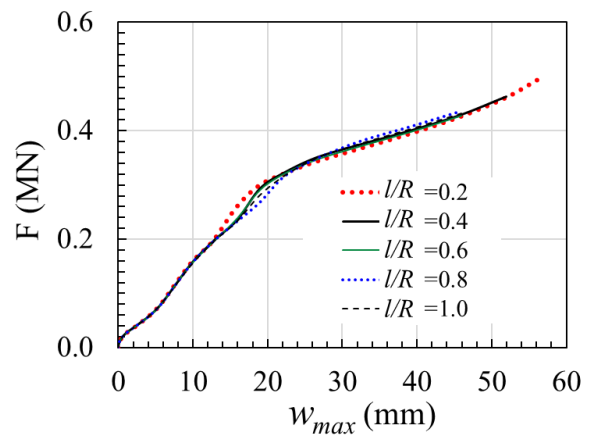
(a) Equivalent stress with respect to applied pressure



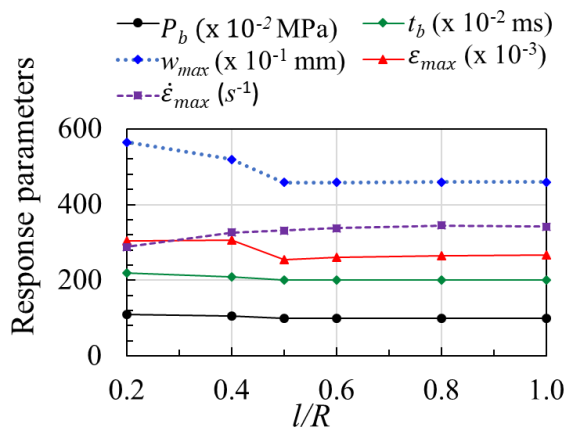
(b) Equivalent strain with respect to applied pressure



(b) Strain rate with respect to applied pressure



(d) Reaction force with respect to central deflection



(e) Responses with respect to (l/R) ratio

Figure 3.16: Effect of score's length-to-disc radius (l/R) ratio

The summary of maximum values of all responses such as P_b , t_b , w_{max} , ϵ_{max} and $\dot{\epsilon}_{max}$ with the increase in l/R ratio is shown in Figure 3.16(e) and given in Table 3.5. It is seen that P_b , t_b and w_{max} decrease gradually for l/R up to 0.4, beyond which these responses remain constant. The ϵ_{max} is very much insensitive to variations in l/R . The $\dot{\epsilon}_{max}$ increases from 0.6 /s to 0.9 /s for $0.2 \leq l/R \leq 0.4$, and afterwards, it remains unchanged with any further increase in l/R . This study reveals that the responses in FSMD are sensitive only to the score's length, up to 50% of the disc radius. By and large, they are relatively insensitive to any variations in the l/R ratio.

Table 3.5: Influence of l/R on the response of FSMD

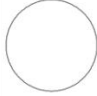




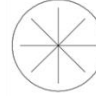
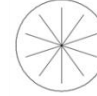
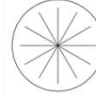
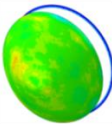
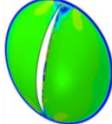
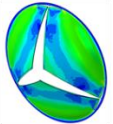
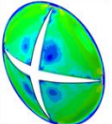
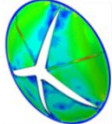
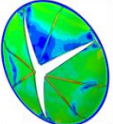

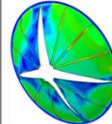
	l/R					
	0.2	0.4	0.5	0.6	0.8	1.0
P_b (MPa)	1.1	1.05	1.0	1.0	1.0	1.0
t_b (ms)	2.2	2.1	2.0	2.0	2.0	2.0
w_{max} (mm)	56.5	52	45.8	45.9	45.9	45.9
ϵ_{max}	0.3	0.31	0.25	0.26	0.26	0.27
$\dot{\epsilon}_{max}$ (/s)	288	326	332	338	345	342

Score pattern, i.e. the number of scores (N)

Scores provided in the disc act as stress concentration regions in the FSMD. The introduction of 2 scores across the diagonal of the disc reduced the burst pressure of the disc. As the number of scores N is increased further, it has minimal effect on the burst pressure and burst time. Failure propagation and failure pattern entirely depend on the pressure acting on petals after the initial burst. However, for this analysis, the pressure is assumed to be acting continuously on the disc throughout the simulation, causing failure propagation and petal separation. When $N > 4$, the failure is observed only along a few scores, which reveals that, as the number of scores increases, the failure may not be initiated and propagated in all the scores.

The effect of the number of scores on the flat SMD is analysed by varying the number of scores from 0 to 12, *i.e.* at $N = 0, 2, 3, 4, 6, 8, 10$ and 12. During this variation, the plate thickness ($t = 2$ mm), score's width ($b = 5$ mm), and score's depth ($t_1 = 0.8$ mm) are maintained constant. The predicted failure patterns with N ranging from 0 to 12 are shown in Table 3.6 just after the burst.

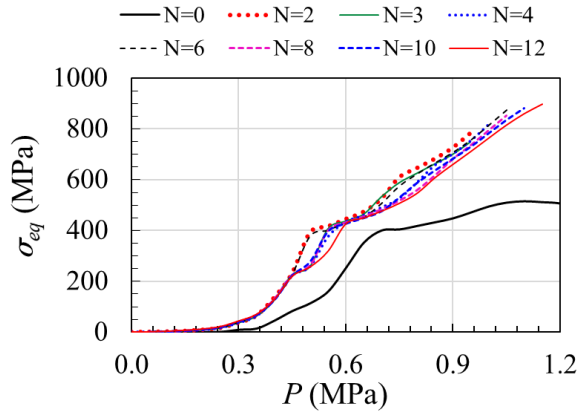
Table 3.6 Predicted failure pattern without and with the number of scores in the FSMD

Number of scores	0	2	3	4	6	8	10	12
Schematic								
Predicted failure pattern								

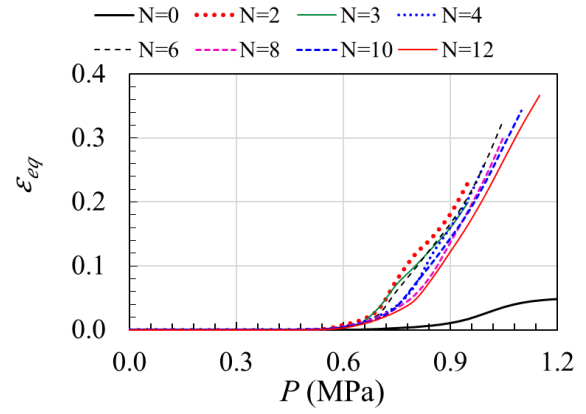
Clear petal separation is observed for all FSMD along the scores with $N = 3$ to 4, and they can bend freely at the fixed boundary after the petal formation upon the increase in fluid pressure. For $N > 4$, the failure is observed only along a few scores, which reveals that, as the N increases, the failure may not be initiated and propagated along all the scores, as seen in Table 3.6 because only a few scores experienced the failure limits and underwent petal separation along these scores and the remaining scores in between the separated scores did not reach the failure limits and remained intact without any separation. This can also be triggered by non-uniformities in dimensional tolerances in the score cross-sections. This reveals that the minimum number of scores recommended in FSMD can be 3 or 4 to achieve a clear separation and subsequent bending along the fixed boundary. The predicted failure patterns just after the burst with N ranging from 0 to 12 are shown in Table 3.6.

The behaviour of flat SMD with variations in the number of scores captured from simulations is shown in Figure 3.17(a-e). The variation of σ_{eq} , ϵ_{eq} and $\dot{\epsilon}$ at the centre of the disc in score location with the increase in applied pressure for different score patterns is shown in Figure 3.17(a-c). Except for plain disc, these responses remain the same with an increase in N . Whilst the responses are almost closer for all variations in N , the response for the flat SMD with $N = 0$ shows a relatively lower magnitude. The equivalent stress and equivalent plastic strain increase with the increase in N from 2 to 12. In all cases, the responses for $N = 4, 6$ and 8 resulted in almost the same results.

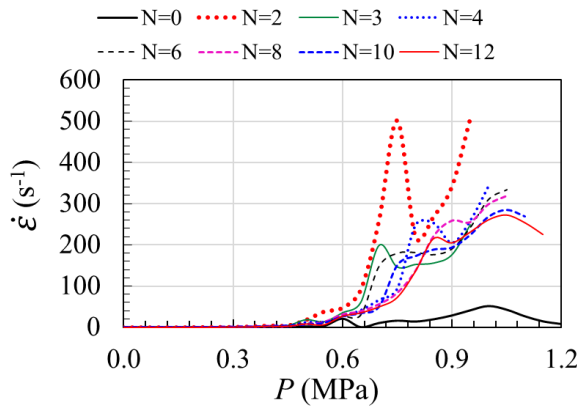
The reaction force, F at the fixed boundary with respect to the central deflection is shown in Figure 3.17(d) for different values of N . It is noticed that both the maximum F and the w_{max} increase with the increase in N from 2 to 12. This increase is considerable, with the increase in N from 2 to 3, 3 to 4 and 4 to 6. The metallic disc with $N = 2$ fails with very minimum central deflection. The disc with $N = 0$ exhibits maximum central deflection and maximum reaction force, which are significantly higher than the metallic discs having scores.



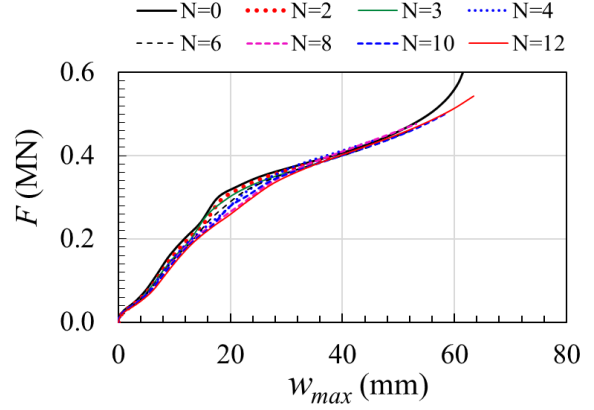
(a) Equivalent stress with respect to applied pressure



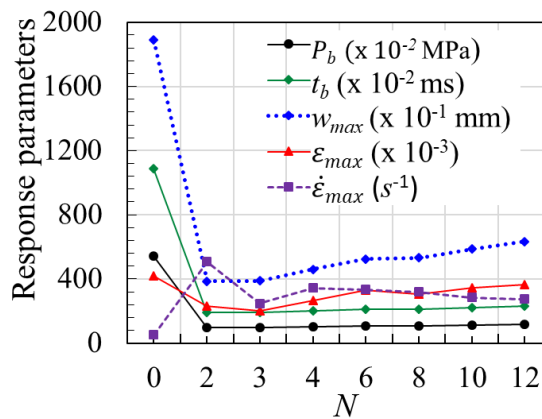
(b) Equivalent strain with respect to applied pressure



(b) Strain rate with respect to applied pressure



(d) Reaction force with respect to central deflection



(e) Responses with respect to the number of scores

Figure 3.17: Effect of the number of scores

Table 3.7: Influence of the number of the scores on the response of FSMD

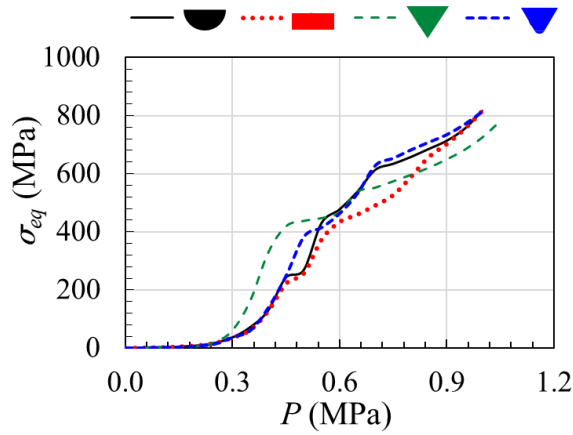
	Number of scores							
	0	2	3	4	6	8	10	12
P_b (MPa)	5.45	0.95	0.95	1.0	1.05	1.05	1.1	1.15
t_b (ms)	10.9	1.9	1.9	2.0	2.1	2.1	2.2	2.3
w_{max} (mm)	189	38.6	38.8	45.9	52.5	53.1	58.7	63.4
ϵ_{max}	0.42	0.23	0.2	0.26	0.33	0.30	0.34	0.37
$\dot{\epsilon}_{max}$ (/s)	52	507	248	343	334	320	284	273

The introduction of 2 scores along the diagonal of the disc reduced the responses such as P_b , t_b , w_{max} and ϵ_{max} significantly compared to an unscored flat metallic disc, as shown in Figure 3.17(e). These responses are very minimal for $N = 3$, and for $N > 3$, their increase is very gradual, and after $N > 8$, the responses are almost constant. The $\dot{\epsilon}_{max}$ is insensitive to an increase in $N > 3$. The Burst pressure of discs remains constant for any number of scores. Failure propagation and failure pattern entirely depend on the pressure acting on petals after the initial burst. However, for this analysis, the pressure is assumed to be acting continuously on the disc throughout the simulation, which causes failure propagation and petal separation. The strain rate is relatively higher in FSMD with $N = 2$ compared to discs with a higher number of scores, as seen in Table 3.7 and Figure 3.17(e). This is because the petals are formed after the burst along the two scores, and they are forced to undergo tearing at the fixed boundary before the petals experience bending under the effect of increasing fluid pressure. This tearing at the petal ends results in large displacements, *i.e.*, strain in a given time increment and therefore leading to a large strain rate.

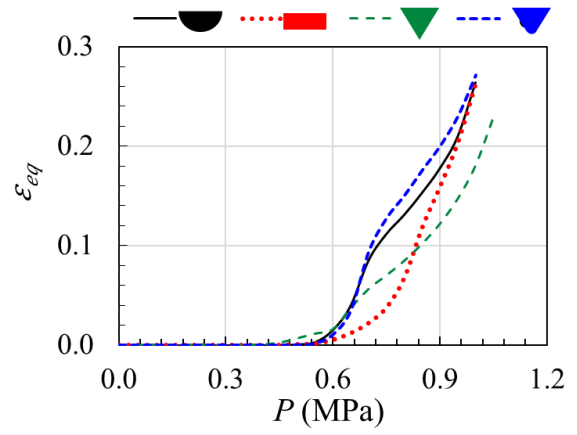
Score geometry

A rectangular score geometry is considered in all the previous studies thus discussed. The score geometry can be semi-circular, rectangular, triangular or triangular with a filleted tip in cross sections. They are analysed here to understand their influence on the deformation and rupture in the flat SMD. In all investigations with geometric variations in the score, constant dimensions are maintained for the plate thickness ($t = 2.0$ mm), score's width ($b = 5.0$ mm) and score's depth ($t_1 = 0.8$ mm).

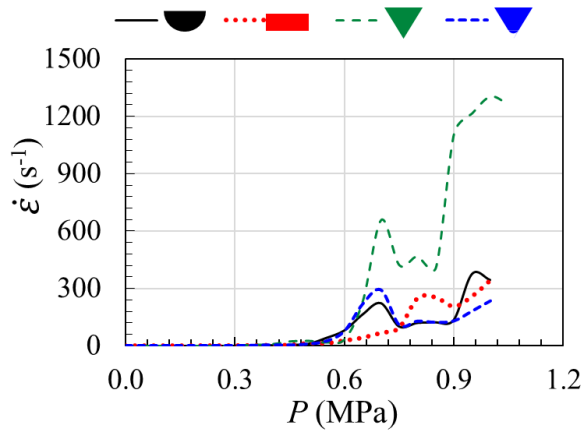
The variation of σ_{eq} , ϵ_{eq} and $\dot{\epsilon}$ at the centre of the disc in the score location with an increase in applied pressure for different cross-sections of the score geometry is shown in Figure 3.18(a-c). The maximum σ_{eq} and ϵ_{eq} experienced by the flat SMD are almost the same for all cross-sections. Their variations during loading are almost the same for the semi-circular and filleted triangular cross-sections compared to the rectangular score geometry, as seen in Figure 3.18(a-b). Even the $\dot{\epsilon}_{max}$ in the score's semi-circular geometry is smaller than the rectangular score geometry.



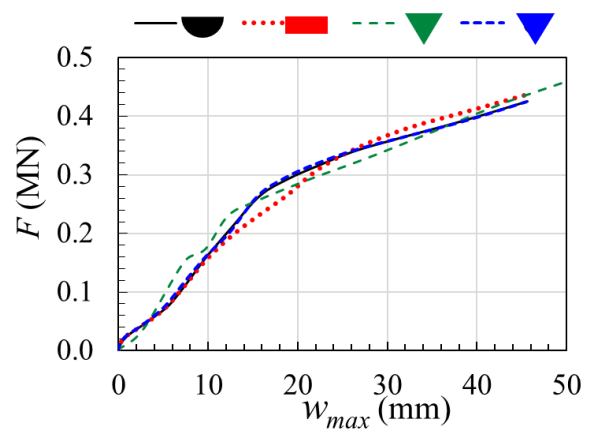
(a) Equivalent stress with respect to applied pressure



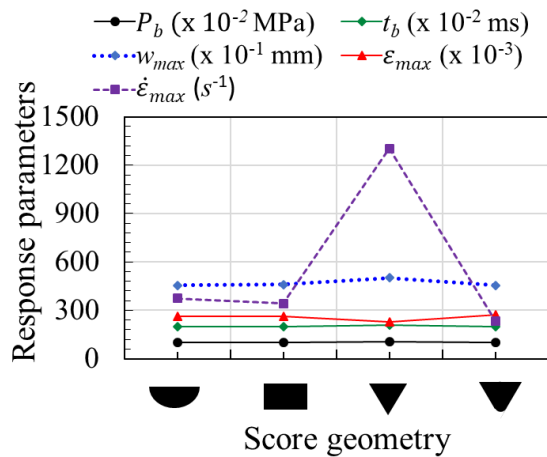
(b) Equivalent strain with respect to applied pressure



(c) Strain rate with respect to applied pressure



(d) Reaction force with respect to central deflection




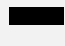


(e) Responses with respect to the score's geometry

Figure 3.18: Effect of the score's geometry

But the triangular score geometry resulted in strain rate oscillations just before the burst due to extreme strain localisation and instantaneous deformation before the burst, as seen in Figure 3.18(c). The reaction force F at the fixed boundary with respect to w_{max} is shown in Figure 3.18(d) for different cross-sections of the score. It is noticed that the reaction force increases with the increase in the central deflection irrespective of the type of score's geometry, and their variations are almost close. The maximum F and w_{max} , *i.e.* the maximum failure energy achieved for the rectangular and triangular score cross-sections and are almost the same.

The summary of maximum values of all responses such as P_b , t_b , w_{max} , ϵ_{max} and $\dot{\epsilon}_{max}$ for the semi-circular, rectangular, triangular and triangular with filleted tip score geometries is shown in Figure 3.18(e) and given in Table 3.8. All response parameters are almost identical for the semi-circular, rectangular and filleted triangular score geometries. Triangular score geometry exhibit marginally higher responses. Except for a higher value of $\dot{\epsilon}_{max}$ for the triangular score geometry, which may be attributed to the sharp stress concentration effect on the triangular score tip, all the other response parameters are almost the same for the four score cross-sections studied. Based on this study, the score geometry with a rectangular cross-section is preferable, considering the manufacturing easiness and dimensional control. The next recommendable geometry is the tip-filleted triangular score which can be made by press tools.

Table 3.8: Influence of score's geometry on response of FSMD

	Geometry			
				
P_b (MPa)	1.0	1.0	1.05	1.0
t_b (ms)	2.0	2.0	2.01	2.0
w_{max} (mm)	45.6	45.9	50.1	45.8
ϵ_{max}	0.26	0.26	0.23	0.27
$\dot{\epsilon}_{max}$ (/s)	374	343	1304	236

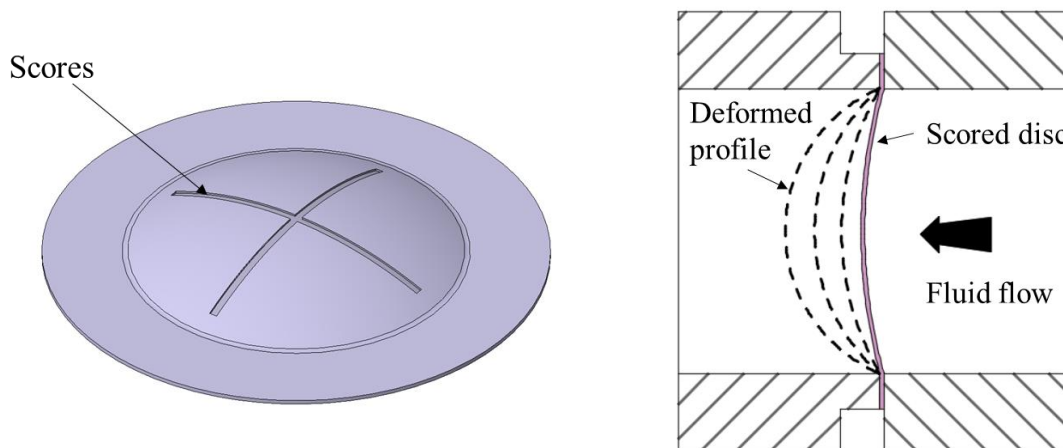
3.4 Summary

FE methodology for simulating the failure behaviour of a thin flat scored metallic disc subjected to an impulsive pressure loading has been investigated in this chapter by comparing the FE results with the experimental results available in literature. The predicted plastic strains, burst pressure and deformation pattern agreed well with the experimental results for the reference case. Based on this methodology, the behaviour of an FSMD under the effect of loading rates (2.5-500 MPa/s), diameter-to-plate thickness ratio (50-500), score's depth-to-plate thickness ratio (0.05-0.95), score's width-to-plate thickness ratio (1.5-3.5), score's length-to-disc radius ratio (0.2-1.0), score pattern (with the number of scores from 0-12), and score geometry (semi-circular, rectangular, triangular and triangular with filleted tip) were thoroughly investigated.

Behaviour of Domed Scored Metallic Disc

4.1 Introduction

Standard flat scored metallic discs have significantly less operating ratios for a given burst pressure, which are unsuitable for applications involving storage and failure conditions. The dome shaped disc is considered for this application as the dome shape can withstand constant internal storage pressure compared to a flat disc with an adequate safety margin. They behave differently than flat discs. For the present study, forward a domed scored metallic disc, as shown in Figure 4.1, is considered.



(a) Domed scored metallic disc (DSMD) (b) DSMD in conditional burst application

Figure 4.1: Forward domed metallic rupture disc with scores

In this chapter, an attempt is made to understand the behaviour of clamped, solid forward domed thin metallic rupture disc with scores, subjected to an impulsive air blast (as seen in Figure 4.1(b)) on the concave side of the disc and intended to meet both storage and the loading requirements of containers. FEA methodology and material model considered for FSMD in Chapter-3 are used. The behaviour of a domed-thin scored metallic disc is numerically investigated for the aforementioned loadings in a motor container. The effect of loading rates (\dot{P}), score depth and width-to-disc thickness ratio (t_1/t and b/t), diameter-to-disc thickness ratio (D/t), dome height (*i.e.* crown)-to-disc diameter ratio (H/D), score length-to-disc radius ratio (l/R), score pattern (N), and score geometry on the deformation and rupture characteristics of the domed-scored metallic disc is investigated and discussed in detail.

4.2 Operating parameters

These are the parameters which define the operational performance of the disc during application.

4.2.1 Operating ratio

The operating ratio defines the maximum static operating pressure up to which the disc can be used for a given burst pressure. For the present research, it is given by,

$$OR = \frac{MSOP \text{ at } \sigma_y}{P_b} \quad (4.1)$$

where *MSOP* is the maximum static operating pressure corresponding to the yield strength of material, or maximum pressure the disc withstands at material's yield strength and P_b is the disc's burst pressure. It should be as high as possible to achieve maximum functional efficiency.

4.2.2 Impulse

The impulse generated up to the burst of the disc defines the amount of energy absorbed and suddenly released at the time of the burst. It indicates how quickly the disc fails under a given load. The impulse generates shock loads on the rupture disc support structure. Impulse is given by,

$$I = \sum Ft_b \quad (4.2)$$

where F is reaction force and t_b is burst time. Higher impulse indicates disc transmits more impulse to fixity during failure.

4.3 Domed SMD under storage pressure

The domed and scored metallic disc under consideration is attached to one end of the motor container and continuously subjected to a constant internal pressure of 0.02 MPa during storage and to a sudden impulsive pressure during the initiation of the motor. The disc is fixed on its outer flat surface between the flanges.

4.3.1 Actual geometry and model for FEA

The geometry considered for the FEA of the domed disc is shown in Figure 4.2(a). It is provided with scores in the '+' configuration, as shown in Figure 4.2(a), on the convex side of the disc. The disc geometry and score geometry are shown in Figure 4.2(b) and the values are given in Table 4.1.

Table 4.1: Initial values of geometric features for DSMD

Geometric feature	Size (mm)
Outer diameter	800
Opening diameter (D) (fluid exposed diameter)	720
Sheet thickness (t)	2
Crown height or Dome height (H)	50
Score width (b)	5
Score depth (t_1)	0.8
Score length (l)	350

The FEA methodology adopted for the simulation of flat SMD discussed in Chapter 3 is adopted here in modelling the geometry and material for FEA simulation. The geometry is discretised with 8-node C3D8R brick elements. Four elements are maintained through the thickness of the domed disc. A total of 1301878 elements are generated using the swept meshing technique. Scores are provided on the convex side of the disc and fluid pressure is applied on the concave side of the disc.

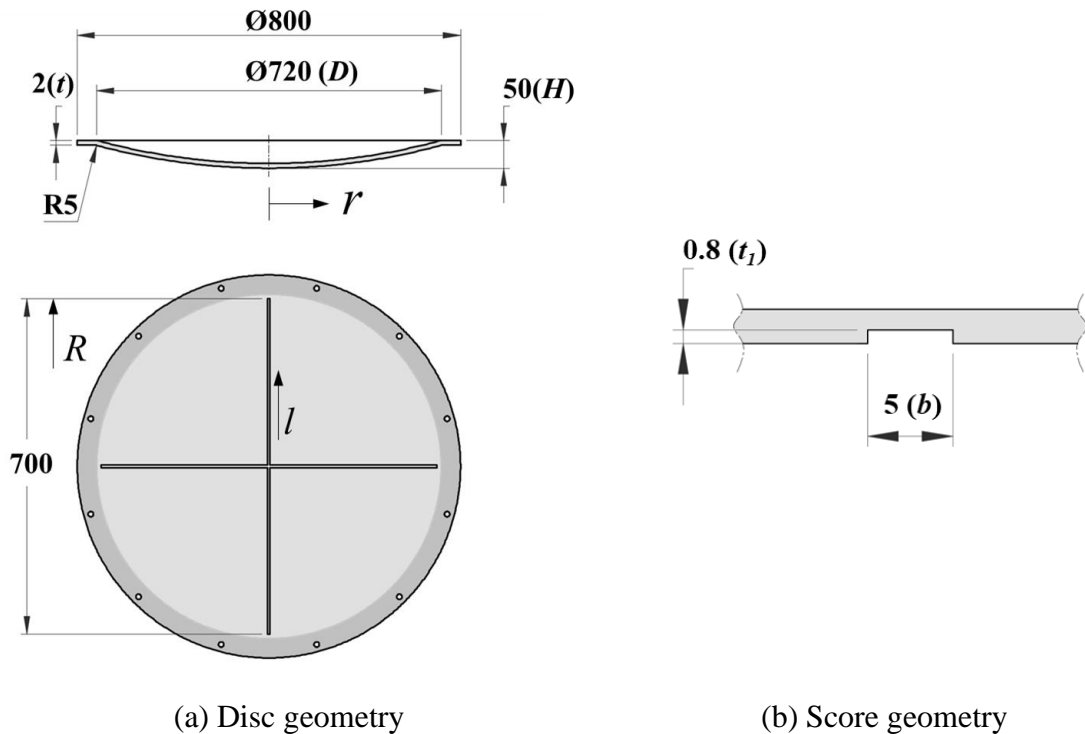


Figure 4.2: Geometry of domed metallic disc with scores

4.3.2 Domed SMD under constant internal pressure

The loading and boundary conditions are shown in Figure 4.3. All displacement degrees of freedom are constrained at all nodes in the flat portion of the disc between the diameters 720 and 800 mm. These two diameters, respectively, correspond to the typical outer and inner diameters of the container. A pressure load of 0.02 MPa is applied on the spherical inner surface of the disc.

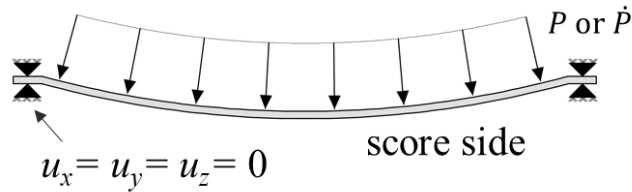
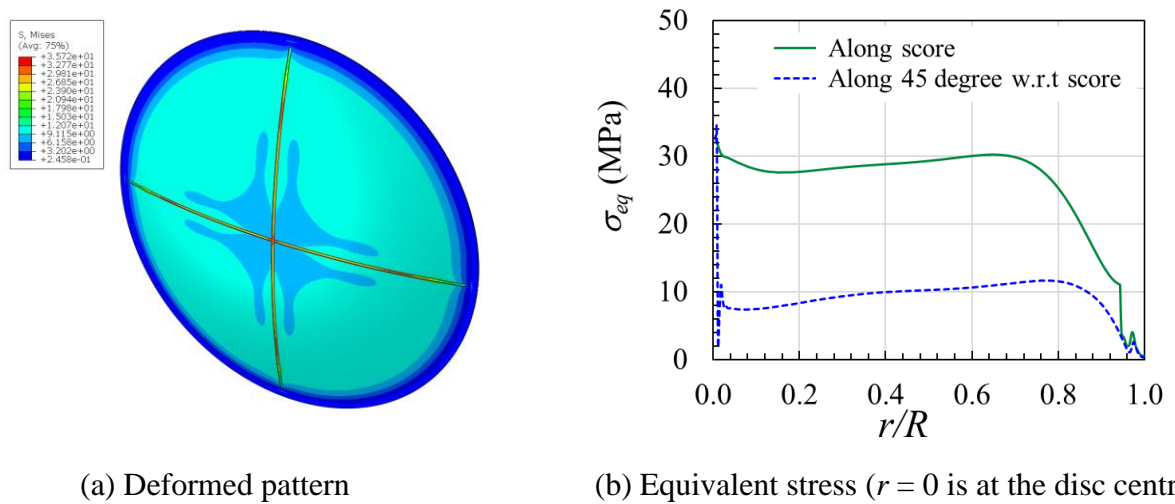


Figure 4.3: Loads and boundary conditions for DSMD

4.3.3 FEA and results

Static structural analysis is conducted using ABAQUS/CAE [59, 60] on the domed rupture disc, model and results are shown in Figure 4.4, where the deformed pattern is shown in Figure 4.4(a) and the von Mises stresses along the score and at 45° to the score are shown in Figure 4.4(b).



(a) Deformed pattern

(b) Equivalent stress ($r = 0$ is at the disc centre)

Figure 4.4: Deformation and stresses in domed metallic disc under uniform pressure loading

The maximum stress developed is 36 MPa at the centre of the disc and the equivalent stress is close to about 30 MPa for almost 70% of the disc radius along the score from the centre. The stress developed along the radius at 45° from the score is only about 10 MPa. It is observed that maximum stress is developed within the score location and is about 1/7th of the initial yield strength of the material and therefore the scored metallic disc satisfies the storage pressure requirement of the container.

4.4 Simulation of domed SMD under impulsive loading

The pressure loading rate on the scored metallic disc can reach as maximum as 500 MPa/s due to the instantaneous release of propulsion energy during the initiation of the motor within the container in a hot launch mode. Therefore, the non-linear explicit dynamic analysis is conducted using ABAQUS/Explicit code [61]. The material and damage model, as adopted in the simulation of FSMD described in Chapter 3, is adopted here. Mesh convergence studies are conducted for the domed scored metallic disc with different element sizes under an impulsive pressure loading rate of 500 MPa/s on the concave side of the disc. The solution time is considered up to 6 ms. The variation of various response parameters on the scored metallic disc, such as equivalent plastic stress σ_{eq} and strain ϵ_{eq} , P_b , t_b , w_{max} , ϵ_{max} and the plastic strain rate $\dot{\epsilon}_{max}$ developed at the centre of disc at the instant of burst and the reaction force F on the fixed boundary are studied during the analyses with four different element sizes such as 0.25, 0.33, 0.5 and 1.0 mm, as shown in Figure 4.5.

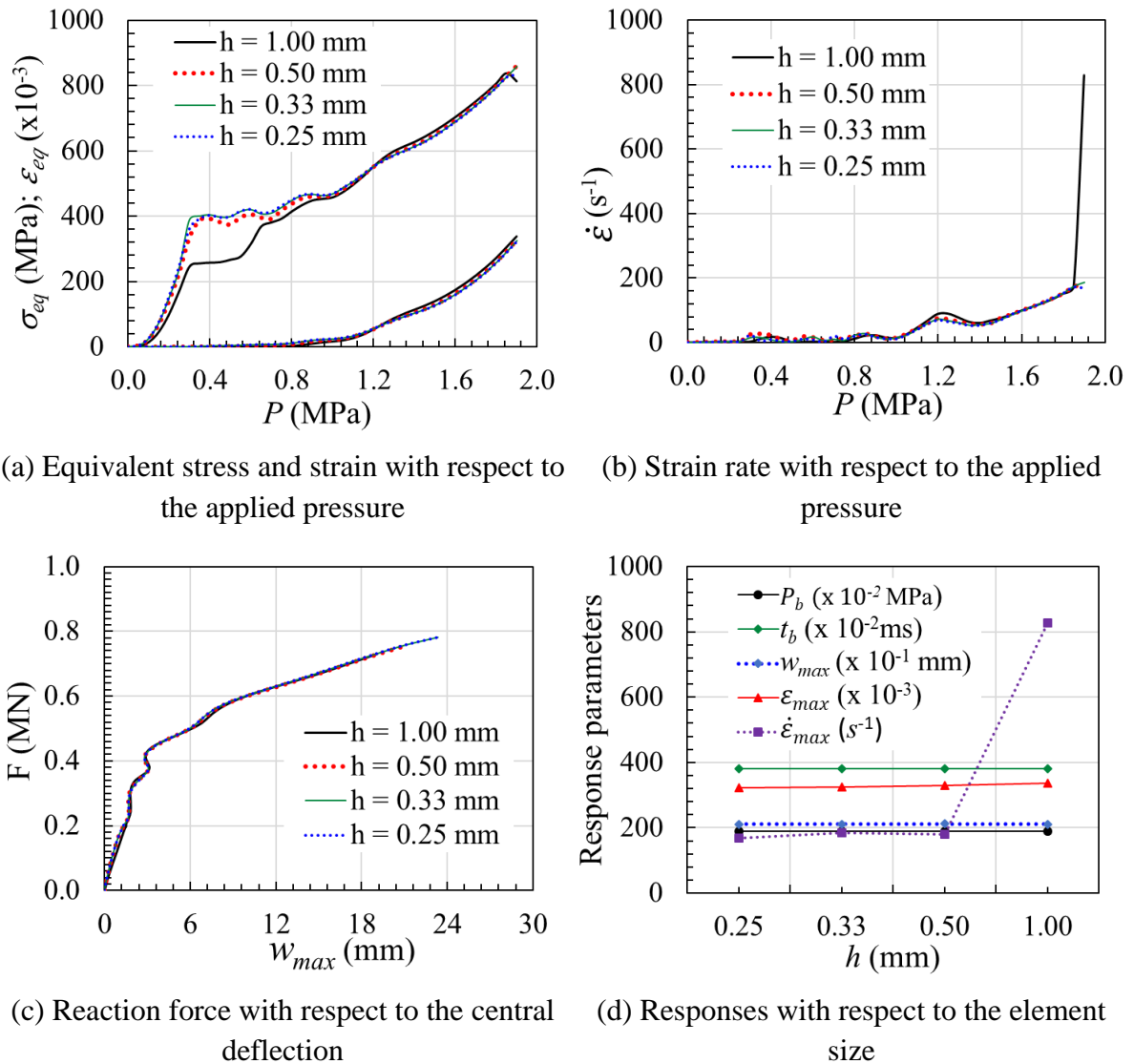
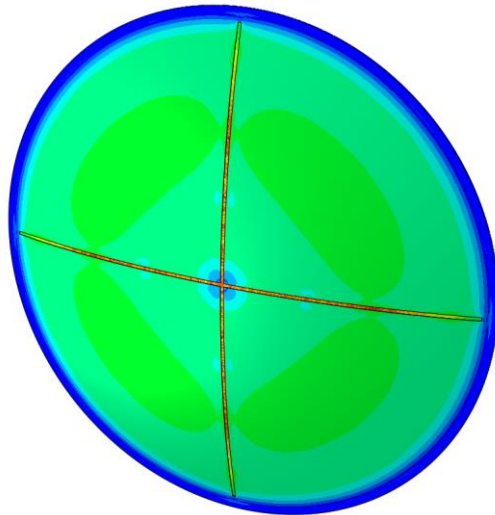
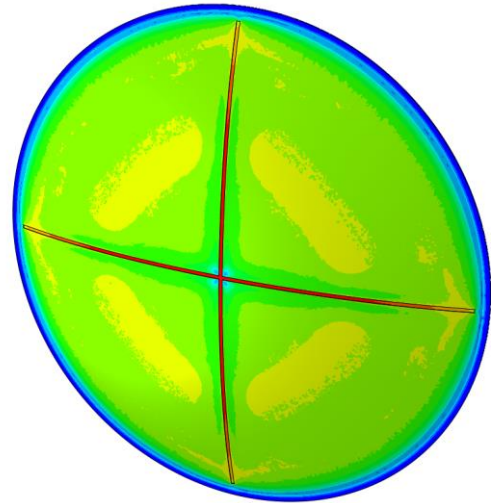


Figure 4.5: Results from mesh convergence studies of domed SMD

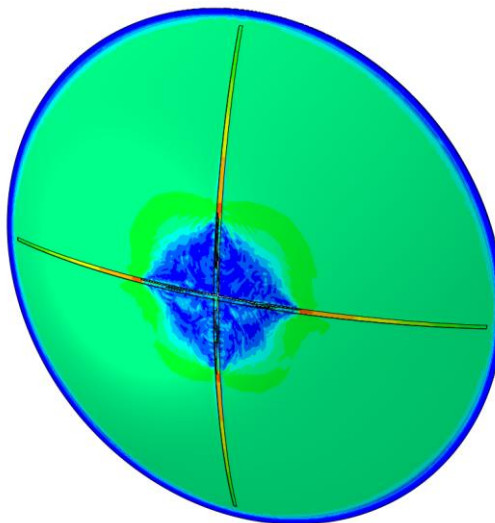
It is observed that all identified responses in the domed SMD attained converged values with an element size of 0.5 mm and below. Hence, four elements through the thickness are considered for all further numerical investigations.



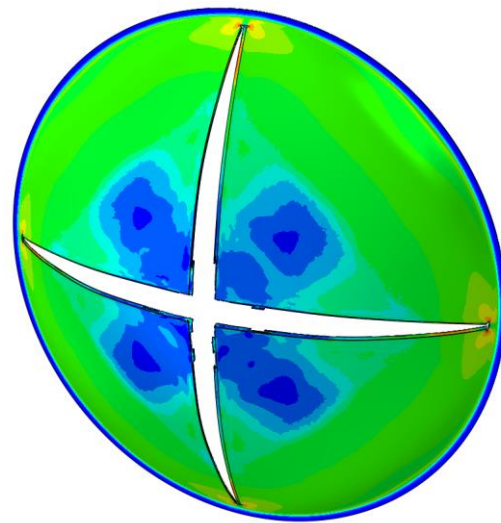
$P = 0.5 \text{ MPa}; \sigma_{eq[max]} = 921 \text{ MPa};$
 $\varepsilon_{eq[max]} = 0.006$
 (a) At time = 1 ms



$P = 1.0 \text{ MPa}; \sigma_{eq[max]} = 943 \text{ MPa};$
 $\varepsilon_{eq[max]} = 0.037$
 (b) At time = 2 ms



$P = 1.9 \text{ MPa}; \sigma_{eq[max]} = 957 \text{ MPa};$
 $\varepsilon_{eq[max]} = 0.430$
 (c) At time = 3.8 ms



$P = 2.3 \text{ MPa}; \sigma_{eq[max]} = 926 \text{ MPa};$
 $\varepsilon_{eq[max]} = 0.432$
 (d) At time = 4.6 ms

Figure 4.6: Failure initiation and propagation in domed scored disc under $\dot{P} = 500 \text{ MPa/s}$

The deformation pattern and the corresponding σ_{eq} , ε_{eq} , and P are shown in Figure 4.6 at different time instances during loading. During loading, equivalent plastic strains are concentrated along the scores similar to that observed in the flat SMD seen in Figure 3.5(b).

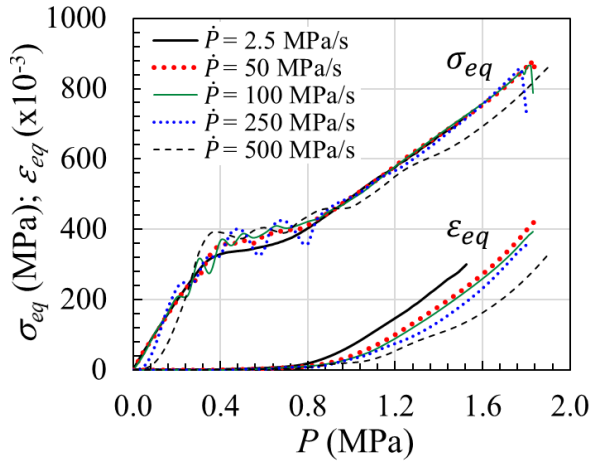
Still, maximum strain is always attained at the centre in domed SMD, as noticed in Figure 4.6(c), unlike the flat SMD in which the maximum strain is seen at away from the centre. The scored metallic disc achieved a P_b of 1.9 MPa and the t_b is around 3.8 ms. The failure initiated at the centre of the disc in the score location is propagated along the score until the outer periphery of the metallic disc.

4.4.1 Effect of loading rate

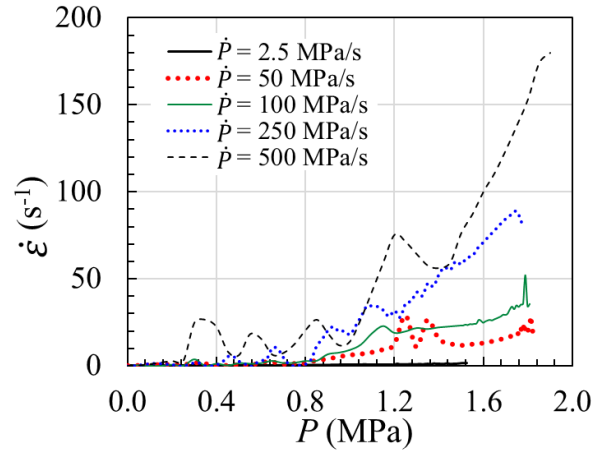
In order to understand the effect of the increase in the loading rate on the failure behaviour of the domed SMD, numerical studies are conducted at five different loading rates, such as 2.5, 50, 100, 250 and 500 MPa/s. Different responses in the scored disc, such as σ_{eq} , ε_{eq} , and equivalent strain rate $\dot{\varepsilon}$ at the centre of the disc in score location with the increase in applied P , are shown in Figure 4.7(a-b). The variations of σ_{eq} and ε_{eq} along the score just before the burst are shown in Figure 4.7(c-d) and the reaction force F at the fixed boundary with respect to the central deflection is shown in Figure 4.7(e) and the summary of all responses are shown with respect to the applied pressure loading rate in Figure 4.7(f). It is observed that σ_{eq} increases with applied P and its variation is almost the same irrespective of the loading rates except for the maximum higher loading rate of 500 MPa/s. On the other hand, ε_{eq} increase is similar to that of the σ_{eq} with the applied pressure, but its variation is almost the same for the loading rates of 50, 100 and 250 MPa/s except for the two extreme loading rates, *i.e.* 2.5 and 500 MPa/s which are different from the intermediate loading rates as seen in Figure 4.7(a).

The equivalent strain rate increases with the applied P loading and is higher for higher loading rates. More fluctuations are observed in $\dot{\varepsilon}$ through the course of loading due to large instantaneous deformation experienced at the central element of the disc at the score location. Maximum $\dot{\varepsilon}$ varied from 7.5 to 175 /s, respectively, for the minimum to maximum loading rates considered in the studies, as seen in Figure 4.7(b). The maximum stress and strain variations at the score along the radius of the disc show a parabolic pattern, as seen in Figures 4.7(c-d). It reveals that the maximum σ_{eq} attained at all loading rates is close to about 900 MPa and a slight variation is observed in the induced σ_{eq} up to about 50% of the radius along the score beyond which all loading rates resulted in almost the same variation except for the lowest loading rate. But, the variation of ε_{eq} is different for different loading rates. The maximum ε_{eq} experienced by the disc at the score exhibits a reducing trend with an increase in loading rate from 2.5 to 500 MPa/s. The equivalent stresses and strains reach convergence and attain a minimal value close to the fixed boundary along the score, irrespective of the applied loading rate.

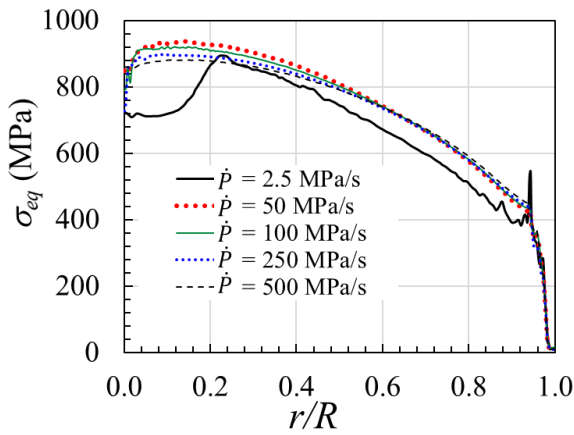
The reaction force, F experienced at the fixed boundary increases with the increase in w_{max} for all loading rates, but the maximum force is almost the same for all loading rates except the lowest loading rate, as seen in Figure 4.7(e). The P_b , t_b and w_{max} are almost constant beyond the loading rate of 100 MPa/s and exhibit no sensitivity to loading rates. On the other hand, both the maximum equivalent plastic strain and maximum strain rate exhibit sensitivity to loading rates. The maximum $\dot{\varepsilon}$ increases with the increase in loading rates.



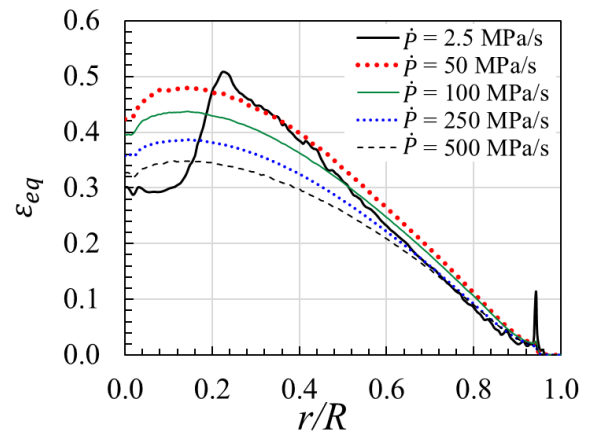
(a) Equivalent stress and strain with respect to the applied pressure



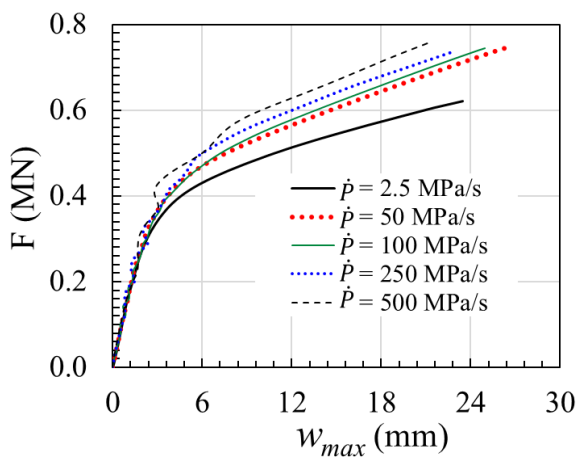
(b) Strain rate with respect to the applied pressure



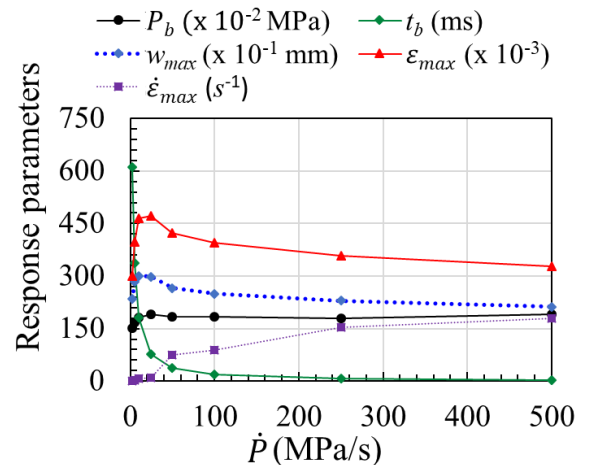
(c) Equivalent stress along the radius of the disc in the score



(d) Equivalent strain along the radius of the disc in the score



(e) Reaction force with respect to the central deflection



(f) Responses with respect to loading rate

Figure 4.7: Effect of the loading rate on domed scored disc

The equivalent ε_{max} decreases with the increase in loading rates beyond the loading rate of 50 MPa/s. All responses exhibit an increase from the lowest loading rate of 2.5 to 50 MPa/s. The burst time decreased significantly from the lowest loading rate to 50 MPa/s and afterwards, it almost remained insensitive to the loading rates, as observed in Figure 4.7 (f).

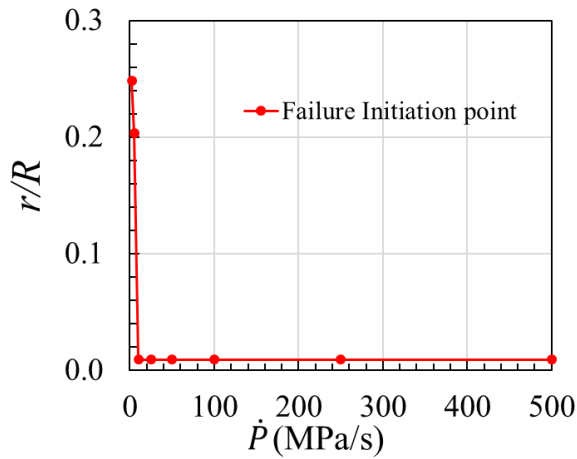
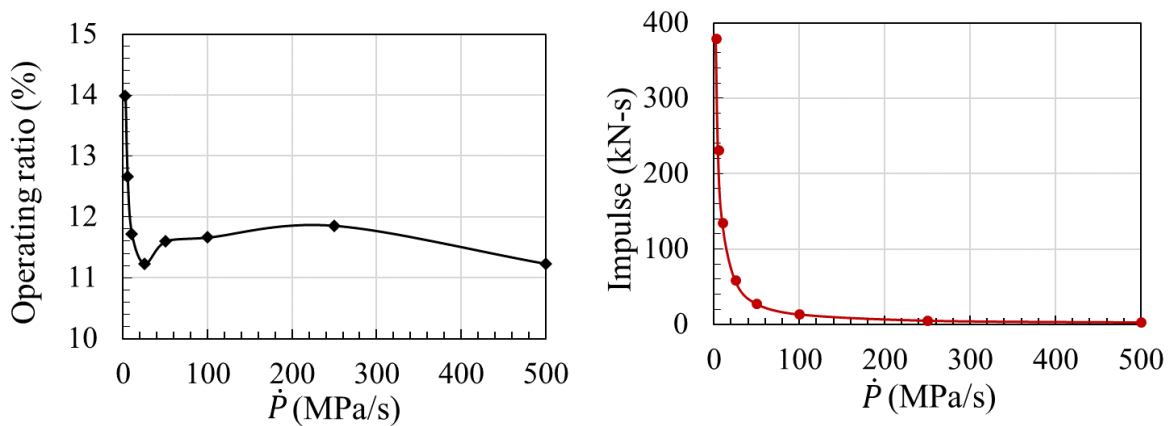


Figure 4.8: Failure initiation location with respect to the loading rate

One peculiar observation is appreciable with regard to the location of failure initiation with respect to the loading rates, as observed in Figure 4.8. When the loading rate is 2.5 MPa/s, the failure is initiated in the score location at about 90 mm (*i.e.* at $r = 0.25R$) away from the centre. The failure initiation is at $r = 0.2R$ for 5.0 MPa/s loading rate. For loading rates > 10.0 MPa/s, the failure initiation is close to the centre of the disc ($r \approx 0$) at the score location and is insensitive to the higher loading rates. This is because at lower loading rates of less than 5.0 MPa/s, the plastic hinges are generated in the score location at 20-25% of the disc radius, as evidenced in Figure 4.7(c-d) and this hinge slowly shifts close to the centre of the disc along score as loading rate is increased.



a) Operating ratio with respect to the loading rate b) Impulse with respect to the loading rate

Figure 4.9: Operating parameters with respect to the loading rate

Under the influence of loading rate, operating ratio and Impulse initiated for DSMD are given in Figure 4.9 (a-b). At the lowest loading rate of 2.5 MPa/s, DSMD exhibited the highest operating ratio of 14%, which stabilised between 11% and 12%. Even though the reaction force absorbed by DSMD at the loading rate is almost the same, Impulse initiated is higher at the lowest loading rate of 2.5 MPa/s and reduced exponentially with an increase in the loading rate.

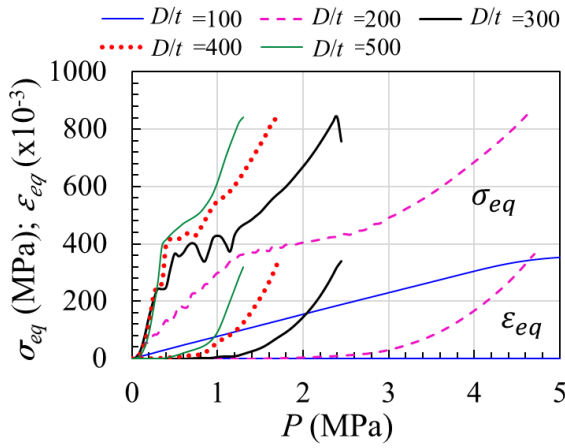
4.4.2 Influence of geometrical features on the behaviour of domed SMD

The geometrical features in the domed-scored metallic rupture disc significantly influence the deformation, failure and rupture behaviour when exposed to a given loading rate caused by fluid pressure. The influencing geometrical features can be i) diameter-to-plate (*i.e.* disc) thickness (D/t) ratio, ii) dome height-to-disc diameter (H/D) ratio, iii) score depth-to-plate thickness (t_1/t) ratio, iv) score width-to-plate thickness (b/t) ratio, v) score length-to-disc radius (l/R) ratio, vi) score pattern, *i.e.* the number of scores (N), and vii) score geometry. Numerical studies are conducted to investigate the effects of these geometrical features on the characteristics of thin domed scored metallic discs, featured with four numbers of rectangular scores of width 5 mm and depth 0.8 mm as considered in Section 4.3.1 (and seen in Figure 4.2), under a pressure loading rate of 500 MPa/s. Only one geometrical feature to be investigated is changed while maintaining the other features as constant in these sensitivity studies.

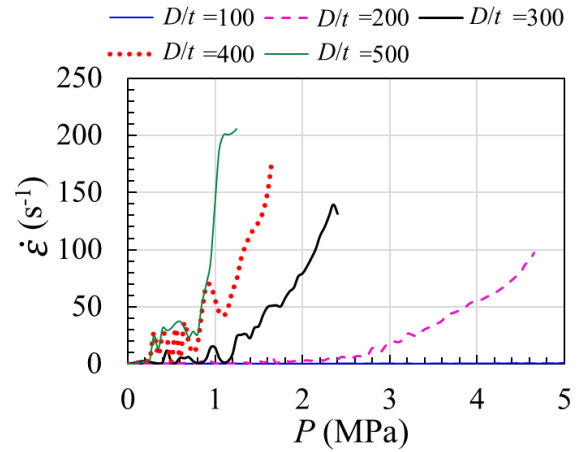
4.4.2.1 Diameter-to-plate thickness (D/t) ratio

The effect of the disc's diameter-to-plate thickness, *i.e.* D/t ratio, is investigated by varying the diameter of the disc from 100 mm to 1000 mm in steps of 100 mm by keeping the plate thickness at $t = 2$ mm. This variation of the disc's diameter provides $D/t = 50$ to 500 in steps of 50. The complete behaviour of the domed SMD extracted from simulations is shown in Figure 4.10(a-f).

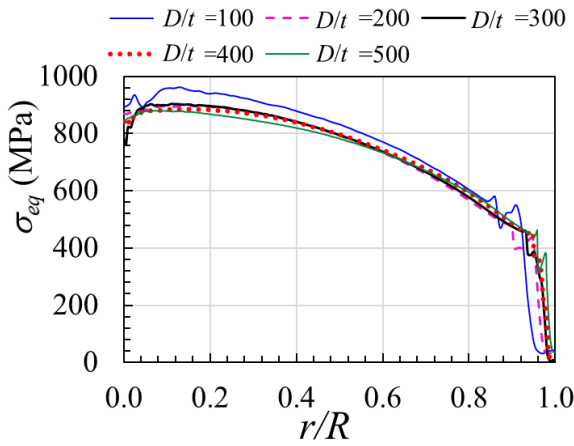
The equivalent stress, *i.e.* von-Mises stress σ_{eq} , equivalent plastic strain ϵ_{eq} , and plastic strain rate $\dot{\epsilon}$ at the centre of the disc in score location with increase in applied pressure are shown in Figure 4.10(a-b). It is observed that both σ_{eq} and ϵ_{eq} increase with the increase in the disc's D/t ratio. Their maximum values remained almost same for $D/t \geq 200$ but their rate of increase with applied pressure gradually increase and is significant beyond $D/t > 300$. On the other hand, their rate of rise is very shallow for $D/t < 100$ as seen in Figure 4.10(a). As the diameter of the disc increases, steep increase in the equivalent stress and equivalent strain can be observed which can be attributed to the behaviour of the disc where plate stretching phenomenon is more significant than plate bending. They remained same at the point of burst indicating all of them undergoing similar failure mode at the centre. The plastic strain rate increases from 2 to 200 /s with the increase in the D/t ratio from 100 to 500 as observed in Figure 4.10(b) and its increase with an increase in applied pressure varies from very shallow to significantly steep with increase in D/t ratio.



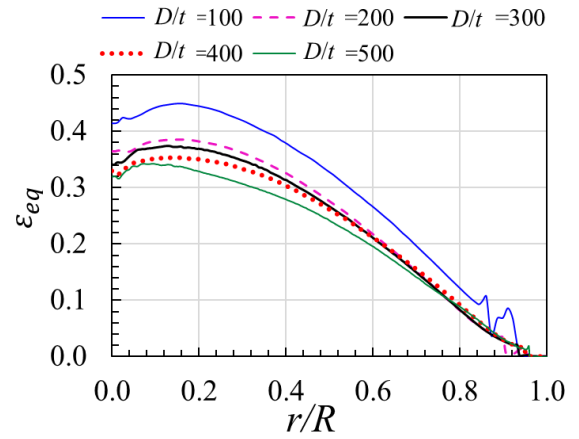
(a) Equivalent stress and strain with respect to the applied pressure



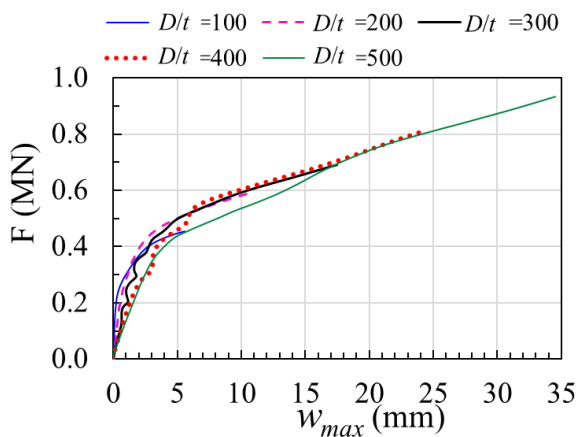
(b) Strain rate with respect to the applied pressure



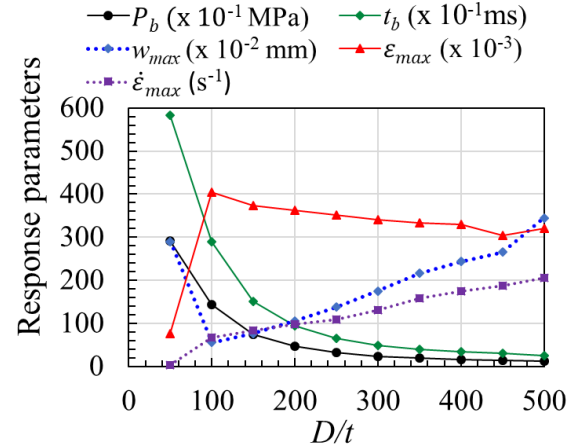
(c) Equivalent stress along the radius of the disc in the score



(d) Equivalent strain along the radius of the disc in the score



(e) Reaction force with respect to the central deflection



(f) Responses with respect to (D/t) ratio

Figure 4.10: Effect of the diameter-to-plate thickness (D/t) ratio

The variation of σ_{eq} and ε_{eq} along the score at an instant just before burst are shown in Figure 4.10(c-d). Both these responses are higher at close to the centre of the disc, gradually decrease with the increase in the radius r of the disc and follow a similar pattern. They exhibit decreasing trend with the increase in D/t ratio but this decrease is insignificant for σ_{eq} up to $r/R = 0.92$ and is considerable for ε_{eq} up to $r/R = 0.6$. Both σ_{eq} and ε_{eq} variations for $D/t = 100$ exhibited a relatively higher magnitude with increase in r/R ratio as compared with higher values of D/t . The plastic stress variations remained almost same for all values of $D/t > 100$ and they decreased from 900 MPa to 440 MPa for r/R ranging from 0.06 to 0.92 and eventually reach 0 MPa at maximum radius of the disc. The plastic strain attained maximum value at r/R ranging between 0.12 and 0.16 for all D/t ratios of the disc.

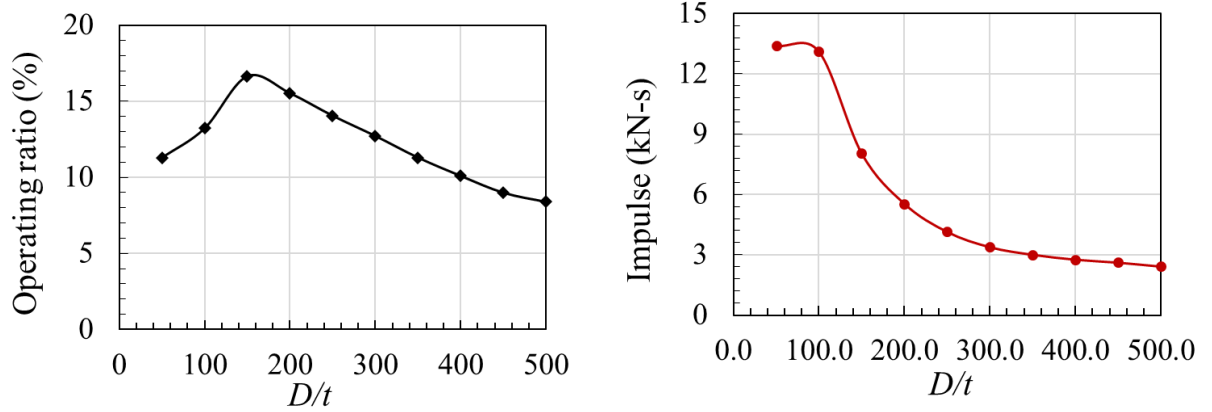
Variation of reaction force, F at the fixed boundary with respect to the central deflection w_{max} is shown in Figure 4.10(e) for all values of D/t ratio considered. Initial stiffness of the domed SMD increases with decrease in the discs' D/t ratio. Area under the $F-w$ curve, *i.e.* energy absorbed before burst increases with increase in D/t ratio and so is their maximum values. The summary of maximum values of all responses such as P_b , t_b , w_{max} , ε_{max} and $\dot{\varepsilon}_{max}$ with increase in D/t ratio is shown in Figure 4.10(f) and is also given in Table 4.2.

Table 4.2: Influence of D/t on response of DSMD

	D/t				
	100	200	300	400	500
P_b (MPa)	14.5	4.70	2.45	1.70	1.30
t_b (ms)	28.9	9.40	4.9	3.4	2.6
w_{max} (mm)	5.6	10.6	17.5	24.4	34.5
ε_{max}	0.41	0.36	0.34	0.33	0.32
$\dot{\varepsilon}_{max}$ (/s)	67	98	132	174	206

It can be observed that both P_b and t_b decrease exponentially with increase in D/t and their variations are small for $D/t > 300$. Variation of $\dot{\varepsilon}_{max}$ is a linear and gradual increase from 2 to 200 /s for increasing values of D/t from 50 to 500. The ε_{max} increases from 0.08 to 0.40 for $50 < D/t < 100$ and subsequently decreases linearly from 0.40 to 0.30 for $100 < D/t < 500$. Maximum mid-deflection decreases from 3.0 mm to 0.6 mm for increase in D/t from 50 to 100 and subsequently exhibited a linear increase from 0.6 mm to 3.5 mm for increase in D/t from 100 to 500.

Operating parameters of DSMD with respect to D/t ratio is shown in Figure 4.11 (a-b). Operating ratio is maximum at 17% at $D/t = 150$ indicating highest operating efficiency. Impulse is maximum for $D/t \leq 200$ and reduced with increase in D/t ratio or diameter of the disc. Minimum impulse is observed for maximum diameter of the disc *i.e.* higher diameter disc fails with less transmitted impulse.



a) Operating ratio with respect to the (D/t) ratio b) Impulse with respect to the (D/t) ratio

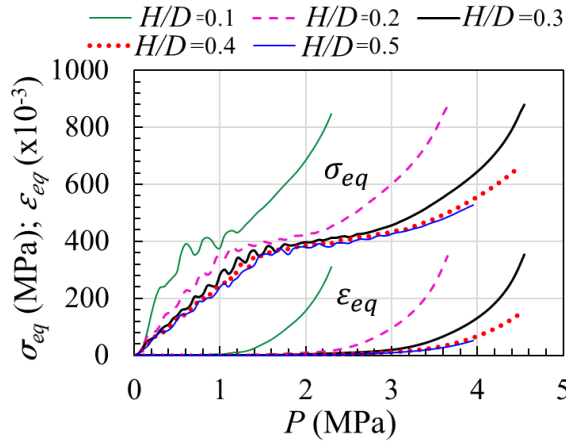
Figure 4.11: Operating parameters with respect to the (D/t) ratio

4.4.2.2 Dome height-to-disc's diameter (H/D) ratio

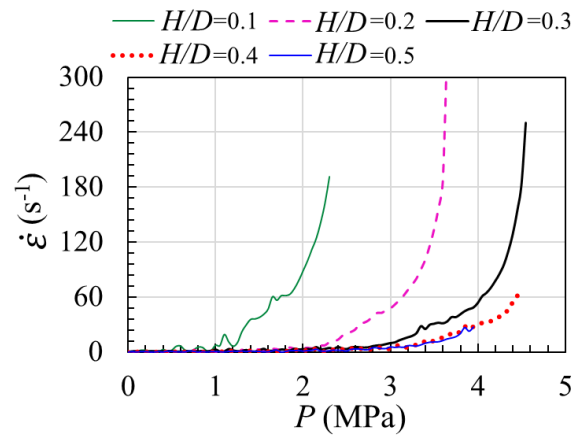
The influence of the disc's dome height-to-diameter ratio, *i.e.* H/D ratio is analyzed by varying the dome height from 72 mm to 360 mm for a constant disc diameter of 720 mm so as to achieve H/D ratios ranging from 0.1 to 0.5 in steps of 0.1. Other geometric parameters of the disc and score are kept constant. The behaviour of the domed SMD for the analysed H/D variations is shown in Figure 4.12(a-f).

The equivalent stress, equivalent plastic strain, and plastic strain rate at the centre of the disc in the score location with the increase in applied pressure are shown in Figure 4.12(a-b). It can be noticed that the decrease of σ_{eq} and ε_{eq} with respect to the applied pressure decrease with the increase in H/D ratio up to 0.3 and beyond which the rate of decrease is insignificant. Their maximum values remained almost constant for $H/D \leq 0.3$ beyond which the spherical dome effect becomes significant which causes both σ_{eq} and ε_{eq} to decrease with increase in loading. Their maximum values start to decrease with any further increase in H/D as seen in Figure 4.12(a). Both strain and strain rate sensitivity with the applied loading increase gradually and slowly with the increase in H/D ratio. The maximum strain rate increases with loading up to $H/D = 0.2$ and beyond which it slowly start to decrease as observed in Figure 4.12(b). Maximum strain and strain rate are very small at $H/D = 0.5$ as compared to any other values.

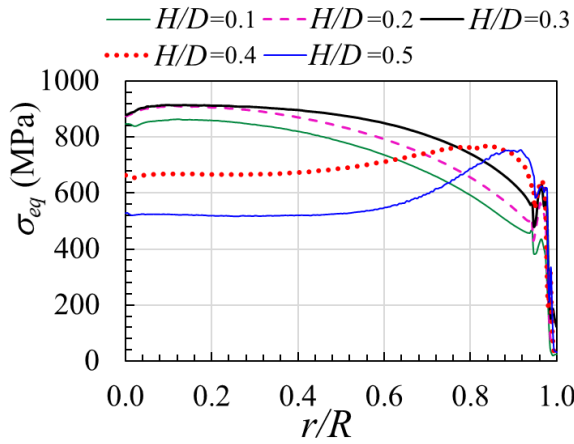
The variation of σ_{eq} and ε_{eq} along the score at an instant just before burst are shown in Figure 4.12(c-d). Both these responses are higher at close to the centre of the disc, *i.e.* at $r/R = 0.08$ for $H/D \leq 0.3$ whereas these are maximum only at regions near fixity, *i.e.* at $r/R = 0.95$ for $H/D > 0.3$ due to shift in the formation of plastic hinges to fixed region. The distribution of their values at score along the radius r decrease with increase in H/D ratio except for $0.2 \leq H/D \leq 0.3$ for which their values along radius in score are higher than that of $H/D = 0.1$. Their distribution is almost constant along radius up to $r/R = 0.60$ for $H/D > 0.3$ unlike other cases for which their values decrease with increase in H/D up to 0.3.



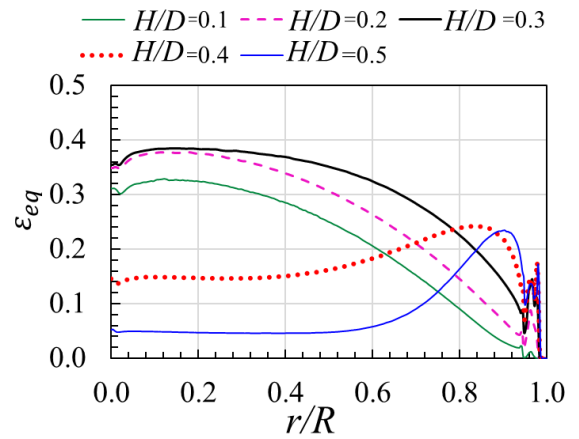
(a) Equivalent stress and strain with respect to the applied pressure



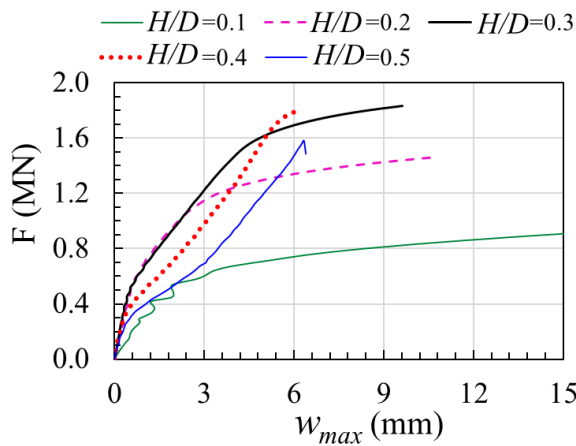
(b) Strain rate with respect to the applied pressure



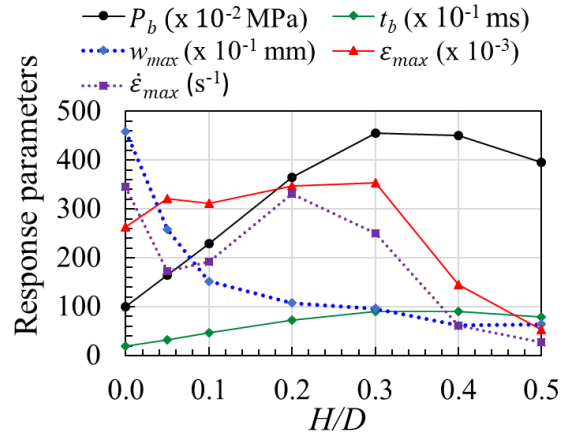
(c) Equivalent stress along the radius of the disc in the score



(d) Equivalent strain along the radius of the disc in the score



(e) Reaction force with respect to the central deflection



(f) Responses with respect to the (H/D) ratio

Figure 4.12: Effect of the dome height-to-plate diameter (H/D) ratio

Variation of reaction force, F at the fixed boundary with respect to the central deflection w_{max} is shown in Figure 4.12(e) for all values of H/D ratio. Initial stiffness of the domed disc is almost same for $0.2 \leq H/D \leq 0.3$ and it is also same for $H/D = 0.1$ and 0.5 . The F - w_{max} response is almost steady and attains a plateau after w_{max} crosses 6.0 mm for $H/D = 0.1$.

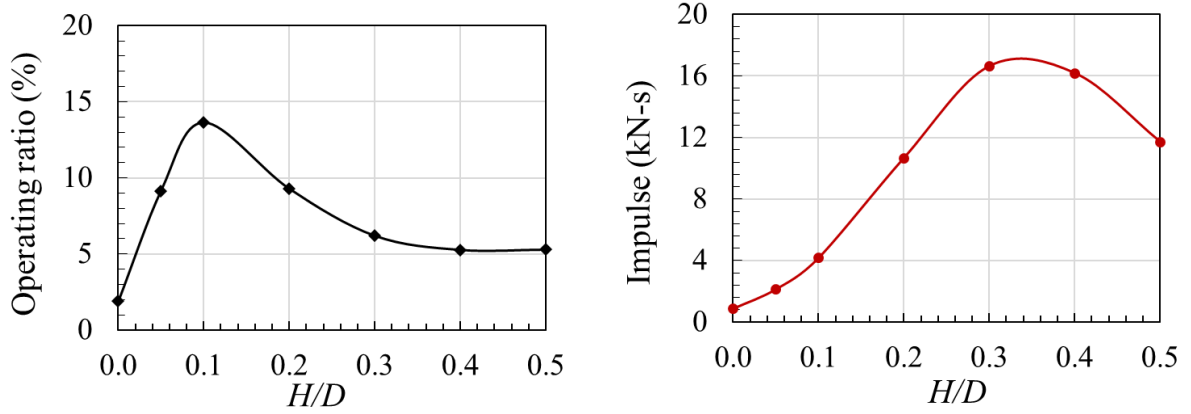
The summary of maximum values of all responses such as P_b , t_b , w_{max} , ε_{max} and $\dot{\varepsilon}_{max}$ with increase in H/D ratio is shown in Figure 4.12(f) and given in Table 4.3

Table 4.3: Influence of H/D on response of DSMD

	H/D					
	0	0.1	0.2	0.3	0.4	0.5
P_b (MPa)	1.0	2.3	3.7	4.6	4.5	4.0
t_b (ms)	2.0	4.6	7.3	9.1	9.0	7.9
w_{max} (mm)	45.9	15.2	10.7	9.6	6.2	6.4
ε_{max}	0.26	0.31	0.35	0.35	0.15	0.05
$\dot{\varepsilon}_{max}$ (/s)	345	192	331	250	62	27

It is seen that both P_b and t_b increase gradually for $0.01 \leq H/D \leq 0.3$ and remained constant for $0.3 \leq H/D \leq 0.4$ and subsequently decrease marginally for $H/D > 0.4$. The ε_{max} increases from 0.26 to 0.35 for $0.01 \leq H/D \leq 0.3$ and subsequently decreases linearly from 0.35 to 0.06 for $0.4 < H/D < 0.5$. The w_{max} decreases exponentially from 46.0 mm to 10.0 mm for $0.01 \leq H/D \leq 0.2$ and afterwards its decrease is only up to 8.0 mm for $0.2 \leq H/D \leq 0.5$. Variation of $\dot{\varepsilon}_{max}$ is a linear decrease from 350 to 170 /s for $0.01 \leq H/D \leq 0.05$, it increases gradually to 320 /s for $0.05 \leq H/D \leq 0.2$ and afterwards it decreases to 40 /s at $H/D = 0.5$. The behaviour of the domed SMD is affected significantly with H/D ratio and the responses are benign after $H/D = 0.4$ when the geometry attains a spherical profile.

Operating parameters of DSMD with respect to H/D ratio is shown in Figure 4.13 (a-b). Operating ratio at $H/D = 0$ is 2% for flat disc and increased gradually and maximum at 17% at $H/D = 0.1$ indicating highest operating efficiency and reduced gradually to 5% when $H/D = 0.5$ for hemi-spherical disc. Flat disc and hemi spherical discs are not suitable for current application because of least operating efficiencies. Impulse is least for flat disc and high for hemi spherical disc indicating flat disc is good for failure application where hemispherical disc is good for storage application.



a) Operating ratio with respect to the (H/D) ratio b) Impulse with respect to the (H/D) ratio

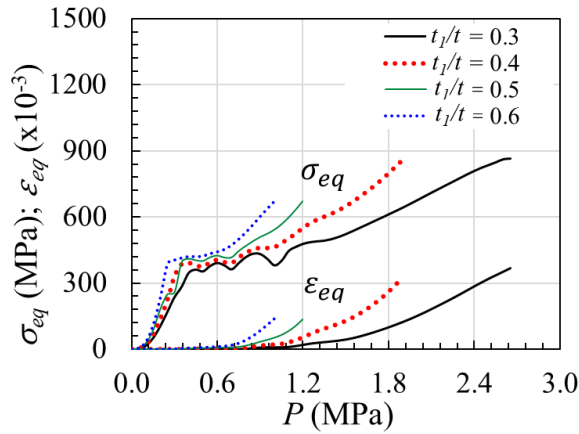
Figure 4.13: Operating parameters with respect to the (H/D) ratio

4.4.2.3 Score's depth-to-plate thickness (t_1/t) ratio

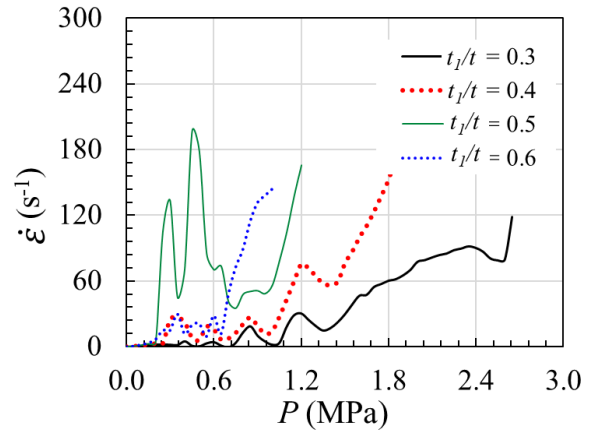
The effect of score depth t_1 is analysed by varying the score's depth from 0.2 mm to 1.4 mm in steps of 0.2 mm by keeping constant values for the plate thickness $t = 2$ mm and score's width $b = 5$ mm. This variation of score's depth provides a depth-to-plate thickness ratio of $t_1/t = 0.1$ to 0.7 in steps of 0.1. The complete behaviour of the domed SMD extracted from simulations is shown in Figure 4.14(a-f).

The equivalent stress, *i.e.* von-Mises stress, equivalent plastic strain, and plastic strain rate at the centre of the disc in score location with increase in applied pressure are shown in Figure 4.14(a-b). It is observed that both σ_{eq} and ε_{eq} decrease with increase in the scores' t_1/t ratio. Their maximum values remained almost same for the two adjacent ratios of $t_1/t = 0.3$ and 0.4 and similar is the response for $t_1/t = 0.5$ and 0.6, although these maximum values reach at different burst pressures, as seen in Figure 4.14(a). The $\dot{\varepsilon}$ increases with the increase in t_1/t ratio as observed in Figure 4.14(b) and it exhibits more oscillations at higher score depths, due to more localized and instantaneous deformations occurring in the region.

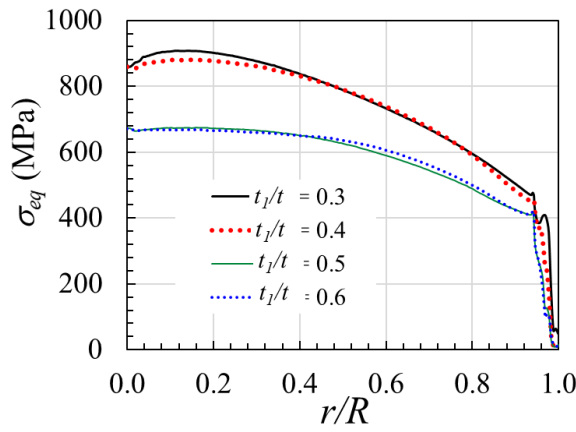
The variation of σ_{eq} and ε_{eq} along the score at an instant just before the burst are shown in Figure 4.14(c-d). Both these responses are higher at close to the centre of the disc, *i.e.* at $r/R = 0.1$, gradually decrease with the increase in the radius of the disc and follow a similar pattern. They exhibit decreasing trend with the increase in t_1/t ratio. The variation of induced stress for $t_1/t = 0.3$ and 0.4 are almost close and exhibited a higher magnitude while it is relatively less and closer for $t_1/t = 0.5$ and 0.6, as noticed in Figure 4.14(c). The variation of equivalent strain at score, along radius of the disc shows a clear decrease until about 60% of the radius with increase in t_1/t ratio from 0.3 to 0.4 and beyond which both these t_1/t ratios resulted in almost same strains until the fixed boundary. But the response of the equivalent strain is reduced by almost $1/3^{\text{rd}}$ and its variation is almost same for $t_1/t = 0.5$ to 0.6, along the radius at score, as observed in Figure 4.14(d).



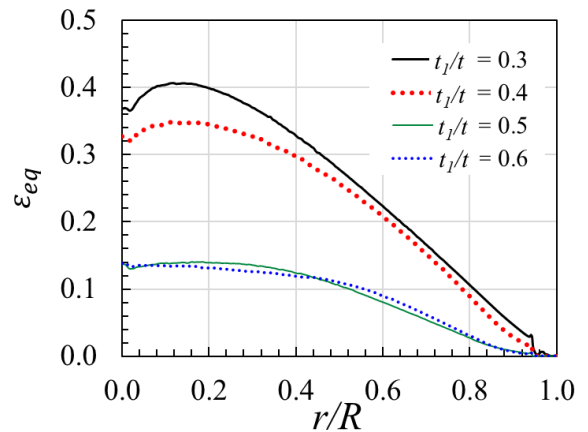
(a) Equivalent stress and strain with respect to the applied pressure



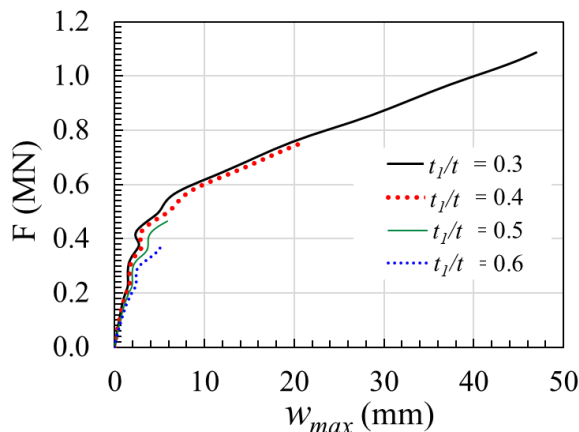
(b) Strain rate with respect to the applied pressure



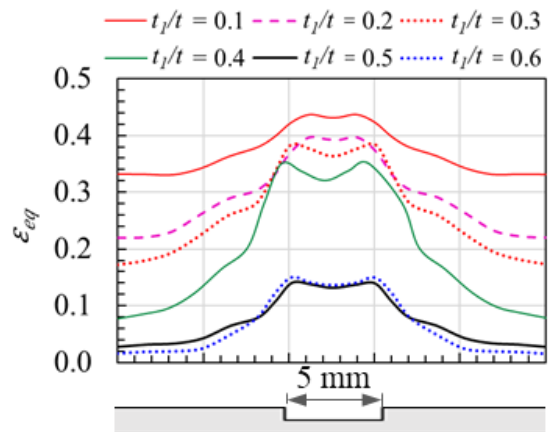
(c) Equivalent stress along the radius of the disc in the score



(d) Equivalent strain along the radius of the disc in the score



(e) Reaction force with respect to the central deflection



(f) Equivalent strain around the score just before the failure

Figure 4.14: Effect of the score's depth-to-plate thickness ratio (t_1/t); $t = 2$ mm

The reaction force at the fixed boundary with respect to the central deflection is shown in Figure 4.14(e) and it is noticed that both the maximum F and the w_{max} decrease considerably with increase in t_1/t ratio from 0.3 to 0.6. This is caused by the weakening of the score's region due to the increase in the score's depth. Further, the stiffness exhibited by the domed SMD for different t_1/t ratio is almost the same until before the burst. The distribution of equivalent strain around the score just before failure is shown in Figure 4.14(f) for t_1/t ratios ranging from 0.1 to 0.6. It can be noticed that the ratio of local strain in score to ligament strain increases with increase in t_1/t up to 0.4 and afterwards, it decreases and remains unchanged for $t_1/t \geq 0.5$. The ε_{max} at score decreases with increase in t_1/t ratios but it stabilizes and remained constant after $t_1/t = 0.5$. This reveals that the score weakens the domed SMD and it is significantly influenced for $0.1 \leq t_1/t \leq 0.5$ and afterwards this influence is unnoticeable.

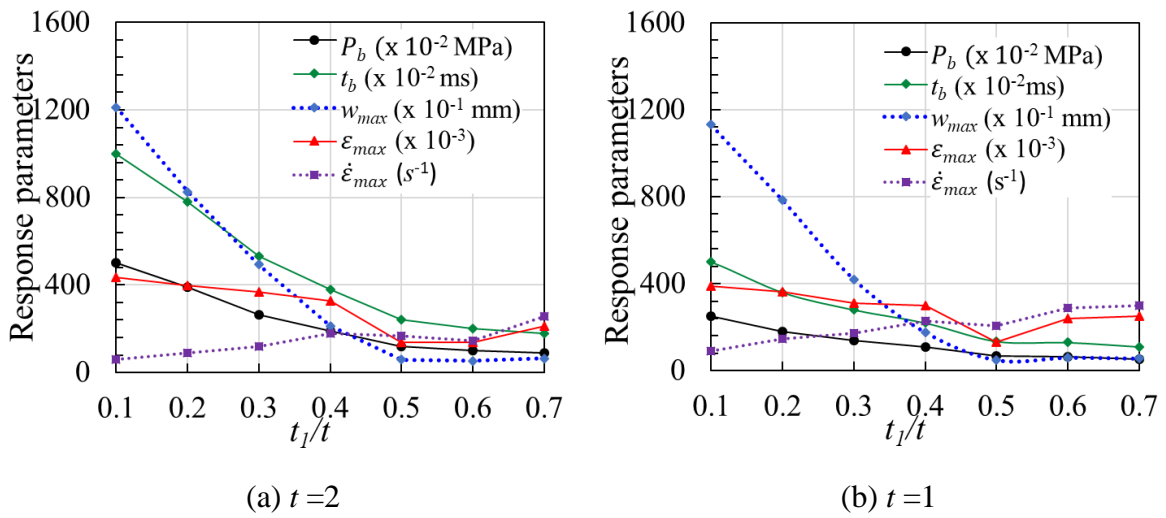


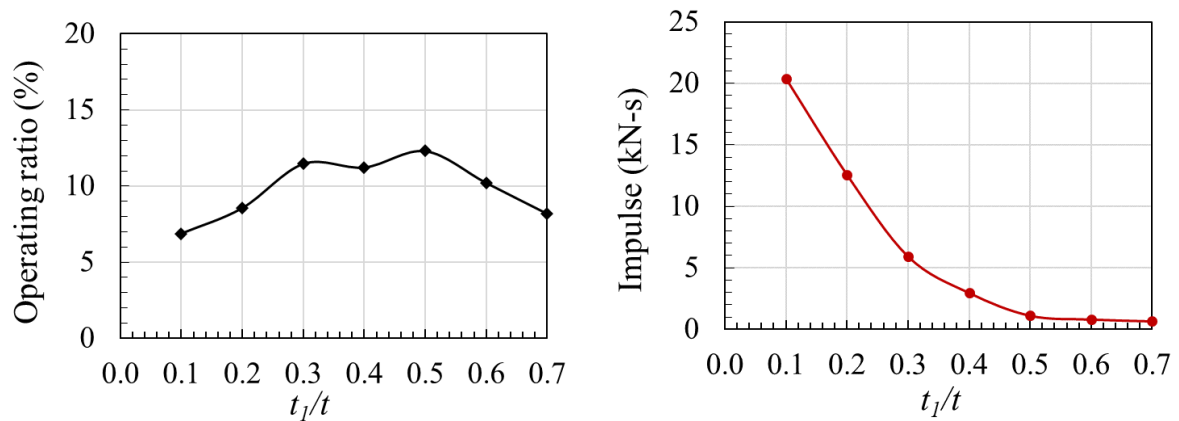
Figure 4.15: Responses with respect to the score's depth-to-plate thickness (t_1/t) ratio

The summary of maximum values of all responses such as P_b , t_b , w_{max} , ε_{max} and $\dot{\varepsilon}_{max}$ with increase in t_1/t ratio for $t = 2$ mm and 1 mm are shown respectively in Figures 4.15(a-b) and given in Table 4.4.

Table 4.4: Influence of t_1/t on response of DSMD

	$t_1/t; t=2$ mm					$t_1/t; t=1$ mm				
	0	0.3	0.4	0.5	0.6	0	0.3	0.4	0.5	0.6
P_b (MPa)	5.00	2.65	1.90	1.20	1.00	3.00	1.40	1.10	0.68	0.65
t_b (ms)	10.0	5.3	3.8	2.4	2.0	6.00	2.80	2.20	1.35	1.30
w_{max} (mm)	120	49.3	21.2	5.8	5.3	153	42	17.7	4.8	5.9
ε_{max}	0.31	0.37	0.34	0.14	0.14	0.45	0.31	0.30	0.13	0.24
$\dot{\varepsilon}_{max}$ (/s)	40	118	180	165	143	137	173	227	206	287

It can be observed that the burst pressure, burst time and central deflection decreased almost asymptotically with the increase in t_1/t ratio. The variation in maximum strain rate is insignificant from $t_1/t = 0.4$ onwards. On the other hand, the maximum strain decreases with the increase in t_1/t ratio, but its rate of decrease with t_1/t ratio is very much considerable between 0.4 and 0.5. This study reveals that the score's t_1/t ratio influences the important response parameters in the domed SMD. Almost all the important response parameters are relatively less and exhibit insensitivity to t_1/t ratio for $t_1/t > 0.5$. The magnitude of all responses are comparably lesser for $t = 1$ mm as compared to $t = 2$ mm.



a) Operating ratio with respect to the (t_1/t) ratio b) Impulse *with* respect to the (t_1/t) ratio

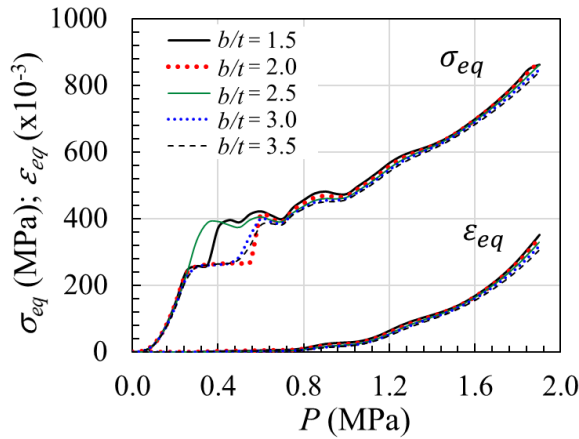
Figure 4.16: Operating parameters with respect to the (t_1/t) ratio

The operating parameters of DSMD with respect to t_1/t ratio is shown in Figure 4.16 (a-b). The operating ratio at $t_1/t = 0.1$ is 7% for less score depth and increased gradually and maximum at 12% at $t_1/t = 0.5$ indicating highest operating efficiency at score depth half the plate thickness and reduced gradually to 8% when $t_1/t = 0.7$ for more score depth. Impulse is most for minimum score depth indicating no score or minimum score depth is good for storage application and least for more score depth indicating increased score depth is good for failure application.

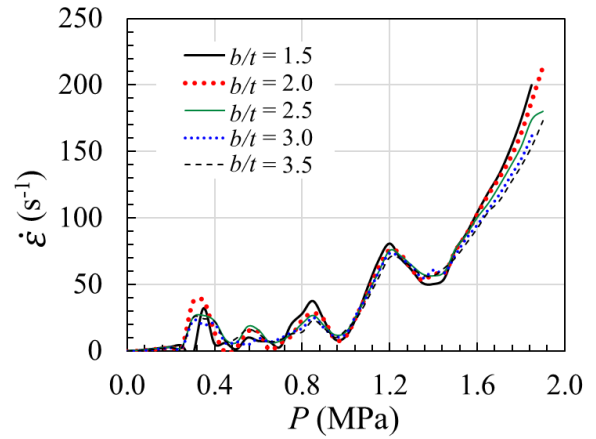
4.4.2.4 Score's width-to-plate thickness (b/t) ratio

The influence of score's width b is analysed by varying b from 3.0 mm to 7.0 mm in steps of 1.0 mm by keeping constant values for the plate thickness at $t = 2.0$ mm and score's depth at $t_1 = 0.8$ mm. This variation of score's width provides a width-to-plate thickness ratio of $b/t = 1.5, 2.0, 2.5, 3.0$ and 3.5 . The behaviour of the domed SMD is captured from simulations and shown in Figure 4.17(a-f).

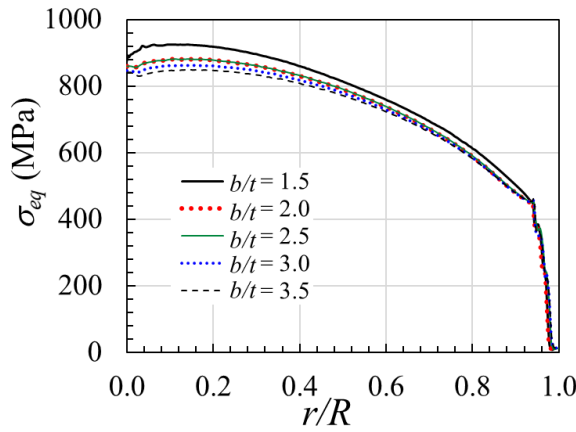
The variation of $\sigma_{eq}, \epsilon_{eq}$ and $\dot{\epsilon}$ at the centre of the disc in score location with increase in applied pressure is shown in Figure 4.17(a-b). These responses are almost the same irrespective of any variation in score's b/t ratio, except a small decrease in the maximum strain rate with the



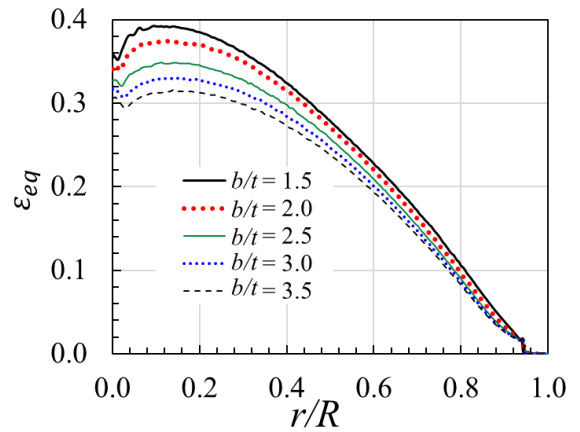
(a) Equivalent stress and strain with respect to the applied pressure



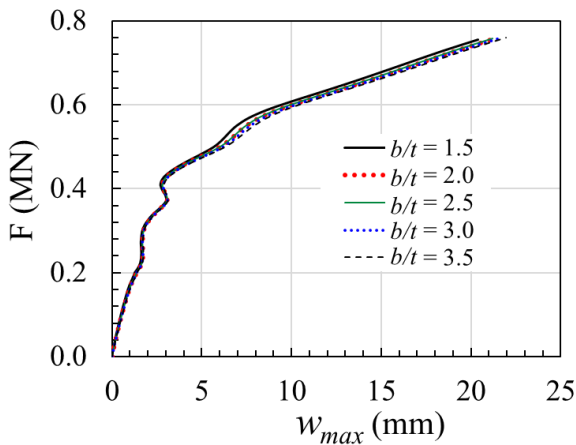
(b) Strain rate with respect to applied pressure



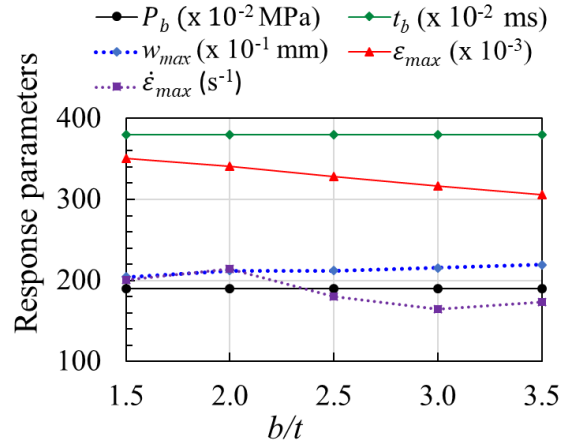
(c) Equivalent stress along the radius of the disc



(d) Equivalent strain along the radius of the disc



(e) Reaction force with respect to the central deflection



(f) Summary of responses with respect to the (b/t) ratio

Figure 4.17: Effect of the score's width-to-plate thickness (b/t) ratio

increase in b/t ratio before the actual burst as seen in Figure 4.17(b). A maximum strain rate of around 170 to 210 /s is observed with decrease in b/t ratio from 3.5 to 1.5.

The variation of σ_{eq} and ε_{eq} along the score before burst for different b/t ratios are shown in Figure 4.17(c-d). Both these responses are higher at $r/R = 0.1$, *i.e.* at close to the centre of the disc and gradually decrease with the increase in radius of the disc and follow a similar pattern. They exhibit a decreasing trend with the increase in b/t ratio. The variation of equivalent stress for $b/t = 2.0$ and 2.5 are almost the same as seen in Figure 4.17(c). The variation of equivalent plastic strain at score, along radius of the disc decreases until the fixed boundary, and it also decreases with the increase in the b/t ratio, as observed in Figure 4.17(d). The maximum σ_{eq} near the centre of the disc in score decreased from 930 to 840 MPa with the increase in the b/t ratio from 1.5 to 3.5. Similarly, the corresponding reduction in the ε_{eq} is from 0.39 to 0.31.

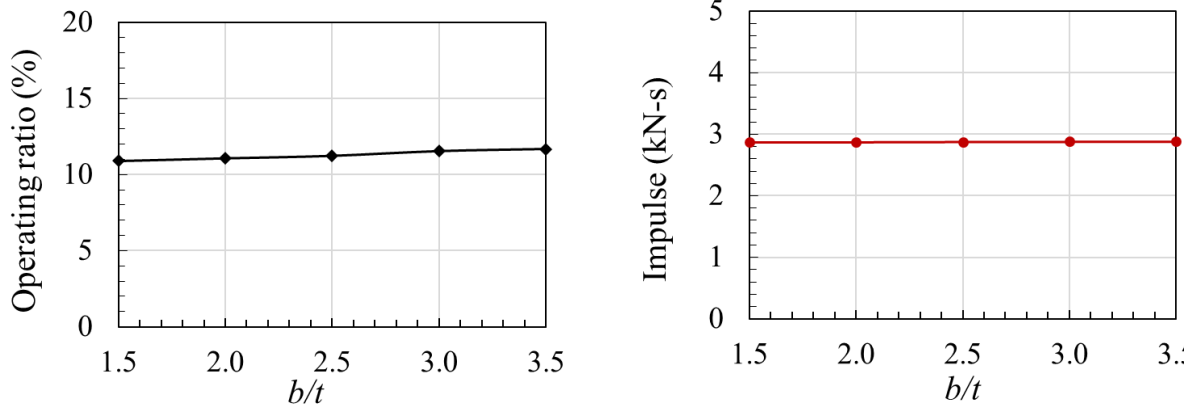
The reaction force F at the fixed boundary with respect to the central deflection w_{max} is shown in Figure 4.17(e) for different b/t ratio of score. No major variation is observed within the values considered for the change in b/t ratio. Further, the stiffness exhibited by the domed SMD for different b/t ratio is almost the same until the burst. The summary of maximum values of all responses such as burst pressure, burst time, maximum central deflection, maximum equivalent strain and maximum strain rate, with increase in b/t ratio is shown in Figure 4.17(f) and given in Table 4.5.

Table 4.5: Influence of b/t on response of DSMD

	b/t				
	1.5	2	2.5	3	3.5
P_b (MPa)	1.90	1.90	1.90	1.90	1.90
t_b (ms)	3.8	3.8	3.8	3.8	3.8
w_{max} (mm)	20.4	21.2	21.2	21.6	21.9
ε_{max}	0.35	0.34	0.34	0.32	0.31
$\dot{\varepsilon}_{max}$ (/s)	200	214	180	164	173

It can be observed that the P_b , t_b and w_{max} remained almost constant with the increase in b/t ratio. Only a small variation of about ± 20 /s is observed with the increase in the b/t ratio from minimum to maximum value. Even the reduction in maximum equivalent plastic strain is observed to be from 0.35 to 0.30 with the increase in the b/t ratio from 1.5 to 3.5. This study demonstrates that the score's b/t ratio does not significantly influence the important response parameters in the domed SMD.

Operating parameters of DSMD with respect to b/t ratio is shown in Figure 4.18 (a-b). Both operating ratio and impulse almost same for all variations of score width indicating score width has least influence.



a) Operating ratio with respect to the (b/t) ratio b) Impulse with respect to the (b/t) ratio

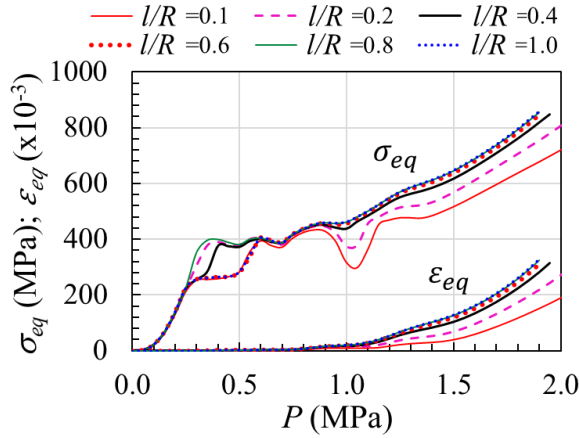
Figure 4.18: Operating parameters with respect to the (b/t) ratio

4.4.2.5 Score length-to-disc radius (l/R) ratio

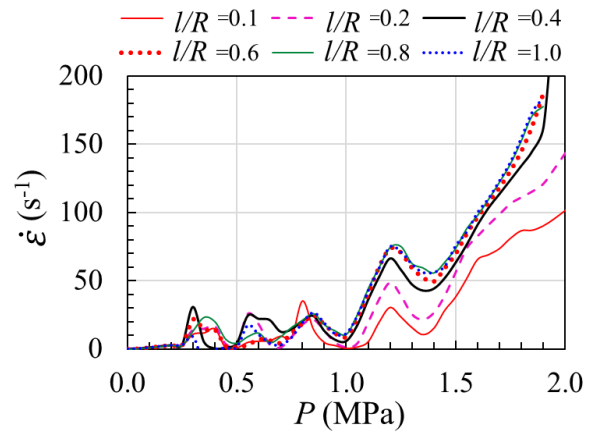
The effect of score's length-to-disc radius (*i.e.* l/R) ratio is investigated by varying the score's length from 36 mm to 360 mm for a constant disc radius of 360mm so as to achieve l/R ratios of 0.1, 0.2, 0.4, 0.5, 0.6, 0.8 and 1.0. Other geometric parameters of the disc and score are kept constant. The behaviour of the domed SMD for the analyzed l/R variations is shown in Figure 4.19(a-f).

The equivalent stress, equivalent plastic strain, and plastic strain rate at the centre of the disc in score location with increase in applied pressure are shown in Figure 4.19(a-b). It can be noticed that σ_{eq} , ε_{eq} and $\dot{\varepsilon}$ with respect to the applied pressure increase with the increase in l/R ratios up to 0.4, beyond which the responses are almost the same. The variation of σ_{eq} and ε_{eq} along the score at an instant just before burst are shown in Figure 4.19(c-d). Both these responses are higher at close to the centre of the disc. The distribution of their values at score along its length l appears maximum along the score and drop to a significantly lower value after the end of score with increase in r/R . Both responses are almost same after the end of score and until the maximum radius of the disc.

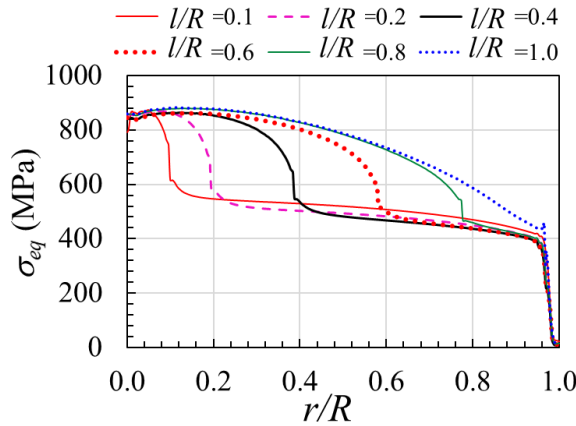
The variation of F at the fixed boundary with respect to w_{max} at every increment of loading is shown in Figure 4.19(e) for all values of l/R ratios considered. The initial and subsequent stiffness of the domed disc is almost same for all l/R ratios. The maximum F and w_{max} increases with l/R up to 0.4 only beyond which the F - w_{max} response is almost constant. This implies that the energy absorbed before burst is same in all cases of $l/R \geq 0.4$. The summary of maximum values of all responses such as P_b , t_b , w_{max} , ε_{max} and $\dot{\varepsilon}_{max}$ with increase in l/R ratio is shown in Figure 4.19(f) and given in Table 4.6.



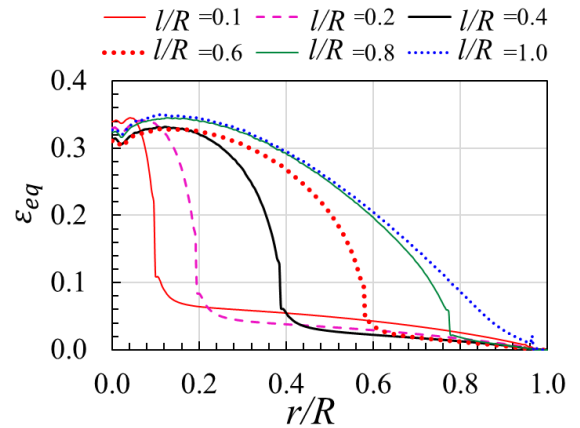
(a) Equivalent stress and strain with respect to the applied pressure



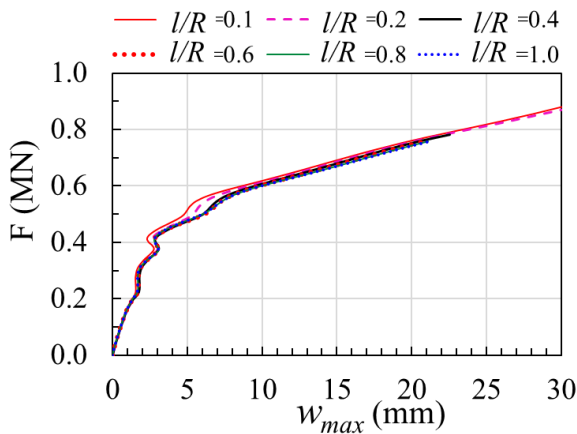
(b) Strain rate with respect to the applied pressure



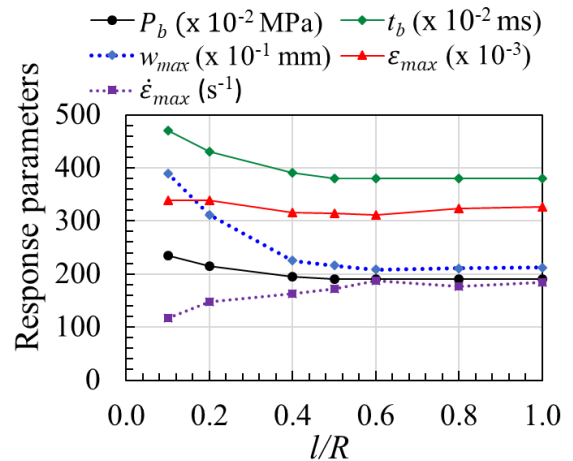
(c) Equivalent stress along the radius of the disc in the score



(d) Equivalent strain along the radius of disc in the score



(e) Reaction force with respect to the central deflection



(f) Responses with respect to the score's (l/R) ratio

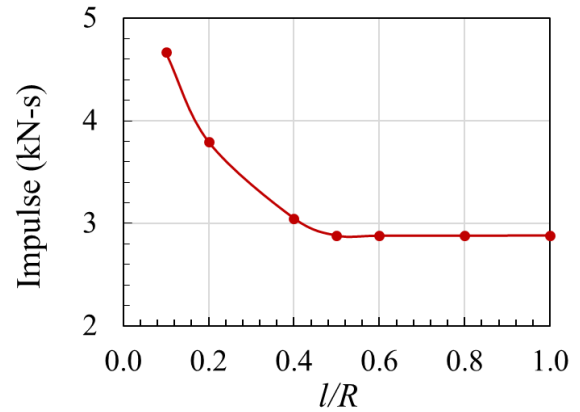
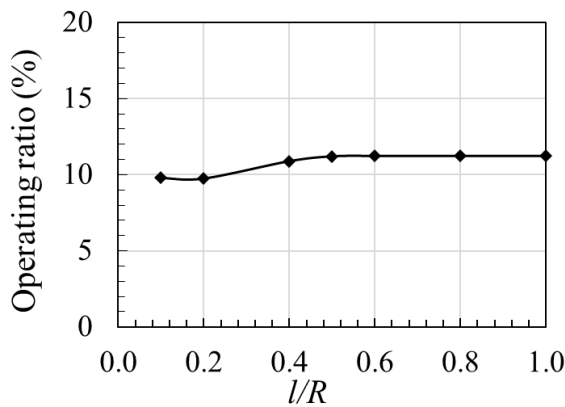
Figure 4.19: Effect of the score's length-to-disc radius (l/R) ratio

Table 4.6: Influence of l/R on response of DSMD

	l/R					
	0.2	0.4	0.5	0.6	0.8	1.0
P_b (MPa)	2.15	1.95	1.9	1.9	1.9	1.9
t_b (ms)	4.3	3.9	3.8	3.8	3.8	3.8
w_{max} (mm)	31.1	22.5	21.6	20.8	21.1	21.2
ε_{max}	0.34	0.32	0.31	0.31	0.32	0.33
$\dot{\varepsilon}_{max}$ (/s)	148	163	172	187	177	184

It is seen that P_b , t_b and w_{max} decrease gradually for l/R up to 0.5 beyond which these responses remain constant. The ε_{max} is almost constant within a variation of 0.025 for all values of l/R . The $\dot{\varepsilon}_{max}$ increases linearly from 120 /s to 200 /s for $0.1 \leq l/R \leq 0.6$ and afterwards it remains unchanged with any further increase in l/R . This study reveals that the responses of domed SMD are influenced with variation in l/R up to 0.5 only.

Operating parameters of DSMD with respect to l/R ratio is shown in Figure 4.20 (a-b). The operating ratio is slightly lesser for $l/R = 0.1$ and stabilized and remained maximum for $l/R > 0.5$ Impulse is most for minimum score length and stabilized and least for $l > 0.5$ indicating no score or minimum score length is good for storage application whereas score length more than half the radius of the disc is good for failure application.



a) Operating ratio with respect to the (l/R) ratio

b) Impulse with respect to the (l/R) ratio

Figure 4.20: Operating parameters with respect to the (l/R) ratio

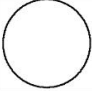


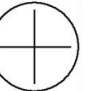

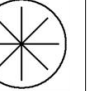
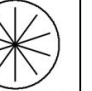
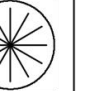
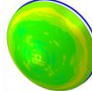

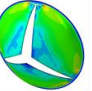
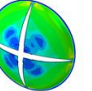


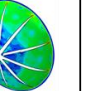
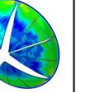
4.3.2.6 Score pattern, i.e. the number of scores (N)

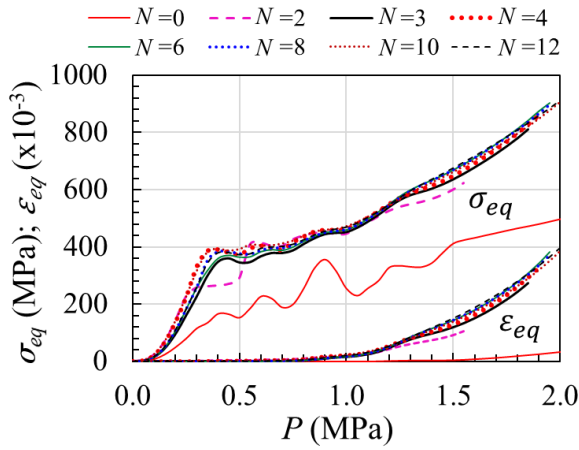
Scores provided in the disc act as regions of stress concentration in the domed metallic disc. Introduction of 2 scores across the diagonal of the disc reduced the burst pressure of the disc. As the number of scores N is increased further, it has minimal effect on the burst pressure and burst time. Failure propagation and failure pattern entirely depends on the pressure acting on petals after the initial burst. However, for this analysis the pressure is assumed to be acting continuously on the disc throughout the simulation which is causing failure propagation and petal separation. When $N = 12$, the failure is observed only along few scores which reveals that, as the number of scores increases, the failure may not be initiated and propagated in all the scores.

The effect of the number of scores on the domed SMD is analysed by varying the number of scores from 0 to 12, i.e. at $N = 0, 2, 3, 4, 6, 8, 10$ and 12. During this variation, the plate thickness ($t = 2$ mm), score's width ($b = 5$ mm), and score's depth ($t_1 = 0.8$ mm) are maintained constant. The predicted failure patterns with N ranging from 0 to 12 are shown in Table 4.7 just after the burst.

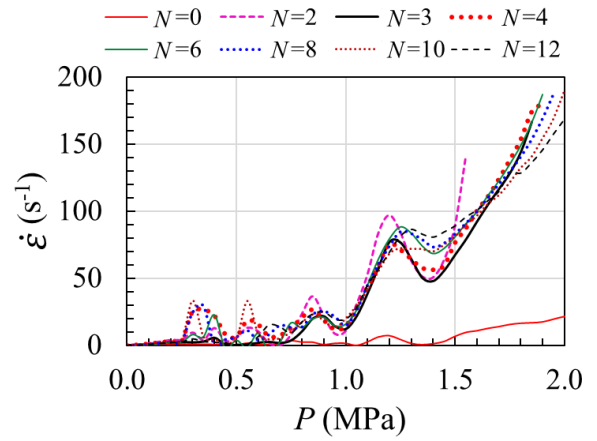
It shows that with $N = 2$, the petals are formed after the burst which need to undergo tearing at the fixed boundary before the petals can bend under the effect of increasing fluid pressure. Clear petal separation is observed for all domed SMD along the scores with $N = 3$ to 10 and they can bend freely at the fixed boundary after the petal separation upon increase in fluid pressure. When $N = 12$, only four scores experienced the failure limits and underwent petal separation along these scores and the remaining three scores in between the separated scores did not reach the failure limits and remained intact without any separation. This reveals that the number of scores that can be recommended to be employed in domed SMD can be from 3, 4, 6, 8 or 10 to achieve a clear separation and subsequent bending along the fixed boundary.

Table 4.7: Predicted failure pattern without and with number of scores in DSMD

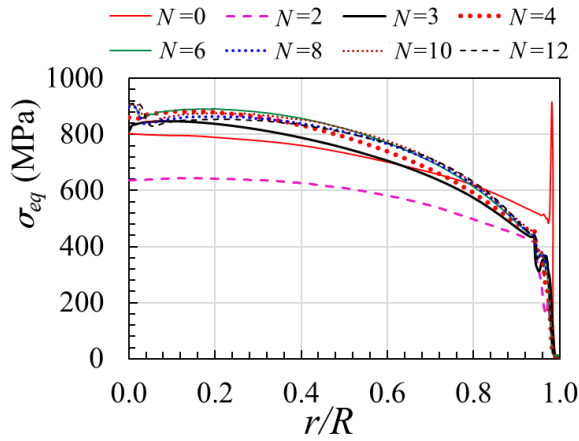
Number of scores	0	2	3	4	6	8	10	12
Schematic								
Predicted failure pattern								



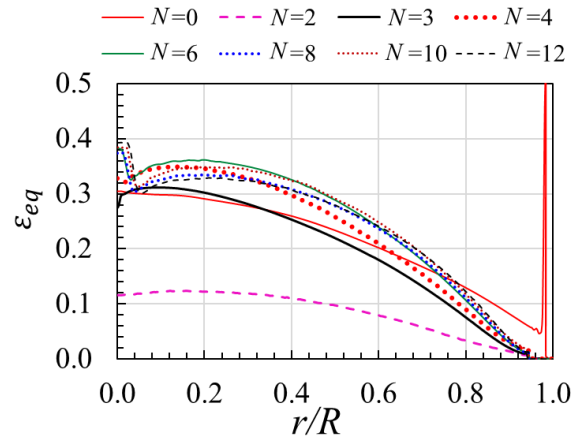
(a) Equivalent stress and strain with respect to the applied pressure



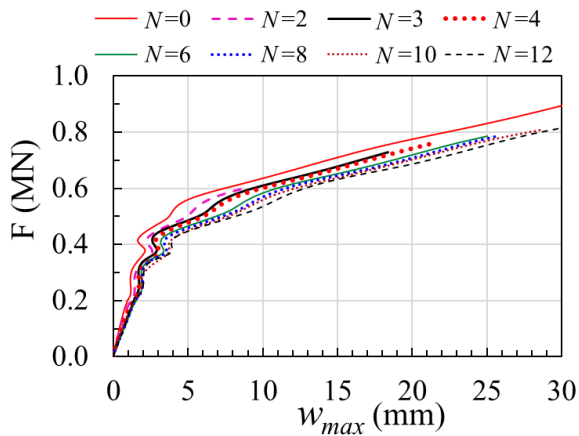
(b) Strain rate with respect to the applied pressure



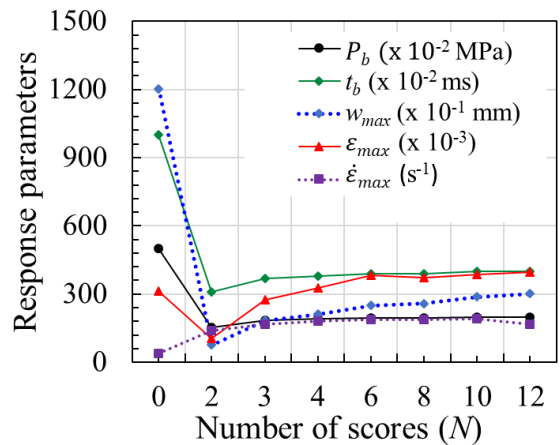
(c) Equivalent stress along the radius of the disc in the score



(d) Equivalent strain along the radius of the disc in the score



(e) Reaction force with respect to the central deflection



(f) Responses with respect to the number of scores

Figure 4.21: Effect of the number of scores

The behaviour of domed SMD with variations in number of scores as captured from simulations is shown in Figure 4.21(a-f). The variation of σ_{eq} , ε_{eq} and $\dot{\varepsilon}$ at the centre of the disc in score location with increase in applied pressure for different score pattern is shown in Figure 4.21 (a-b). These responses increase with the increase in N . Whilst the responses are almost closer for all variations in N , response for the domed SMD with $N = 0$ show a relatively lower magnitude. The equivalent stress and equivalent plastic strain increase with the increase in N from 2 to 12. In all cases, the responses for $N = 4, 6$ and 8 resulted in almost same results. The variation of σ_{eq} and ε_{eq} along the score before the burst for different score pattern is shown in Figure 4.21 (c-d). Both these responses are higher at the centre of the disc and gradually decrease with the increase in the radius of the disc and follow a similar pattern. The σ_{eq} increase with the increase in N from 2 to 12. While the increase in the maximum σ_{eq} is negligibly small for $N = 3$ to 12, this increase is significant from $N = 2$ to 3. Only for the disc without score, *i.e.* $N = 0$, the induced σ_{eq} and ε_{eq} at the fixed boundary instantaneously peak up to their maximum values. This is due to the fact that there are no stress concentrations introduced by design in geometry with $N = 0$, the fixed region at the boundary experiences the maximum equivalent stress and the failure initiates at this boundary region upon further increase in the pressure loading. When there are no scores, the plastic hinges are generated only at the fixed region from where the failure initiates.

The reaction force, F at the fixed boundary with respect to the central deflection is shown in Figure 4.21(e) for different values of N . It is noticed that both the maximum F and the w_{max} increase with the increase in N from 2 to 12. This increase is considerable with increase in N from 2 to 3, 3 to 4 and 4 to 6. On the other hand, the variation of F with respect to w_{max} for $N = 6, 8, 10$ and 12 result in almost the same behaviour and is insignificant. After the initial 10% of w_{max} , the stiffness of the domed SMD decreases with the increase in N , although this decrease in stiffness is marginal. The metallic disc with $N = 2$ fails with very minimum central deflection which is less than 40% of the maximum deflection experienced by the disc with $N = 3$. The disc with $N = 0$ exhibits maximum central deflection and maximum reaction force which are significantly higher compared to the metallic discs having scores and their maximum values are higher by four times and two times respectively, as compared to the scored discs.

The summary of maximum values of all responses such as P_b , t_b , w_{max} , ε_{max} and $\dot{\varepsilon}_{max}$ with increase in N is shown in Figure 4.21(f) and given in Table 4.8. It can be observed that the P_b , t_b , and $\dot{\varepsilon}_{max}$ are almost invariant after $N = 3$. The w_{max} and ε_{max} increase gradually with the increase in N from 2 to 6 and they remained almost constant with any further increase in N from 6 to 12. All these responses except the $\dot{\varepsilon}_{max}$ decrease significantly with the increase in N from 0 to 2. All responses remained almost the same and exhibited insensitivity for $N > 6$. Based on this study, it can be concluded that the recommended number of scores in the domed SMD can be from 3 to 6. Selection of a particular number of scores between 3 and 6 is to be decided based on the operational requirements and the manufacturing considerations.

Table 4.8: Influence of number of scores on response of DSMD

	Number of scores							
	0	2	3	4	6	8	10	12
P_b (MPa)	5.00	1.55	1.85	1.90	1.95	1.95	2.00	2.00
t_b (ms)	10.0	3.1	3.7	3.8	3.9	3.9	4.0	4.0
w_{max} (mm)	120	7.6	18.4	21.2	25.0	25.9	28.8	30.2
ε_{max}	0.31	0.1	0.27	0.34	0.38	0.37	0.39	0.4
$\dot{\varepsilon}_{max}$ (/s)	40	140	167	180	187	187	190	169

Operating parameters of DSMD with respect to number of scores is shown in Figure 4.22 (a-b). Operating ratio is slightly least at 7% when $N = 0$. Addition of 2 scores increased the operating ratio and maximum when $N = 3$ and then stabilized after $N > 4$. Impulse is most for plain disc minimum for any number of scores indicating plain disc is good for storage application and introduction of scores makes it suitable for failure application.

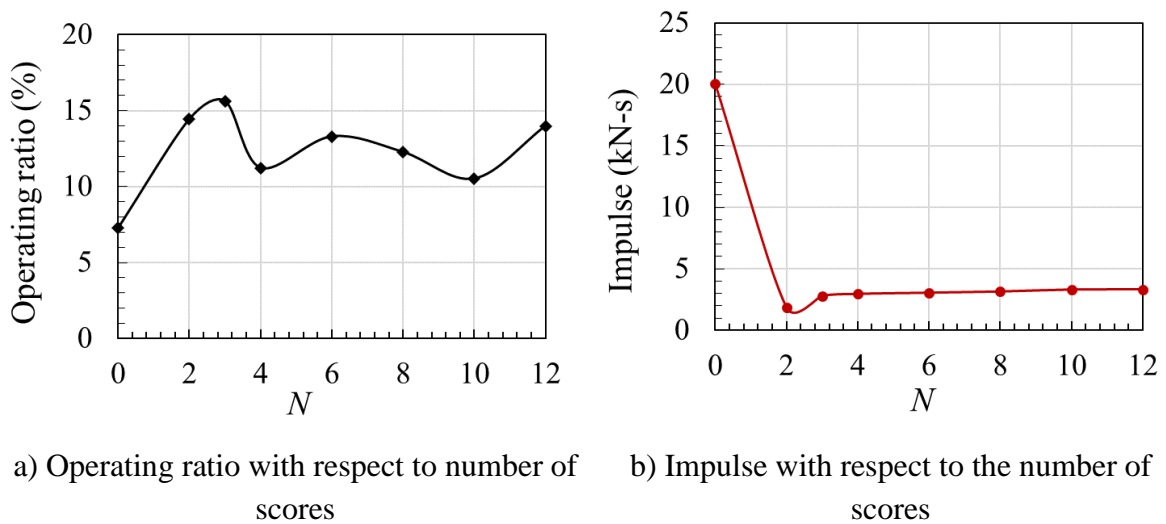
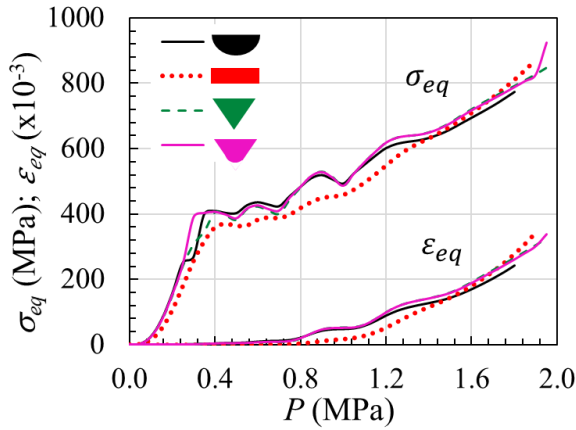


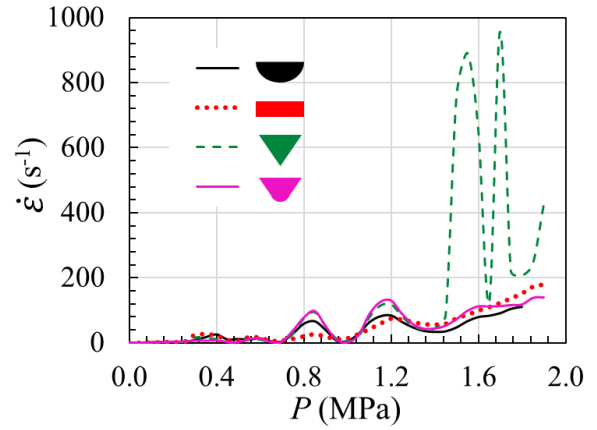
Figure 4.22: Operating parameters with respect to the number of scores

4.4.2.7 Score geometry

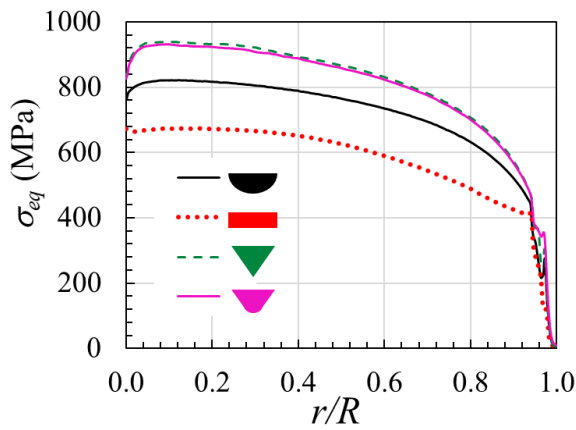
In all the previous studies thus discussed, a rectangular score geometry is considered. The score geometry can be with semi-circular, rectangular, triangular or triangular with filleted tip in cross sections and they are analysed here in order to understand their influence on the deformation and rupture in the domed SMD. In all investigations with geometric variations in score, constant dimensions are maintained for the plate thickness ($t = 2.0$ mm), score's width ($b = 5.0$ mm) and score's depth ($t_1 = 0.8$ mm).



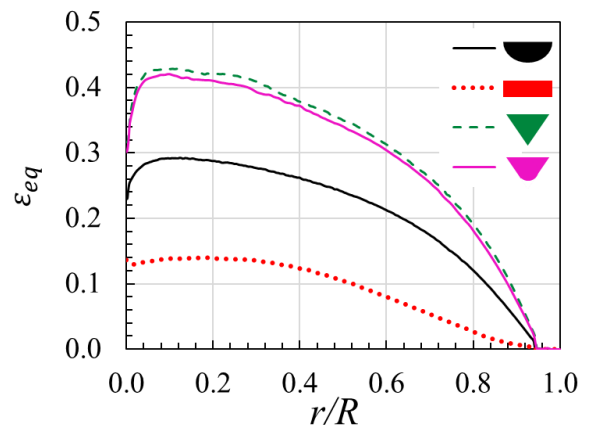
(a) Equivalent stress and strain with respect to applied pressure



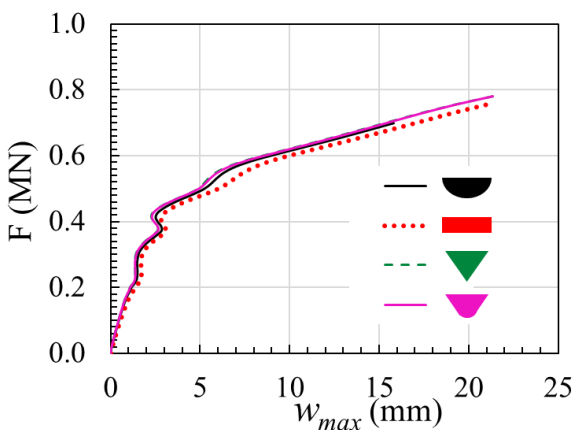
(b) Strain rate with respect to the applied pressure



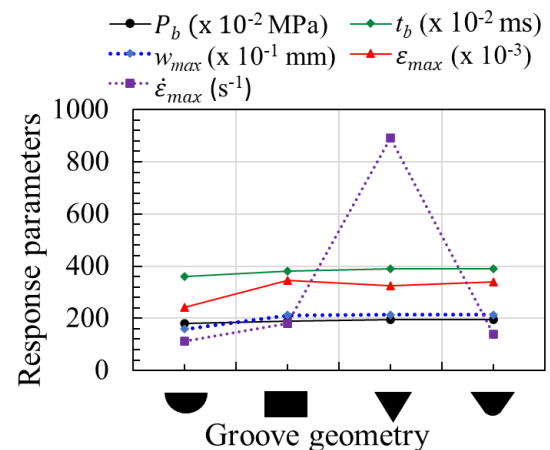
(c) Equivalent stress at the score along the radius of the disc



(d) Equivalent strain at the score along the radius of the disc



(e) Reaction force with respect to the central deflection







(f) Responses with respect to the geometry of scores

Figure 4.23: Effect of the score geometry

The variation of σ_{eq} , ε_{eq} and $\dot{\varepsilon}$ at the centre of the disc in score location with increase in applied pressure for different cross-section of the score geometry is shown in Figure 4.23(a-b). These responses increase with the increase in applied pressure loading. The maximum σ_{eq} and ε_{eq} experienced by the domed SMD are relatively less for the semi-circular cross-section whereas they are almost the same for the rectangular and triangular cross-sections. This is due to appearance of high stress triaxiality at sharp edges within the rectangular and triangular scores. Their variations during loading are almost the same for the semi-circular and triangular cross-sections as compared relatively to the rectangular score geometry as seen in Figure 4.23(a). Even the $\dot{\varepsilon}_{max}$ in the score's semi-circular geometry is smaller as compared to the rectangular score geometry. But the triangular score geometry resulted in strain rate oscillations just before the burst due to extreme strain localization and instantaneous deformation before the burst as seen in Figure 4.23(b).

The variation of σ_{eq} and ε_{eq} along the score at an instant just before the burst for different cross-section of score geometry is shown in Figure 4.23(c-d). Both these responses are higher at close to the centre of the disc and gradually decrease with increase in the radius of the disc and follow a similar pattern. Both the σ_{eq} and ε_{eq} along the score are smaller for the rectangular score cross-section, relatively higher for the semi-circular score geometry and highest for the triangular score geometry. Triangular score geometry resulted in almost same response as that of the similar geometry with filleted tip. With respect to the rectangular score cross-section, the maximum σ_{eq} along the score increases by about 20% and the maximum ε_{eq} increases by about 115%, for the semicircular score geometry. The triangular score geometry exhibits an additional σ_{eq} of around 200 MPa and almost triple the maximum ε_{eq} as compared to the rectangular score geometry. The reaction force, F at the fixed boundary with respect to w_{max} is shown in Figure 4.23(e) for different cross-sections of the score. It is noticed that the reaction force increases with the increase in the central deflection irrespective of the type of score's geometry, and their variations are almost close. The maximum F and w_{max} , *i.e.* the maximum failure energy is achieved for the rectangular and triangular score cross-sections and are almost the same. Comparably, the semi-circular score geometry exhibits about 30% less w_{max} and 12.5% less maximum F just before the burst.

Table 4.9: Influence of score geometrical features on response of DSMD

	Geometry			
				
P_b (MPa)	1.8	1.9	1.95	1.95
t_b (ms)	3.6	3.8	3.9	3.9
w_{max} (mm)	15.8	21.2	21.3	21.3
ε_{max}	0.24	0.34	0.33	0.34
$\dot{\varepsilon}_{max}$ (/s)	112	180	890	139

The summary of maximum values of all responses such as P_b , t_b , w_{max} , ε_{max} and $\dot{\varepsilon}_{max}$ for the semi-circular, rectangular, triangular and triangular with filleted tip score geometries is shown in Figure 4.23(f) and given in Table 4.9.

All these response parameters are relatively and marginally less for the semi-circular score cross-section among the four score geometries. Except a higher value of maximum plastic strain rate for the triangular score geometry, all the other response parameters are almost the same for the four score cross-sections studied. Based on this study, the score geometry with rectangular cross-section is preferable considering the relatively lower magnitude of σ_{eq} and ε_{eq} before failure along the score, manufacturing easiness and dimensional control.

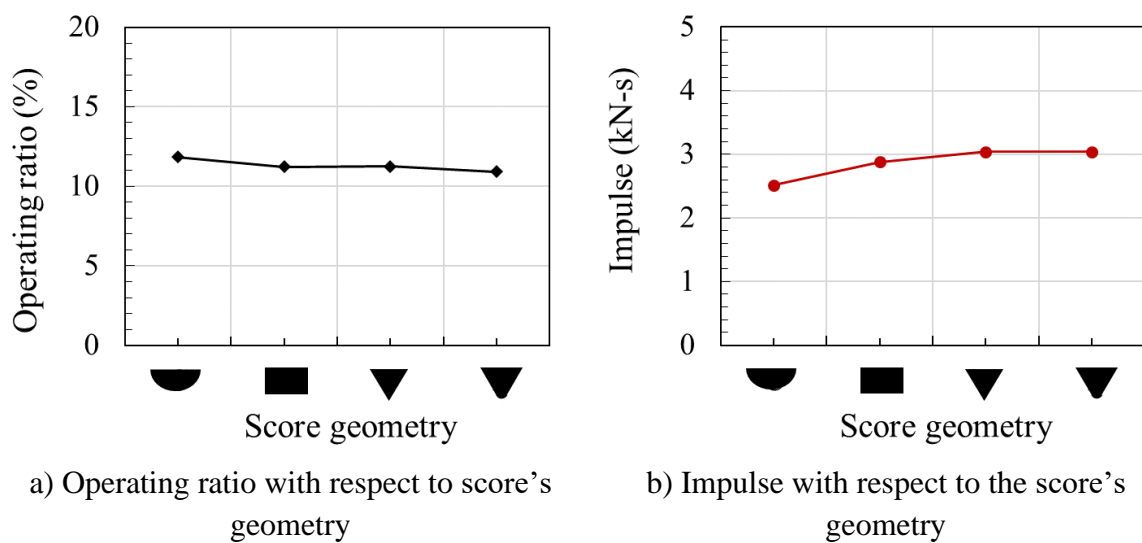


Figure 4.24: Operating parameters with respect to the score's geometry

Operating parameters of DSMD with respect to score's geometry is shown in Figure 4.24 (a-b). Operating ratio is almost same for all types of score's geometries although it is slightly higher for circular cross section. Impulse less for circular disc and increased for other score geometries indicating circular cross section is good for failure application although its effect is not significant. Any cross section is good for current application.

4.4.3 Results and discussions

The numerical analyses and investigations demonstrated a strong influence of geometrical parameters of the domed-scored metallic disc on the deformation, failure and rupture behaviour when subjected to a pressure loading at a given loading rate. The influence of various geometrical features such as i) D/t ratio, ii) H/D ratio, iii) t_1/t ratio, iv) b/t ratio, v) l/R ratio, vi) score pattern, *i.e.* the number of scores (N), and vii) score's geometric cross-section, are thoroughly examined. Consolidated list of various response parameters *viz.* P_b , t_b , w_{max} , ε_{max} and $\dot{\varepsilon}_{max}$ experienced at the centre of the disc at the time of burst are presented in Tables 4.2 to 4.9.

4.4.3.1 Effect of loading rate

The burst pressure increased and burst time decreased with increase in loading rate and remained almost constant beyond $\dot{P} \geq 100$ MPa/s. Central deflection and plastic strain increased up to $\dot{P} = 25$ MPa/s, later reduced and stabilized after loading rate beyond 100 MPa/s while strain rate increased with increase in loading rate. There exists a threshold of loading rate (100 MPa/s in the present case) where rupture disc is insensitive to the increase in loading rates. This is due to the rapid loading rate inducing stress waves in the disc that exceed the limiting plastic stress wave in the material.

Burst pressure increases and burst time reduces with increase in loading rate. At higher loading rates, there is a marginal variation in operating ratio and reduction in the generated impulse indicating that higher loading rates are preferable.

4.4.3.2 Effect of D/t ratio

The burst pressure and burst time decrease exponentially as diameter-to-plate thickness ratio D/t is increased from 50 to 250, beyond which these two responses are almost constant while the central deflection and strain rate increase linearly, as seen in Figure 4.10(f). The required P_b and t_b can be chosen within D/t of 250. The domed SMD with $D/t < 100$ exhibit high stiffness, thereby requiring high P_b and t_b . This disc fails at lowest plastic strain at score which allows more global deformation before burst.

Higher D/t i.e. low sheet thickness (for a given diameter) is preferable to achieve low burst pressure and low impulse during burst. Operating ratio reduces marginally with reduction in sheet thickness indicating lower sheet thickness is preferable.

4.4.3.3 Effect of H/D ratio

As dome height-to-plate diameter H/D ratio is increased from 0.05 to 0.3, the behaviour of the domed SMD approaches to a spherical dome, where the burst pressure, burst time and central deflection are stabilized, as observed in Figure 4.12(f). This implies that more energy is required to burst the scored disc when H/D is more than 0.3. While this will provide a higher safety margin for the container in static storage condition, this may not be a recommended choice for the rupture disc application in motor containers because it needs more failure energy and burst pressure. Higher the burst pressure, higher will be the loss of active thrust generated by the motor placed inside the container.

Low H/D ratio is preferable to achieve low burst pressure and low impulse and high H/D ratio is preferable to achieve high operating ratio. Dome height less than 10 % of disc diameter is preferable choice to achieve low burst pressure and high operating ratio.

4.4.3.4 Effect of t_1/t ratio

As the score's depth-to-plate thickness ratio t_1/t is increased from 0.1 to 0.5, the burst pressure, burst time and the central deflection are gradually reduced to minimum values, as shown in Figure 4.14, indicating that the failure of the domed SMD is dependent on the remaining available plate thickness at the score region. For $t_1/t > 0.5$, less variation in response parameters is observed which indicates that the score's depth, equivalent to half the plate thickness is an optimum value. However, the static capacity of the domed SMD under a constant storage pressure in motor container needs to be considered additionally to achieve safety factors before deciding upon the score depth beyond $t_1/t = 0.5$. Further, it can be observed that the deformation and failure of the SMD is going to be very much instantaneous with very minimum central deflection for $t_1/t \geq 0.5$. It may introduce higher levels of reverse shock loading in the motor container. Almost all response parameters in SMD are sensitive up to $t_1/t < 0.5$. Therefore, $t_1/t > 0.5$ is the most desirable ratio based on the present investigations.

Score depth closer to 50% sheet thickness is preferable to achieve low burst pressure and optimum values of operating ratio and generated impulse and can be selected based on static strength requirement of disc.

4.4.3.5 Effect of b/t ratio

As the score's width-to-plate thickness ratio b/t is increased from 1.5 to 3.5, no significant change is observed in the predicted response parameters in the domed SMD as seen in Figure 4.17(f), which once again confirms the importance of plate thickness at the score region.

Burst pressure, operating ratio and generated impulse release during burst are unaffected due to variation in b/t ratio indicating, score width, b , can be selected based on manufacturing suitability.

4.4.3.6 Effect of l/R ratio

When the ratio of length of the score-to-maximum disc radius, *i.e.* l/R is more than 0.4, all response parameters achieve a stabilized value, as observed in Figure 4.19(f) which means that the variable parameters of a scored metallic rupture disc can be varied only when the length of the score is less than 40% of the disc's radius.

*Score length has less effect on burst pressure, operating ratio and generated impulse at higher loading rates when score length is less than 40% of disc radius. However, it effects the crack propagation. So, maximum possible score length *i.e.* score length up to full radius of disc is preferable choice.*

4.4.3.7 Effect of number of scores, N

For the plain, *i.e.* the domed metallic disc without any score, a maximum burst pressure of 5 MPa is predicted as seen in Table 4.8 and in Figure 4.21(f) and the failure is observed at intersection of the flat and domed region of the disc, *i.e.* at the fixed curved boundary. However, when two scores are introduced, the failure is initiated at the centre of the disc and propagated along the score up to the flat portion of the disc towards the fixed boundary. Further increase in the number of scores resulted in same failure phenomena as observed in Table 4.7. Even though a minimum burst pressure is observed with 2 score configuration, the energy required will be high for further opening out the petals for an obstruction free operation of the motor and it results in minimum opening for the plume to escape the motor container in which both are undesirable. Increase in the number of scores more than 12 also does not necessarily results in failure initiation and propagation through all the scores which can be observed with 12 score geometry where failure propagated through only 4 scores leaving the remaining 8 scores unseparated. This reveals that the number of scores that can be recommended in domed SMD can be 3, 4, 6, 8 or 10 to achieve a clear separation as seen in Table 4.7 and subsequent bending along the fixed boundary. But the predicted responses remained almost constant with any increase in number of scores N from 6 to 12 as observed in Figure 4.21(f).

Marginal variation of burst pressure, operating ratio and generated impulse are observed for $N \geq 3$ indicating that number of scores that can be opted in the domed SMD can be from 3 to 6. But, the selection of a particular number of scores between 3 and 6 is to be decided based on the 1) resulting safety factor under storage pressure in motor container, 2) the required symmetry in the opening of the petals, and 3) the manufacturing economy.

4.4.3.8 Effect of score geometry

Influence of the score geometry on the deformation and failure behaviour of the domed SMD is studied with four different cross-sectional geometries for the score such as semi-circular, rectangular, triangular and triangular with filleted tip, as shown in Figure 4.23. All response parameters are almost the same for the four score cross-sections investigated as seen in Figure 4.23(f).

Score geometry has less effect on the burst characteristics of the disc at higher loading rates. Score geometry can be selected based on manufacturing easiness. The rectangular, triangular with filleted tip and semi-circular score geometries are preferable as they experience relatively less magnitude of equivalent stress and plastic strain before failure along the score. However, semi-circular cross-section proves to be difficult in control of dimensional tolerances during manufacturing, filleted triangular cross section requires separate cold or

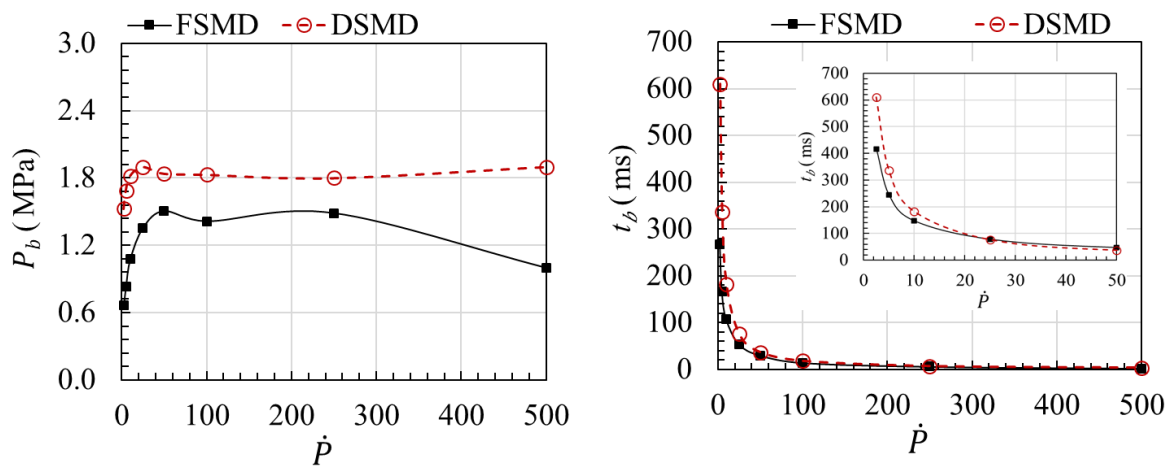
hot-pressing operation with punch and die setup for manufacturing and hence, rectangular cross section can be a preferable choice of score geometry.

4.5 Comparison on behaviour of FSMD and DSMD

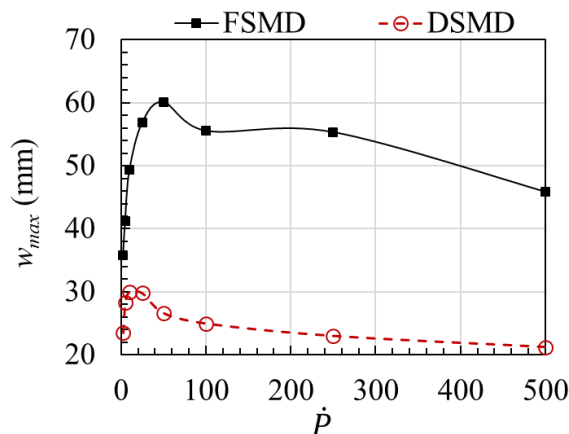
The behaviour of FSMD, as shown in Figure 3.8 and DSMD, as shown in Figure 4.2, are compared with respect to the parameters like i) loading rate (\dot{P}), ii) D/t ratio, iii) t_1/t ratio, iv) b/t ratio, v) l/R ratio, vi) score pattern, *i.e.* the number of scores (N), and vii) score's geometric cross-section in order to understand the difference in their behaviours.

4.5.1 Effect of loading rate (\dot{P})

Comparison of burst pressure, burst time, central deflection and operating ratio of flat scored metallic disc and domed scored metallic disc are shown in Figure 4.25(a-c).



a) Burst pressure with respect to the loading rate b) Burst time with respect to the loading rate



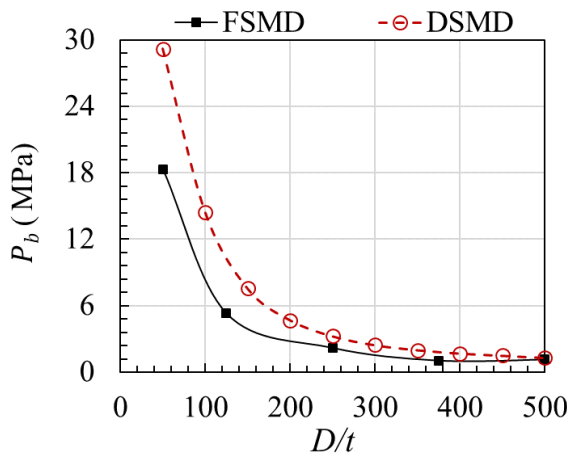
c) Central deflection with respect to the loading rate

Figure 4.25: Comparison of FSMD and DSMD with respect to the loading rate

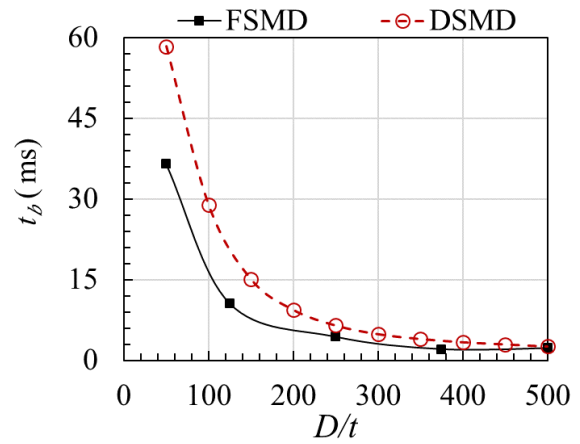
In both FSMD and DSMD, the burst pressure of discs increased sharply up to a certain threshold of loading rate and it remained almost the same, as shown in Figure 4.25(a). Domed disc exhibited more resistance to failure compared to the flat disc. Burst time for both discs reduced sharply with increase in loading rate up to 100 MPa/s and it remained almost constant above this value, as shown in Figure 4.25(b). Flat discs failed quickly compared to domed discs for given loading rate. Flat discs deformed more before failure than domed discs, as shown in Figure 4.25(c).

4.5.2 Effect of D/t ratio

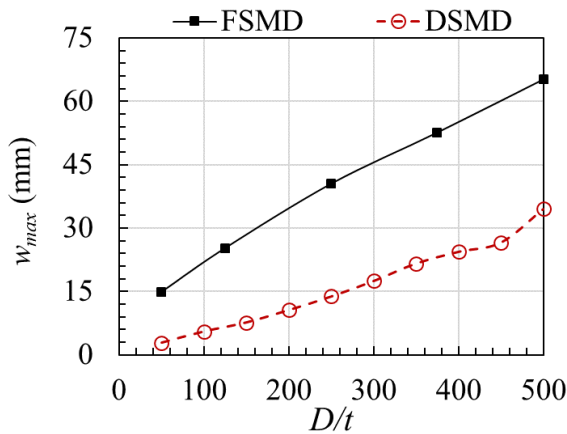
Comparison between FSMD and DSMD due to the variation in D/t ratio is shown in Figure 4.26(a-c).



a) Burst pressure with respect to the (D/t) ratio



b) Burst time with respect to the (D/t) ratio



c) Central deflection with respect to the (D/t) ratio

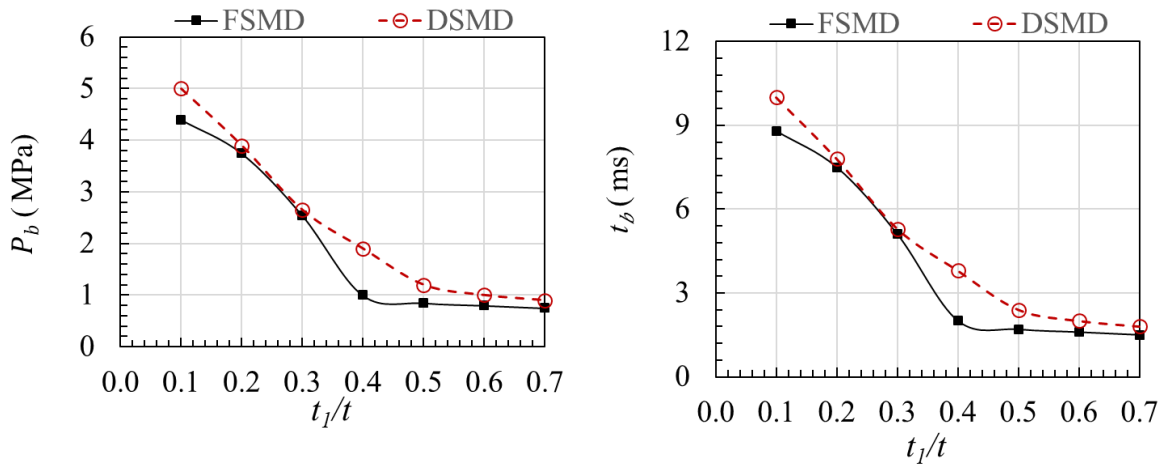
Figure 4.26: Comparison of FSMD and DSMD with respect to the (D/t) ratio

For same D/t ratio, domed disc exhibits more burst pressure and burst time than flat discs. In both types of discs, burst pressure and burst time reduced exponentially with increase in

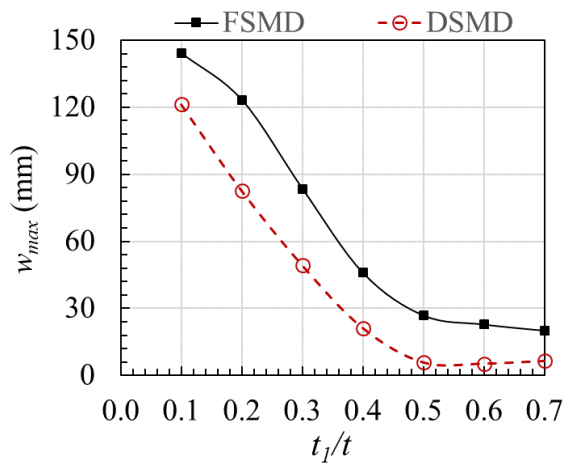
diameter of the disc for same sheet thickness, as shown in Figure 4.26 (a-b). FSMD deformed more at the centre compared to DSMD for a given diameter of the disc and in both cases, central deflection increased with increase in the discs diameter, as shown in Figure 4.26 (c).

4.5.3 Effect of t_1/t ratio

Comparison between FSMD and DSMD due to the variation in t_1/t ratio is shown in Figure 4.27 (a-c).



a) Burst pressure with respect to the (t_1/t) ratio b) Burst time with respect to the (t_1/t) ratio



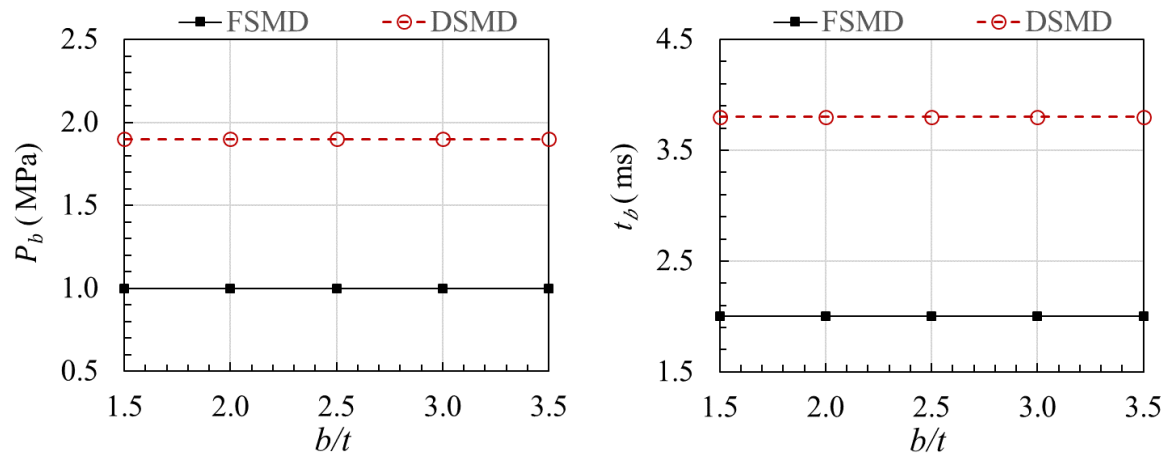
c) Central deflection with respect to the (t_1/t) ratio

Figure 4.27: Comparison of FSMD and DSMD with respect to the (t_1/t) ratio

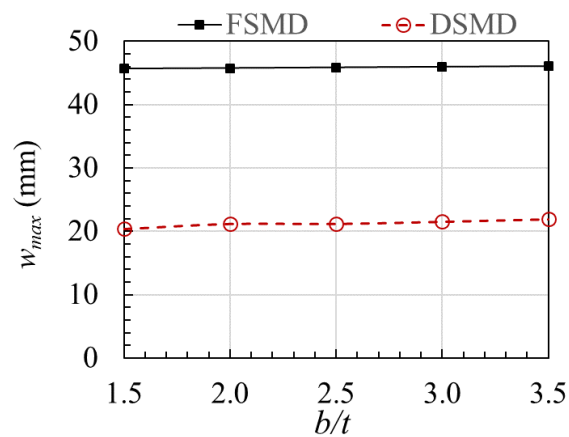
Comparison of burst pressure and burst time between FSMD and DSMD for the same t_1/t ratio, is shown in Figure 4.27 (a-b). The difference between central deflection is almost same between both FSMD and DSMD for a given score depth, as shown in Figure 4.27 (c) and it gradually reduced with increase in score depth. As the score depth is more than half of sheet thickness, all parameters remained constant in both cases.

4.5.4 Effect of b/t ratio

Comparison between FSMD and DSMD due to the variation in b/t ratio is shown in Figure 4.28 (a-c).



a) Burst pressure with respect to the (b/t) ratio b) Burst time with respect to the (b/t) ratio



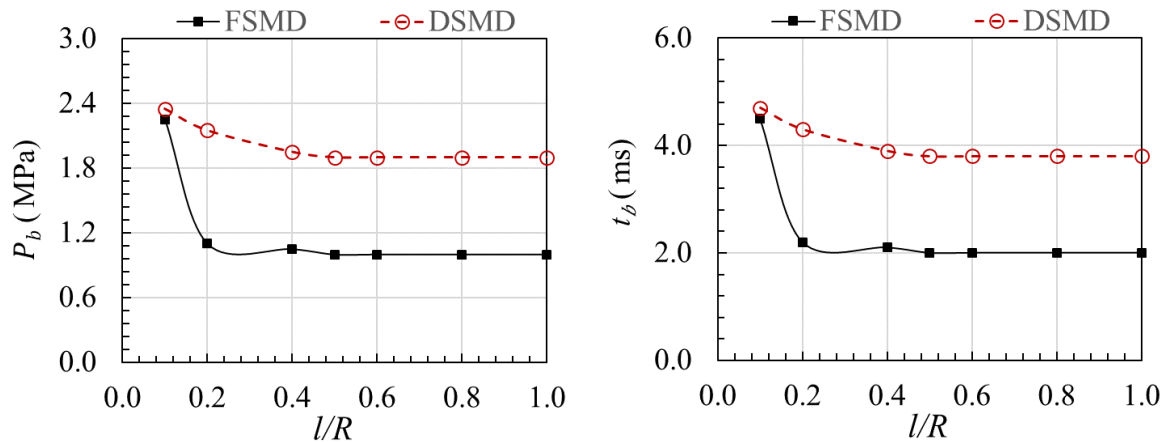
c) Central deflection with respect to the (b/t) ratio

Figure 4.28: Comparison of FSMD and DSMD with respect to the (b/t) ratio

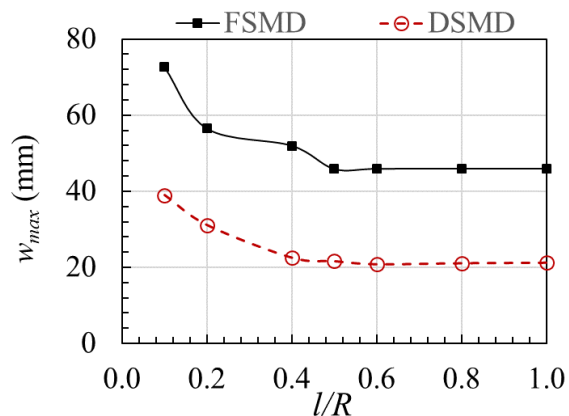
The parameters remained almost constant in both types of the discs irrespective of score width. FSMD exhibited less burst pressure, burst time and more central deflection for a given score width.

4.5.5 Effect of l/R ratio

Comparison between FSMD and DSMD due to the variation in l/R ratio is shown in Figure 4.29(a-c).



a) Burst pressure with respect to the (l/R) ratio b) Burst time with respect to the (l/R) ratio



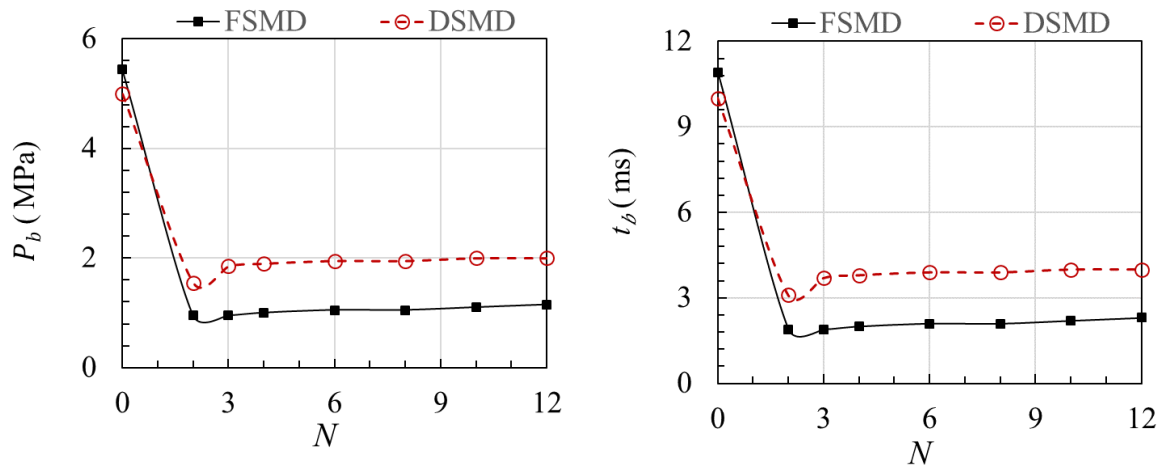
c) Central deflection with respect to the (l/R) ratio

Figure 4.29: Comparison of FSMD and DSMD with respect to the (l/R) ratio

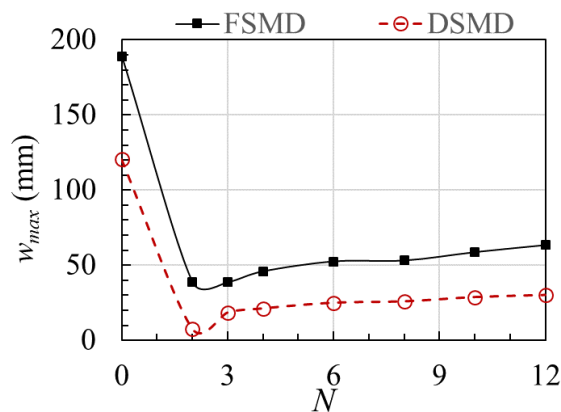
From the comparison of burst pressure and burst time, as shown in Figure 4.29 (a-b), they are almost same when l/R is 0.1. The difference is increased for $l/R > 0.1$ and almost remained same. From Figure 4.29 (c), central deflection of flat disc is more than the domed disc and, in both cases, it remained same for $l/R > 0.6$.

4.5.6 Effect of number of scores (N)

Comparison between FSMD and DSMD due to the variation in number of scores is shown in Figure 4.30(a-c).



a) Burst pressure with respect to the number of scores b) Burst time with respect to the number of scores



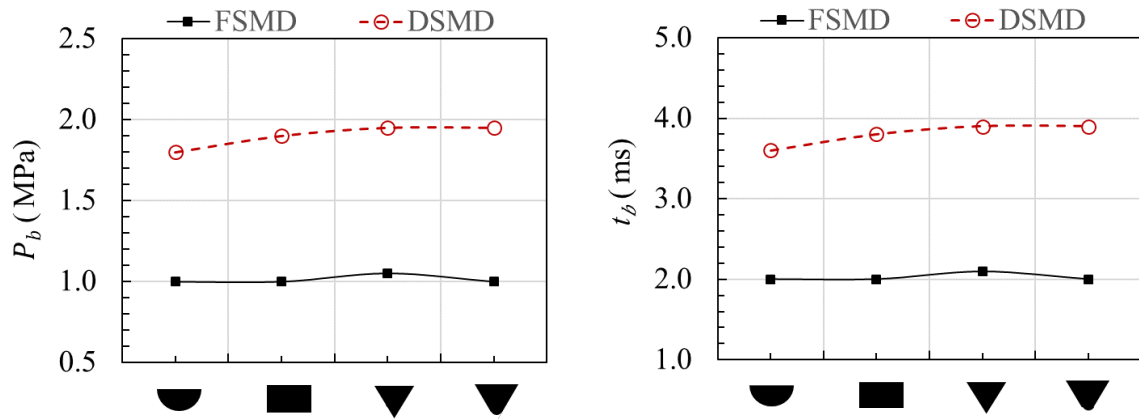
c) Central deflection with respect to the number of scores

Figure 4.30: Comparison of FSMD and DSMD with respect to the number of scores

For plain disc, *i.e.* no scores, FSMD has higher burst pressure and burst time than DSMD. As the scores are introduced, both burst pressure and burst time reduced significantly, as shown in Figure 4.30(a-b). Central deflection is higher in FSMD compared to DSMD, as shown in Figure 4.30(c).

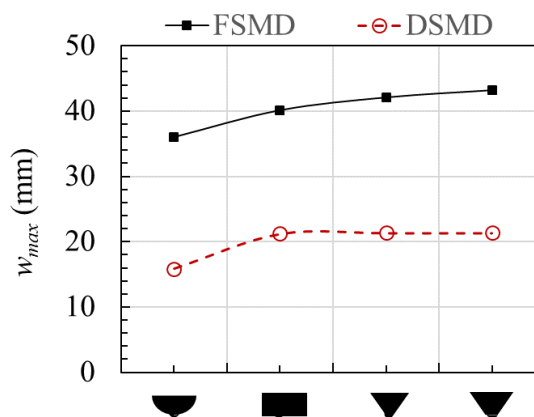
4.5.7 Effect of score's geometry

Comparison between FSMD and DSMD due to the variation in score's geometry is shown in Figure 4.31(a-c).



a) Burst pressure with respect to the score's geometry

b) Burst time with respect to the score's geometry



c) Central deflection with respect to the score's geometry

Figure 4.31: Comparison of FSMD and DSMD with respect to the score's geometry

As shown in Figure 4.31(a-b), burst pressure and burst time for FSMDs are lesser than DSMDs but almost remained same for all geometries. The central deflection for semi-circular cross section is lesser than other cross sections for both FSMD and DSMD, as shown in Figure 4.31 (c).

4.6 Preliminary DSMD configuration

Based on the studies, the proposed geometry of the DSMD for given in Figure 4.32. It is proposed to be made from *E250 structural steel* which is available in Indian market and is closely equivalent to S235 JR structural steel. Score depth is increased from 0.8 mm to 1.4 mm based on i) static strength requirement of having a factor of safety of more than 1 and ii) considering the manufacturing difficulty in producing more than 1.4 mm score depth on domed surface.

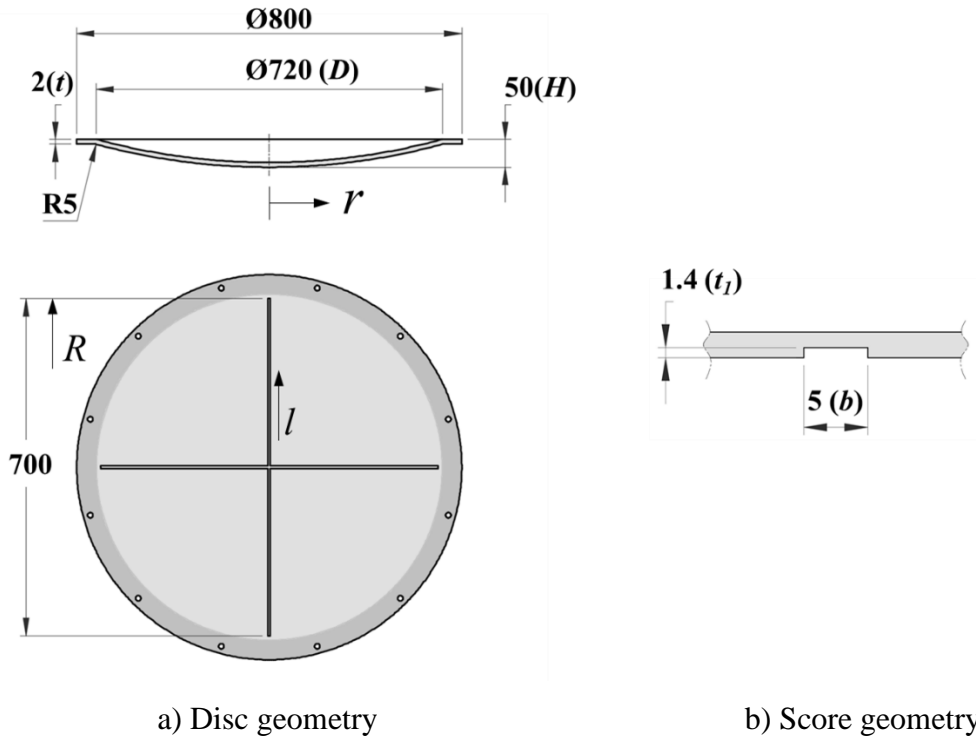


Figure 4.32: Proposed preliminary disc configuration

4.7 Summary

This chapter has presented the large deformation and failure behaviour of a domed thin scored metallic disc for application at the bottom of a pressurised motor container where it withstands a constant internal pressure during storage, and rupture instantaneously upon generation of an internal impulsive pressure loading. Based on the numerical simulation methodology and material parameters from previous chapter, the behaviour of a domed-scored thin metallic disc was numerically investigated for the storage and failure loadings in a motor container. Two critical parameters Operating ratio and Impulse transmitted were defined. The effect of loading rates (2.5-500 MPa/s), diameter-to-plate thickness ratio (50-500), dome height-to-plate diameter ratio (0.01-0.5), score's depth-to-plate thickness ratio (0.3-0.7), score's width-to-plate thickness ratio (1.5-3.5), score's length-to-plate radius ratio (0.1-1.0), score pattern (with number of scores from 0 to 12), and score geometry (semi-circular, rectangular, triangular and triangular with filleted tip) were investigated.

Manufacturing of Domed Metallic Disc

5.1 Introduction

Metallic sheets are subjected to several hot and cold forming processes to manufacture desired geometry and shape. Thin metallic sheets in the form of discs are used for making domed geometries such as forward or reverse domed rupture discs, dish antennae, etc. Typically, they are manufactured through the press (*i.e.* punch) and die. They can also be manufactured through hydro-forming or explosive-forming processes [70-72]. The adaptability of a given manufacturing process depends on the accuracy achieved in the final formed geometry, manufacturing cost, easiness in developing the manufacturing setup and repeatability in the final formed disc. Several products require the formation of domes from initially flat thin metallic discs. Among all manufacturing techniques, the hydro-forming process helps to form a desired dome shape with relatively less manufacturing setup and controllable process parameters.

Hydro-forming is a forming process in which a pressurised hydraulic medium is used to deform a work piece beyond the elastic limit against a die or into an open space to form the desired shape [70]. Hydro-forming has many advantages over the conventional deep drawing, such as higher drawing ratio, dimensional accuracy, surface quality and less spring back. Determination of correct process parameters, such as pressure in the pot and blank holding force concerning the deformation of the blank, determines the successful hydro-forming process without experiencing any defects such as wrinkles and cracks. The numerical simulations help estimate the optimum loading path for pressure in the pot and the blank holding force [70-73]. The hydro-forming provides greater scope for nonsymmetrical components and has been proposed as a good candidate for the production of complex stampings in the automotive industry, offering fewer difficulties with rigid tools [74-85].

Before starting to experiment with the hydro-forming process, resorting to numerical simulations to arrive at process parameters helps to study the feasibility of achieving the required dome geometry, variations, if any, observed in the thickness of the metallic disc, the magnitude of hydraulic pressure, etc. This numerical simulation can be conducted through non-linear finite element analysis (FEA) using implicit or explicit methods. Hydro-forming the thin metallic disc can be completed in less than a few seconds under pressure loading. The explicit method gives the advantage of capturing the variations in the deforming metallic disc under the action of hydraulic pressure in a short duration, *i.e.* in a few seconds, as it adopts a direct solver [43]. But the minimum size of the elements in the finite element model depends on the time the stress wave travels through the element. However, if the loading duration is more, then implicit methods give proper results.

Several researchers [75-85] have attempted to simulate the manufacturing process of hydro-forming operation numerically. Cherouat *et al.* [75] presented a numerical methodology to improve the 3D thin sheet hydro-forming processes based on elastoplastic constitutive equations accounting for non-linear anisotropic hardening. They identified the material parameters from the global measure of sheet displacement, thickness evolution and internal pressure expansion. Parsa *et al.* [76] investigated alternate methods to the conventional manufacturing processes for a three-piece shell fender of an automobile by one piece, based on a sheet hydro-forming process. They proposed two possible manufacturing procedures, *viz.* pure stretching and draw-in and evaluated them numerically. Their results demonstrated the superiority of the draw-in procedure.

Although significant research has been conducted on the hydro-forming of sheet metals, their studies are focused on varied and specific applications. The observations from each study are unique, although the procedures may have commonality. The loading rate decides the forming speed and, thereby, the time involved in the hydro-forming operation.

5.2 Hydro-forming of GS (galvanised steel) disc

To prove the FE simulation and manufacturing methodology, first, the hydro-forming of a flat thin metallic GS disc is designed and manufactured to achieve a forward domed disc, as shown in Figure 5.1, which will be subsequently adopted to manufacture a rupture disc. A higher thick sheet with less diameter requires more hydro-forming pressure. Due to the unavailability of sheet thickness less than 2 mm in E250 material, GS sheet is used. The tensile tests are conducted to determine the full range stress-strain behaviour of the adopted galvanised steel sheet. This constitutive data is used in the numerical simulations.

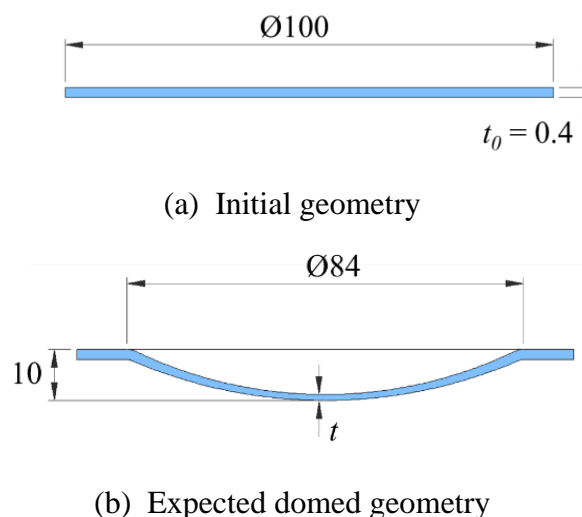


Figure 5.1: Thin flat metallic GS disc before and after hydro-forming

The plastic deformation induced by the hydraulic energy is simulated through an incremental isotropic hardening plasticity model using a non-linear explicit finite element analysis. The variation of central deformation, thickness, equivalent plastic stress and equivalent plastic strain in the metallic disc with respect to the applied hydraulic pressure is numerically

determined. The hydro-forming setup is then designed and manufactured, and the metallic disc has experimented with under the hydro-forming process. The reduction in thickness due to the stretching of the thin steel disc is evaluated from experiments and simulations. This study helped finalise the hydraulic pressure, feasibility and accuracy of practically achieving the desired geometry of the metallic disc. The material property evaluation, numerical modelling and analysis, design and development of hydro-forming die assembly setup and metallic discs, the hydro-forming experiments and discussion of results are presented in subsequent sections.

5.2.1 Evaluation of GS material properties

The material used is a 0.4 mm thin galvanised steel sheet as per standard [86] and a diameter of 100 mm. Three tensile test specimens in sheet form are wire cut from the same galvanised steel sheet where the flat metallic disc is prepared for hydro-forming. The standard dimensions of the tensile test specimens are shown in Figure 5.2(a). Three tensile specimens are wire cut as per Figure 5.2(a) are shown in Figure 5.2(b).

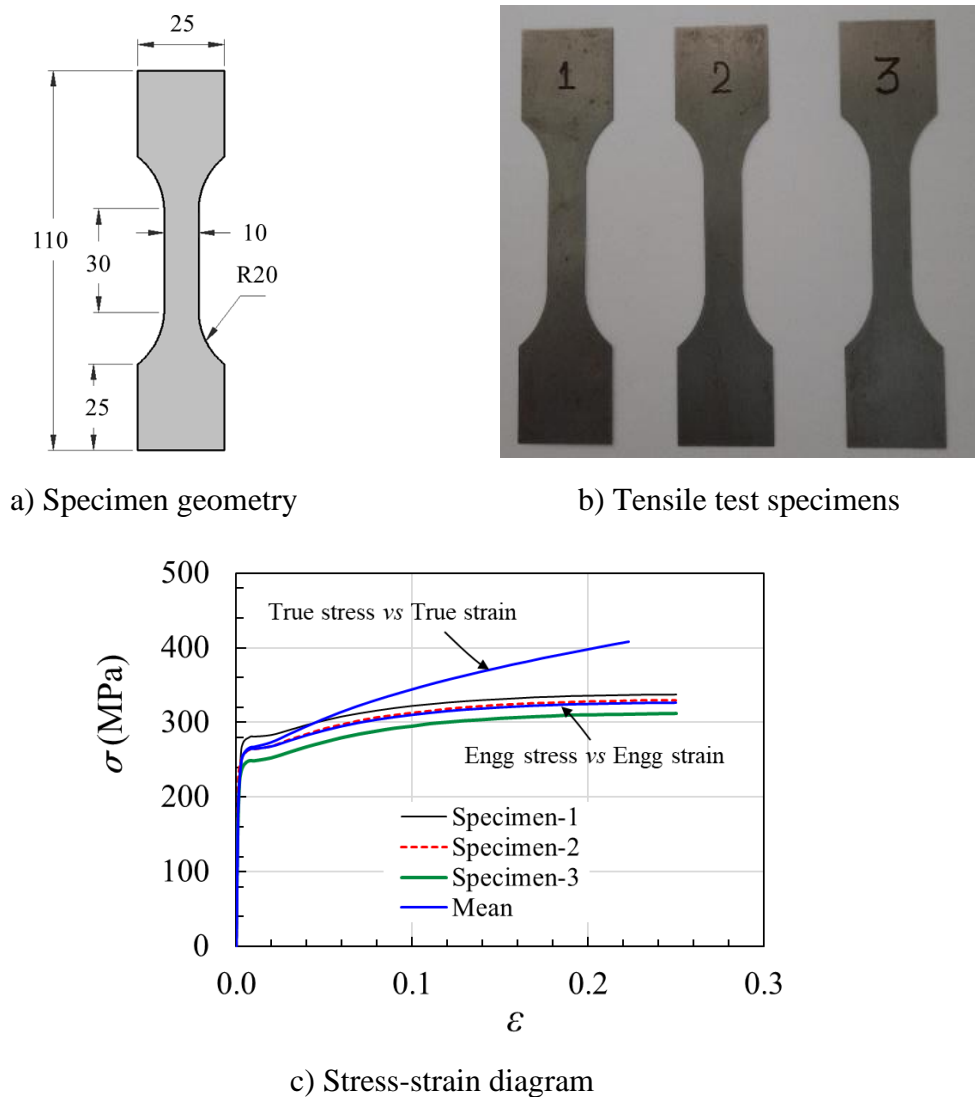


Figure 5.2: Material properties evaluation of GS (all dimensions in mm)

Tensile tests are performed as per ASTM E8 [55] standard on three specimens as per the standard procedure on an MCS universal testing machine. The engineering stress versus engineering strain curve obtained for all three tensile tests is plotted in Figure 5.2(c), including the mean of the three tensile test results. Material properties obtained from tension tests are Young's modulus = 180 GPa; Poisson's ratio = 0.29; yield strength = 258 MPa; ultimate tensile strength = 326 MPa; and elongation at break = 33%. The mean true stress-strain curve (Figure 5.2(c)) derived from the mean engineering stress-strain curve data from the test results is considered for numerical simulations in explicit FEA.

5.2.2 Numerical simulation of the hydro-forming process

A symmetric two-dimensional model of the flat metallic disc is modelled as shell elements-SAX1 in ABAQUS explicit [61]. The 8 mm outer edge is constrained in two displacements ($u_x = u_y = 0$) and one rotational ($\theta_z = 0$) degree of freedom. The inner domed profile of the die is modelled as an analytical rigid surface and is fixed in the middle. A kinetic friction contact is established between the metallic disc and the rigid profile surfaces with a friction coefficient of 0.1. The true stress-true strain curve obtained from tensile tests shown in Figure 5.2(c) is implemented in simulation using the isotropic hardening plasticity model. The pressure loading rate of 100 MPa/s is applied to reduce the computational time. The solution time of 100ms is considered. The FE model with loads, boundary conditions and loading is shown in Figure 5.3. The problem is solved in a non-linear explicit solver [61].

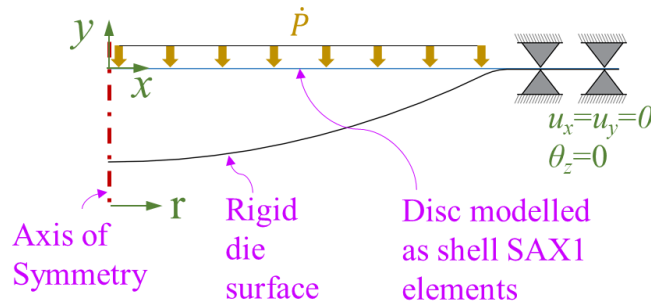
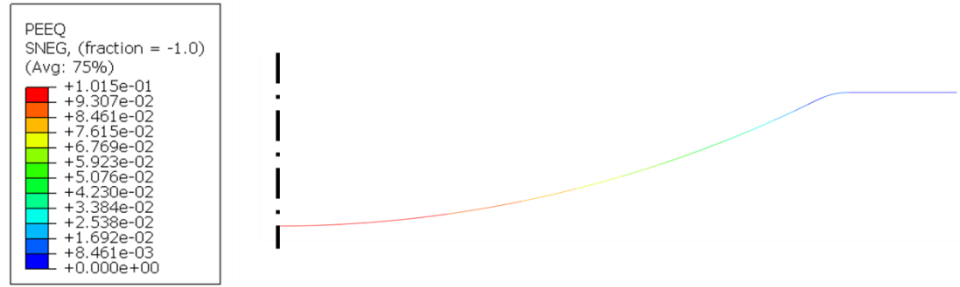


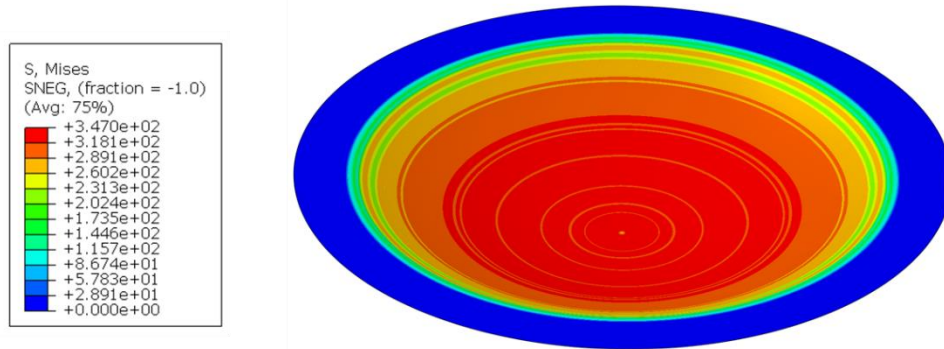
Figure 5.3: Loads and boundary conditions of GS disc FE analysis

5.2.3 Simulation results

The results obtained from explicit FEA simulations are presented in this section. After the complete deformation of the flat metallic disc, the disc attained a domed shape matching the profile of the rigid die surface, as shown in Figure 5.4. The maximum equivalent plastic strain is reached at the middle of the formed disc and is observed as 10.015% (Figure 5.4(a)), and the corresponding equivalent plastic stress is 347MPa (Figure 5.4(b)) at the middle region of the disc. The equivalent plastic stress and strain are maximum up to about 0.5 times the radius r of the disc and gradually decrease to a minimum value with an increase in the radius to $r_{max} = 42$ mm.



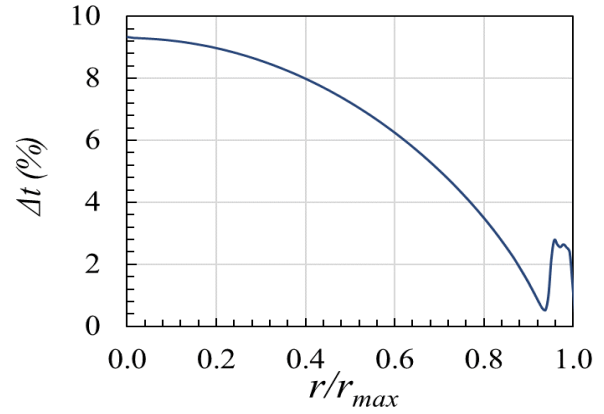
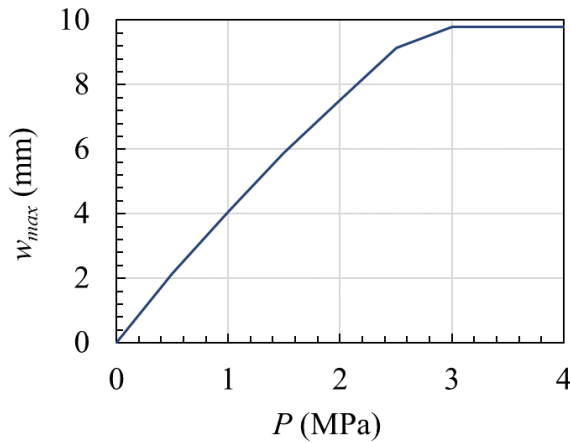
(a) Equivalent plastic strain distribution



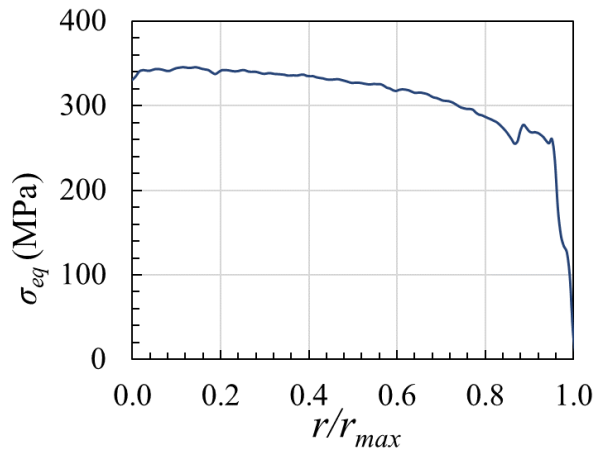
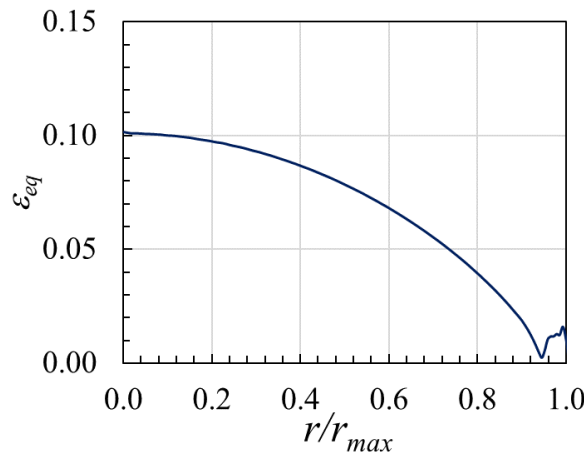
(b) Equivalent plastic stress distribution

Figure 5.4: Equivalent plastic strain and stress after hydro-forming of GS disc

A maximum central deflection w_{max} of 9.8 mm is reached in the middle of the dome at 3 MPa pressure, as shown in Figure 5.5(a). This deflection remains constant at 9.8 mm once the disc reaches the rigid surface. A difference of 0.2 mm is observed as the mid-surface reference is taken in the shell element representing the metallic disc. Under applied hydraulic pressure, the flat metallic disc undergoes bending and stretching deformations. The stretching deformation induces a reduction in thickness t along the radius of the disc during the formation of the dome shape. This reduction in thickness Δt is maximum at the middle of the dome and is about 9.2% of the original sheet thickness $t_0 = 0.4$ mm. This thickness reduction gradually reduces to about 0.5% following a parabolic path until the radius $r = 0.96r_{max}$. Just after $r = 0.96r_{max}$, *i.e.* at the end of the radius of the disc, there is an abrupt reduction in thickness due to the geometry change offered by the die's horizontal surface. This reduction in thickness increases from 0.5% to 3% within a narrow radial region of $0.04r_{max}$ near fixity, as seen in Figure 5.5(b).



(a) Central deflection versus applied pressure (b) Percentage of thickness variation along the radius



(c) Variation in equivalent plastic strain along the radius (d) Variation in equivalent stress along the radius

Figure 5.5: Response of GS disc under pressure loading

The equivalent plastic strain decreases from 10.015% at $r = 0$ to 0.5% at $r = 0.96r_{max}$. Beyond $0.96r_{max}$, the strain increases to about 1.8%, just before $r = r_{max}$, and decreases to 0 at r_{max} . as shown in Figure 5.5(c). Unlike reduction in strain and thickness, as the radius increases from 0 to r_{max} , the equivalent plastic stress decreases gradually from 340 MPa at $r = 0$ to 260 MPa at $r = 0.96r_{max}$. A slight oscillation occurs in stress value after $0.96r_{max}$ but gradually decreases to 0 MPa at r_{max} , as seen in Figure 5.5(d).

5.2.4 Hydro-forming experimental setup

5.2.4.1 Design and fabrication of hydro-forming die assembly

The design of the hydro-forming die assembly with and without hydraulic pressure is shown in Figure 5.6. The hydro-forming die assembly is designed with the die at the bottom having a $\phi 1.0$ mm air vent hole in its middle and a top plate at the top. The top plate is featured with a provision for connecting the hydraulic inlet. The flat metallic disc specimen is sandwiched between the die and the top plate through flat gaskets for leak protection, as shown in Figure 5.7. They are bolted together using eight numbers of M10 fasteners.

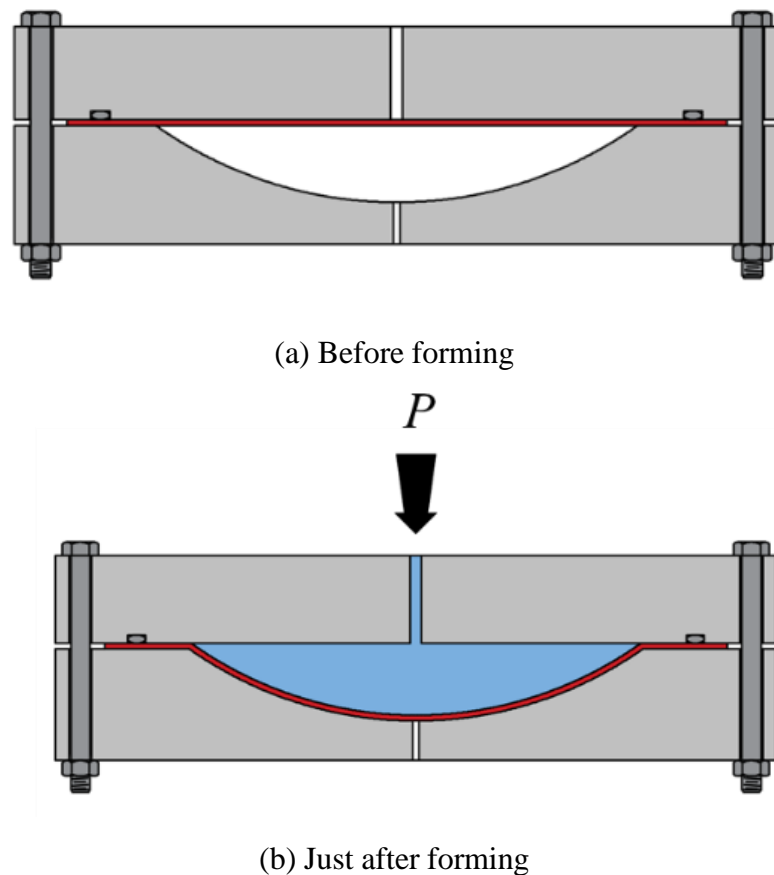


Figure 5.6: Hydro-forming die setup

Figure 5.7(a) shows the engineering model of the designed hydro-forming die setup, Figure 5.7(b) shows the exploded view of the assembly and Figure 5.7(c) shows the fabricated components of the die assembly. The metallic components of the die assembly are machined from EN24 alloy steel [87] material and surface protected with Zn coating of 0.006 mm thickness. A flat thin metallic disc specimen is fabricated by wire cut operation.

5.2.4.2 Experimental setup and hydro-forming experiment

The machined components of the die assembly are integrated as per the sequence shown in Figure 5.7(b) and the final setup is realised as shown in Figure 5.8(a). The hydraulic inlet is connected to the top plate. The hydraulic pump with an accumulator capacity of 50 litres and

a flow rate of 0.5 lpm is used in this experiment, as shown in Figure 5.8(b). The hydraulic valve is gradually opened until the pressure increase raises sharply. The hydro-forming process is completed within 4 seconds. This sharp increase in pressure occurs once the flat metallic disc deforms and touches the bottom die surface. The experiment is stopped by bringing the hydraulic pressure to zero. The assembly is dismantled and the final hydro-formed metallic disc is shown in Figure 5.9. The right side picture in Figure 5.9 is the top surface of the domed disc exposed to hydraulic pressure and the left is the bottom surface of the formed disc, which contacted and touched the die's top surface.

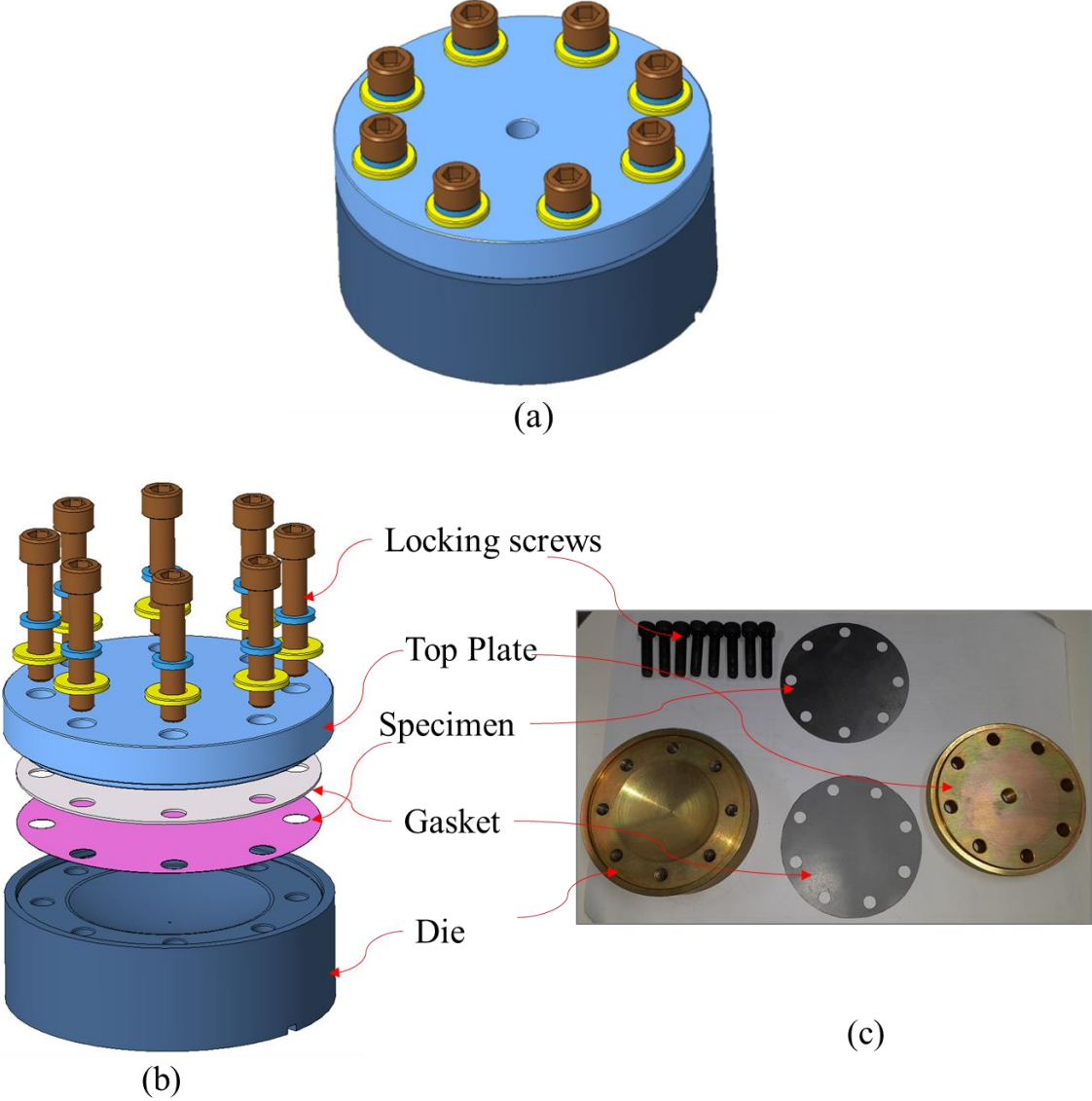


Figure 5.7: Hydro-forming setup: (a) assembly, (b) exploded view of components, and (c) individual fabricated components



(a) Die assembly connected to the hydraulic supply



(b) Hydraulic pump

Figure 5.8: Experimental setup



Figure 5.9: Hydro-formed domed GS disc (finished component)

5.2.5 Results and discussions on GS disc

The thickness variation in the hydro-formed disc is measured through a micro-meter of 0.01 mm least count along eight equi-spaced markings on the dome covering the entire 360° of the domed disc. The variation of measured thickness is compared with that from numerical simulation as shown in Figure 5.10. The thickness reduction measured after the experiment varied from 7.6% at $r = 0$ to 0 % at $r = 0.96r_{max}$. Beyond $r \geq 0.96r_{max}$, the measurement was a challenge in capturing the thickness values at the sharp curvature close to the fixed region and hence, is not reported. The maximum reduction is observed at $r = 0$ in numerical simulation and is about 9.2% of the original sheet thickness. It decreased to about 0.50 % at $r = 0.96r_{max}$.

There is a reasonable agreement between the experiment and simulation on the reduction sheet thickness. The maximum difference between the experiment and numerical simulation is only about 1.6%. This simulation validated by experiment confirmed the feasibility of manufacturing the domed disc by the hydro-forming process. The numerical simulation helped investigate and understand the variations in geometric parameters such as central deflection and thickness and the equivalent plastic stress and strain subjected to the domed disc.

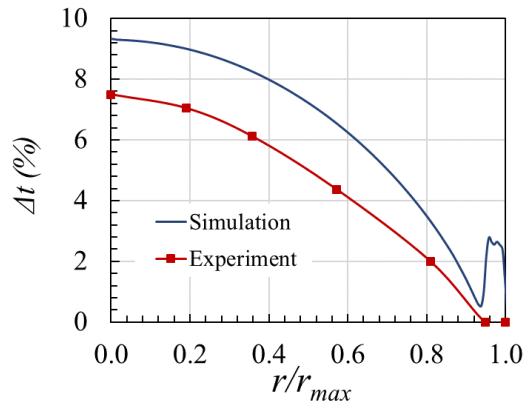


Figure 5.10: Percentage reduction in thickness of domed GS disc along radius - experiment vs simulation

5.3 Hydro-forming of E250 structural steel disc

A similar procedure is followed for the hydro-forming of the E250 structural steel disc and is explained in this section.

5.3.1 Disc geometry

The geometry of the initial disc and the expected final disc geometry is shown in Figure 5.11.

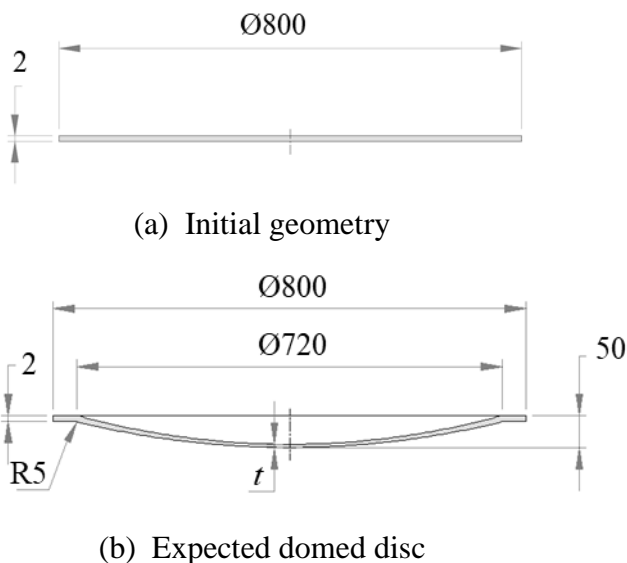


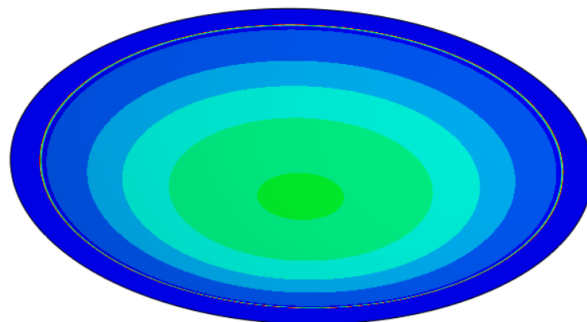
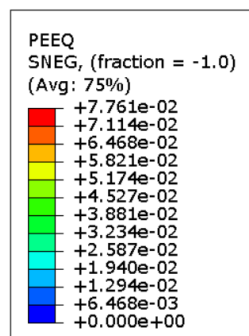
Figure 5.11: E250 structural steel disc before and after hydro-forming

5.3.2 FE model setup and analysis of E250 structural steel disc

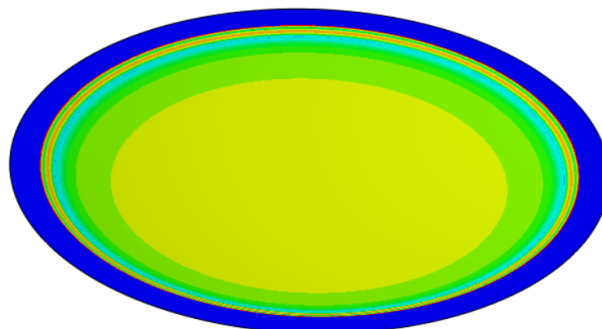
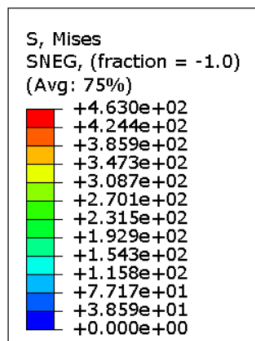
As explained in Section 5.2.2, a symmetric two-dimensional model of the flat metallic disc is modelled as shell elements-SAX1 with an element size of 1 mm. The 40 mm outer edge is constrained in two displacements ($u_x = u_y = 0$) and one rotational ($\theta_z = 0$) degree of freedom. The inner domed profile of the die is modelled as an analytical rigid surface and is fixed in the middle. A kinetic friction contact is established between the metallic disc and the rigid profile surfaces with a friction coefficient of 0.1. The extracted J-C material model parameters, as given in Chapter-2, are implemented in simulation using the isotropic hardening plasticity model. The pressure loading rate of 10 MPa/s is applied to reduce the computational time. A solution time of 2 seconds is considered. The FE model with loads, boundary conditions and loading is shown in Figure 5.3. The problem is solved in a non-linear implicit solver [60].

5.3.3 FE simulation results

After the complete deformation of the flat metallic disc, the disc attained a domed shape matching the profile of the rigid die surface. The maximum equivalent plastic strain is reached at the middle of the formed disc and is observed as 7.7% (Figure 5.12(a)) and the corresponding stress is 463 MPa (Figure 5.12(b)) at the middle region of the disc. The equivalent plastic stress and strain are maximum at the centre of the disc and gradually decrease to a minimum value at radius $r_{max} = 350$ mm.



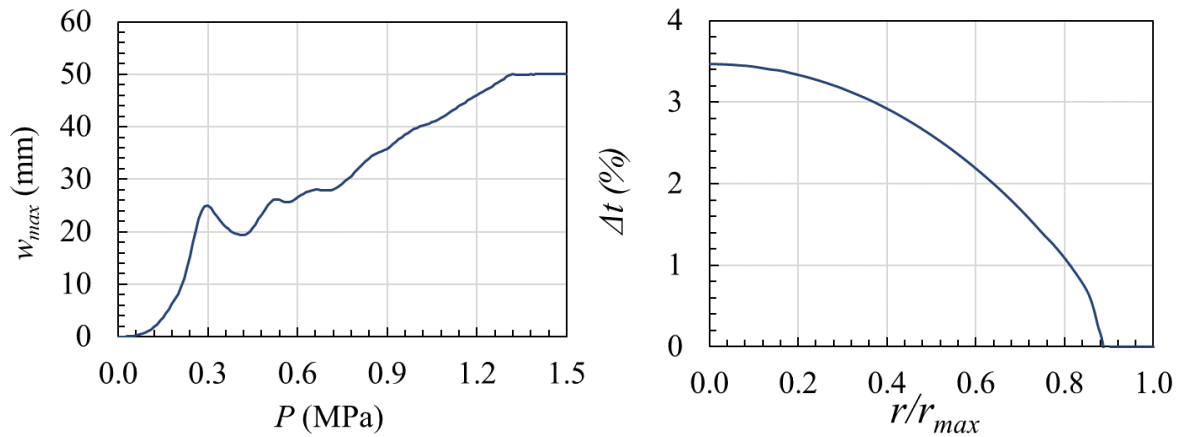
(a) Equivalent plastic strain distribution



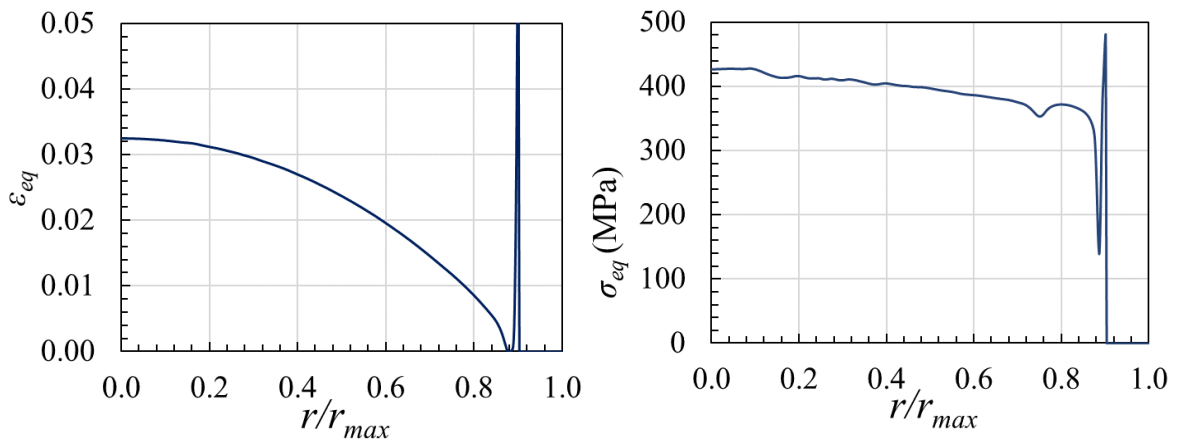
(b) Equivalent plastic stress distribution

Figure 5.12: Equivalent plastic strain and stress after hydro-forming of E250 disc

A maximum central deflection w_{max} of 50 mm is reached in the middle of the dome at 1.31 MPa pressure, as shown in Figure 5.13(a). This deflection remains at 50 mm once the disc reaches the rigid surface. Under applied hydraulic pressure, the flat metallic disc undergoes bending and stretching deformations. The stretching deformation induces a reduction in thickness t along the radius of the disc during the formation of a dome shape. This reduction in thickness Δt is maximum at the middle of the dome and is about 3.2% of the original sheet thickness $t_0 = 2$ mm and gradually reduced up to fixity, as seen in Figure 5.13(b).



(a) Central deflection versus applied pressure (b) Percentage of thickness variation along the radius



(c) Variation in equivalent plastic strain along the radius (d) Variation in equivalent stress along the radius

Figure 5.13: Response of E250 disc subjected to the hydro-forming

The equivalent plastic strain decreases from 3.2% at $r = 0$ to 0% at $r = 0.9r_{max}$. Plastic strain suddenly increased up to 5% in the fillet region near fixity. Beyond $0.9r_{max}$, the strain remains close to 0% near fixity, as observed in Figure 5.13(c). Unlike reduction in strain and thickness as the radius increases from 0 to r_{max} , the equivalent plastic stress decreases gradually from 410 MPa at $r = 0$ to 340 MPa at $r = 0.9 r_{max}$. A slight oscillation occurs in stress value after $0.96 r_{max}$ but gradually decreases to 0 MPa at r_{max} , as seen in Figure 5.13(d).

5.3.4 Hydro-forming experimental setup

5.3.4.1 Design of hydro-forming die assembly

The engineering model of hydro-forming die assembly is shown in Figure 5.14(a). The hydro-forming die assembly is designed with the die at the bottom having a $\phi 1.0$ mm air vent hole in its middle and a top plate at the top. The top plate is featured with a provision for connecting the hydraulic inlet. The flat metallic disc specimen is sandwiched between the die and the top plate. Two O-rings are provided between the flat disc and bottom die for leak-proof. They are bolted together using 24 numbers of M12 fasteners. Figure 5.14(b) shows fabricated components of the die assembly and Figure 5.14(c) shows the exploded view of the assembly. The metallic components of the die assembly are machined from C45 high carbon steel [88] material. The flat thin metallic disc from E250 structural steel material is fabricated by wire cut operation.

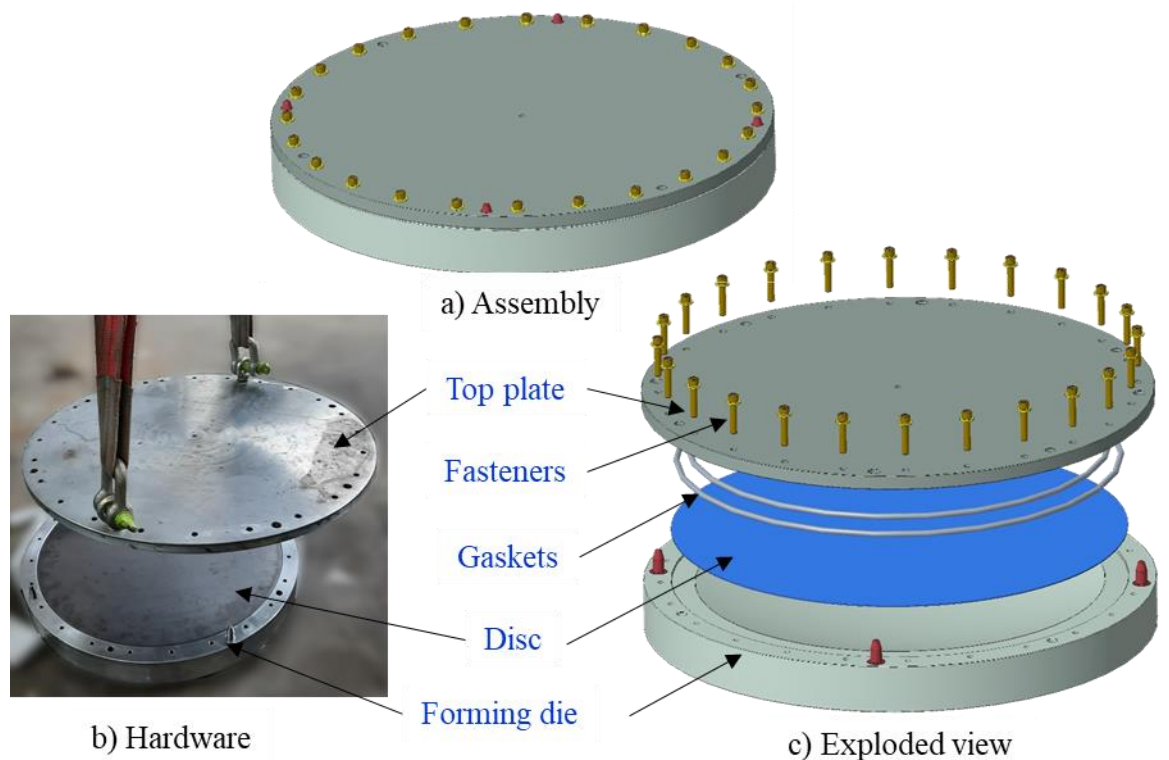


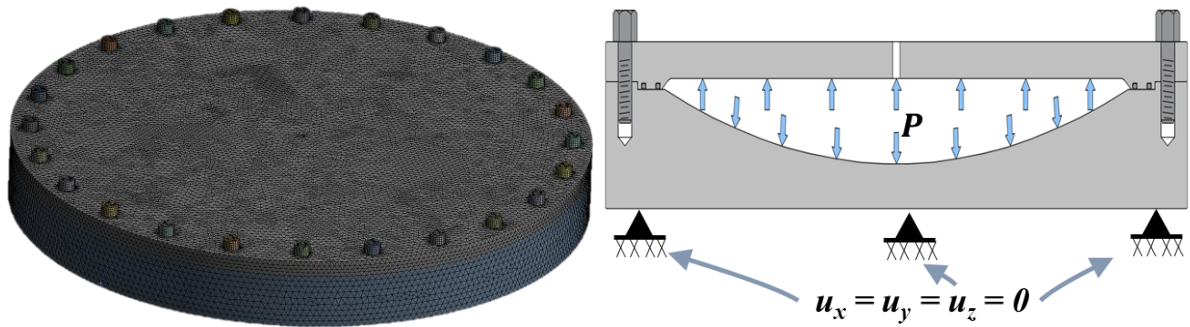
Figure 5.14: Hydro-forming setup for E250 steel disc

5.3.5 FE analysis of hydro-forming experimental setup

DSMD is formed from a 2 mm thick E250 structural steel sheet. From analysis, the required hydro-forming pressure is 1.3 MPa. The hydro-forming setup is designed to withstand 1.5 MPa to account for uncertainties. The bottom die and Top plate are made of C-45 steel, with an ultimate strength of 610 MPa and a minimum yield strength of 320 MPa. The top plate is clamped to cylindrical housing using 24 numbers of M12 bolts by applying pre-tightening torque of 56 N-m.

5.3.5.1 Loads and boundary conditions

The FE model of the experimental setup is shown in Figure 5.15(a). ANSYS 2019 [89] is used for static structural analysis. The model is discretised using 589052 ten-node tetrahedral elements with three DOF per node, with a minimum element size of 3 mm and an average element size of 5 mm. The bottom member (plate) is rigidly clamped to the floor, fixed in FE analysis. A pressure of 1.5 MPa is applied to all interior surfaces, as shown in Figure 5.15(b).



a) Discretized model

b) Loads and Boundary conditions

Figure 5.15: FE model, loads and boundary conditions for E250 steel disc

5.3.5.2 Results

The results of the analysis are shown in Table 5.1. All components have a sufficient factor of safety (*FS*) under the given load.

Table 5.1: Results for static structural analysis of hydro-forming setup components

Component	Induced von-Mises stress	Maximum deflection	FS
Top plate	 $\sigma_{avg} = 146 \text{ MPa}$	 $\delta_{max} = 2.1 \text{ mm}$	2.4
Die	 $\sigma_{avg} = 30 \text{ MPa}$		11

Thus, all the components are safe under given loading conditions.

5.3.6 Experimental setup and hydro-forming experiment

The machined components of the die assembly are integrated as per the sequence shown in Figure 5.14(b) and the final setup is realised as shown in Figure 5.16(a). The hydraulic inlet is connected to the top plate. The hydraulic pump with an accumulator of capacity 50 litres and a flow rate of 0.5 lpm is used in this experiment. The hydraulic valve is gradually opened until the pressure increase raises sharply. This sharp increase in pressure occurs once the flat metallic disc deforms and touches the bottom die surface. The experiment is stopped by bringing the hydraulic pressure to zero and then the assembly is dismantled after keeping the assembly in the same position for 1 hour. The final hydro-formed metallic disc is shown in Figure 5.16(b). No spring back is observed in the formed disc.

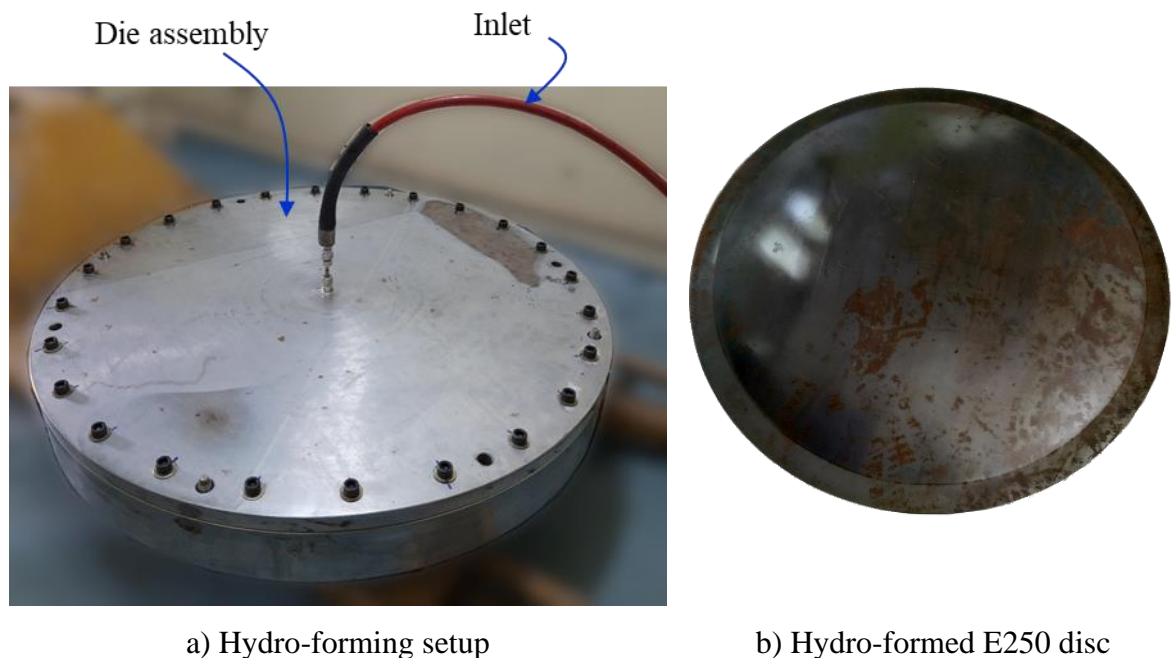


Figure 5.16: Hydro-forming of E250 domed disc

5.3.7 Results and discussions on hydro-forming of E250 disc

The reduction in the thickness from the simulation is shown in Figure 5.17. The thickness at the centre is 1.93 mm and variation is parabolic up to fixity. The disc's thickness increased up to 2.06 mm in the fillet portion of the disc. Thickness remains constant in the fixity portion of the disc from $r = 0.9r_{max}$ to $r = r_{max}$. The numerical simulation helped investigate and understand the variations in geometric parameters such as central deflection and thickness, the equivalent plastic stress and strain subjected to the domed disc, and the minimum fluid pressure required for hydro-forming operation. However, the experimentally observed thickness could not be measured due to its geometry and handling challenges. It is believed that the same percentage reduction in thickness might be observed in this E250 structural steel disc as observed in the 100 mm GS disc discussed at the beginning of this Chapter.

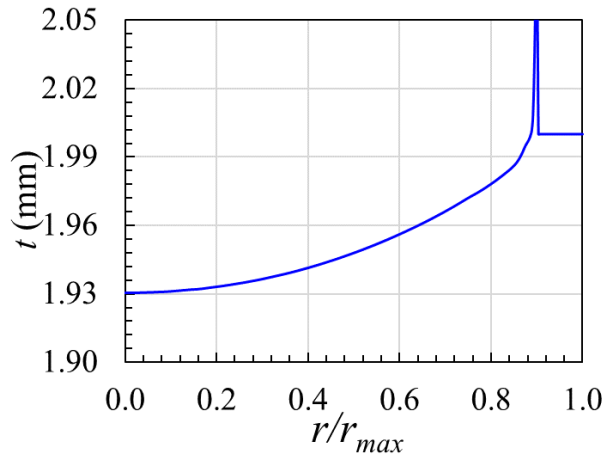


Figure 5.17: Thickness of E250 domed disc along the radius from simulation

5.4 Summary

The manufacturing feasibility of the domed metallic disc from an original flat disc through the hydro-forming process was explored through a small ($\phi 100$ mm and 0.4 mm thick) galvanic steel disc. The material property of the galvanised steel disc was obtained from three tensile experiments. These material properties were considered in numerically simulating the deformation behaviour of the flat metallic disc using an isotropic plastic hardening model. The hydro-forming process under pressure loading was simulated through a simplified axisymmetric FEA model and solved using a non-linear explicit FEA code. The feasibility of manufacturing dome discs through this process is established.

A similar approach is followed for E250 structural steel disc. Simulation is conducted through non-linear implicit FEA code because of more duration of loading time. J-C material properties derived in Chapter-2 are considered for simulation. An experimental setup is designed and fabricated. The disc is manufactured through the hydro-forming operation. The thickness variation of the disc along the radius of the disc is investigated.

Experiments on Scored Metallic Discs

6.1 Introduction

The experiments are conducted on Flat Scored Metallic Discs (FSMD) and Domed Scored Metallic Discs (DSMD) to ascertain the burst pressure of both discs and validate the structural response of the discs up to failure. Both types of discs are made of E250 structural steel. A separate experimental setup is designed and realised to achieve the maximum possible loading rate conditions with the available facilities in the laboratory. By considering the safety requirements, tests are conducted in two phases. In the first phase, experiments are conducted using hydraulic pressure at a quasi-static loading rate to determine the burst pressure and verify its agreement with the predicted burst pressure. In the second phase, experiments are conducted under pneumatic pressure at a higher loading rate. This chapter explains experiments on both the FSMD and DSMD under hydraulic and pneumatic loadings.

6.2 Geometry of discs

6.2.1 Flat scored metallic disc

The geometry of FSMD used for experimentation is shown in Figure 6.1(a). It is a circular disc of 800 mm diameter, laser cut from a 2 mm thick hot rolled E250 structural steel sheet. On one side of the disc, two rectangular scores with a length of 700 mm, a width of 5 mm and a depth of 1.4 mm are milled in a ‘+’ configuration, as shown in Figure 6.1(b). Twenty-four numbers of 13 mm diameter holes are drilled at a pitch circle diameter of 780 mm. These holes are used for clamping the disc to the experimentation chamber.

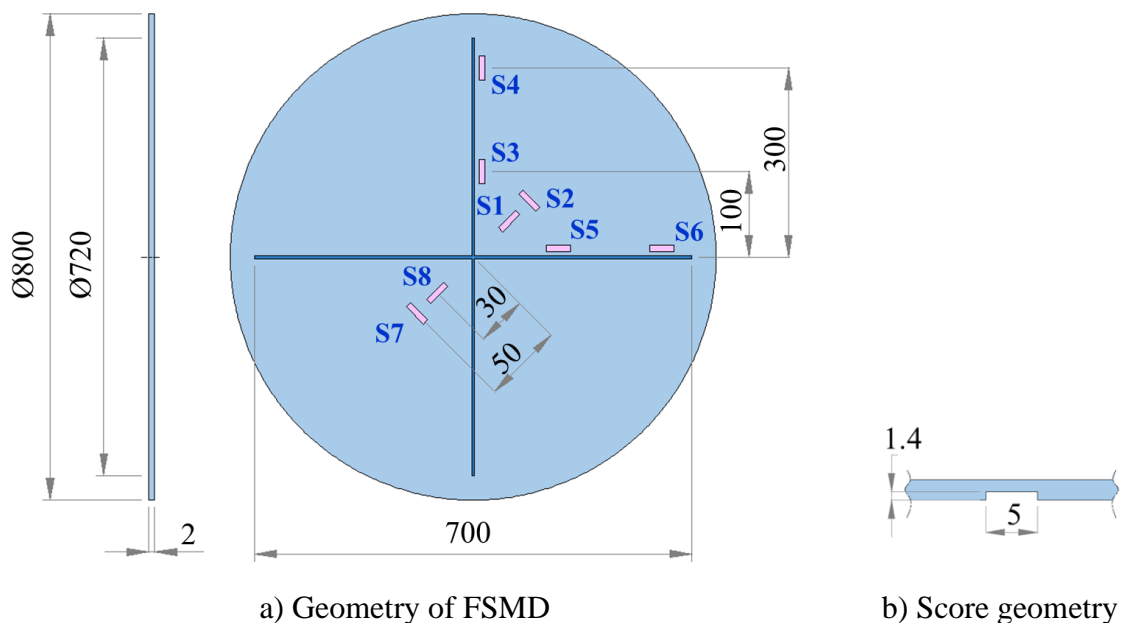


Figure 6.1: Experimental disc geometry of FSMD

Three numbers of FSMD, F2, F3 and F4 are realised, as shown in Figure 6.2.

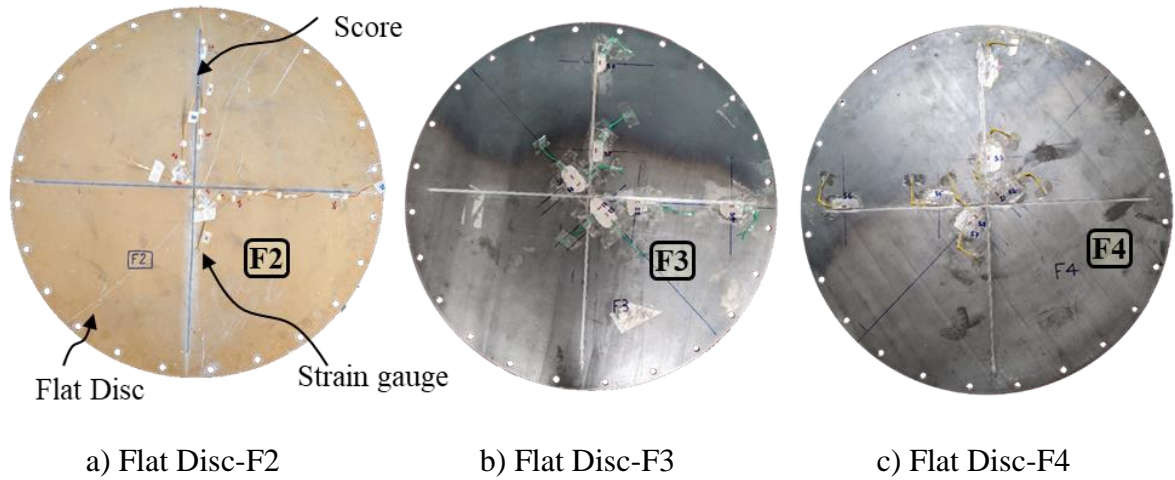


Figure 6.2: Realized FSMDs

6.2.2 *Domed scored metallic disc*

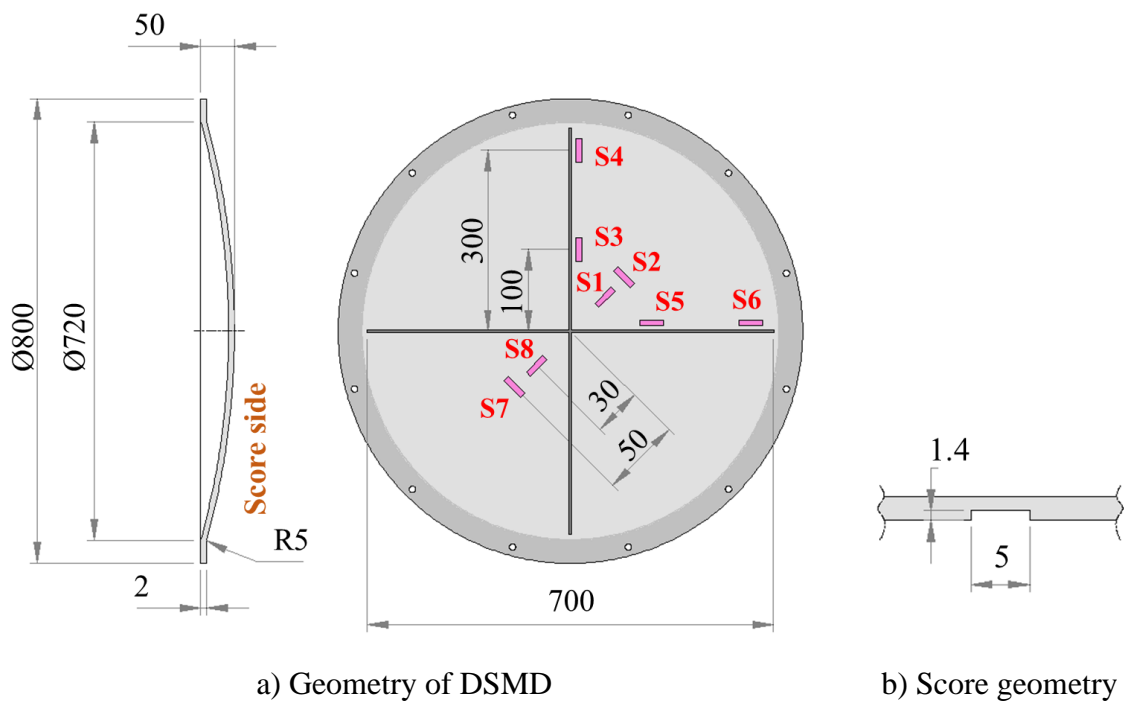


Figure 6.3: Experimental disc geometry of DSMD

The geometry of DSMD used for experimentation is shown in Figure 6.3(a). First, flat circular discs of 800 mm diameter are laser cut from 2 mm thick E250 structural steel sheets. These flat discs are formed to dome shape using hydro-forming operation as discussed in Chapter-6. Afterwards, two rectangular scores are milled in a ‘+’ configuration. While milling these scores, support in the form of a fixture is provided in the concave portion of the disc to avoid local deformation in the scored region during milling. Both scores have a length of 700 mm,

width of 5 mm and depth of 1.4 mm, as shown in Figure 6.3(b). Like flat discs, 24 numbers of 13 mm diameter holes are drilled at a pitch circle diameter of 780 mm.

Three numbers of DSMD, D1...D3, are realised, as shown in Figure 6.4.

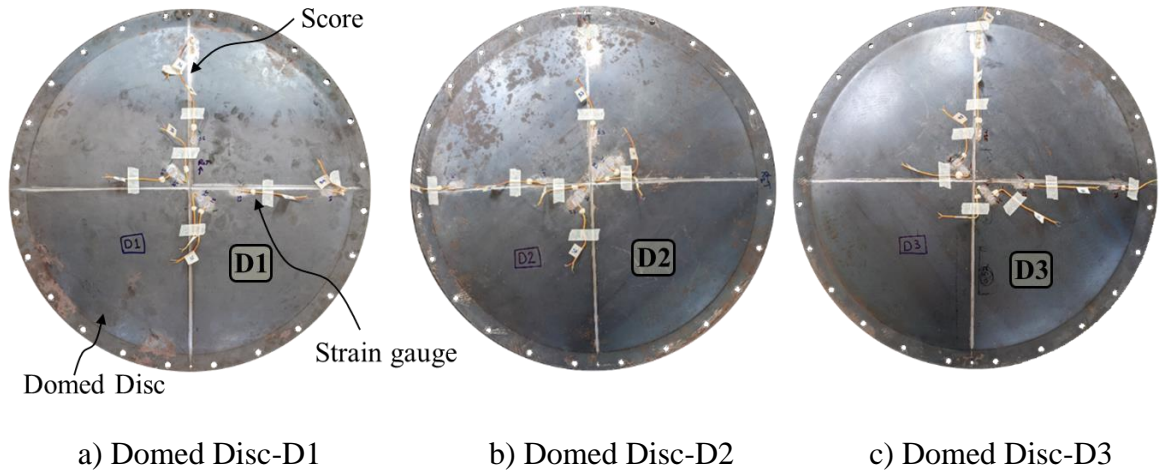


Figure 6.4: Realized DSMDs

6.3 Design and analysis of experimental setup

6.3.1 Configuration of the experimental setup

A schematic view of the experimental setup of the burst experiment is shown in Figure 6.5. The experimental setup mainly consists of a cylindrical housing having an inside diameter of 720 mm and height of 200 mm with a pressurised chamber volume of 0.081 m³. It is made of two parts, one is the bottom plate and the other one is the cylindrical chamber, which is welded together.

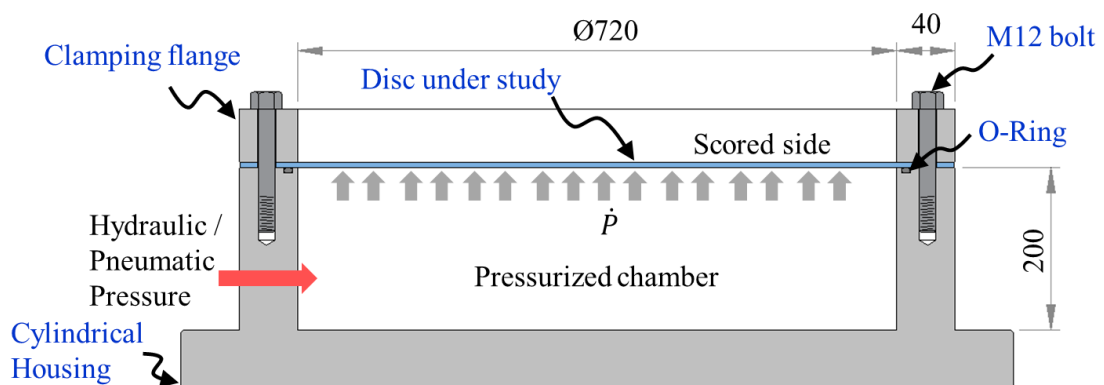
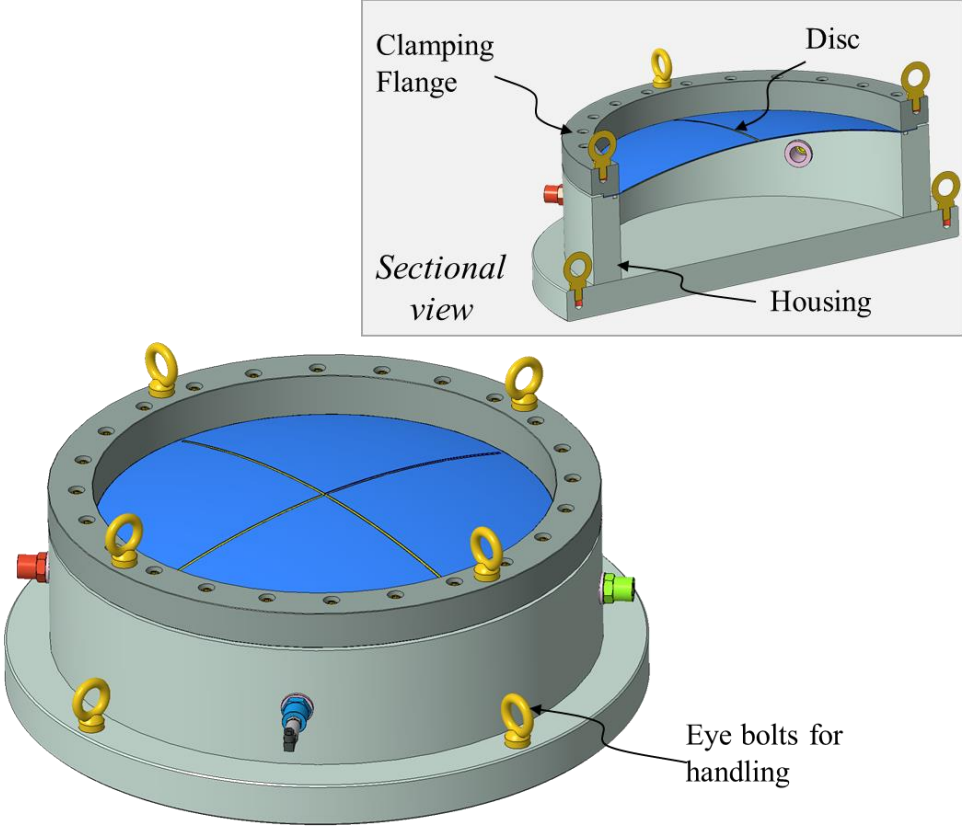


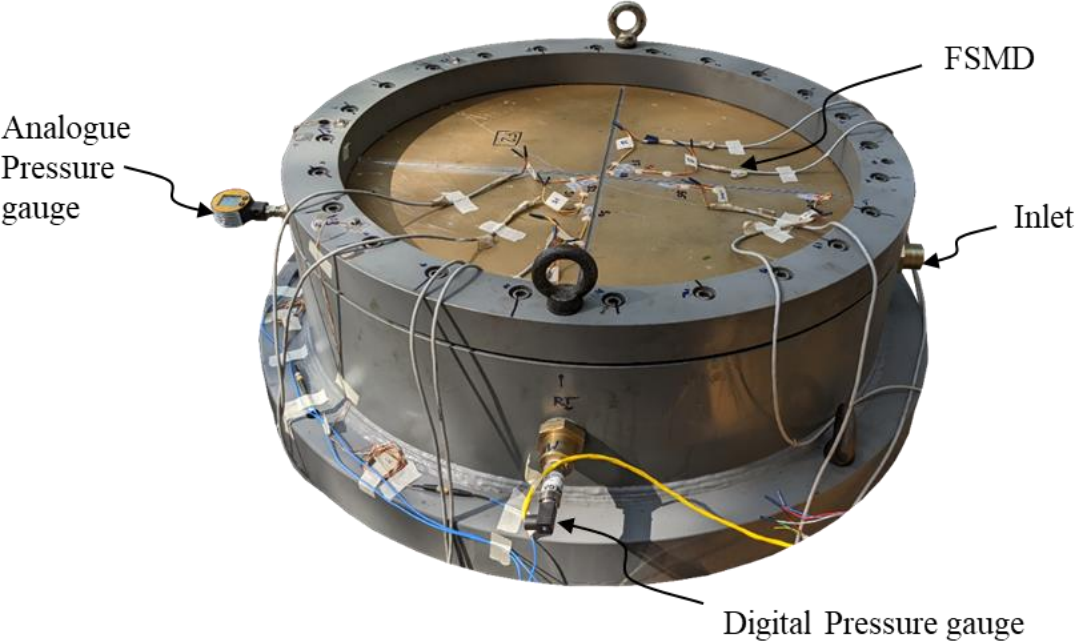
Figure 6.5: Schematic view of the experimental setup

Discs are clamped to the open end of the cylindrical housing with the help of a clamping flange and 24 numbers of M12 bolts. The plain side of the disc is exposed to the applied pressure. A pre-tightening torque of 100 N-m is applied to the bolts, which induces 1000 kN of clamping force or closing pressure of 10 MPa. An O-ring is placed between the disc and

cylindrical housing for sealing the chamber. The three-dimensional model of the experimental setup is shown in Figure 6.6(a) realised hardware is shown in Figure 6.6(b).



a) Three-dimensional configuration of the setup



b) Realized hardware

Figure 6.6: Experimental setup

6.3.2 Measurement plan

A quartz-based pressure transducer with a measurement range of 0 - 6.9 MPa, an accuracy of 2% and a response time of less than 1 ms is attached to the chamber to record the pressure inside the chamber during the test. Eight foil-type strain gauges S1, S2 ... S8 having a nominal resistance of 350Ω are bonded to scored side of discs as shown in Figure 6.1(a) and 6.3(a) to record the strain response of the disc under applied pressure. Quarter bridge setup is used to connect the strain gauges to the signal conditioner. Two strain gauges, S1 and S2, are placed at 45° to score and closer to the centre of the disc, one in radial and the other in tangential directions, at a distance of 50 mm and 30 mm, respectively. As shown, two more strain gauges, S7 and S8, are placed on the other side of the groove. Two more strain gauges, S3 and S4, are placed on the disc aligned to the groove, one nearer to the centre at 100 mm and the other nearer to the clamping end of the disc at 300 mm from the centre of the disc. The last two strain gauges, S5 and S6, are placed at a similar location on the adjacent score. Minimum four strain gauges S1...S4 are planned to monitor the behaviour in a single formed petal in which two gauges along the groove and two away from the groove. Since the crack formation through all the scores is unpredictable, and conducting each experiment is time consuming and expensive, four more redundant strain gauges S5...S8 are additionally used.

6.3.3 FE analysis of the experimental setup

The expected burst pressure of DSMD is 0.62 MPa. The experimental setup is designed to withstand 2.5 MPa to account for uncertainties. A top plate is designed to conduct the proof pressure experiment, as shown in Figure 6.7(a). The sectional view is shown in Figure 6.7(b).

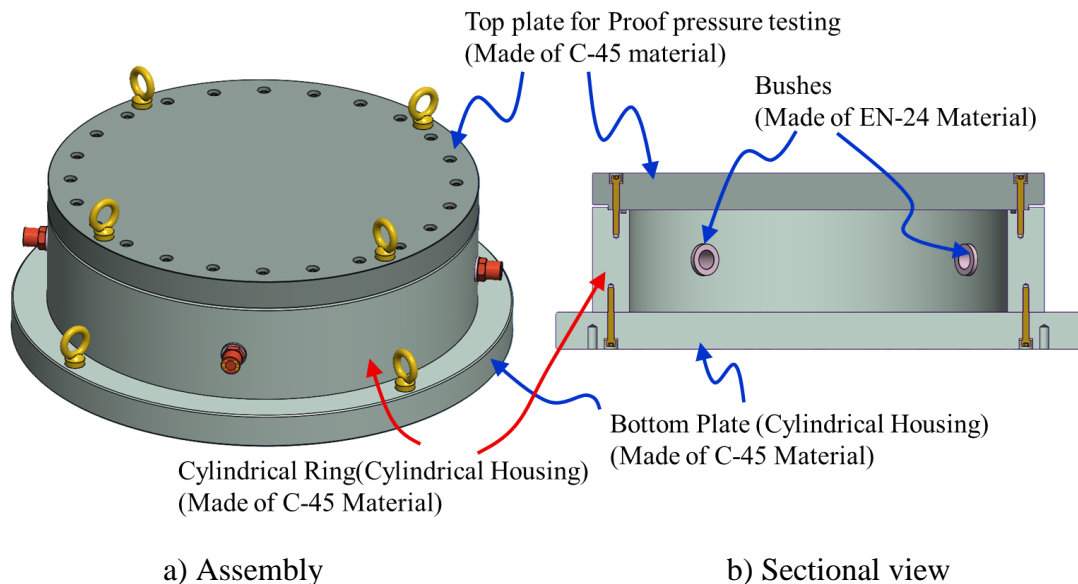


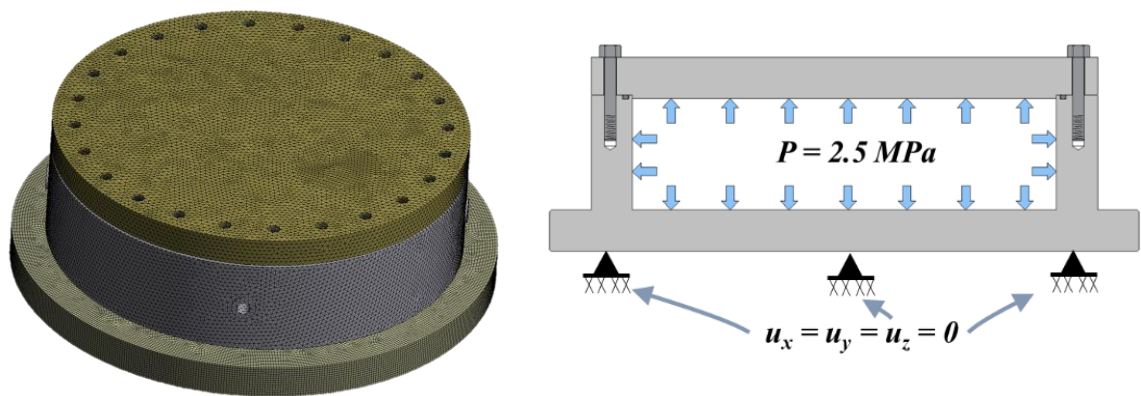
Figure 6.7: Model for proof pressure experiment and FE analysis

FE simulation is also carried out with this plate. All parts of the experimental setup, viz. cylindrical housing (bottom plate and cylindrical ring), bushes, clamping flange and top plate, are made of C-45 steel with an ultimate tensile strength of 610 MPa and minimum yield

strength of 320 MPa. The top plate is clamped to the cylindrical housing using 24 numbers of M12 bolts by applying pre-tightening torque of 56 N-m.

6.3.3.1 Loads and boundary conditions

The FE model of the experimental setup is shown in Figure 6.8(a). ANSYS 2019 [89] is used for static structural analysis. The model is discretised using 1393636 ten-node tetrahedral elements with three degrees of freedom (DOF) per node are used with a minimum element size of 3 mm and an average element size of 8 mm. The bottom plate is rigidly clamped to the floor, fixed in FE analysis. A pressure of 2.5 MPa is applied to all interior surfaces, as shown in Figure 6.8(b).



a) Discretized model

b) Loads and boundary conditions

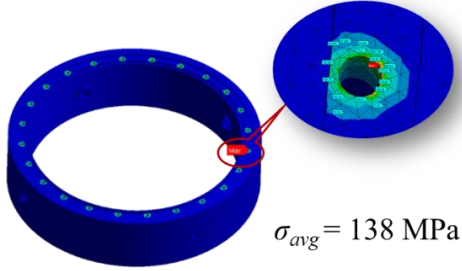
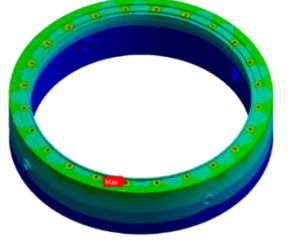
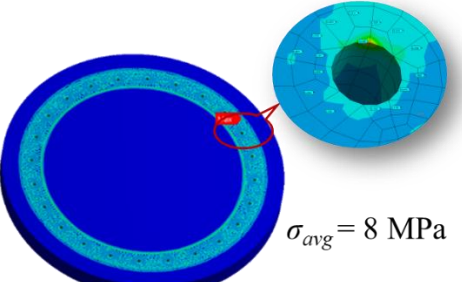
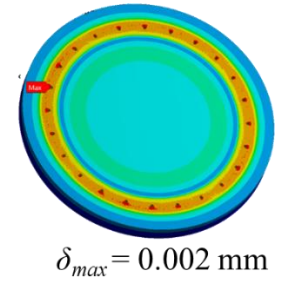
Figure 6.8: FE model, loads and boundary conditions

6.3.3.2 Results

The results of the FE analysis are shown in Table 6.1. All components have a sufficient factor of safety under the given load.

Table 6.1: Results for static structural analysis of experimental setup components

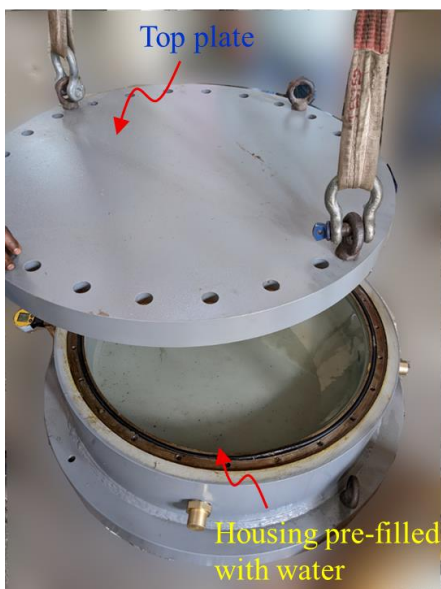
Component	Induced Von-Mises stress	Maximum deflection	FS
Top plate	 $\sigma_{avg} = 118 \text{ MPa}$	 $\delta_{max} = 0.52 \text{ mm}$	2.7

Housing	 $\sigma_{avg} = 138 \text{ MPa}$	 $\delta_{max} = 0.007 \text{ mm}$	2.3
Bottom plate	 $\sigma_{avg} = 8 \text{ MPa}$	 $\delta_{max} = 0.002 \text{ mm}$	40

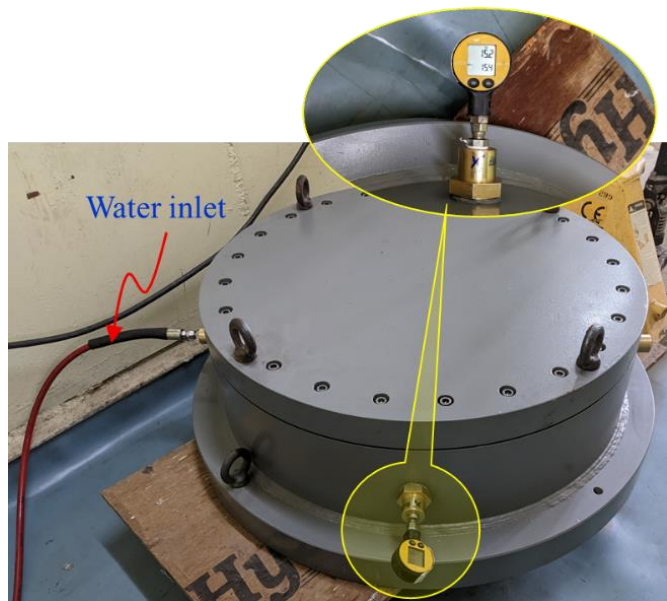
Thus, all the components are safe under given loading conditions.

6.3.3.3 Proof pressure experiment

Due to high-pressure application, the experimental setup is subjected to proof pressure loading to qualify the workmanship, such as leakage at welded joints. The experimental setup is subjected to 2.5 times the maximum expected burst pressure of the disc, *i.e.* 1.5 MPa. The proof pressure experimental setup is shown in Figure 6.9.



a) Preparation for the experiment



b) Experimental setup with pressure gauge reading (inset)

Figure 6.9: Proof pressure experimental setup

The housing is pre-filled with water and securely tightened with the top plate. An O-ring is placed between the housing and the top plate for leakproof. Bolts are tightened to 56 N-m pre-tightening torque. Water is supplied at a rate of 0.5 lpm until the pressure inside the chamber is reached 1.5 MPa or 15 bar. The setup is held for 30 minutes in this condition, and no pressure reduction is observed. As a result, the experimental setup is qualified for further experimentation of SMDs.

6.4 Experimental procedure

The experiment is conducted in two phases. In the first phase, one FSMD (F2) and one DSMD (D1) are subjected to hydraulic pressure loading to determine the burst pressure. In the second phase, two FSMD (F3 and F4) and two DSMD (D2 and D3) are subjected to pneumatic pressure at a high loading rate.

During the hydraulic experiment, the chamber is pre-filled with water and the input port is connected to a reciprocating hydraulic pump which can supply 0.5 lpm. During pneumatic testing, the input port is connected to the pneumatic supply at higher pressure, *i.e.* more than 150 bar. When the manually operated inlet valve is opened, the air suddenly enters the chamber, and the disc is subject to a higher loading rate. During the experiment, the pressure inside the chamber is monitored using a pressure transducer and strains developed in discs are monitored using strain gauges.

6.5 Observations and results

6.5.1 Hydraulic experiment of FSMD – F2

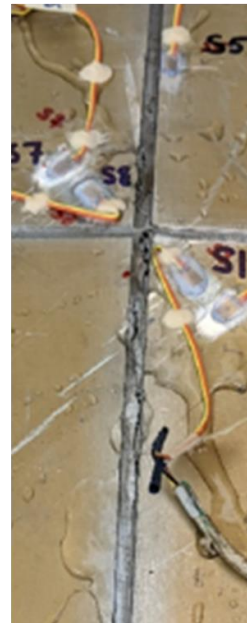
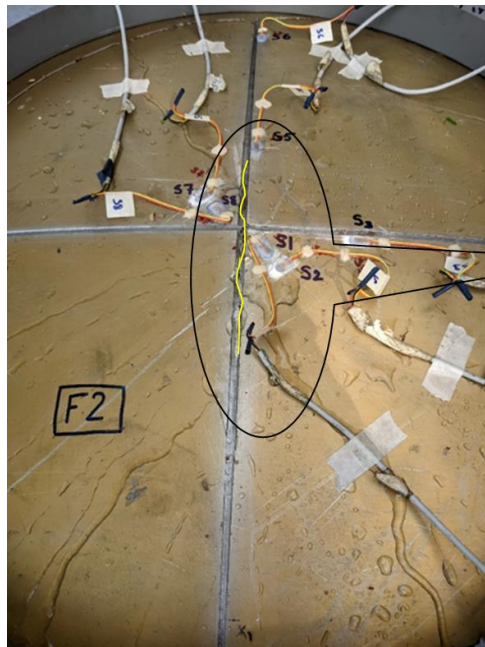
The hydraulic experiment on flat disc F1 could not be completed successfully due to damage to the disc before experimentation. The hydraulic experiment on FSMD-F2 is conducted by subjecting the discs to hydraulic pressure. The disc before the experiment is shown in Figure 6.10(a), the disc after the experiment is shown in Figure 6.10(b), and the crack developed during the experiment is shown in Figure 6.10(c). The chamber is pre-filled with water, and additional water is supplied by a reciprocating hydraulic pump at 0.5 lpm. The pressure and strains are monitored continuously during the test. The pressure with respect to time inside the chamber is shown in Figure 6.11(a) and the loading rate of the experiment is 0.0003 MPa/s.



a) Before the experiment



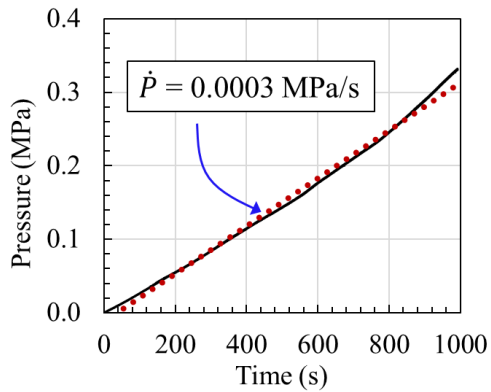
b) After the experiment



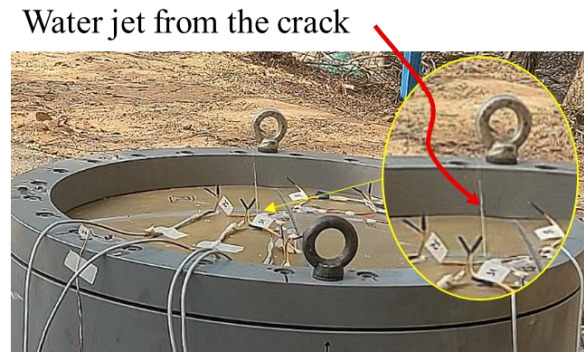
c) Crack formed during the experiment

Figure 6.10: Experiment on FSMD F2

The experiment continued for 16.5 minutes before forming a small crack away from the centre of the disc, as shown in Figure 6.11(b) and the observed peak pressure is 0.31 MPa which is noted as the burst pressure of the disc. After the initiation of the crack, water started leaking through the crack, and as a result, a pressure drop was observed. As the crack is propagated, the leak rate becomes more than the input rate and further pressure rise could not be observed.



a) Pressure with respect to time



b) Crack initiation

Figure 6.11: Experiment on FSMD F2 during crack initiation

6.5.2 Pneumatic experiment of FSMD – F3

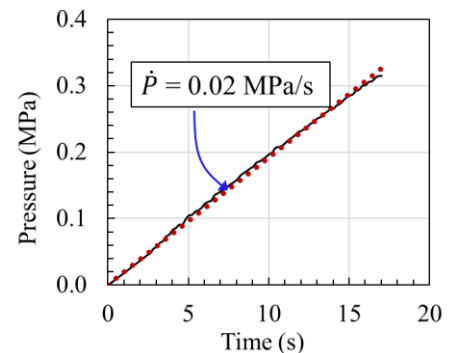
The pneumatic experiment on FSMD-F3 is conducted by subjecting the disc to a pneumatic supply of 200 bar. The disc before the experiment is shown in Figure 6.12(a), and the disc after the experiment is shown in Figure 6.12(b).



a) Before experiment



b) After experiment



c) Pressure with respect to time

Figure 6.12: Experiment on FSMD F3

The loading rate during the experiment is observed to be 0.02 MPa/s and the peak pressure is 0.31 MPa which is noted as the burst pressure of the disc. The experiment continued for 17 seconds, and the pressure with respect to loading rate is shown in Figure 6.12(c). During this experiment, the formation of the dome along with failure along a single score by the formation of crack is observed.

6.5.3 Pneumatic experiment on FSMD – F4

The pneumatic experiment on FSMD-F4 is conducted by subjecting the disc to a pneumatic supply of 250 bar. The disc before the experiment is shown in Figure 6.13(a), and the disc after the experiment is shown in Figure 6.13(b).

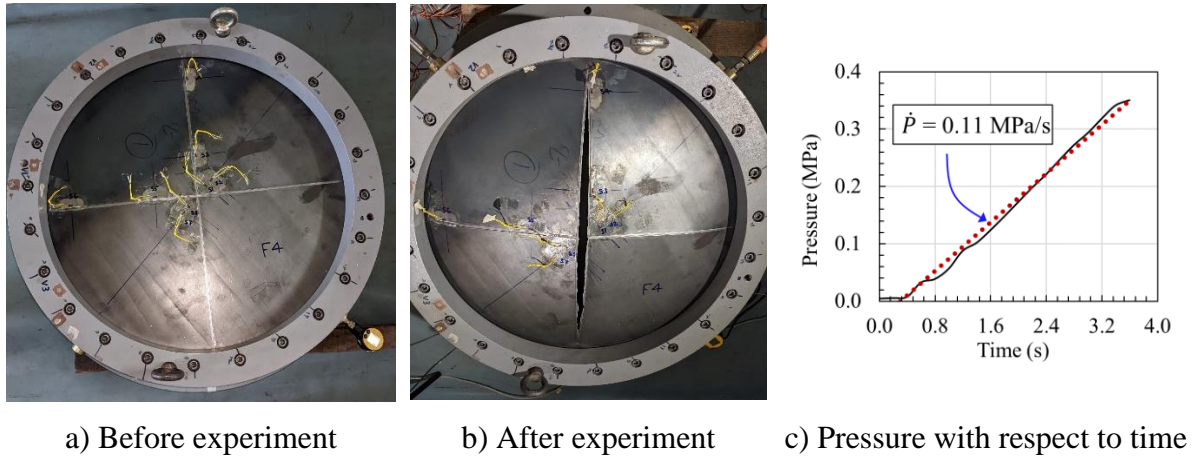
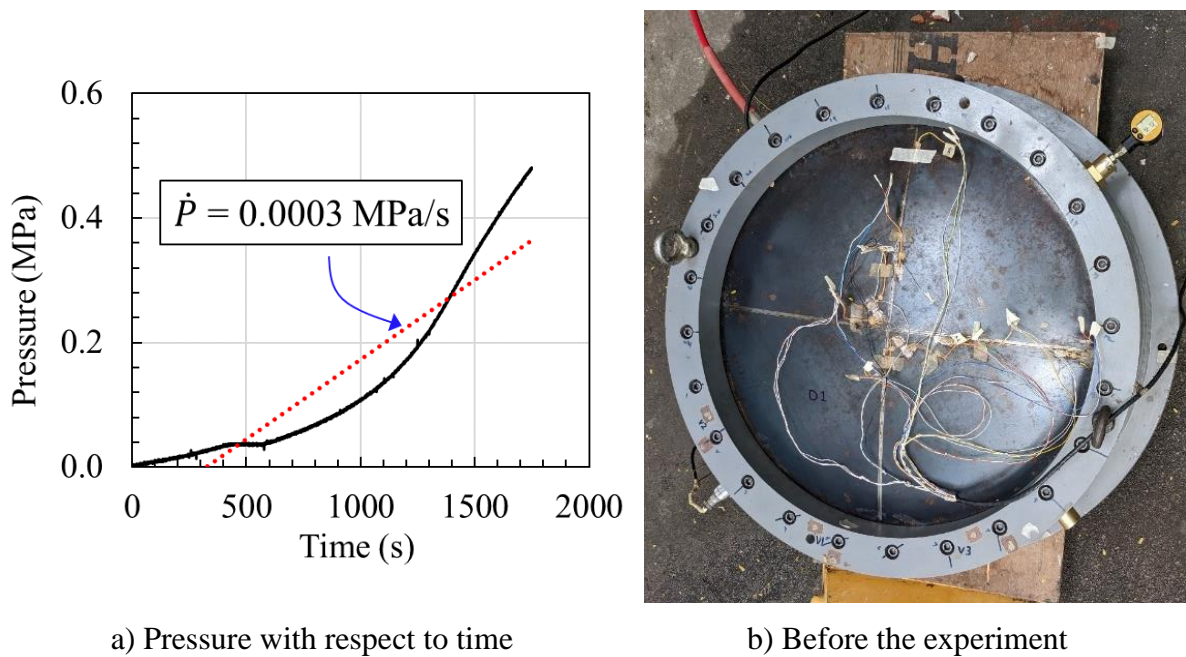


Figure 6.13: Experiment on FSMD F4

The loading rate during the experiment is observed to be 0.11 MPa/s and the peak pressure is 0.35 MPa which is noted as the burst pressure of the disc. The experiment continued for 3.6 seconds, and the pressure *with respect to* loading rate is shown in Figure 6.13(c). During this experiment, similar to disc F3, the formation of a dome and failure along a single score by forming a crack is observed.

6.5.4 Hydraulic experiment on DSMD – D1

The hydraulic experiment on DSMD-D1 is conducted by subjecting the disc to hydraulic pressure. The pressure with respect to time is shown in Figure 6.14(a), the disc before the experiment is shown in Figure 6.14(b), and the disc after the experiment is shown in Figure 6.14(c).



Crack formation away from centre



c) Crack initiation during the experiment

Figure 6.14: Experiment on DSMD D1

The chamber is pre-filled with water and additional water is supplied by a reciprocating hydraulic pump at 0.5 lpm and the observed loading rate of the experiment is 0.0003 MPa/s. The experiment continued for 29.1 minutes before forming a small crack away from the centre of the disc, as shown in the inset of Figure 6.14(c) and the observed peak pressure is 0.582 MPa which is noted as the burst pressure of the disc. After the crack initiation, water started leaking through the crack and as a result, the pressure drop was observed, due to which the crack propagation was not observed.

6.5.5 Pneumatic experiment of DSMD – D2

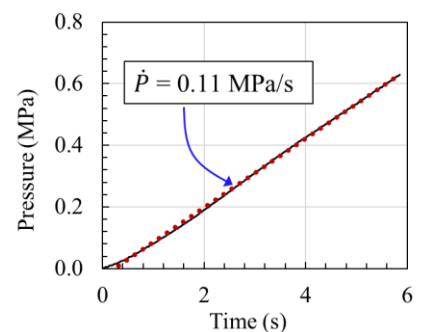
The pneumatic loading experiment on DSMD-D2 is conducted by subjecting the disc to a pneumatic supply of 250 bar. The disc before the experiment is shown in Figure 6.15(a), and the disc after the experiment is shown in Figure 6.15(b).



a) Before experiment



b) After experiment



c) Pressure with respect to time

Figure 6.15: Experiment on DSMD D2

The loading rate during the experiment is observed to be 0.11 MPa/s and the peak pressure is 0.63 MPa, which is noted as the burst pressure of the disc. The experiment continued for 5.9 seconds and the pressure with respect to loading rate is shown in Figure 6.15(c). In this experiment, crack propagated along both scores and the disc bursts by forming four proper petals.

6.5.6 Pneumatic experiment of DSMD – D3

The pneumatic experiment on DSMD-D3 is conducted by subjecting the disc to a pneumatic supply of 250 bar. The disc before the experiment is shown in Figure 6.16(a), and the disc after the experiment is shown in Figure 6.16(b).

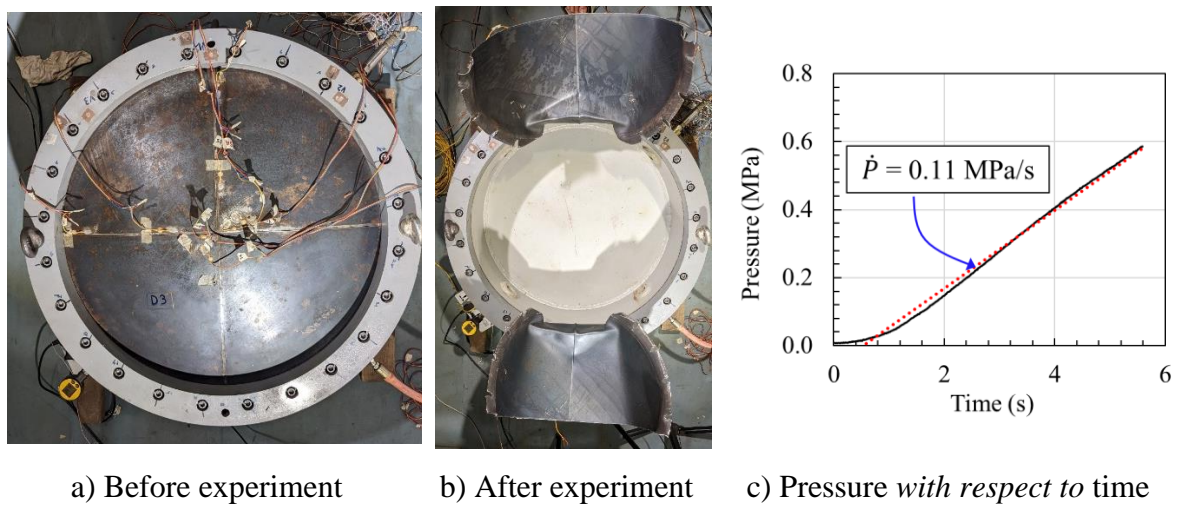


Figure 6.16: Experiment on DSMD D3

The loading rate during the experiment is observed to be 0.11 MPa/s and the peak pressure is 0.59 MPa, which is noted as the burst pressure of the disc. The experiment continued for 5.6 seconds and the pressure with respect to loading rate is shown in Figure 6.16(c). In this experiment, the crack propagated along only one score and the disc bursts by forming two petals.

6.5.7 Summary of experimental results

In all the experiments, crack initiated and propagated along the scored region except in D1. In D1, a crack is initiated but cannot be propagated due to pressure loss before propagation. Mode-1 failure is observed, which is the most common failure behaviour in membranes. The crack propagation is entirely random behaviour. Among pneumatically loaded discs, only disc D2 exhibited four regular petals where, as in all other discs *viz.* F3, F4 and D3 crack propagation happened through only one score. This can be attributed to the variations in the depth of scores in both directions, which is a practical challenge in manufacturing scored discs. This problem can be avoided by forming scores through punching to maintain uniform score depth in all scores. Another method is to ensure a higher loading rate which will allow the formation of a crack near the centre of the disc, increasing the probability of crack propagation through all scores.

6.6 Numerical simulation

The numerical simulation methodology explained in Chapter 3 is followed to predict the behaviour of FSMD and DSMD. Quarter geometry is modelled by assuming symmetric boundary conditions. Johnson-Cook material and damage model parameters of E250 structural steel determined and given in Table 2.4 are used for the numerical simulation of discs. A uniformly distributed pressure load was applied on the plain side of the disc. To reduce the analysis time, the loading rate is accelerated by the method explained in Section 3.2.4.

6.6.1 Numerical simulation of FSMD

6.6.1.1 FE Model, loads and boundary conditions

Due to the symmetry of the problem, a quarter model is considered for simulation. The model is discretised with 246558 elements using the C3D8R element, an eight-node brick element with reduced integration and hourglass control. Symmetrical boundary conditions are imposed on vertical and horizontal surfaces of geometry, as shown in Figure 6.17(a) and all three degrees of freedom of nodes in the annular area of the disc between diameters 720 mm and 800 mm are fully constrained, as shown in Figure 6.17(b).

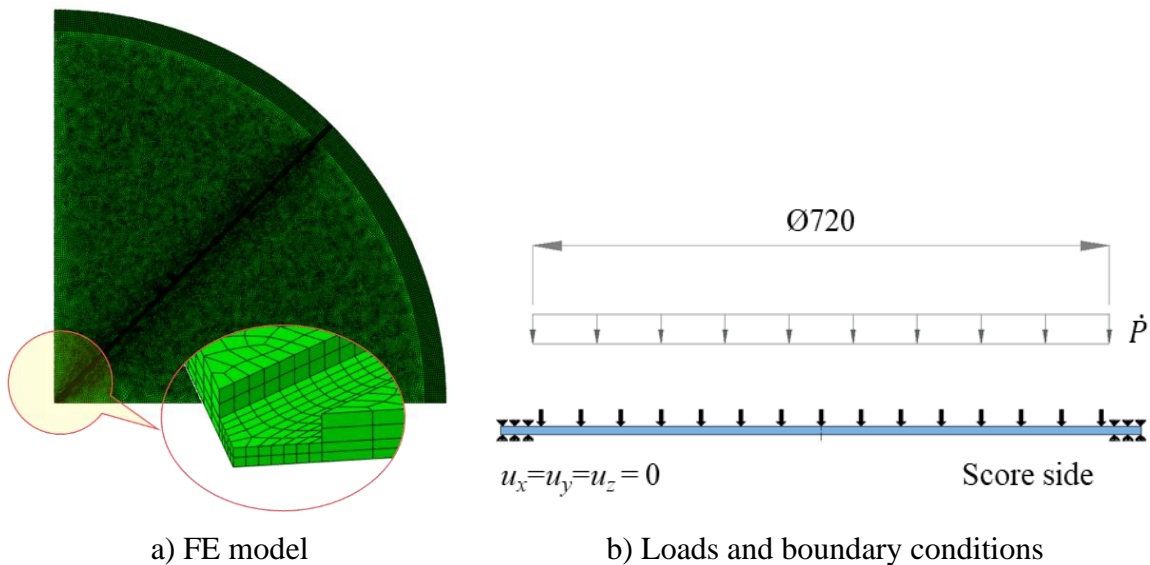


Figure 6.17: FE model, loads and boundary conditions of FSMD

6.6.1.2 Loading rate

The modal analysis of the thin FSMD shown in Figure 6.17(a) resulted in the fundamental natural frequency ω_n as 36.67 Hz. Therefore, Eq. (3.4) results in $t_d = 1.09$ s. Considering the experimentally achieved average P_b of 0.332 MPa and the calculated t_d , the rate of loading rate for the quasi-static regime was determined as 0.306 MPa/s. It was adopted in the present numerical simulation.

6.6.1.3 Results

From the numerical results shown in Figure 6.18(a), as the pressure applied on the disc increased to 0.2 MPa, the equivalent stress was higher along the score and reached 322 MPa. Strain in the scored region reached the plastic stage and the equivalent plastic strain is around 0.02. The stress distribution in FSMD just before failure is shown in Figure 6.18(b), where equivalent stress reached 727 MPa and plastic strain reached 1.18.

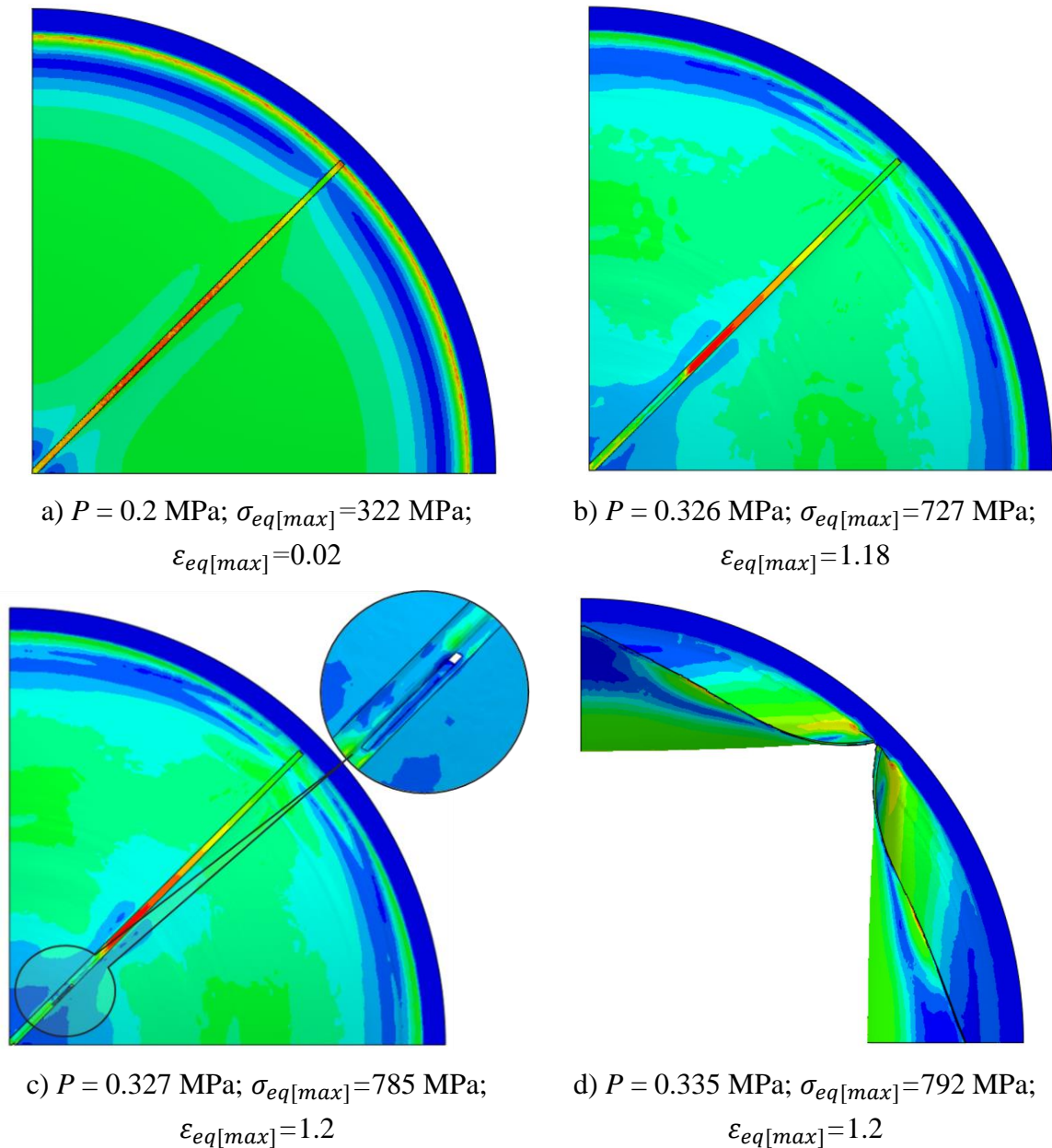


Figure 6.18: Failure initiation and propagation in FSMD

Element deletion is observed at $P = 0.327 \text{ MPa}$, as shown in Figure 6.18(c). Equivalent stress reached up to 785 MPa and equivalent plastic strain reached 1.2. As the pressure increased, the crack propagated along the score and petal formation was observed, as shown in Figure 6.18(d). But this is a hypothetical situation, as practically, due to the formation of the crack,

fluid escapes through the crack and the pressure acting on the disc comes down, which may not support the formation of petals under hydraulic loading.

6.6.2 Numerical simulation of DSMD

6.6.2.1 Hydro-forming of DSMD

Hydro-forming operation is carried out to obtain the semi-spherical shape of the DSMD, as shown in Figure 6.19. The manufacturing procedural details and FE simulation results are discussed in Section 5.3. Due to the hydroforming operation, a thickness reduction along the disc's radius is observed, as shown in Figure 5.17. The thickness of the disc is reduced to 1.93 mm at the centre. Then scores are made to a uniform depth of 1.4 mm. As a result, the disc's thickness at the score region below the disc is reduced gradually from 0.59 mm at the end of the score to 0.53 mm at the centre of the disc.

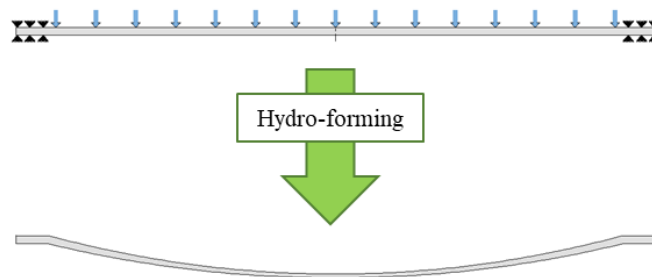
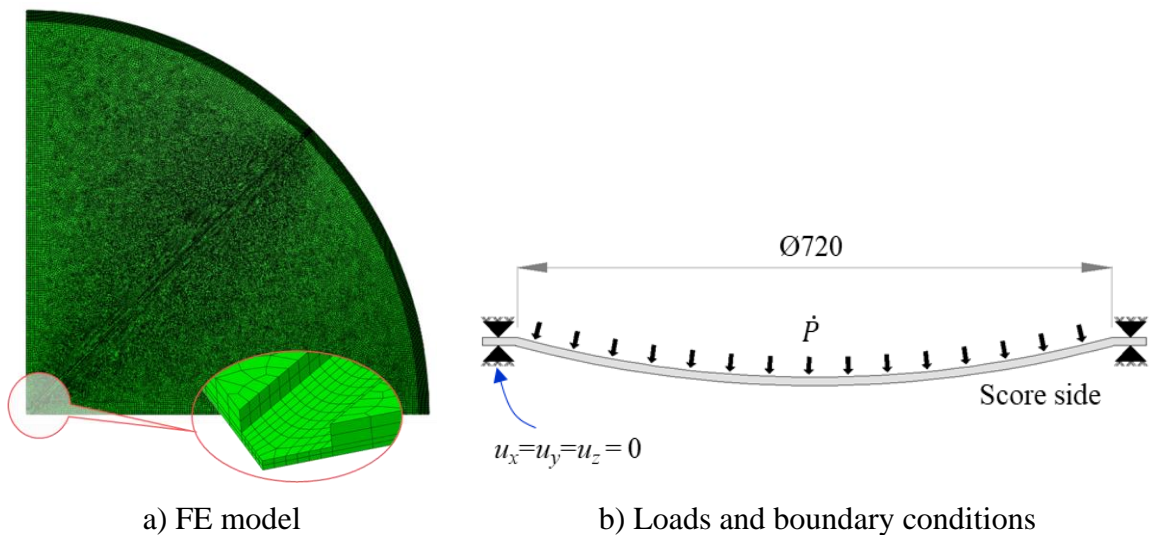


Figure 6.19: Hydro-forming operation on DSMD

6.6.2.2 FE model, loads and boundary conditions



a) FE model

b) Loads and boundary conditions

Figure 6.20: FE model, loads and boundary conditions of DSMD

Due to the symmetry of the problem, a quarter model is considered for simulation. The model is discretised with 251378 elements using the C3D8R element, an eight-node brick element with reduced integration and hourglass control. Symmetrical boundary conditions are imposed

on vertical and horizontal surfaces of geometry, as shown in Figure 6.20(a) and all three degrees of freedom of nodes in the annular area of the disc between diameters 720 mm and 800 mm are fully constrained, as shown in Figure 6.20(b).

6.6.2.3 Loading rate

The modal analysis of the thin DSMD shown in Figure 6.20(a) resulted in the fundamental natural frequency ω_n as 452.1 Hz. Therefore, Eq. (3.4) results in $t_d = 0.088$ s. Considering the experimentally achieved average P_b of 0.601 MPa and the calculated t_d , the rate of loading for the quasi-static regime is determined as 6.8 MPa/s. It is adopted in the present numerical simulation.

6.6.2.4 Results

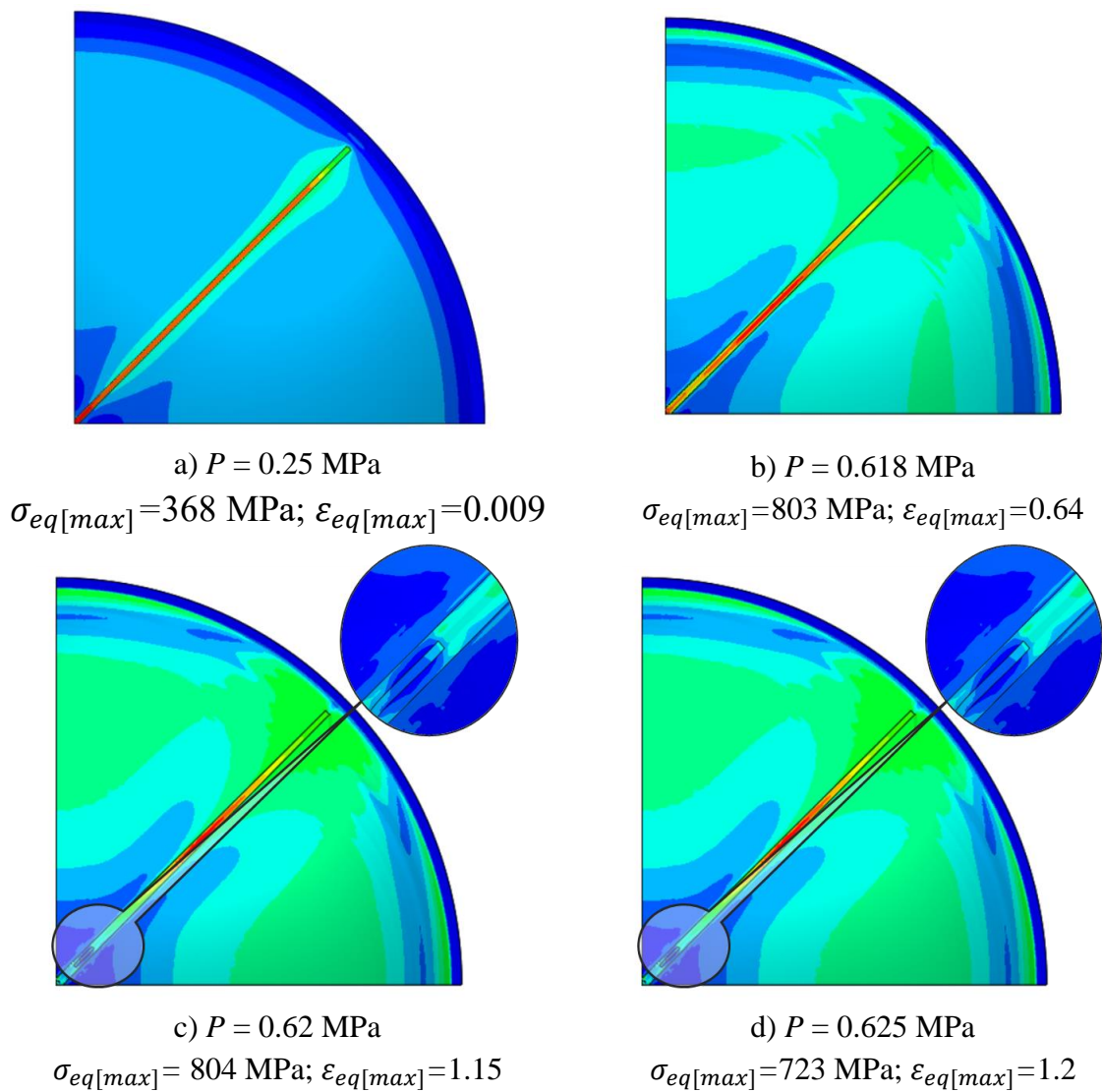


Figure 6.21: Failure initiation and propagation in DSMD

From the numerical results shown in Figure 6.21(a), as the pressure applied on the disc increased to 0.25 MPa, the equivalent stress was higher along the score and reached 368 MPa.

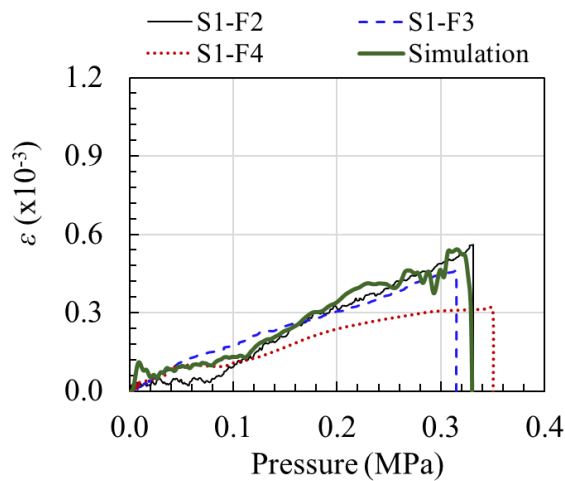
Strain in the scored region reached the plastic stage and the equivalent plastic strain is around 0.009. The stress distribution in DSMD just before failure is shown in Figure 6.21(b), where equivalent stress reached 803 MPa and plastic strain reached 0.64. Element deletion is observed at $P = 0.62$ MPa, as shown in Figure 6.21(c). Equivalent stress reached up to 804 MPa and equivalent plastic strain reached 1.15. As the pressure increased, the crack propagated along the score and petal formation was observed, as shown in Figure 6.21(d). But this is a hypothetical situation, as practically, due to the formation of the crack, fluid escapes may not support the formation of petals under less loading rate as discussed for FSMD.

6.7 Comparison of experimental results with predictions

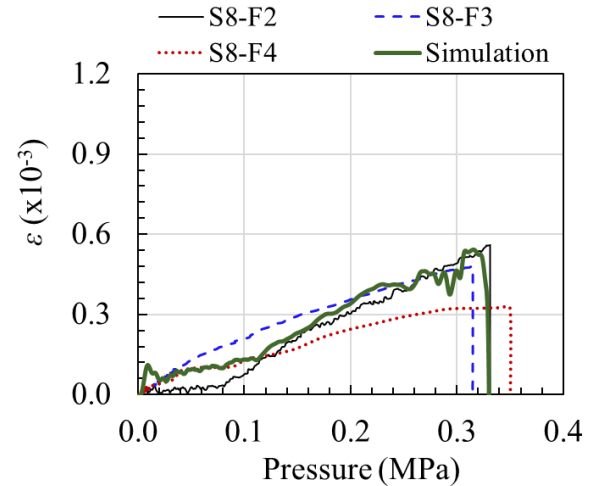
Experimental results are compared with numerical simulations for both FSMD and DSMD.

6.7.1 Comparison of results for FSMD

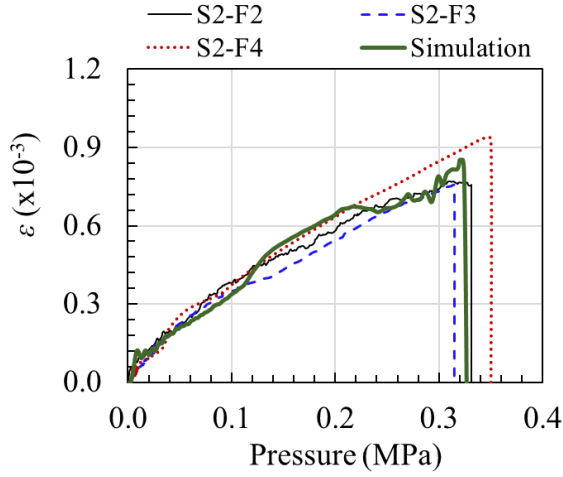
Experimental and numerical simulation results are compared at eight strain gauge locations, as shown in Figure 6.22.



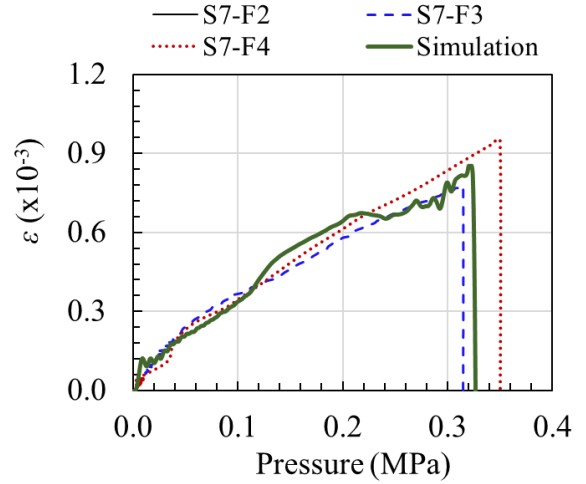
a) Strain gauge location at S1



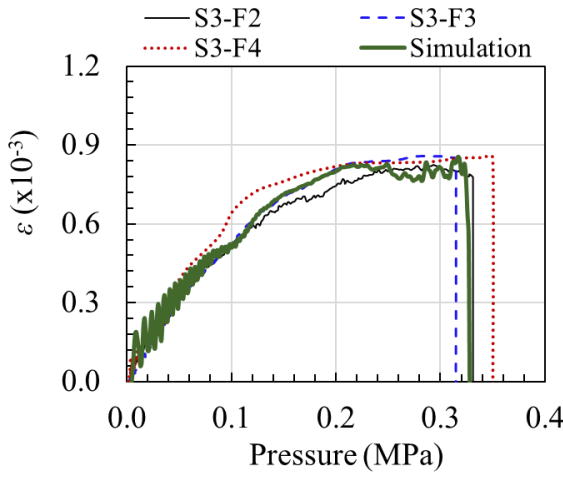
b) Strain gauge location at S8



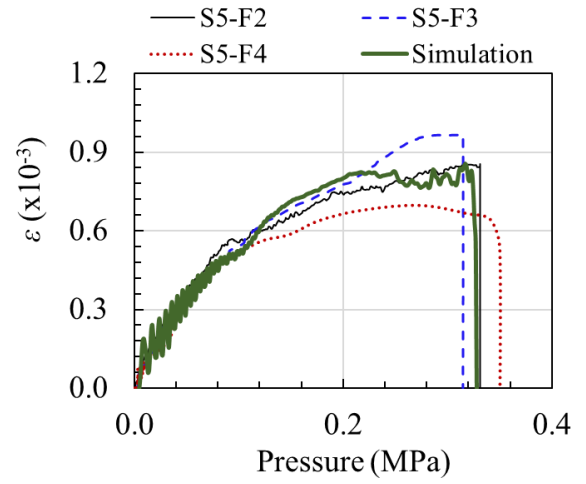
c) Strain gauge location at S2



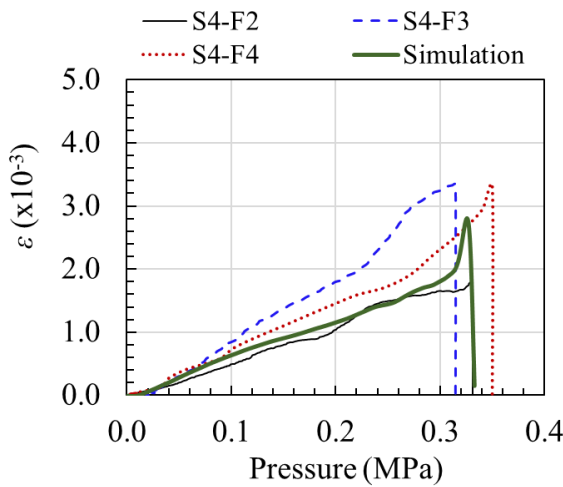
d) Strain gauge location at S7



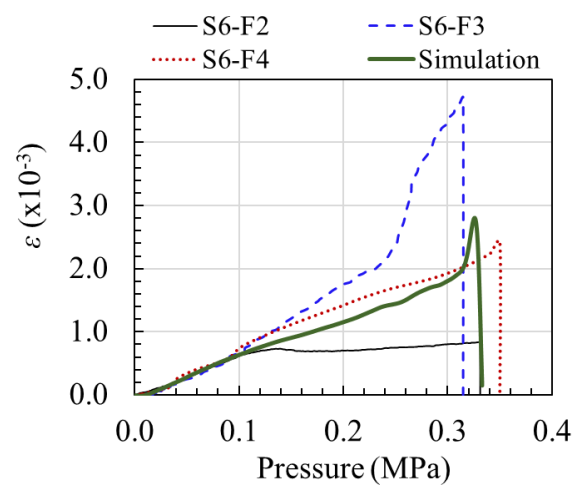
e) Strain gauge location at S3



f) Strain gauge location at S5



g) Strain gauge location at S4

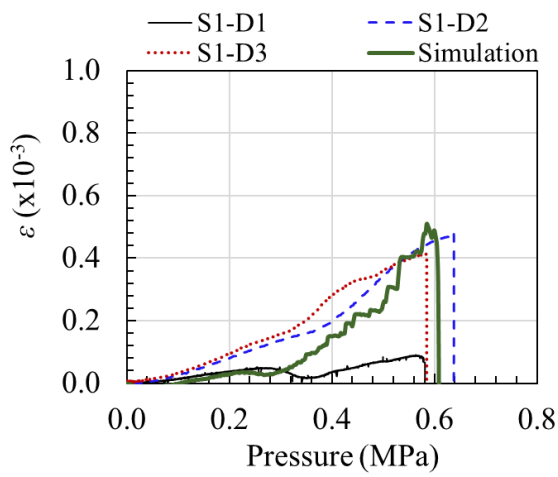


h) Strain gauge location at S6

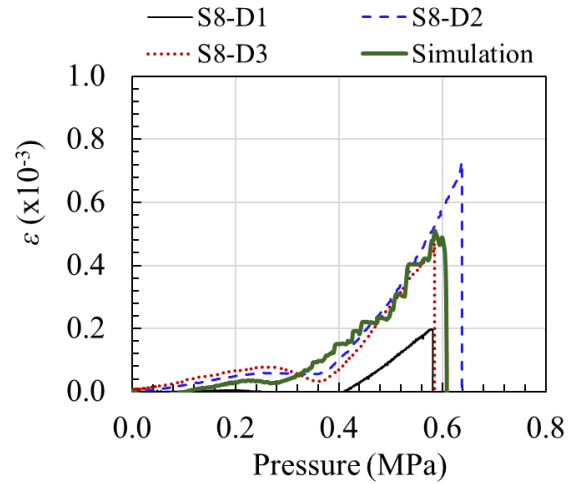
Figure 6.22: Comparison of experimental and numerical results for FSMD

6.7.2 Comparison of results for DSMD

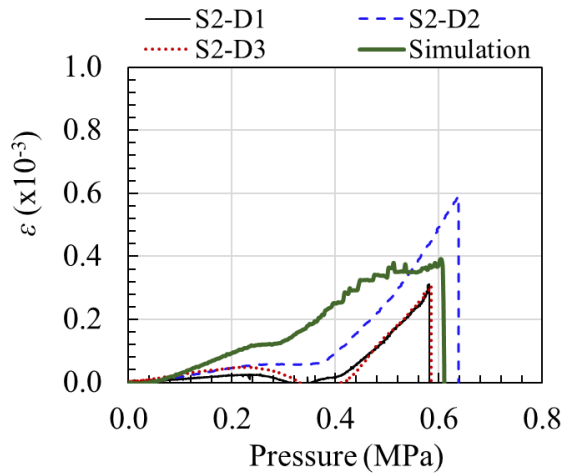
Experimental and numerical simulation results are compared at eight strain gauge locations, as shown in Figure 6.23 for the DSMD.



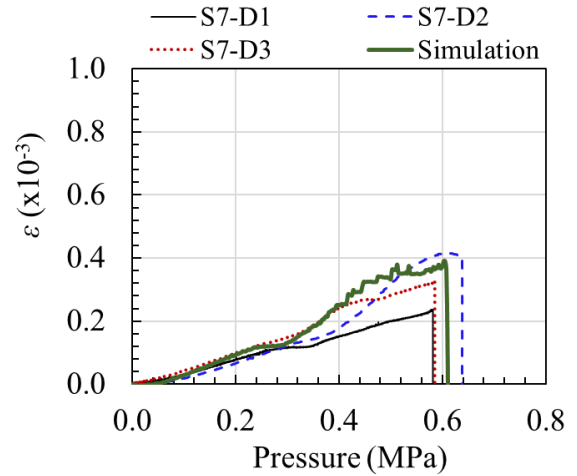
a) Strain gauge location at S1



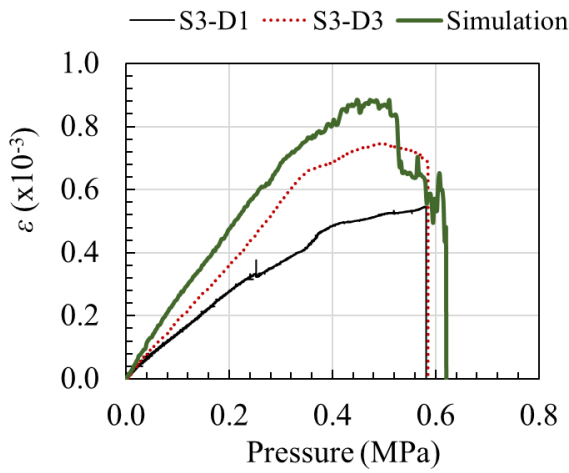
b) Strain gauge location at S8



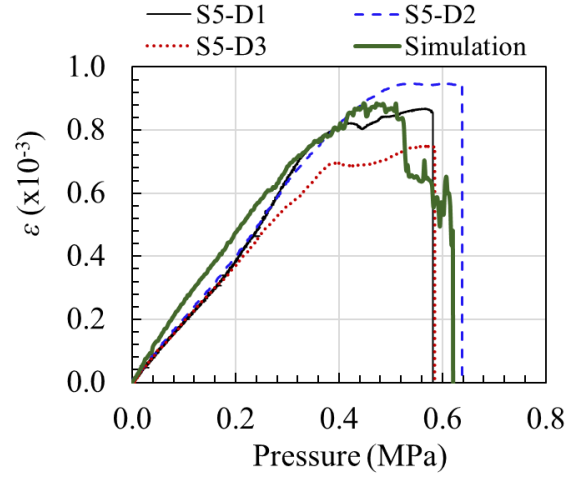
c) Strain gauge location at S2



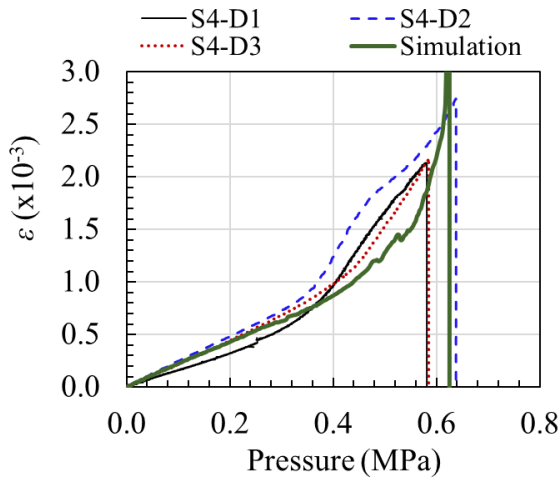
d) Strain gauge location at S7



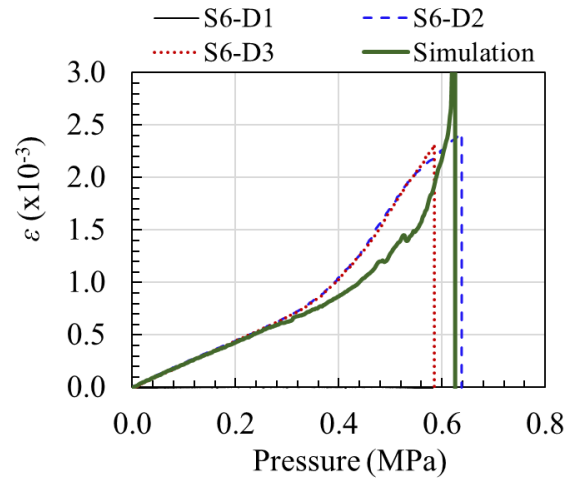
e) Strain gauge location at S3



f) Strain gauge location at S7



g) Strain gauge location at S4



h) Strain gauge location at S6

Figure 6.23: Comparison of experimental and numerical results for DSMD

6.8 Summary

In the experiments conducted on both FSMD and DSMD, strain gauges S1, S2, S7 and S8 are located near the centre of the disc at 45° to score location, as shown in Figure 6.1(a) and 6.3(a). Strain gauges S3, S4, S5, and S6 are mounted just adjacent to the score in the score direction. Among these, S3 and S5 are nearer to the centre as S4 and S6 are near to fixity. A similarity in strain data can be observed between S1-S8, S2-S7, S3-S5 and S4-S6.

A total of six experiments were conducted, and the summary of the results is given in Table 6.2.

Table 6.2: Comparison of experimental and numerical simulation results

Disc	Loading type	Loading rate (MPa/s)	Experimental burst pressure (bar)		Predicted burst pressure (bar)	% Difference	Remarks
			P_b	P_b (avg)			
F1	-	-	-	-	3.27	1.5%	Damaged disc
F2	Hydrostatic	0.0003	3.31	3.32			A crack formed along the groove in one direction
F3	Pneumatic	0.02	3.14				A crack formed along the groove in one direction
F4	Pneumatic	0.11	3.5				A crack formed along the groove in one direction
D1	Hydrostatic	0.0003	5.82	6.01	6.2	3.1%	A crack formed at a single location
D2	Pneumatic	0.11	6.3				Four petals formed
D3	Pneumatic	0.11	5.85				Two petals formed

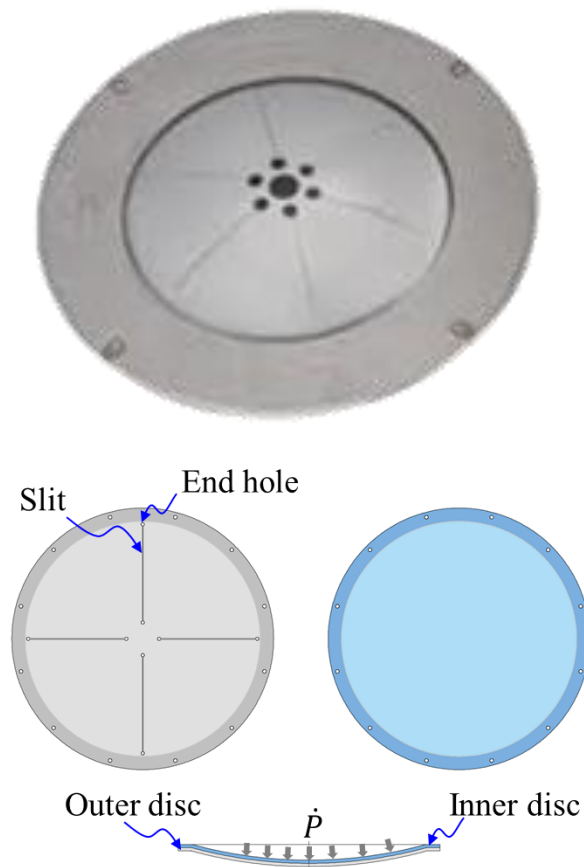
The loading rate for the quasi-static regime of FSMD is 0.306 MPa/s and DSMD is 6.8 MPa/s. Since all the experiments are conducted below these loading rates, burst pressure obtained from the experiments is averaged. The average burst pressure of FSMD in the quasi-static regime is 3.32 bar and the average burst pressure of DSMD is 6.01 bar. The difference in prediction for FSMD is 1.5% and DSMD is 3.1% which validates the material model, numerical simulation procedure and experimental methodology. This procedure can be confidently adopted for RDs made of different materials or RDs made with a different configuration.

Non-Monolithic Design of Rupture Disc

7.1 Introduction

The rupture disc (RD) design discussed so far in previous chapters is a monolithic configuration where scores are provided to induce stress concentration and facilitate crack initiation and propagation. However, there are limitations in using such scored discs for application in motor containers where the disc exhibits high burst pressure and poses manufacturing challenges in producing scores accurately to the required depth over entire radius.

Several RD configurations are available, as discussed in Chapter-1. A non-monolithic type of RD design is also considered for motor container application, where slits/holes are provided to reduce the burst pressure. These slits are easy to manufacture. But, such type of RD configuration requires an additional membrane like a member to provide the sealing during static storage conditions. Typical slit type RD is shown in Figure 7.1(a).



a) Typical slit type RD [2]

b) Configuration of slit type RD

Figure 7.1: Slotted type non-monolithic rupture disc

This non-monolithic configuration of RD consists of an outer disc with slits made of high strength material and an inner disc with low-strength material. The slit configuration helps select low sheet thickness, resulting in reduced burst pressure. Usually, these slits are very narrow and made using wire-cut electric discharging machining (EDM) or milling operations. These slits are provided with holes at the end, as shown in Figure 7.1(b), to avoid the stress concentration during static loading and increase the static strength of the disc.

7.2 RD selection criteria

RD selection criteria has been formulated to meet the following criteria so that the selected RD meets the functional requirements for the current application.

7.2.1 Burst Pressure and Factor of Safety

Burst pressure, P_b , is a disc characteristic that defines its ability to fail and should happen as quickly as possible. In contrast, the factor of safety, FS , is characteristic of the disc, which defines the ability of the disc to withstand load under storage conditions. The factor of safety is given by,

$$FS = \frac{\text{Stress developed in static condition}}{\text{Yield strength of material}} \quad (7.1)$$

To shortlist the discs to meet the essential functional requirement, the criteria imposed for the selection of RD for the current application are:

Burst pressure, $P_b < 4$ bar and Factor of safety, $FS > 1$.

7.2.2 Operating ratio

The operating ratio, OR , is calculated based on Eq. (4.1). Higher OR indicates higher $MSOP$ for the same burst pressure.

7.2.3 Impulse

The impulse, I , generated up to the burst is given by Eq. (4.2). Lower impulse indicates quickness with disc fails, and the disc generates less generated impulse during the burst.

7.3 Geometrical configurations

The design of the basic geometrical configuration of slit type RD is shown in Figure 7.2. For comparison, 2 mm sheet thickness is considered. The basic geometric parameters, such as outer diameter, dome height, etc., are kept identical to the domed scored metallic disc (DSMD).

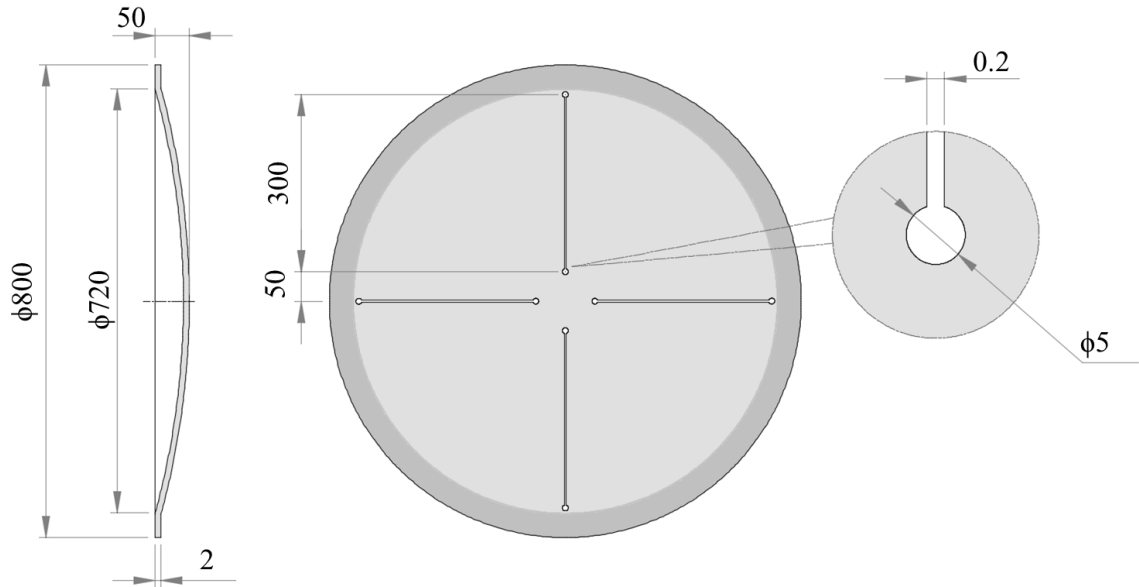
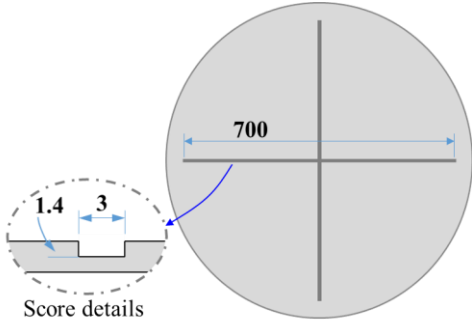
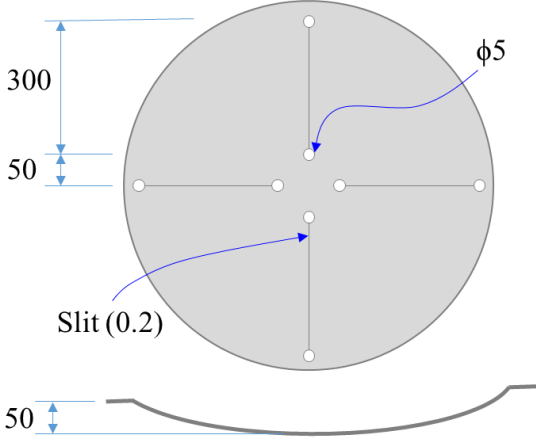
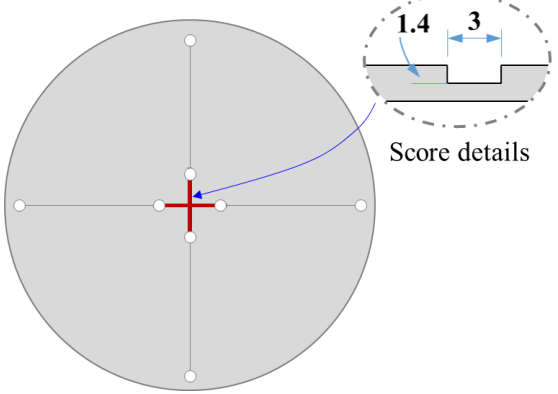
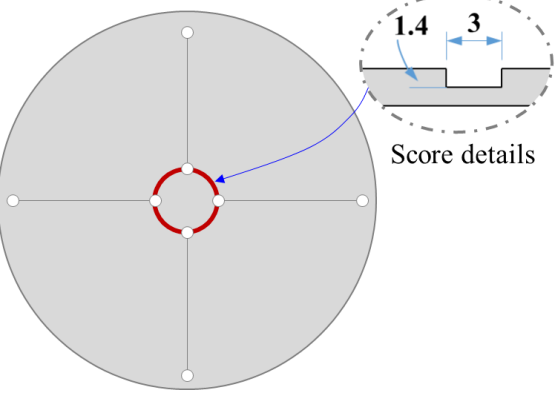


Figure 7.2: Geometric configuration of slit RD

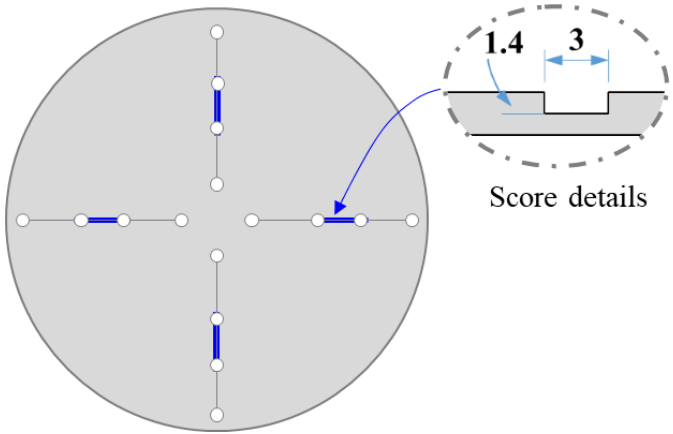
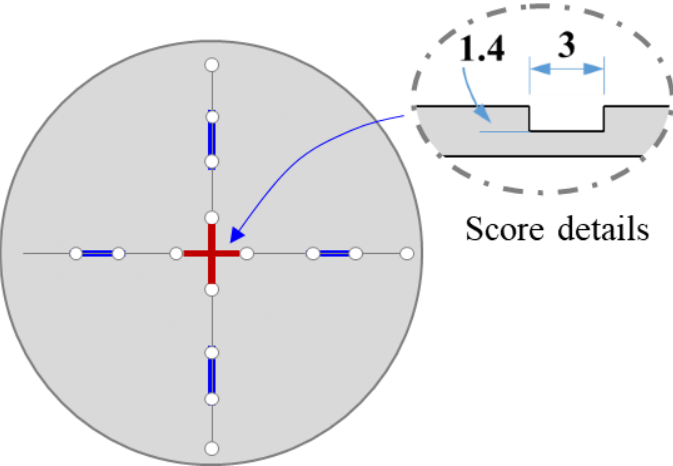
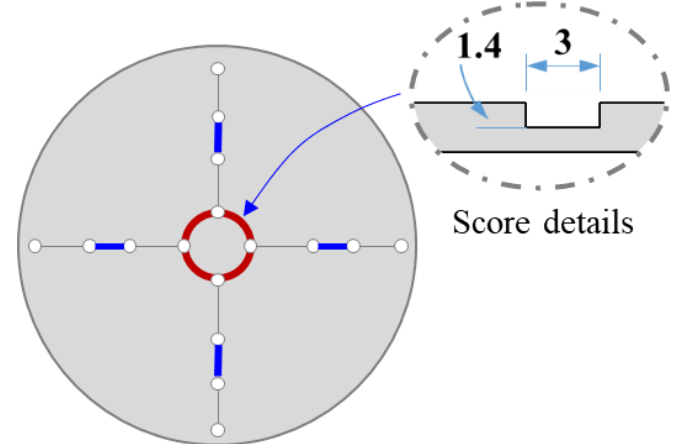
Four slits are provided in the ‘+’ configuration. Each slit starts at 50 mm from the centre of the disc and the length of the slit is around 300 mm. Holes of 5 mm diameter are provided on both ends of slits. This is the basic variant considered and slit geometry is changed for each variant to improve the operating ratio of the disc. In some of the variants, scores are provided with limited length connecting these slots to further reduce the burst pressure. All the variants are provided in Table 7.1.

Table 7.1: Variants of RD considered for the present study

Variant	Geometry	Remarks
DSMD		As discussed in previous chapters, the domed scored metallic disc with two scores provided in the ‘+’ configuration.

Variant	Geometry	Remarks
Variant-1	 <p>300 50 Slit (0.2) $\phi 5$ 50</p>	Slit disc with four slits provided in '+' configuration.
Variant-1A	 <p>Score details 1.4 3</p>	Variant-1, in which slits are joined by scores in the direction of the slit.
Variant-1B	 <p>Score details 1.4 3</p>	Variant-1, in which slits are joined by the score in a pitch circle diameter (PCD) concentric to disc diameter.

Variant	Geometry	Remarks
Variant-2		<p>Slit disc with four slits provided in ‘+’ configuration wherein each slit is divided into two slits.</p>
Variant-2A		<p>Variant-2, in which inside slits are joined by scores in the direction of the slit at the centre.</p>
Variant-2B		<p>Variant-2, in which inside slits are joined by the score in a pitch circle diameter (PCD) concentric to the disc diameter.</p>

Variant	Geometry	Remarks
Variant-3	 <p>The diagram shows a circular disc with four radial slits (top, bottom, left, right). Each slit contains a blue score. A detail view labeled 'Score details' shows a cross-section of the score between two slits, with a width of 1.4 and a depth of 3.</p>	<p>Variant-2, in which scores are provided between two slits in the same direction.</p>
Variant-3A	 <p>The diagram shows a circular disc with four radial slits. A red cross-shaped score is located at the center, joining the inner ends of the slits. A detail view labeled 'Score details' shows a cross-section of the score between two slits, with a width of 1.4 and a depth of 3.</p>	<p>Variant-3, in which inside slits are joined by scores in the direction of the slit at the centre.</p>
Variant-3B	 <p>The diagram shows a circular disc with four radial slits. A red circular score is located at the center, joining the inner ends of the slits. A detail view labeled 'Score details' shows a cross-section of the score between two slits, with a width of 1.4 and a depth of 3.</p>	<p>Variant-3, in which inside slits are joined by the score in a pitch circle diameter (PCD) concentric to the disc diameter.</p>

7.4 Numerical simulation of slit disc (Variant-1)

As explained in section 5.3.7, during the hydroforming of DSMD, a thickness reduction of 0.07 mm at the centre is observed and the same is considered in present numerical simulations.

7.4.1 FE model, loads and boundary conditions

The FE model of a typical slit disc is shown in Figure 7.3(a). Due to the symmetry of the problem, the quarter model is considered for simulation. The model is discretised with 246136 elements using the C3D8R element, an eight-node brick element with reduced integration and hourglass control. The model is discretised using a minimum element size of 0.3 mm and an average element size of 0.5 mm. Symmetric boundary conditions are imposed on vertical and horizontal surfaces of geometry as shown in Figure 7.3(b), and all three degrees of freedom of nodes in the annular area of the disc between diameters 720 mm and 800 mm are fully constrained.

7.4.2 Simulation under static loading

The static structural analysis uses ABAQUS/Standard [60] for the FE model shown in Figure 7.3(a). Storage pressure load of 0.02 MPa is applied on the disc's concave side, and the DOF of nodes between 720 mm and 800 mm diameter of the disc is constrained, as shown in Figure 7.3(b). The maximum equivalent stress developed is 166.3 MPa, and from Eq. (7.1), a factor of safety, $FS = 1.5$. The static structural analysis iterations have been carried out to find the maximum static operating pressure of the slit disc, which causes yielding in the disc, which is found to be 0.3 bar.

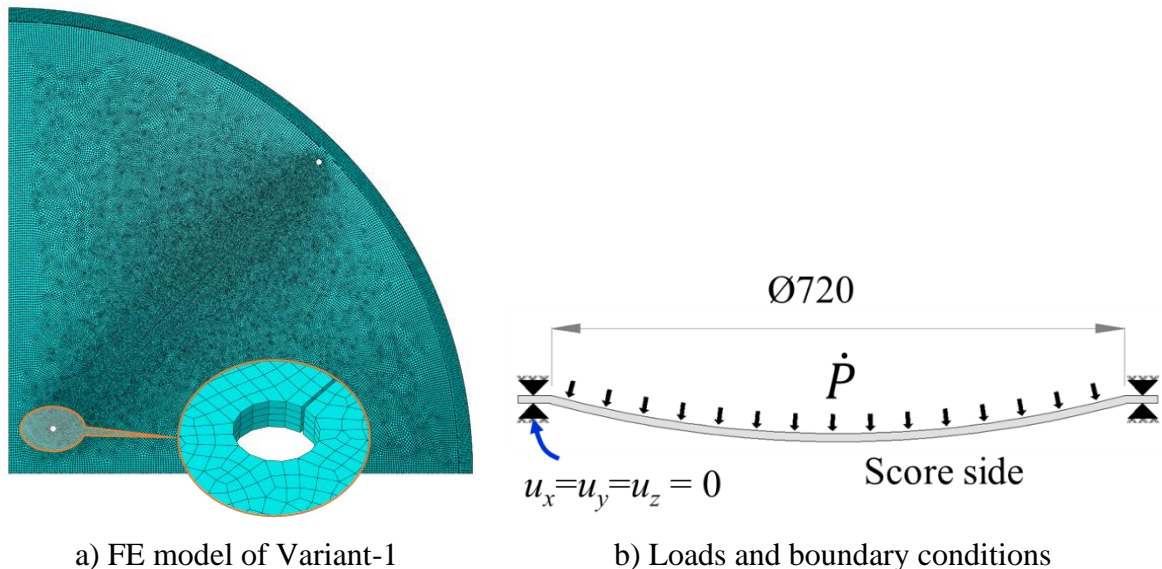


Figure 7.3: FE model, loads and boundary conditions in RD variants

7.4.3 Simulation under impulsive loading

The non-linear dynamic explicit analysis is carried out using ABAQUS/Explicit [61], similar to the procedure explained in Section 6.6 adopted for simulation.

7.4.3.1 Loading rate

For comparison, a loading rate of 6.8 MPa/s followed for DSMD, as explained in Section 6.6.2, is adopted in the present numerical simulations.

7.4.3.2 Results

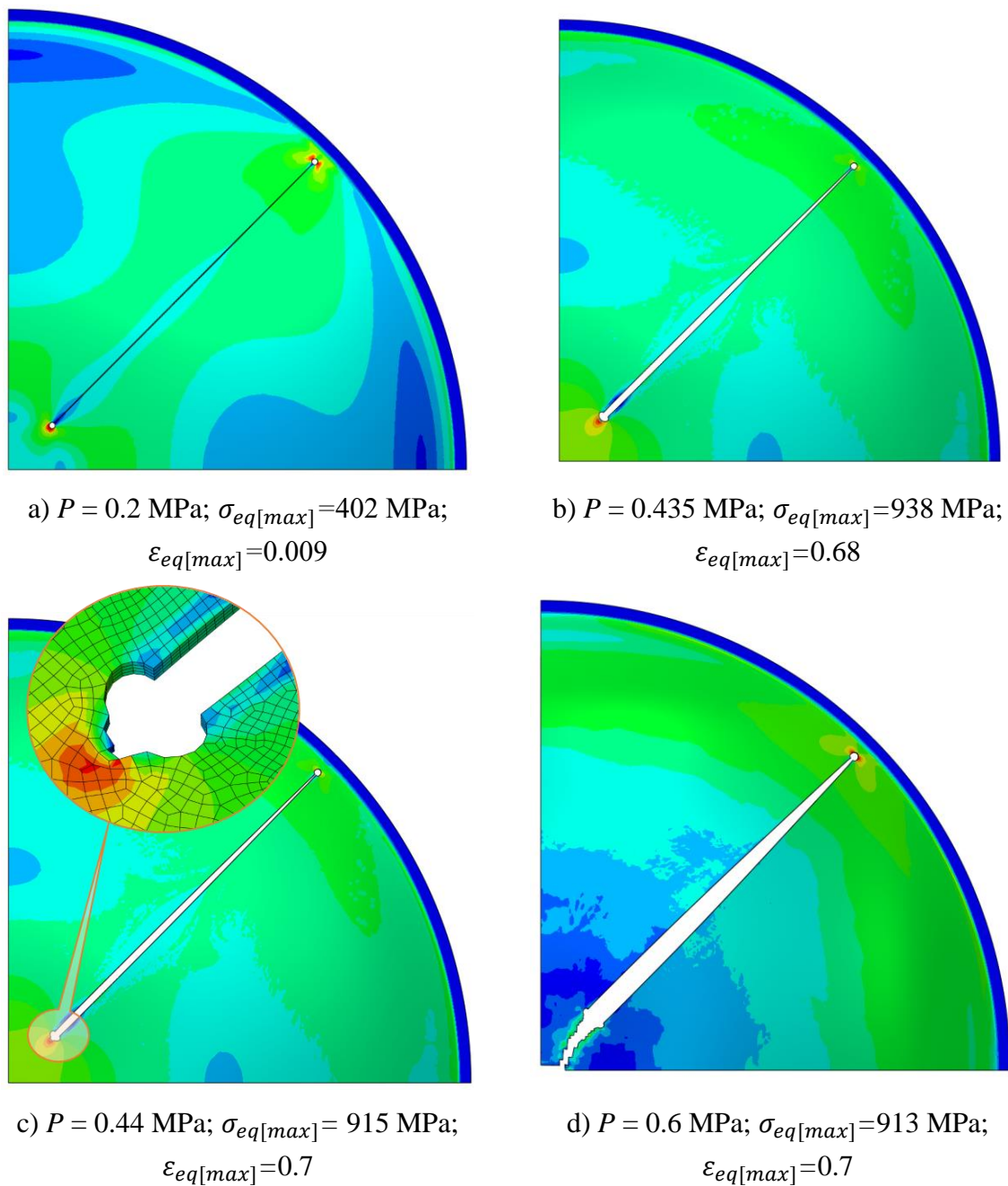


Figure 7.4: Failure initiation and propagation in slit disc (Variant-1)

From the numerical results shown in Figure 7.4(a), as the pressure applied on the disc increases to 0.2 MPa, the equivalent stress near the hole at the slit end reaches 402 MPa. The strain in this location reached the plastic stage, and the equivalent plastic strain is around 0.009. The stress distribution in the slit disc just before the failure is shown in Figure 7.4(b) where equivalent stress reached 938 MPa and plastic strain reached 0.68. Element deletion is observed at $P = 0.44$ MPa, as shown in Figure 7.4(c). Equivalent stress reached up to 915 MPa, and equivalent plastic strain reached 0.7. As the pressure increases, the crack is propagated towards one axisymmetric edge, and the petal formation is observed, as shown in Figure 7.4(d). The Burst pressure of the slit disc is 4.4 bar with an MSOP of 0.03 MPa, and the operating ratio from Eq. (4.1) is 7%. With a reaction force of 216.1 kN and a burst time of 26.5 ms, the impulse transmitted to the fixity up to initiation of failure is found to be 6 kN-s.

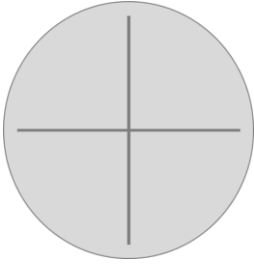
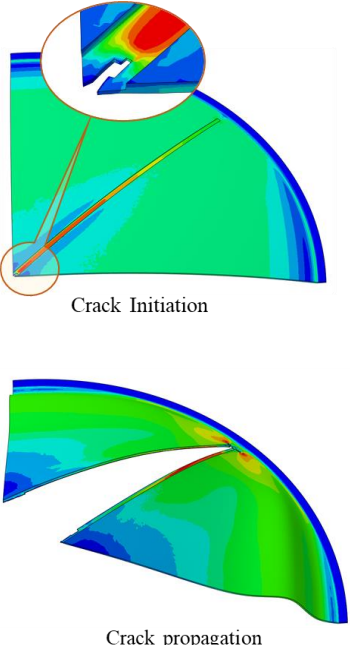
7.5 Results and discussions

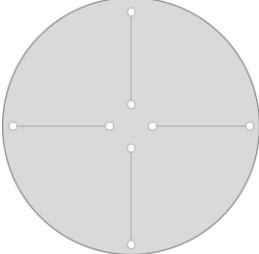
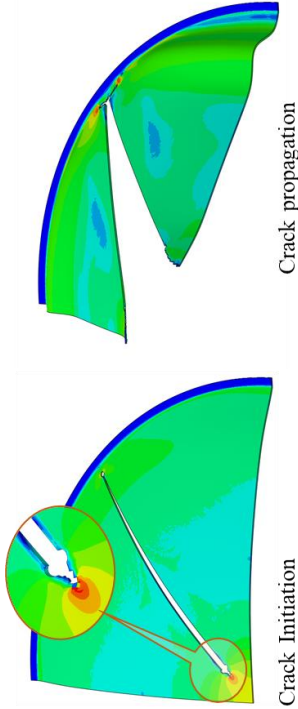
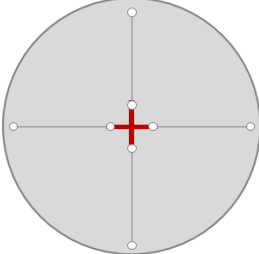
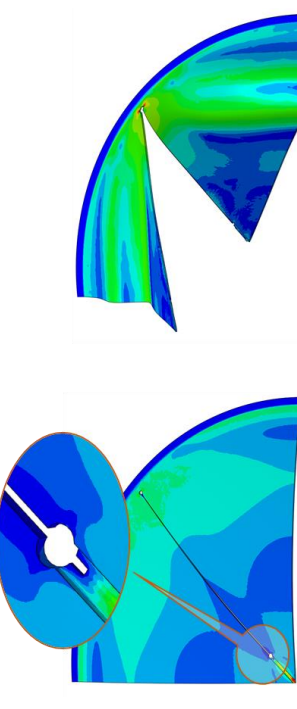
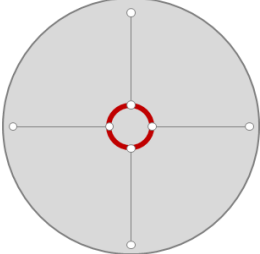
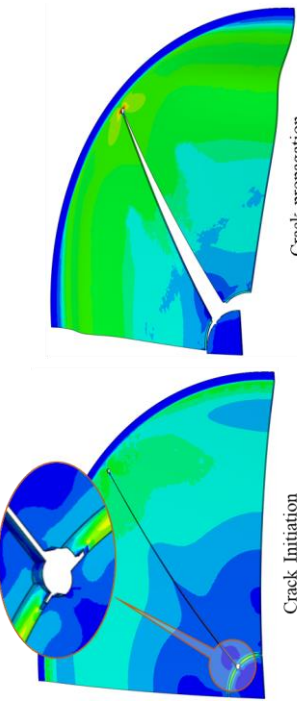
The numerical simulation procedure explained in Section 7.4 is repeated for all other variants and the consolidated results, failure pattern is presented in Table 7.2.

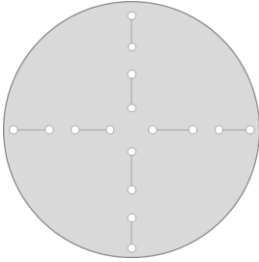
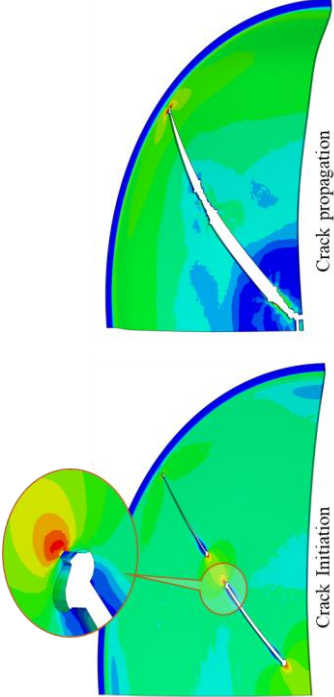
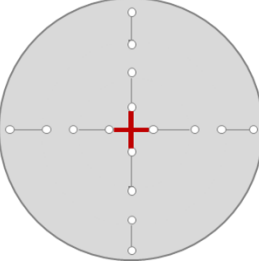
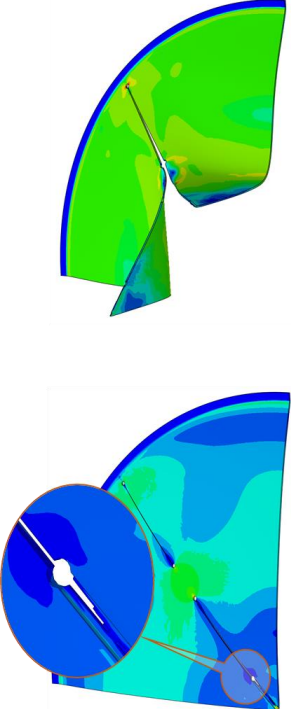
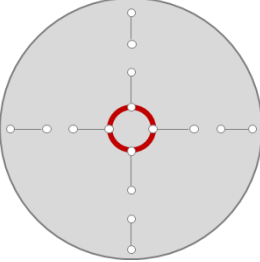
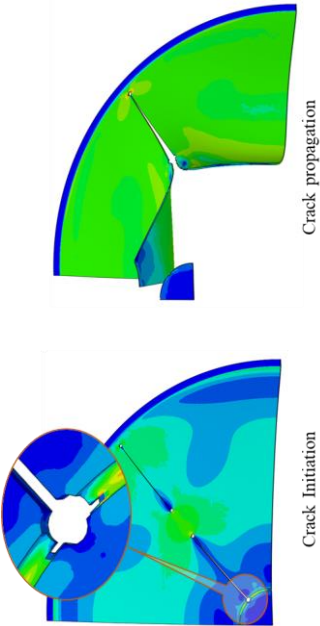
7.5.1 FE analysis results

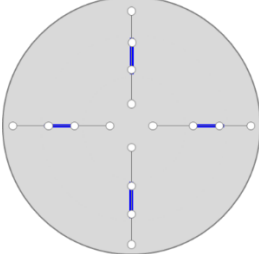
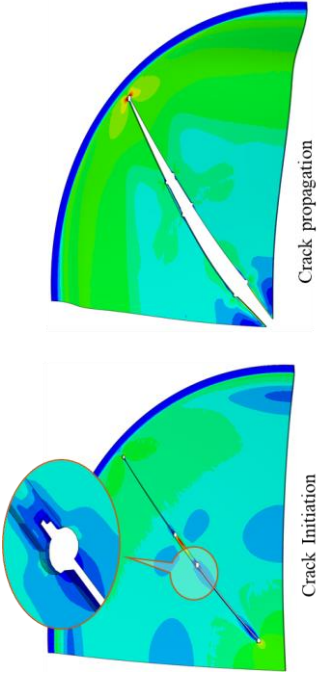
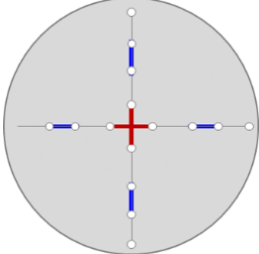
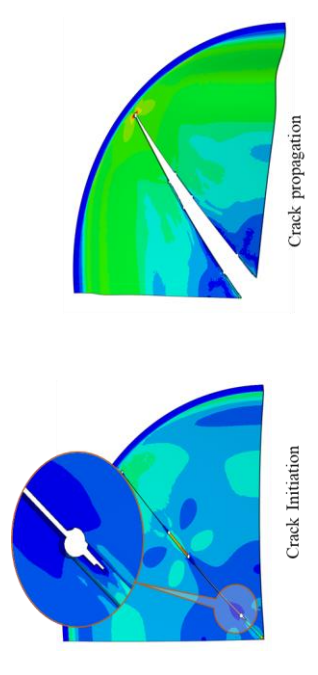
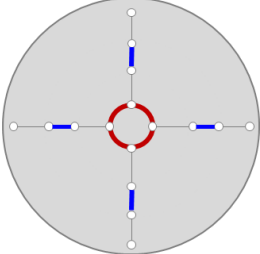
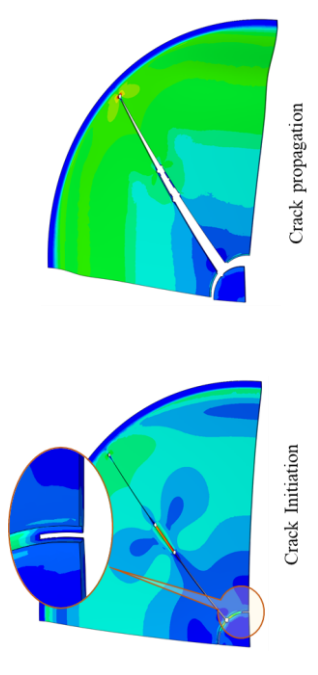
All the variants of non-monolithic configuration are variants of slit configuration. In all the failure modes, due to the application of pressure, slits are widened towards the centre of the disc, which causes failure initiation at the hole near the end of the slits.

Table 7.2: Results of numerical simulation for RD variants

Variant	Geometry	Failure pattern	Results
DSMD			$P_b = 6.2$ bar $FS = 5.2$ $OR = 17\%$ $I = 37$ kN-s

Variant	Geometry	Failure pattern	Results
1			$P_b = 4.4 \text{ bar}$ $FS = 1.5$ $OR = 7\%$ $I = 6 \text{ kN-s}$
1A			$P_b = 2.3 \text{ bar}$ $FS = 1.3$ $OR = 11 \%$ $I = 2 \text{ kN-s}$
1B			$P_b = 3.4 \text{ bar}$ $FS = 1.4$ $OR = 8 \%$ $I = 3 \text{ kN-s}$

Variant	Geometry	Failure pattern	Results
2			<p> $P_b = 6$ bar $FS = 2.8$ $OR = 9\%$ $I = 10$ kN-s </p>
2A			<p> $P_b = 3.4$ bar $FS = 1.5$ $OR = 9\%$ $I = 4$ kN-s </p>
2B			<p> $P_b = 3.5$ bar $FS = 2$ $OR = 11\%$ $I = 4$ kN-s </p>

Variant	Geometry	Failure pattern	Results
3			<p> $P_b = 3.4$ bar $FS = 1.3$ $OR = 8\%$ $I = 4$ kN-s </p>
3A			<p> $P_b = 2.9$ bar $FS = 1.3$ $OR = 9\%$ $I = 3$ kN-s </p>
3B			<p> $P_b = 3.1$ bar $FS = 1.3$ $OR = 8\%$ $I = 3$ kN-s </p>

Wherever slots are provided, failure is initiated in the slot portion due to lower thickness which is evident from the results in Table 7.2.

7.5.2 Summary of results

Summary of results for all disc variants is presented in this section.

7.5.2.1 Burst pressure

The burst pressure of all disc variants is shown in Figure 7.5 and a total of seven variants meets the minimum burst pressure requirement of $P_b < 4$.

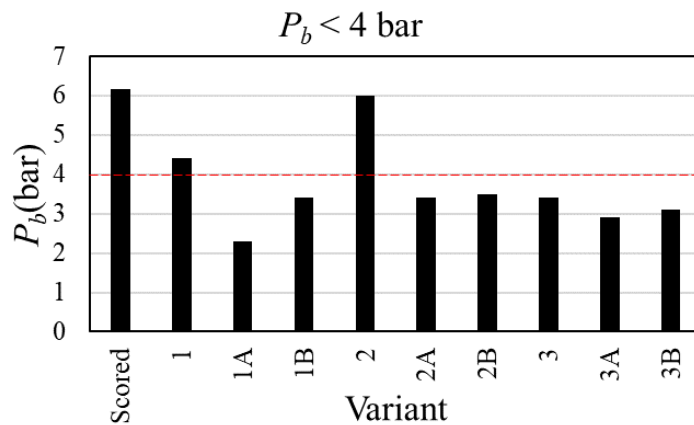


Figure 7.5: Burst pressure for RD variants

7.5.2.2 Factor of safety

The factor of safety of all variants calculated as per Eq. (7.1) is shown in Figure 7.6 and all the variants meets the minimum requirement of $FS > 1$.

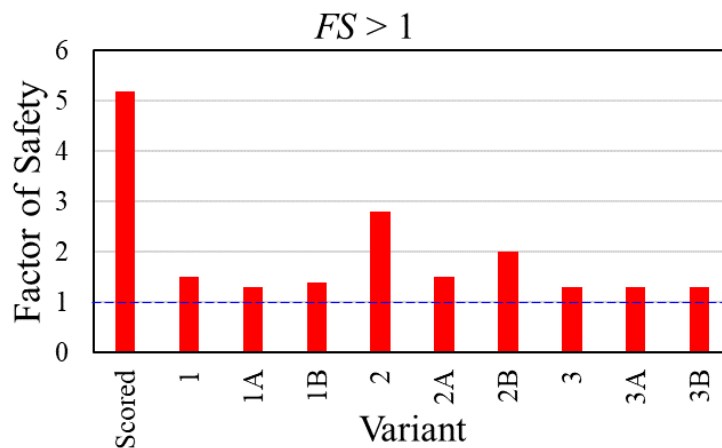


Figure 7.6: Factor of safety in different RD variants

7.5.2.3 Operating ratio

The operating ratio of all variants, which are calculated as per Eq. (4.1), are arranged in descending order and given in Figure 7.7. The maximum operating ratio of 17% can be observed in the scored disc and the minimum in the slit disc.

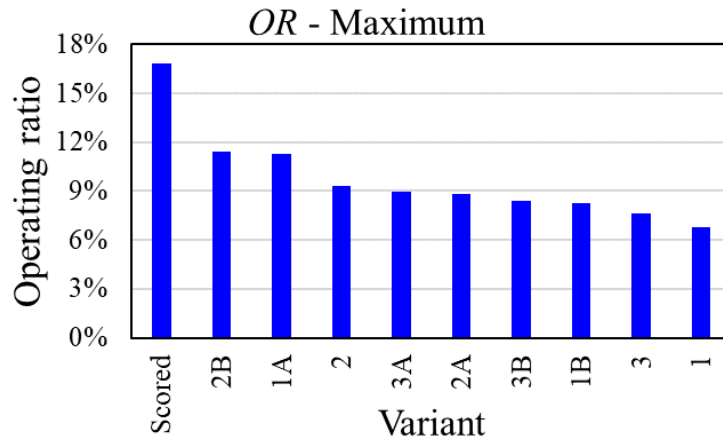


Figure 7.7: Operating ratio of different RD variants

7.5.2.4 Impulse transmitted

Impulse transmitted up to burst for rupture disc variants calculated as per Eq. (4.2) are arranged in ascending order and given in Figure 7.8. Variant-1A has a minimum impulse of 1.8 kN-s, whereas scored disc has a maximum impulse of 11.1 kN-s.

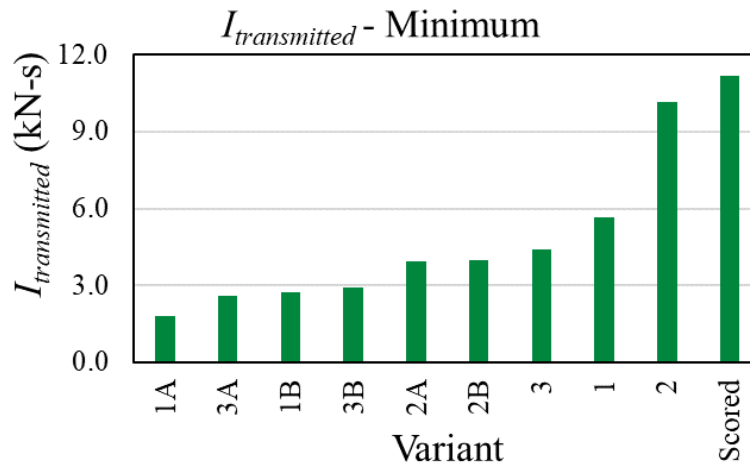


Figure 7.8: Transmitted impulse from different RD variants

7.5.3 Discussion of results and recommendation

From Figure 7.9, Variant-1A, Variant-1B, Variant-2A, Variant-2B, Variant-3, Variant-3A and Variant-3B meet the minimum essential requirements of burst pressure of less than 4 bar and factor of safety of more than 1. They are listed in Table 7.3 and arranged in descending order of operating ratio. Variant-1A has the highest operating ratio, minimum burst pressure, a

factor of safety higher than 1, and minimum transmitted impulse. Therefore, Variant 1A can be recommended for the present application.

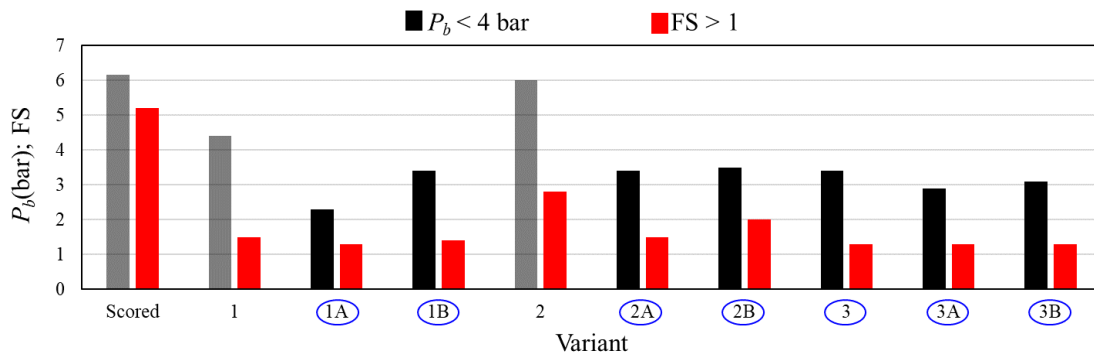


Figure 7.9: RD selection meeting minimum criteria

Table 7.3: RD selection

Variant	P_b (bar)	FS	OR	$I_{transmitted}$ (kN-s)
1A	2.3	1.3	11%	1.8
2B	3.5	2	11%	4.0
3A	2.9	1.3	9%	2.6
2A	3.4	1.5	9%	3.9
1B	3.4	1.4	8%	2.7
3B	3.1	1.3	8%	2.9
3	3.4	1.3	8%	4.4

7.6 Summary

A RD selection criterion for selection of RD for motor container application is proposed in this chapter. Non-monolithic variants of rupture discs have been attempted to achieve a higher operating ratio, low burst pressure, a reasonably higher factor of safety in a static storage state, and a minimum transmitted impulse to the fixity. The finalisation of the design has been achieved through a series of different variants of the rupture disc, having improvements achieved over the progress based on their responses. The best performing Variant-1A of RD selected based on the proposed criterion, as given in Table 7.3, can be manufactured and experimented with to validate the results and achieve higher confidence levels in the future.

Chapter - 8

Conclusions and Future Work

The current research focused on the rupture disc as the removable bottom cover of a motor container. As a cover, it should withstand a static storage pressure of 0.02 MPa and break open instantaneously under a high transient impulse pressure due to motor plume which can go as high as 500 MPa/s. After the literature review, established the non-linear explicit FEA methodology using elastic-plastic material model and continuum damage mechanics-based failure model proposed by Johnson-Cook to simulate the response and failure of thin flat scored metallic disc. This is validated by the available experimental results. Parametric studies have been carried out to understand the effect of various geometric features on the burst characteristics of FSMD. Using the established numerical methodology, investigations have been carried out on domed-scored metallic disc for the current application. Parametric studies have been carried out to understand the influences of various geometric features on the disc burst characteristics of the DSMD.

Based on these studies, a rupture disc configuration has been proposed to meet the present application and is made of structural steel material which is most commonly used in explosion panels. Established the J-C material and damage parameters for the selected material of the rupture disc *i.e.* E250 structural steel based on fracture energy-based damage evolution. Proposed hydroforming-based manufacturing approach for forming the dome shape of the rupture disc and numerically studied the effect of forming operation on the geometric response of the disc. Designed and realised an experimental setup to test the proposed rupture disc configuration. Realised flat and scored metallic discs and conducted experiments at low and higher loading rates through hydrostatic and pneumatic loading setups and validated the results through FEA simulations. By using established FEA simulation methodology and validated material model, proposed non-monolithic rupture disc configurations to meet the present requirement. Finally, an RD selection criterion is proposed to select the RD for the current application among the studied variants.

8.1 Conclusions

Important conclusions which can be drawn from the present thesis are enumerated below.

8.1.1 Studies on scored metallic discs

- Dome shape provided on the scored thin metallic disc satisfies both the rupture disc's storage and failure loading requirements applied in a motor container.
- Scores provided on the thin flat and domed metallic discs facilitate the failure initiation and propagation along them.

8.1.2 Effect of influencing parameters on the behaviour of DSMD

- Loading rate (\dot{P})
 - *At higher loading rates, DSMD fails quickly with marginally higher burst pressure but with less generated impulse, which is a favourable condition for the operation of DSMD.*
 - *There exists a threshold of loading rate (100 MPa/s in present case) beyond which DSMD is insensitive to the increase in loading rate.*
- D/t ratio
 - *Burst pressure, operating ratio ($(D/t) > 150$) and transmitted impulse decrease with the increase in (D/t) ratio indicating the choice of preference for a lower disc thickness. However, this ratio alone is insufficient for arriving at a conclusion on thickness due to reduction in operating ratio due to increase in D/t ratio.*
- H/D ratio
 - *Burst pressure, Operating ratio ($(H/D) > 0.1$) and transmitted impulse increase with the increase in (H/D) ratio indicating $(H/D) = 0.1$, i.e. for a given 720 mm diameter of the disc, less than 72 mm disc height is preferable.*
- t_1/t ratio
 - *Burst pressure and transmitted impulse decrease and the operating ratio is maximum for $(t_1/t) = 0.5$, indicating the score depth of more than 50% of sheet thickness is the preferable value for the current application.*
- b/t ratio
 - *All the parameters almost remain constant for a change in (b/t) ratio, indicating any value of $(b/t) = 1.5$ to 3.5 can be selected based on manufacturing feasibility.*
- l/R ratio
 - *For values of $(l/R) > 0.5$, all the parameters remain constant and at preferable limits, indicating that a minimum score length of more than half the radius of the disc is required. However, score length throughout the radius of the disc facilitates easy score propagation up to fixity. So maximum possible score length is preferable.*

- Number of scores
 - *Plain disc shows the highest Burst pressure and lowest Operating ratio, which is not suitable for the current application*
 - *There is no clear separation of all petals for $N > 3$.*
 - *Predicted responses remained almost constant with any increase in the number of scores N from 6 to 12. The number of scores from 3 to 4 results in slight variations leading to stabilised response and can be preferable.*
- Score geometry
 - *Marginal variation in burst parameters with respect to score geometry indicating RD characteristics more dependent on ligament thickness under the score rather than score geometry itself.*
 - *Semi-circular cross-section seems to be a good choice for the current application but is very difficult to measure.*
 - *Rectangular and triangular with fillet score geometries offer manufacturing easiness and dimensional control. Hence, they can be recommended choices.*
- Thickness of the disc at the score location (ligament thickness = $(t-t_1)$) played an important role in the burst characteristics of the disc than the sheet thickness itself.
- A similar variation in behaviour is observed between Flat and Domed scored metallic discs, with domed scored metallic discs showing higher burst pressure and the highest operating ratio, which makes them the most suitable choice for the current application.
- In both flat and domed scored metallic discs, at loading rates < 25 MPa/s, the failure is initiated in the score at $r/R \approx 0.25$ and propagated towards the disc centre, whereas at all higher loading rates, the failure is always initiated at $r/R \approx 0$ and propagated towards the fixed boundary.
- Both burst pressure and operating ratios can't be considered in isolation for the criterion of the selection rupture disc.

8.1.3 RD selection for motor container

- Operating ratio is proven to be critical in finalising the rupture disc for a given burst pressure.
- Even though the scored metallic discs have higher operating ratios and are simple in geometry and construction, they fail at high burst pressure and impose manufacturing difficulties in accurately producing the scores, making them unsuitable for the motor container application.

- Non-monolithic variants of rupture discs help achieve a higher operating ratio, low burst pressure, a reasonably higher factor of safety in the static storage state, and a minimum transmitted impulse to the fixity.
- Slotted discs are the suitable choice for the present application compared to scored discs.
- The best performing Variant-1A of RD, as given in Table 7.3, can be manufactured and experimented with to validate the FEA results and achieve higher confidence levels in the future.

8.1.4 Johnson-Cook material and damage models

- Conventional J-C material model in combination with fracture energy-based damage evolution criterion can be used to simulate the failure of scored metallic discs with reasonable accuracy.
- The proposed modification to the J-C model retains the primary advantage of the conventional J-C model in isolating material effects for ease of calibration. It offers potential flexibility to be adopted for other materials as well.

8.1.5 Hydro-forming for domed RDs

- Hydro-forming experiments have shown close agreement with numerical predictions regarding the reduction in thickness of the disc due to stretching during the course of deformation. However, the difference is about 1.6% for galvanic steel.
- Hydro-forming is proven to be an effective manufacturing technique for producing domed RDs in limited quantities.

8.1.6 Overall conclusion

- The difference in prediction of burst pressure for FSMD is 1.5% and DSMD is 3.1%, which validates the adapted material model, numerical simulation procedure and experimental methodology.

8.2 Specific research contributions

The specific research contributions made through present research on rupture disc for a motor container are summarised below.

- Primarily, the research has culminated in developing a rupture disc which can meet both storage pressure of the motor container with sufficient safety factors and also undergoes instantaneous rupture with a desired failure pattern when subjected to a transient impulse pressure upon initiation of a motor inside the container.

- Established a non-linear explicit FEA simulation procedure to numerically simulate the deformation and failure of a rupture disc under different loading rates with reasonable accuracy.
- Proposed a methodology for selecting rupture discs for both storage and breakaway conditions.
- Redefined the operating ratio (*OR*) of a rupture disc in the current research and it is calculated as a ratio of maximum static operating pressure (*MSOP*) to burst pressure so that this ratio can be estimated from numerical results.
- Provided a step-by-step approach in characterising the Johnson-Cook material and damage model parameters. In this process, adopted a fracture energy-based damage evolution which can be directly implemented in any explicit FEA simulation software for a given material.
- Proposed a modification to the strain rate parameter of the Johnson-Cook material model to take care of large strain rate variations, which can still retain the advantage of isolating material effects during characterisation.
- Explored and implemented a cost-effective hydroforming method for manufacturing of domed rupture disc.

8.3 Limitation in present research

- Present research is limited to only two types of rupture discs, *viz.* scored RD and slit RD, which are circular.
- Only one type of material *i.e.* E250 structural steel is studied.
- Effects of temperature on the failure characteristics of RD is not considered in experiments.
- Anisotropy of rupture disc and work hardening in hydro-forming are neglected.

8.4 Scope for future work

The present research has provided considerable outcomes to overcome the research gaps identified at the beginning of the thesis. From the limitations of current research work, some areas of research that can be undertaken as an extension of this thesis is summarised below.

- Suitability of other types of rupture disc configurations like reverse domed rupture discs, geometric configurations like square or rectangular shapes, and other materials like stainless steel. Their numerical simulation and experimental validations can be explored.
- Simulation of fluid temperature's effect on rupture's burst characteristics can be studied.

- Anisotropic behaviour of RD sheet and work hardening due to forming can be accounted in FEA simulations.
- In the present research, the Lagrangian approach is followed to simulate the failure of the rupture disc. The continuous flow of the plume acting on the rupture disc and its subsequent failure pattern can be well captured through the combined Eulerian-Lagrangian approach in explicit FEA simulations, which can be explored in future studies.
- Experimentation on larger diameter rupture discs at higher loading rates proved to be a great challenge as it requires a huge setup and has taken more than 70% of the total duration of research. Therefore, scale-down approaches can be investigated.
- Modified J-C model, which is applicable for an extensive range of strain rate variations, can be built-in explicit software code to simulate the response.

References

- [1] Somayajulu D and Narayanamurthy V. “Analysis of rupture disc”. In: *Proceedings of Indian Conference on Applied Mechanics (INCAM 2017), MNNIT Allahabad*. 2017. Paper no.49:1-7.
- [2] Smith P and Zappe R W. “Valve selection handbook”. 5th ed, Elsevier, Amsterdam, Netherlands. 2004. 227-267.
- [3] Aune V, Fagerholt E, Langseth M and Børvik T. “A shock tube facility to generate blast loading on structures”. *International Journal of Protective Structures*. 2016. 7(3):340–366; doi:10.1177/2041419616666236
- [4] “Rupture Disc Types”. [monograph on internet] *Mechanical Engineering Site*. <http://www.mechanicalengineeringsite.com/rupture-disk-types>. Available from: Mar 16, 2017.
- [5] Lake G F and Inglis N P. “The design and manufacturing of bursting discs”. In: *Proceedings of Institution of Mechanical Engineers*. 1939. 102(1):365-378.
- [6] ASME BPVC VIII-3. “Rules for Construction of Pressure Vessels”. *American Society Mechanical Engineers*.2017.
- [7] ISO 4126-1. “Safety devices for protection against excessive pressure-Part1: Safety Valves”.2013
- [8] ISO 4126-2. “Safety devices for protection against excessive pressure-Part 2: Bursting disc safety devices”.2003.
- [9] ISO 6718. “Bursting discs and bursting disc devices”.1991.
- [10] Murthy D V R, Chennakeshava Reddy A and Bhaskar Rao Y. “Factors to be considered for selection and design of rupture Disc”. In: *Proceedings of ASME*. 2006. Paper no. ICONE14-89634.
- [11] Murthy D V R. “Finite Element Analysis of Rupture Disc”. In: *Proceedings of Int-ANSYS-Conference*. 2006. Paper no.227.
- [12] Murthy D V R and Bhaskar Rao Y. “Computer simulation of rupture disc”. In: *Proceedings ASME Pressure Vessels and Piping Conference*. 2006. Paper no. PVP2006-ICPVT-11-94060:233-240.
- [13] Cichocki K and Perego U. “Rectangular plates subjected to blast loading: the comparison between experimental results, numerical analysis and simplified analytical approach”. *Journal de Physique IV Colloque*. 1997. 07(C3):761-766.
- [14] Ramajeyathilagam K and Vendhan C P. “Underwater explosion damage of ship hull panels”. *Defence Science Journal*. 2003. 53(4):393-400.
- [15] Randers Pehrson G and Bannister K. “Air blast loading model for DYNA 2D and DYNA 3D”. *Army Research Laboratory, Aberdeen Proving Ground, MD, USA*. 1997. Technical Report No.: ARL TR-1310.

- [16] Vo T P, Guan Z W, Cantwell W J and Schleyer G K. “Low-impulse blast behaviour of fibre-metal laminates”. *Composite Structures*. 2012. 94:954-965.
- [17] Sahu R R, and Gupta P K. “Blast diffusion by different shape of vehicle hull”. *International Journal for Automotive Engineering and Technologies*. 2013. 2(4): 132-139.
- [18] Langdon G S, Karagiozova D, Von Klempererc C J, Nuricka G N, Ozinskya A and Pickering E G. “The air-blast response of sandwich panels with composite face sheets and polymer foam cores: Experiments and predictions”. *International Journal of Impact Engineering*. 2013. 54:64-82.
- [19] Hua Y, and Akula P K. “Experimental and numerical investigations of carbon fiber sandwich panels subjected to blast loading”. *Composites Part B*. 2014. 56:456-63.
- [20] Nyström U and Gylltoft K. “Numerical studies of the combined effects of blast and fragment loading”. *International Journal of Impact Engineering*. 2009. 36:995–1005.
- [21] Nurick G N and Martin J B. “Deformation of thin plates subjected to impulsive loading-A review: Part I: Theoretical considerations”. *International Journal of Impact Engineering*. 1989. 8(2):159–170; doi:10.1016/0734-743X(89)90014-6.
- [22] Nurick, G N and Martin J B. “Deformation of thin plates subjected to impulsive loading-a review Part II: Experimental studies”. *International Journal of Impact Engineering*. 1989. 8(2):171-186; doi:10.1016/0734-743X(89)90015-8.
- [23] Yuen S C K, Nurick G N, Langdon G S and Iyer Y. “Deformation of thin plates subjected to impulsive load: Part III - an update 25 years on”. *International Journal of Impact Engineering*. 2017. 107:108–117; doi:10.1016/j.ijimpeng.2016.06.010.
- [24] Nurick G N, and Shave G C. “The deformation and tearing of thin square plates subjected to impulsive loads – An experimental study”. *International Journal of Impact Engineering*. 1996. 18(1):99-116; doi:10.1016/0734-743X(95)00018-2.
- [25] Olson M D. “Efficient modelling of blast loaded stiffened plate and cylindrical shell structures”. *Composites & Structures*. 1991. 40(5):1139-1149; doi:10.1016/0045-7949(91)90385-Y.
- [26] Nurick G N, Gelman M E and Marshall N S. “Tearing of blast loaded plates with clamped boundary conditions”. *International Journal of Impact Engineering*. 1996. 18(7-8):803-827; doi:10.1016/S0734-743X(96)00026-7.
- [27] Smith R G T and Nurick G N. “The deformation and tearing of thin circular plates subjected to impulsive loads”. *International Journal of Impact Engineering*. 1991. 11(1):77–91; doi:10.1016/0734-743X(91)90032-B.
- [28] Bonorchis D and Nurick G N. “The effect of welded boundaries on the response of rectangular hot-rolled mild steel plates subjected to localised blast loading”.

- International Journal of Impact Engineering*. 2007. 34(11):1729-1738;
doi:10.1016/j.ijimpeng.2006.11.002.
- [29] Gupta N K and Nagesh. “Deformation and tearing of circular plates with varying support conditions under uniform impulsive loads”. *International Journal of Impact Engineering*. 2007. 34(1):42–59; doi:10.1016/j.ijimpeng.2006.05.002.
- [30] Marchand K A and Alfawakhiri F. “Blast and Progressive Collapse - Facts for Steel Buildings”. *American Institute of Steel Construction, Inc*. 2004. Technical report No. 2.
- [31] Jacob N, Nurick G N and Langdon G S. “The effect of stand-off distance on the failure of fully clamped circular mild steel plates subjected to blast loads”. *Engineering Structures*. 2007. 29(10):2723–2736;
doi:10.1016/j.engstruct.2007.01.021.
- [32] Goel M D, Matsagar V A and Gupta A K. “Dynamic response of stiffened plates under air blast”. *International Journal of Protective Structures*. 2011. 2(1):139–155;
doi:10.1260/2041-4196.2.1.139.
- [33] Nagesh and Gupta N K. “Large deformations and tearing of circular plates and plate-tube structural combinations under impulsive loading”. *Procedia Engineering*. 2017. 173:526-532; doi:10.1016/j.proeng.2016.12.083.
- [34] Nurick G N, Olson M D, Fagnan J R and Levin A. “Deformation and tearing of blast-loaded stiffened square plates”. *International Journal of Impact Engineering*. 1995. 16(2):273-291; doi:10.1016/0734-743X(94)00046-Y.
- [35] Yuan Y and Tan P J. “Deformation and failure of rectangular plates subjected to impulsive loadings”. *International Journal of Impact Engineering*. 2013. 59:46–59;
doi:10.1016/j.ijimpeng.2013.03.009.
- [36] Rudrapatna N S, Vaziri R and Olson M D. “Deformation and failure of blast-loaded square plates”. *International Journal of Impact Engineering*. 1999. 22(4):449-467;
doi:10.1016/S0734-743X(98)00046-3.
- [37] Sharma P K, Patel B P and Lal H. “On the response of hemispherical shell under blast loading”. *Procedia Engineering*. 2017. 173:533–538;
doi:10.1016/j.proeng.2016.12.085.
- [38] Lee D W, Park J M, Kwon Y D and Kwon SB. “Effect of rupture disc curvature on the compression waves in S/R valve”. *Journal of Mechanical Science and Technology*. 2008. 22:755–760; doi:10.1007/s12206-008-0101-x.
- [39] Jeong J Y, Jo W, Kim H, Baek S H and Lee S B. “Structural analysis on the superficial grooving stainless-steel thin-plate rupture discs”. *International Journal of Precision Engineering and Manufacturing*. 2014. 15:1035–1040;
doi:10.1007/s12541-014-0433-7.

- [40] Aune V, Valsamos G, Casadei F, Langseth M and Børvik T. “On the dynamic response of blast-loaded steel plates with and without pre-formed holes”. *International Journal of Impact Engineering*. 2017. 108:27–46; doi:10.1016/j.ijimpeng.2017.04.001.
- [41] Zhu Z, Xu W, Luo Z and Zheng H. “Finite element analysis on the temperature-dependent burst behavior of domed 316L austenitic stainless steel rupture disc”. *Metals*. 2020. 10(2):232; doi:10.3390/met10020232.
- [42] Colombo M, Martinelli P and di Prisco M. “Validation of a Computational Approach to Predict Bursting Pressure of Scored Steel Plates”. *Experimental Mechanics*, 2014. 54: 1555–1573; doi:10.1007/s11340-014-9916-9.
- [43] Rao C L, Narayanamurthy V, and Simha, K R Y. “Applied Impact Mechanics”. Wiley. 2016; doi:10.1002/9781119241829.
- [44] Johnson G R and Cook W H. “A constitutive model and data from metals subjected to large strains, high strain rates and high temperatures”. In: *Proceedings of 7th International Symposium on Ballistics, Hague, Netherlands*. 1983. 541–547.
- [45] Johnson G R and Cook W H. “Fracture characteristics of three metals subjected to various strains, strain rates, temperatures and pressures”. *Engineering Fracture Mechanics*. 1985. 21(1):31–48.
- [46] Vedantam K, Bajaj D, Brar N S and Hill S. “Johnson - Cook strength models for mild and DP 590 steels”. In: *AIP Conferece. Proceedings*. 2006. 845(1):775–778; doi:https://doi.org/10.1063/1.2263437.
- [47] Xu Z and Huang F. “Plastic behavior and constitutive modeling of armor steel over wide temperature and strain rate ranges”. *Acta Mechanica Solida Sinica*. 2012. 25 (6):598–608; doi: https://doi.org/10.1016/S0894-9166(12)60055-X.
- [48] Banerjee A, Dhar S, Acharyya S, Datta D and Nayak N. “Determination of Johnson cook material and failure model constants and numerical modelling of Charpy impact test of armour steel”, *Material Science Engineering A*. 2015. 640:200–209; doi:10.1016/j.msea.2015.05.073.
- [49] Farahani H K, Ketabchi M and Zangeneh S. “Determination of Johnson–Cook plasticity model parameters for Inconel 718”. *Journal of Material Engineering and Performance*. 2017. 26(11):5284–5293; doi:https://doi.org/10.1007/s11665-017-2990-2.
- [50] Murugesan M and Jung D W. “Johnson Cook material and failure model parameters estimation of AISI-1045 medium carbon steel for metal forming applications”. *Materials*. 2019. 12(4):609; doi:10.3390/ma12040609.
- [51] Majzooobi G H and Dehgolan F R. “Determination of the constants of damage models”. *Procedia Engineering*. 2011. 10:764–773; doi:https://doi.org/10.1016/j.proeng.2011.04.127

- [52] Bal B, Karaveli K K, Cetin B and Gumus B. “The precise determination of the Johnson–Cook material and damage model parameters and mechanical properties of an aluminum 7068-T651 alloy”. *Journal of Engineering Materials and Technology*. 2019. 141(4): 141001; doi:<https://doi.org/10.1115/1.4042870>.
- [53] Børvik T, Langseth M, Hopperstad O S and Malo K A. “Ballistic penetration of steel plates”. *International Journal of Impact Engineering*. 1999. 22(9–10):855–886; [https://doi.org/10.1016/S0734-743X\(99\)00011-1](https://doi.org/10.1016/S0734-743X(99)00011-1).
- [54] Lemaitre J. “A Course on Damage Mechanics”. *Springer, Berlin, Heidelberg, Germany*, 2012.
- [55] ASTM E8/E8M-08. “Standard Test Methods for Tension Testing of Metallic Materials”, *American Society for Testing Materials*. 2008.
- [56] ASTM E21-17. “Standard Test Methods for Elevated Temperature Tension Tests of Metallic Materials”, *American Society for Testing Materials*. 2019.
- [57] Hertzberg and Richard W. “Deformation and fracture mechanics of engineering materials”. *Wiley, United Kingdom*. 1996.
- [58] Satopaa V, Albrecht J, Irwin D and Raghavan B. “Finding a "Kneedle" in a Haystack: Detecting Knee Points in System Behavior”. *In: 31st International Conference on Distributed Computing Systems Workshops*. 2011. 166-171; doi: 10.1109/ICDCSW.2011.20.
- [59] ABAQUS 6.14.3 Documentation. Dassault Systèmes Simulia Corp., Providence, RI, USA. 2014
- [60] ABAQUS Analysis User’s Manual. ABAQUS Version 2019, Dassault Systems. 2017 (Dassault Systems, Providence, RI, USA, 2017)
- [61] ABAQUS/Explicit User’s Manual. ABAQUS Version 2019, Dassault Systems. 2017 (Dassault Systems, Providence, RI, USA, 2017)
- [62] Hillerborg A, Modéer M and Petersson P E. “Analysis of crack formation and crack growth in concrete by means of fracture mechanics and finite elements”. *Cement and Concrete Research*. 1976. 6(6):773-781; doi:[https://doi.org/10.1016/0008-8846\(76\)90007-7](https://doi.org/10.1016/0008-8846(76)90007-7).
- [63] Yu H, Guo Y and Lai X. “Rate-dependent behavior and constitutive model of DP600 steel at strain rate from 10^{-4} to 10^3 s⁻¹”. *Materials & Design*. 2009. 30(7):2501–2505; doi:<https://doi.org/10.1016/J.MATDES.2008.10.001>.
- [64] Wei R, Song R B, Jiang L and Cai H J. “Deformation Behaviors and Constitutive Model of DP1000 under Different Strain Rates”. *In: IUMRS International Conference in Asia*. 2017. 898:810–817; doi:<https://doi.org/10.4028/www.scientific.net/MSF.898.810>.

- [65] Wang X, Huang C, Zou B, Liu H, Zhu H and Wang J. “Dynamic behavior and a modified Johnson–Cook constitutive model of Inconel 718 at high strain rate and elevated temperature”. *Materials Science and Engineering: A*. 2013. 580:385–390; doi:<https://doi.org/10.1016/J.MSEA.2013.05.062>.
- [66] Zhang D N, Shangguan Q Q, Xie C J and Liu F. “A modified Johnson–Cook model of dynamic tensile behaviors for 7075-T6 aluminum alloy”. *Journal of Alloys and Compounds*. 2015. 619:186–194. doi:<https://doi.org/10.1016/J.JALLCOM.2014.09.002>.
- [67] Zhong X, Yan Y and Zhang Q. “Dynamic Deformation Behaviors and Constitutive Relations of High-Strength Weldox700E Steel”. *Acta Mechanica Solida Sinica*. 2019. 32(4):431–445; doi:<https://doi.org/10.1007/s10338-019-00098-3>.
- [68] Zhong W Z, Mbarek I A, Rusinek A, Bernier R, Jankowiak T and Sutter G. “Development of an experimental set-up for dynamic force measurements during impact and perforation, coupling to numerical simulations”. *International Journal of Impact Engineering*. 2016. 91:102–115.
- [69] Baker W E, Cox P A, Westine P S, Kulesz J J and Strehlow R A. “Structural Response: Simplified Analysis Techniques”. In: *Fundamental Studies in Engineering, Explosion Hazards and Evaluation*, Elsevier Science. 1983. 5:273-364; doi: 10.1016/B978-0-444-42094-7.50012-4.
- [70] Siegert K and Wagner S. “Hydroforming sheet metal forming components”, In: *Muammer Koç (Ed.) Hydro-forming for Advanced Manufacturing*, Woodhead Publishing, Cambridge. 2008. 216–237.
- [71] Ceretti E, Fiorentino A and Giardini C. “Hydroforming (Sheets and Tubes)”. In: *Laperrière L and Reinhart G (Eds.), CIRP Encyclopedia of Production Engineering*, Springer, Heidelberg. 2014. 674–682.
- [72] Marciniak Z, Duncan J L and Hu S J. “Hydroforming”, In: *Marciniak Z, Duncan J L, S.J. Hu (Eds.), Mechanics of Sheet Metal Forming, second ed., Butterworth-Heinmann, Oxford*. 2002. 152–163.
- [73] Zhang S H, Wang Z R, Xu Y, Wang Z T, Zhou L X. “Recent developments in sheet hydro-forming technology”. *Journal of Materials Processing Technology*. 2004. 151:237–241.
- [74] Bell C, Corney J, Zuelli N and Savings D. “A state of the art review of hydro-forming technology”. *International Journal Material Forming*. 2020. 13:789–828.
- [75] Cherouat A, Ayadi M, Mezghani N and Slimani F. “Experimental and finite element modelling of thin sheet hydro-forming processes”. *International Journal of Material Forming*. 2008. 1:313–316.

- [76] Parsa M H and Darbandi P. “Experimental and numerical analyses of sheet hydro-forming process for production of an automobile body part”. *Journal of Material Processing Technology*. 2008. 198:381– 90.
- [77] Lei L P, Kim J and Kang B S. “Analysis and design of hydro-forming process for automobile rear axle housing by FEM”. *International Journal of Machine Tools and Manufacture*. 2000. 40:1691–1708.
- [78] Kang B S, Son B M and Kim J. “A comparative study of stamping and hydro-forming processes for an automobile fuel tank using FEM”. *International Journal of Machine Tools and Manufacture*. 2004. 44:87–94.
- [79] Zampaloni M, Abedrabbo N and Pourboghrat F. “Experimental and numerical study of stamp hydro-forming of sheet metals”. *International Journal of Mechanical Sciences*. 2003. 45:1815–1848.
- [80] Zhang S H and Danckert J. “Development of hydro-mechanical deep drawing”. *Journal of Material Processing Technology*. 1998. 83:14–25.
- [81] Zhang S H. “Developments in hydro-forming”. *Journal of Material Processing Technology*. 1999. 91:236–244.
- [82] Kandil A. “An experimental study of hydro-forming deep drawing”. *Journal of Material Processing Technology*. 2003. 134:70–80.
- [83] Nakamura S, Sugiura H, Onoe H and Ikemoto K. “Hydromechanical drawing of automotive parts”. *Journal of Material Processing Technology*. 1994. 46:491–503.
- [84] Lang L H, Wang Z R, Kang D C, Yuan S J, Zhang S H, Danckert J and Nielsen K B, “Hydro-forming highlights: Sheet hydro-forming and tube hydro-forming”. *Journal of Material Processing Technology*. 2004. 151:165–177.
- [85] Zhang S H, Zhou L X, Wang Z T and Xu Y. “Technology of sheet hydro-forming with a movable female die”. *International Journal of Machine Tools and Manufacture*. 2003. 43:781–785.
- [86] IS 277. “Galvanized steel sheets (plain and corrugated)-specification (Sixth revision)”. *Indian Standard*. 2003
- [87] 817M40; BS 970-3. “Specification for wrought steel for mechanical and allied engineering purposes, part 3: Bright bars for general engineering purpose”, *British Standard*. 1991.
- [88] 45C8; IS 1570 (PART-II)-1979(R2009). “Schedules for Wrought Steels – part 2: Carbon steels (unalloyed steels)”. *Indian standard*. 2009.
- [89] ANSYS Engineering Analysis System User’s Manual. Houston, Pa, Swanson Analysis Systems. 2019.

Publications

International Journals

Published

- 1) Gopinath K, Narayanamurthy V, Khaderi SN and Rao YVD. “Determination of Parameters for Johnson-Cook dynamic constitutive and damage models for E250 structural steel and experimental validations”. *Journal of Materials Engineering and Performance, Accepted for publication. Sept 2023, In Press.*
- 2) Gopinath K, Narayanamurthy V and Rao YVD. “Deformation and failure of thin domed-scored metallic disc under impulsive loading”. *International Journal of Protective Structures.* 2022; doi: <https://doi.org/10.1177/20414196221095249>.
- 3) Gopinath K, Narayanamurthy V and Rao YVD. “Response of a Thin Flat Scored Metallic Disc under Pressure Impulse”. *Defense Science Journal.* 2022. 72(3):473-484; doi:<https://doi.org/10.14429/dsj.72.17755>
- 4) Gopinath K, Narayanamurthy V and Rao YVD. “Numerical and Experimental Studies on Hydro-Forming of a Thin Metallic Disc”. *Material Science Forum; Trans Tech Publications.* 2022. 1048.270; doi:<https://doi.org/10.4028/www.scientific.net/msf.1048.270>.

International Conferences

- 1) K. Gopinath, V. Narayanamurthy, and YVD Rao. “Study of a flat scored thin metallic disc under impulsive loading”. *In: Virtual Seminar on Applied Mechanics.* 2020.
- 2) Gopinath K, Narayanamurthy V, and Rao YVD. “Failure behavior of a thin domed steel disc with and without scores under a pressure impulse”. *In: 1st International conference on Industrial Problems in Machines and Mechanisms at BITS Pilani (Hyderabad Campus).* 2020.
- 3) K. Gopinath, V. Narayanamurthy, SN Khaderi and YVD Rao. “Modification of Strain Rate Effect in J-C Material Model”. *In: 13th International Symposium on Plasticity and Impact Mechanics at IIT Madras.* 2022.

Biography of the Candidate

Mr. Gopinath Kanakadandi completed his Bachelor's in Mechanical Engineering from Jawahar Lal Nehru Technological University (JNTUH), Hyderabad and Post Diploma in Tool Design from Central Institute of Tool Design, Hyderabad. He works as Scientist in Research Centre Imarat, Defence R&D Organisation. His area of work involves the design of aerospace structures and mechanisms. His research work primarily focuses on understanding the behaviour of metallic scored plates under impulsive loading and their characterisation.

Biography of the Supervisor-1

Prof. Venkata Daseswara Rao Yendluri holds a Master's in Design Engineering from IIT, Delhi and Ph.D. from NIT Raipur, India. He works as a Professor in the Mechanical Engineering Department of BITS-Pilani, Hyderabad Campus. He has 37 years of Academic experience. He has guided 9 Ph.D. students and two students are currently working under his supervision for their Ph.D. He taught several PG and UG level engineering courses and his area of expertise includes Kinematics of Machines and Robotics, Structural Dynamics, Biomaterials, Fluid induced vibrations and Mechatronics. He has published around 21 technical papers in international journals and 27 technical papers in international conferences. He has authored three book chapters and one text book.

Biography of the Supervisor-2

Dr. Vijayabaskar Narayanamurthy holds a Master's in Applied Mechanics from IIT Madras, India and a Ph.D. from The University of Edinburgh, UK. He is a Technology Advisor (Defence Technology) at the Embassy of India, Washington D.C. USA. He has 22 years of R&D experience in flight structures and mechanisms and one year of R&D experience in agricultural tractors. His areas of expertise include hybrid structures, impact mechanics and crashworthiness and mechanics of fastenings. He holds two granted and two published patents. He authored one text book, edited four books and 15 book chapters. He has published 35 international journals, 24 international and 34 national conference proceedings. He has guided 6 Ph.D. students and presently supervising 7 Ph.D. students.